UNIVERSITAT POLITÈCNICA DE CATALUNYA
BARCELONATECH
Departament d'Enginyeria Electrònica

# On-Chip Adaptive Power Management for WPT-Enabled IoT

Thesis submitted in partial fulfillment of the requirement for the **PhD Degree** issued by the **Universitat Politècnica de Catalunya**, in its **Electronic Engineering Program**

by

**Mohamed Ahmed Saad Abdelhameed**

Thesis advisor:

**Dr. Eduard Alarcón-Cot**

Barcelona, April 2018

# Abstract

Internet of Things (IoT), as broadband network connecting every physical objects, is becoming more widely available in various industrial, medical, home and automotive applications. In such network, the physical devices, vehicles, medical assistance, and home appliances among others are supposed to be embedded by sensors, actuators, radio frequency (RF) antennas, memory, and microprocessors, such that these devices are able to exchange data and connect with other devices in the network. Among other IoT's pillars, wireless sensor network (WSN) is one of the main parts comprising massive clusters of spatially distributed sensor nodes dedicated for sensing and monitoring environmental conditions. The lifetime of a WSN is greatly dependent on the lifetime of the small sensor nodes, which, in turn, is primarily dependent on energy availability within every sensor node. Predominantly, the main energy source for a sensor node is supplied by a small battery attached to it. In a large WSN with massive number of deployed sensor nodes, it becomes a challenge to replace the batteries of every single sensor node especially for sensor nodes deployed in harsh environments. Consequently, powering the sensor nodes becomes a key limiting issue, which poses important challenges for their practicality and cost.

Therefore, in this thesis we propose enabling WSN, as the main pillar of IoT, by means of resonant inductive coupling (RIC) wireless power transfer (WPT). In order to enable efficient energy delivery at higher range, high quality factor RIC-WPT system is required in order to boost the magnetic flux generated at the transmitting coil. However, an adaptive front-end is essential for self-tuning the resonant tank against any mismatch in the components values, distance variation, and interference from close metallic objects. Consequently, the purpose of the thesis is to develop and design an adaptive efficient switch-mode front-end for self-tuning in WPT receivers in multiple receiver system.

The thesis start by giving background about the IoT system and the technical bottleneck followed by the problem statement and thesis scope. Then, Chapter 2 provides detailed backgrounds about the RIC-WPT system. Specifically, Chapter 2 analyzes the characteristics of different compensation topologies in RIC-WPT followed by the implications of mistuning on efficiency and power transfer capability. Chapter 3 discusses the concept of switch-mode gyrators as a potential candidate for generic variable reactive element synthesis while different potential applications and design cases are provided. Chapter 4 proposes two different self-tuning control for WPT receivers that utilize switch-mode gyrators as variable reactive element synthesis. The performance aspects of control approaches are discussed and evaluated as well in Chapter 4. The development and exploration of more compact front-end for self-tuned WPT receiver is investigated in Chapter 5 by proposing a phase-controlled switched inductor converter. The operation and design details of different switch-mode phase-controlled topologies are given and evaluated in the same chapter. Lastly, Chapter 6 proposes a novel approach for real power and reactive power control in phase-controlled converters. Finally, Chapter 7 provides the conclusions and highlight the contribution of the thesis, in addition to suggesting the related future research topic.

# Dedication

*To my respected parents, Ahmed Saad and Faten Mahmoud, for their eternal love and devotion,,,*

*To my wife, Noha, my son, Ahmed, and my daughter, Fayrouz, for their endless love, support and patience,,,*

**إلى أبي العزيز، أحمد سعد، الذي كان ومازال سندي ومصدر فخري، ستظل دائمًا مثلي الأعلى،،،**

**إلى أمي الحبيبة، فاتن محمود، معني الحب والحنان في حياتي، أنتي بسمة حياتي وسر وجودي،،،**

**إلى زوجتي الحبيبة، نهى، لكونك في حياتي، فلولاكي ماكان نجاحي،،،**

**إلى ابني الحبيب، أحمد، وابنتي الجميلة، فيروز، منكم أستمد قوتي وتعلمت معنيً جديدًا للحياة،،،**

“If the doors were to be opened at the first try, with only one knock, there would probably be nothing behind them, except for emptiness... the rooms containing treasures require long and arduous attempts.”

— **Ahmed Khaled Tawfik**

# Acknowledgment

At this time, as a journey of more than four years is coming to an end, it is time to mention all the great people who have turned these arduous days of work and study into bright memories.

First of all, I would like to express my deep gratitude and respect to my advisor, Prof. Eduard Alarcón. It was a real pleasure for me to have such an exceptional scholar and a great person as an advisor. Although I was one among a long queue of PhD students who are always asking for his time and support, he led me through the research as if I have been the only PhD student he is supervising. Strong but supportive, friendly yet firm, he knew perfectly well when to insist on previously determined plans and when to leave me to follow my own independent work. His office door was always open, and I will never forget the hours of constructive discussion we had throughout the past four years. Whenever he felt very busy with a very dense schedule, he used to share his lunchtime with me, where we discuss, think and plan while we are having our meals. His enthusiasm and exceptional visionary understanding of various engineering research areas, and how they relate to our life, is something I would like to inherit and follow in my future work.

The second blessing I had was to have the opportunity to collaborate with other groups at the UPC. Among them, I remember the meetings we have with Prof. Francesc Moll Echeto and his PhD student, David Cavalhiero. As well, I had the pleasure of getting in contact with Prof. Herminio Martinéz, in which we exchanged the valuable scientific knowledge related to our research projects.

I have also been exceptionally blessed to cross paths with many other outstanding people at the Electronics Engineering Department during my PhD journey. At the risk of not mentioning some of them, I would like to specially thank my colleagues David Cavalheiro, Núria Egidos, Elisenda Bou-Balust, Mario Iannazzo, Chen Jin, Dídac Vega, Chenna, Mireya Patricia Zapata, for their friendship, support, and deep intellectual conversations that influenced my ideas and contributed to my creativity.

In addition, I am thankful to all of my friends for bringing comfort and happiness to my life and for helping me in overcoming the challenges of adapting to a new country and new culture. Thank you Ahmed Rabei, Ahmed Elfalah, Mohamed Yousef, Javier Chavarria, Hadeer, without anyone of you it would never be easy for me.

However, there is someone who always stood by me, who always celebrated my victories and encouraged me through tough times, someone whose encouragement, love, and sacrifice were endless. Thank you my wife, Noha, from the bottom of my heart!

Finally, I would like to thank my parents, Ahmed and Faten, for all of their support in the past years, as well as my dear son Ahmed and my little daughter Fayrouz for bringing many happy moments into my life and giving a different meaning to my life.

# Contents

# List of Figures

# List of Tables

Chapter

# 1

# Introduction

Historically, the term of "*Internet of Things*" has been invented by Kevin Ashton, the co-founder of the Auto-ID center at Massachusetts Institute of Technology (MIT) in 1998. The term describes a system where sensor-based physical objects are connected to a huge database that contains information about each physical object. Since 1998, the Internet of Things (IoT) term gained a wide interest and become widely recognized and realized in practice.

The motivation of this chapter is to expose an overview about the technical challenges and the focus of the thesis. A brief revision for the IoT systems and their building blocks will be discussed. Among the different blocks of IoT system, we will focus more on wireless sensor network (WSN) as the most effective pillar in IoT. The techniques for enabling autonomous operation for inaccessible sensor nodes will be also given. The problem statement and the thesis proposal will be disclosed finally, followed by the thesis outline.

## 1.1 Internet of Things — an Overview

In last years, IoT has been given various definitions which they are presented here and discussed in order to raise a clear vision about the concept of IoT.

### 1.1.1 IoT Definition

The first definition for IoT has been given by the inventor of the term itself. Kevin Ashton stated that: "Adding radio-frequency identification and other sensors to everyday objects will create an Internet of Things, and lay the foundations of a new age of machine perception". Out of this early definition, few other definitions have been assigned in the last years. One important reference for IoT definitions is the 2009 final report for CASAGRAS (Coordination and Support Action for Global RFID-related Activities and Standardization) that contains several definitions combined with analysis for each definition where each definition is discussing different perspectives [1]. Nonetheless, every definition considers one or more aspects of IoT

unique features. Needless to say, every time a clear and comprehensive definition for IoT is strongly needed in order to make the open questions more clear and solvable in reality. That's why IoT is still being defined [2]. Figure 1.1 illustrates a generic diagram for the interconnection between the application domain and the end users in IoT [3].

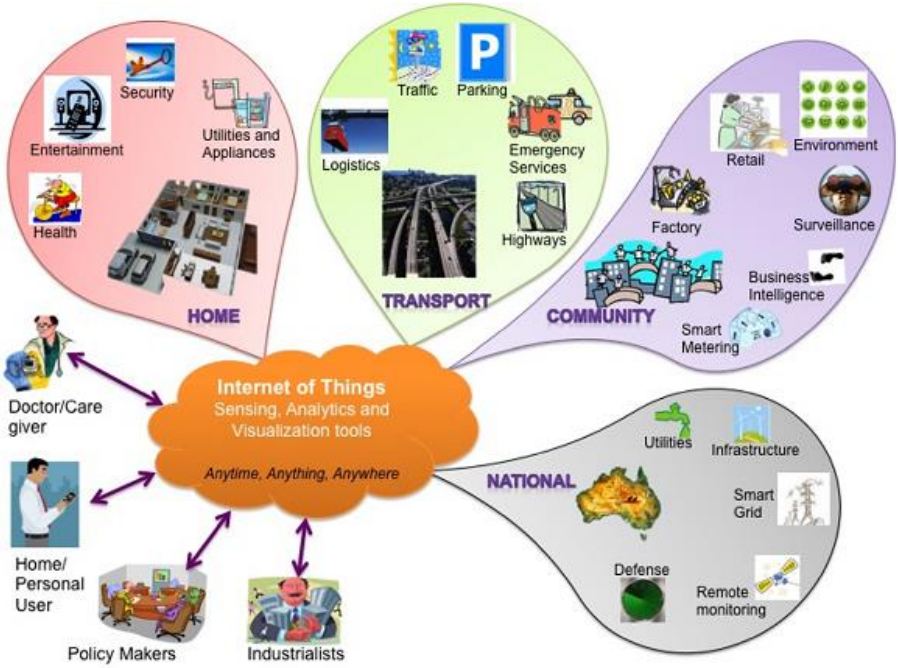


**Figure 1.1** End users and applications of IoT (Reprinted from [3], with permission from Elsevier).

Accordingly, a more expressive definition has also been derived by SAP as: "A world where physical objects are seamlessly integrated into the information network and where the physical objects can become active participants in business processes. Services are available to interact with these 'smart objects' over the Internet, query and change their state and any information associated with them, taking into account security and privacy issues" [4].

## 1.1.2 IoT Modeling

Since a conclusive definition for IoT is always required and new definitions are still being offered, a comprehensive and evident model is required as well. Up to date, many reference models have been developed. Among them, a paradigm that represents a general abstract for the concept of IoT is shown in Figure 1.2 which is mapped as a tree [5]. In the IoT tree, the technology is represented as the tree's roots where the technology comprises a group of devices (including sensors/WSN, tags, actuators...) generating data that are processed by a processing unit. The connection between the sensors and the application side is carried out through a set of communication protocols (Zigbee, GPS,..). On the other hand, a wide variety of applications are enabled through software packages, where the applications represent the leaves of the tree.

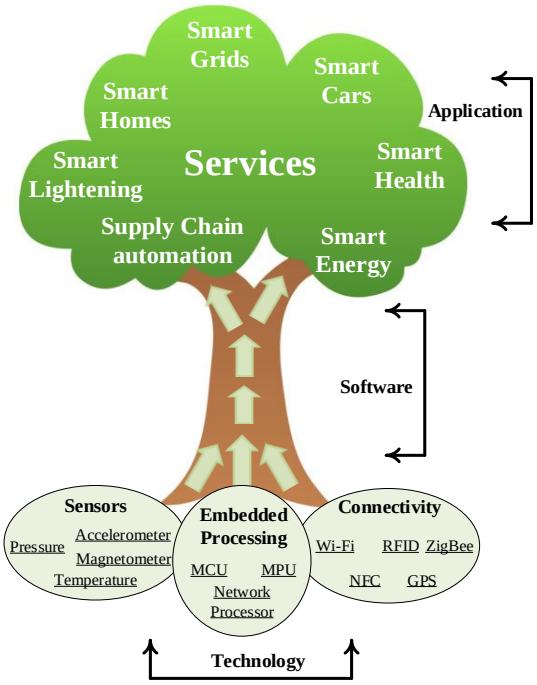


**Figure 1.2** The IoT tree (Reprint from [5]).

Likewise, a simple model that sheds light on the environment of IoT is developed by Maarten Botterman as shown in Figure 1.3. The model depicts the environment of IoT mainly as two entities; humans and objects in which humans (with attached devices) and objects (with remote sensing/monitoring devices) would interact together through an evolving network. Furthermore, the huge network offers the ability for human-to-human communication, object-to-object communication and human-to-object communication [6].

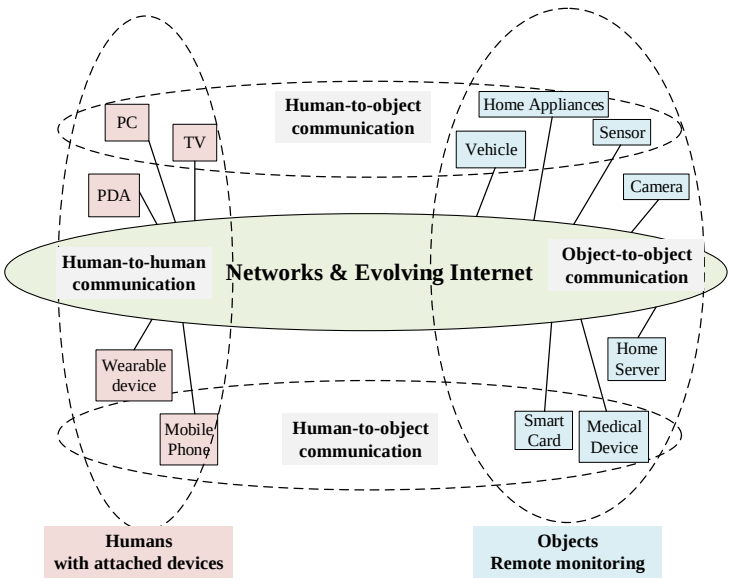


**Figure 1.3** The IoT Environment (Reprint from [6]).

It is evident that sensors are one of the key elements in the IoT. Noting Figure 1.2 and 1.3, the sensors are supposed to monitor the physical and environmental conditions and release their data to the ubiquitous network, where the data could be processed by other objects, devices or even users. A large number of spatially deployed sensors would form a wireless sensor network (WSN). A four-pillar paradigm for the IoT has been presented in [7], where WSN is considered one of the main pillars in the IoT. In order to enable the deployment of very large number of sensors in one environment, these sensors are mostly connected through a short-range wireless communication link. Consequently, the mission of enabling fully autonomous WSN becomes more pressing. The WSN, sometimes called internet of transducers, will be discussed in more detail in the next section.

## 1.2 Wireless Sensor Networks

WSN is a network comprising a set of spatially distributed sensors dedicated to sensing and monitoring environmental conditions such as temperature, pressure, light intensity, humidity, etc. After that, the collected data is sent to a central server where the data is stored or processed.

Historically, the origin of WSN comes back to the Distributed Sensor Network (DSN) project at the USA Defense Advanced Research Projects Agency (DARPA) around 1980 [1]. Before that date, research challenges and promising technologies have been addressed in the Distributed Sensor Networks Workshop that was organized by DARPA in 1978. Since then, many research projects have been driven by universities and academic institutions followed by commercial availability offered by many companies.

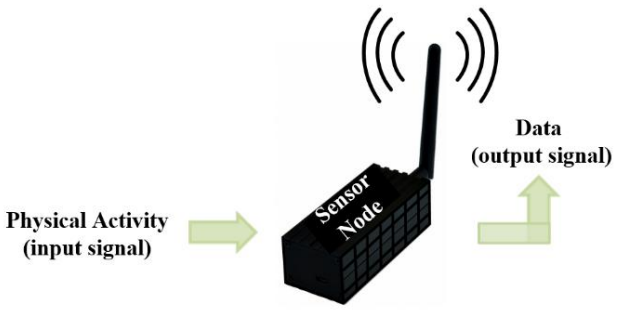


**Figure 1.4** Typical function of a sensor node.

### 1.2.1 WSNs building blocks (Hardware)

WSN network comprises spatially distributed sensor nodes. The sensor node consists of one or more sensors with the ability to process the sensed data independently. A typical functionality of sensor node can be shortened to sensing a physical variable (input signal) and transforming it

to meaningful action or data (output signal). A typical function of a sensor node can be demystified in Figure 1.4 [8]. The recent trend in sensors is the transition from being a simple sensing device to be a multifunctional unit. In addition to sensors, modern sensor nodes are equipped by a processor, a memory, a power supply, a radio and an actuator [9].

It is necessary to have a deeper look on the hardware architecture of a WSN node. The building blocks of a sensor node, as depicted in Figure 1.5, can be separated as follows:

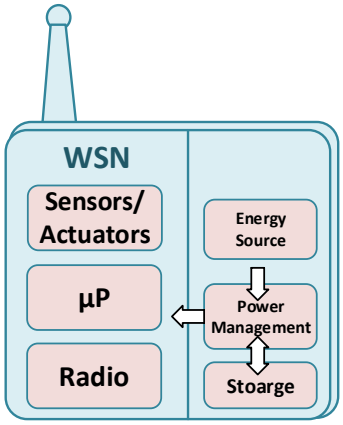


**Figure 1.5** Main building blocks of a sensor node.

### *1.2.1.1 Sensors/Actuators*

Sensors are the key point in wireless sensor networks where a physical quantity or event is measured and then transformed to the form of an electrical signal or any other form. Currently, available sensors are capable of sensing diverse forms of physical quantities such as temperature, humidity, smoke, light, pressure, vibration, acoustic, motion, etc. Rapid advance in MEMS technology enabled tiny sensors to be built on a single chip with a significant reduction in power and cost. It's worth mentioning here that MEMS technology is promising for multi-sensor realization into a single chip motivated by the increased interest in very small high-density sensor nodes.

On the other hand, actuators are small mechanical devices that are normally operated to act to a physical event within the surrounding environments. Similarly, actuators have been supported by the advance in MEMS technology. Tiny three-dimensional mechanical actuators, also known as “microactuators”, with a size range from micrometers to few centimeters have been successfully realized [10].

#### *1.2.1.2 Processor*

Recent sensor nodes are equipped by an embedded processor that process the data generated by the sensor itself. A low-cost Reduced Instruction Set Computer (RISC) microcontroller with a small program and data memory size (about 100kb) is normally employed [11]. Other types of processors include Field Programmable Gate Array (FPGA), Digital Signal Processor (DSP), etc. The selection of the processor among the different types depends on the required functionality; the managed hardware and cost. On other hand, the selection of the processor family follows other requirements such as power consumption and number of external components.

#### *1.2.1.3 Memory*

Although the embedded microcontroller features a small internal flash memory, sometimes an external small flash memory is needed. The external flash is used as an extension for the small internal memory. This additional flash is needed for storing data for a reasonable amount of time until the data being acquired and processed by the microcontroller. Additionally, an external RAM can be added to the sensor node to offer the chance for a wide range of applications without any constraints from the limited processor's memory. The power consumption, however, is a significant aspect for the type of memory that could be used [12].

#### *1.2.1.4 Radio*

It is the part responsible for wireless communication from/to the sensor node. A transceiver is employed for the purpose of communication with other sensor nodes or with a central server. Without a transceiver, sensor node loses its functionality as an integral part of WSNs. Modern sensor nodes apply different communication techniques such as acoustic, optical and RF.

#### *1.2.1.5 Energy Source*

Energy source is the most critical part in WSNs. The energy source in a sensor node is responsible for supplying the required energy for each of the other blocks such as sensor interface, microprocessor, the external memory, the wireless communication device (transceiver), etc.

As a remote device, energy is supplied to the sensor node via small batteries. Limited lifetime of a battery poses a major concern for WSNs. Relying on batteries as the sole source energy is impractical especially at remotely deployed sensor nodes where a battery replacement is a waste for money and functionality. Consequently, two common strategies are followed to alleviate energy poverty. The first strategy is to employ very low-power components for each

part within the sensor node. Likewise, different hardware architectures are sometimes employed to minimize the power consumption in a sensor node [13].

The second strategy is to adopt a secondary energy source or multi-sources that are used to charge the battery whenever needed and whenever these energy sources are available. Energy harvesting is a promising solution for remote deployed sensor nodes. Energy can be harvested from ambient environment using sophisticated transducers and be stored in the battery. Depending on the environment where the sensors are deployed, energy can be available in the form of solar light, kinetic, wind or electromagnetic energy.

**Table 1.1** Output power of different types of energy harvesters (source [15]).

| Energy Harvesting source | Environmental Location | Harvested power | Harvested consideration |
|---|---|---|---|
| **light** | Indoor | 10 μW/cm$^2$ | Light intensity |
| | outdoor | 10 mW/cm$^2$ | |
| **Mechanical Piezoelectric** | Human | 4 μW/cm$^2$ | Amplitude of vibration and resonant frequency |
| | Machine | 250 μW/cm$^2$ | |
| **Mechanical Electromagnetic** | Human | 50 μW/cm$^2$ | |
| | Machine | 2 mW/cm$^2$ | |
| **Thermal** | Human | 25 μW/cm$^2$ | Thermal gradient |
| | Machine | 20 mW/cm$^2$ | |
| **Electromagnetic RF waves** | Background | 0.1 μW/cm$^2$ | Distant from the source |
| | Directed | 1 mW/cm$^2$ | |

## 1.3 Powering Wireless Sensor Nodes

Following the discussion at the previous section, this section considers the potential approaches for increasing WSN lifetime though the adoption of an alternative energy resource. We recall that due to size constraints and stringent energy demand, the ultimate goal is to energize every sensor node by means of an alternative energy source [14]. The alternative energy source would enable an energy-autonomous operation and almost for free. Accordingly, a transducer is used to harvest the ambient energy available at different forms within the environment. This called in

literature as "Energy Harvesting". Usually, the amount of available power is small and strictly depends on the environmental conditions. The ambient energy sources could be in several forms such as light, vibration, thermal and electromagnetic waves. Depending on the environmental conditions, more than one source could be available with a specific application. However, the energy availability is uncertain as an implication for the irregular, random nature of such sources [14]. Furthermore, the average power levels, as shown in Table 1.1, available from different forms are limited to few microwatts, especially for indoor applications.

In Table 1.1., energy harvesting is categorized based on the preliminary form of the harvested energy. Energy harvesting can be categorized into four basic categories, namely light, thermal, mechanical vibration and electromagnetic (RF) waves. The fundamentals of each category will be shortly discussed in the following sections in order to evaluate their feasibility as potential energy source for wireless sensor nodes.

### 1.3.1 Light-Based Energy Harvesting

Harvesting energy from solar light is the most common alternative energy source. Wherein, a solar cell is used to convert the solar light into electrical energy by taking advantage of photovoltaic (PV) effect. A better description for photovoltaic energy harvesters can be explained by examining a model for solar cell. The circuit model and electrical characteristics are shown in Figure 1.6. A PV cell is modeled as a current source in parallel with a diode as well as shunt and series resistances to model non-ideality effects. In the electrical characteristics curve, the red curve shows the relation between the current and voltage across the solar cell. It is clear that increasing illumination has a positive effect on the extracted power by increasing the short-circuit current. While open-circuit voltage of a photovoltaic cell is not affected too much for illumination variations, it is affected greatly by temperature variations [15]. The power curve reaches a peak at particular voltage and current. This peak is called maximum power point (MPP).

Photovoltaic cells can be used as an alternative energy source for autonomous sensor nodes provided that the environmental conditions are convenient. However, many factors should be considered while designing solar energy scavengers such as illumination levels, daylight availability, photovoltaic cell properties, probability of shading on photovoltaic cells and power supply requirements [16].

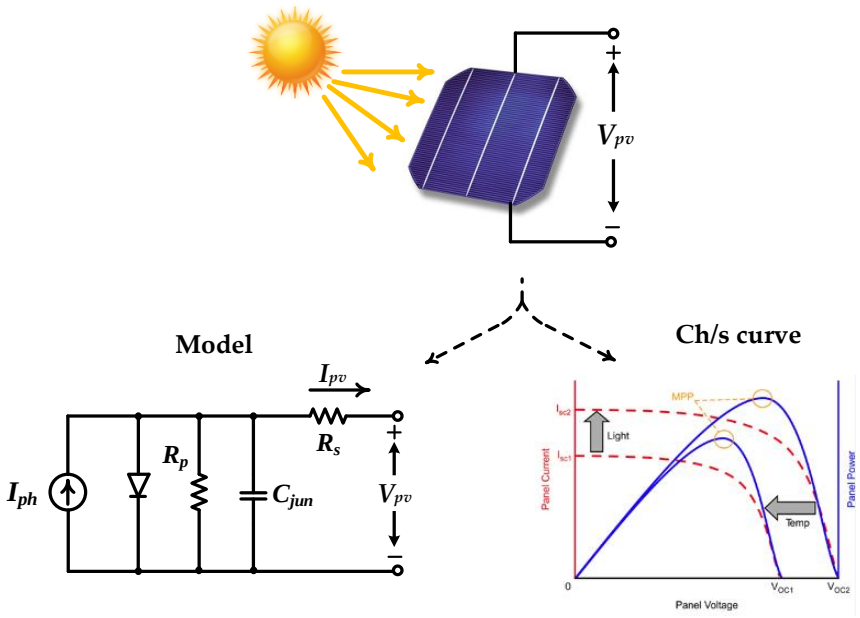


**Figure 1.6** Solar cell model and electrical characteristics.

### 1.3.2 Thermal-Based Energy Harvesting

Thermoelectric energy harvesters offer the opportunity of scavenging energy from the difference in temperature between two conducting objects. Based on Seebeck effect, if two different metals joined in two junctions with a temperature difference between the junctions, an open circuit voltage would be established between them. Fundamentally, thermoelectric phenomena have been used for heating and cooling applications. By reversing the process, a temperature gradient in a conducting material results in heat flow which results in the diffusion of charge carriers. The polarity of the established output voltage is dependent on the polarity of temperature difference between the two conducting metals of a thermoelectric generator.

Thermoelectric generators are realized by connecting two pillars made of two different materials and interconnected electrically in series by another metal. Normally, the two different materials are realized through N-doped and P-doped semiconductor pellets. This configuration, shown in Figure 1.7, is called "thermocouple" which is the core element for forming thermoelectric generators. A thermoelectric generator then is formed by connecting a large number of thermocouple in series and sandwiched between two thermally conductive ceramic plates.

The efficiency of a thermoelectric generator (at 22 $^{o}$C ambient temperature) ranges from 0.8% for human body applications ($\Delta T \sim 15$ K) to 2.7% for machine applications ($\Delta T \sim 50$ K) [17], which is undoubtedly low. Miniaturized thermoelectric generators would generate sub-1

mW at voltage less thang 500 mV, thus, it becomes a challenge to design an efficient energy front-end for converting the energy to a usable voltage level (*e.g.* 3.3 V) [18].

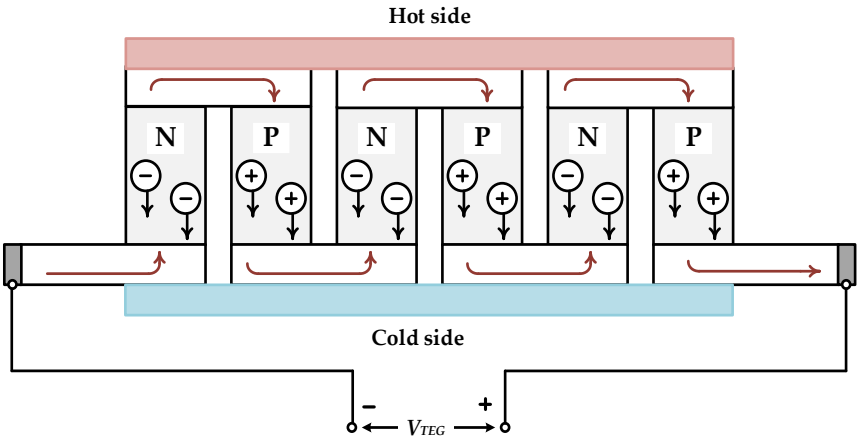


**Figure 1.7** Construction of thermoelectric generator.

## 1.3.3 Vibration-Based Energy Harvesting

Scavenging energy from mechanical vibration or motion involves the subjection of a small device to the vibration source that converts it to an electrical energy. The mechanical energy can be converted to electrical energy using three mechanisms, namely electrostatic, piezoelectric and electromagnetic.

### *1.3.3.1 Piezoelectric Energy Harvesting*

The piezoelectric energy harvesting relies on the piezoelectric effect, which describes the conversion of mechanical strain to an electric current or voltage. In piezoelectric effect, a piezo crystal is mechanically deformed by strain or pressure which generates electrical charges that can be measured as voltage on the electrodes of the piezo material. Different sources for strain include human motion, acoustic noise, and subtle vibrations near machinery, as examples. The basic structure of a piezoelectric energy transducer is depicted in Figure 1.8.

A typical piezoelectric harvester using piezoelectric thin films has been presented in [19], where the results shows the harvesting of 0.5 V at 0.4 g acceleration with a microwatt output power reached at 1.5 g acceleration. A total normalized output power of 220 µW/g/cm2 is achieved which would be sufficient for powering a wireless sensor node during silent mode.

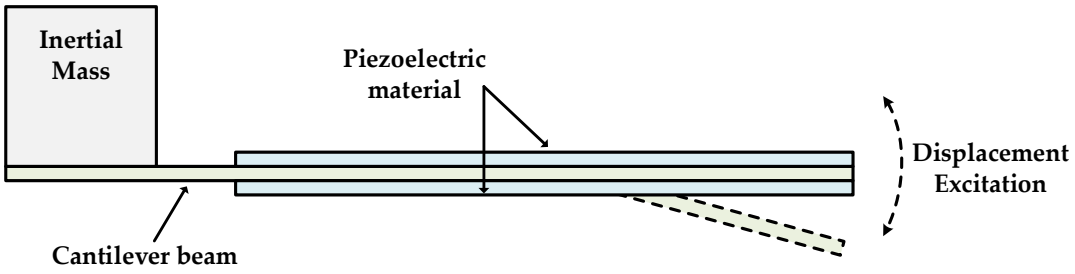


**Figure 1.8** Structure of cantilever piezoelectric energy transducer.

### *1.3.3.2 Electromagnetic Energy Harvesting*

According to Faraday's law of induction, any time-varying magnetic field or a moving magnet induces an electromagnetic force within a coil that is linked by the magnetic flux. Electromagnetic vibration energy harvesters take advantage of this phenomenon by using the motion of a moving magnetic field intersecting a static wound copper coil. A magnet can be stuck on a wobbling cantilever relative to a conductor and make it subjected to vibration from external source. A few micro-currents would be generated within the conductors which can be harvested in the form of microwatts.

The electromagnetic harvesters are well suited for operation at low frequency [20]. Compared to piezoelectric vibration transducers, electromagnetic transducers have low output impedance (< few kΩ's), which facilitates the processing of generated voltage [21]. On the other hand, electromagnetic harvesters are well known by low output voltage with low AC power levels. This adds more challenge to the design of the interface circuit between the electromagnetic harvester and the load [21]. Typical electromagnetic energy transducers are capable of delivering 37 μW for an optimum load resistance of 0.6 Ω with an overall volume of 0.84 $cm^3$ which was reported in [22].

### *1.3.3.3 RF Energy Harvesting*

An alternative available source for energy scavenging is RF signals. Energy can be harvested from ubiquitous radio transmitters used for TV broadcasting and cell phone network coverage. Through using a receiving antenna with a power conditioning circuit, this free flowing energy can be harvested and converted into DC voltage. Typical value for the energy transmitted through RF broadcasting reaches few tens of watts for frequencies in the order of GHz. However, the harvester device has to be close enough to the RF transmitter to harvest a useful amount of this power. Otherwise, the power density level would be very low. Power density levels of 0.1-1 $mW/m^2$ would be expected at distances of 25-100m away from a GSM base station [23]. Intel demonstrated a prototype with an antenna of around 30 cm by 20 cm

where 60μW has been harvested from a TV tower station away from the harvester by 4.1km [24]. While the amount of power would be enough for powering a wireless sensor node, the size constraints of modern tiny sensor nodes make it impractical solution.

#### *1.3.3.4 Multi-Source Energy Harvesting*

The main goal for energy harvesting for sensor nodes is to extend the lifetime of a sensor. The harvested power should be sufficient and sustained. However, energy cannot be available all the time from just a single harvesting source which adds many challenges for current WSNs. This is a little bit far from the main goal of a fully autonomous ubiquitous sensor nodes. Consequently, a hybrid energy scavenging solution that combines multiple energy harvesters would be a feasible solution. For instance, a prototype for testing purpose has been developed that comprises multiplexer module, photovoltaic module, vibration module, supercapacitor module, battery module, and mains module [25].

Similarly, a platform that combines solar and wind energy transducers has been reported in [26]. The power output is connected to power an Eco wireless node as well as to charge a Li-Polymer battery. Likewise, an energy harvesting system presented in [27] to gather the energy from two energy sources (airflow and sunlight) simultaneously in addition to a fuel cell as silent energy storage. Unfortunately, the energy-aware analysis for the average amount of power available for every sensor node is a missing point in most of these research.

## 1.4 Towards Autonomous WSNs

Lifetime is a key issue that is an important characteristic for evaluating WSNs. A clear definition for lifetime of WSNs is not clear yet, however we will relate lifetime of WSN to the lifetime of individual sensor nodes. From that, the lifetime of a sensor node can be defined as the time period during the sensor node is alive and functioning properly [28]. Due to the nature of WSNs, lifetime cannot be discussed apart from maintenance. Mostly, WSNs are inaccessible and been deployed in harsh environments which make it almost impossible or costly to reach them for maintenance. That's why a WSM with extended lifetime is always a concern.

As a result for the limited resources of remotely deployed WSNs, lifetime mainly depends upon the power resources of each sensor node. Consequently, a sensor node would be alive and function normally as long as power is available. On the other hand, sensor nodes are limited in size and weight and the same constraints apply for battery size in use. Thus, employing an alternative energy source such as energy harvesting becomes inevitable for extending the lifetime of the sensor nodes. In general, the lifetime of the sensor node depends basically on two factors; how much energy it consumes over time, and how much energy is available for its use [28]. Consequently, it becomes obvious that even energy harvesting would fail to provide the

sensor node with the required power for autonomous operation. We note in Table 1.1 that the power density of most of energy harvesting technology is limited. It becomes even worse for indoor sensor nodes where the available peak power is limited to few micro-watts. Therefore, two cooperating approaches are normally employed. First, the average power consumption of the sensor node is managed by applying specific power-aware communication protocols that keep tracks of the energy availability and data transmission/reception [9]. Second, the power harvested at each sensor node is increased such that a balance between the energy consumption and energy harvesting is achieved.

Recently, non-radiative wireless power transfer (WPT) has shown a notable progress as a potential energy source for a wide variety of applications. Medical implantable devices, consumer electronics, electric vehicles charging, and robotics are among numerous applications where WPT has been adopted as a key enabling technology. The feasibility of WPT as a power source for single input-multiple output (SIMO) WSNs in IoT systems has been investigated and modeled [29]. As we previously highlighted, it is clear that energy harvesting is a promising technology, yet the chaotic nature and unpredictability make it a limiting factor toward a fully autonomous WSNs. Consequently, it becomes more convenient to alleviate the lifetime bottleneck of WSNs through WPT such that the lifetime is prolonged [30]. It is true that contactless power transmission has been extensively suggested and validated in WSNs by means of far-field RF power transmission by harvesting the already-existed electromagnetic RF power [31], [32]. In these systems, a single antenna or multiple antennas could be utilized to simultaneously receive data and power. On the other hand, near-field non-radiative WPT through inductive coupling has become an interesting area for powering indoor and local-area deployed WSNs. Figure 1.9 shows a conceptual diagram for a WSNs enabled by WPT.

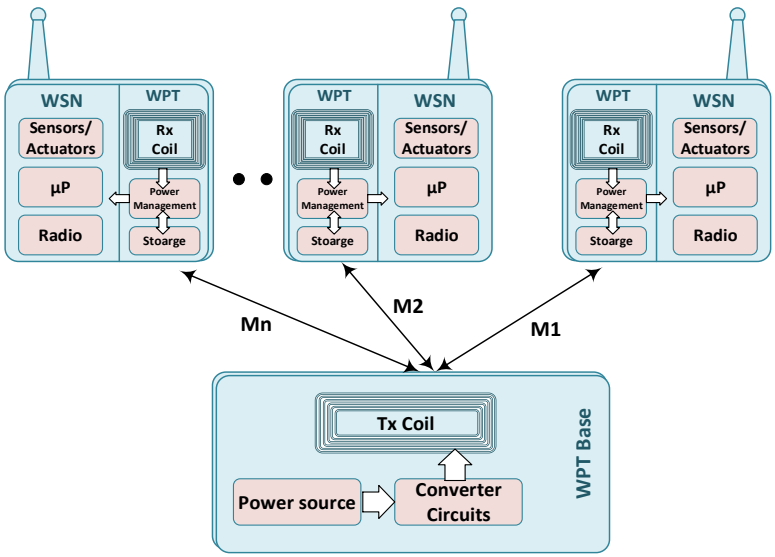


**Figure 1.9** Conceptual schematic diagram for WPT-enabled wireless sensor nodes.

## 1.5 Problem Statement and Thesis Scope

WPT is undoubtedly becoming a promising technology for contactless powering of WSNs among many other applications. Fundamentally, WPT has been limited for point-to-point applications where a single receiver is powered from a single receiver over an approximately fixed distance. Moreover, most of the studied and presented work in WPT work target stationary transmitter and receiver ends during the power transmission time, which is not a practical case for many applications in complex dynamic environments. Thus, WPT becomes less reliable and more vulnerable for power transmission dysfunctionality in a non-stationary wide-distance environment. In this section, the current challenges in WPT systems are shortly discussed towards the description of the thesis scope.

### 1.5.1 Current Challenges in WPT systems

Throughout this chapter we discussed the technical issues related that faces WSN in different application with a major focusing on technical issues related to powering sensor motes in such networks. Despite the fact that a considerable amount of literature has been published in energy harvesting for WSNs, still energy harvesting faces multiple challenges related to the environmental conditions and the available energy sources. An important potential application for WSNs is to deploy sensors for indoor operation at hospitals (biomedical implants) or homes (intelligent appliances) or at any place where energy harvesting is strictly useless due to the scarceness of energy sources. In that case, wireless power transmission emerges as the relevant alternative to power WSNs and eliminate the need for replacing batteries. This would greatly help in reducing the cost of maintenance for such devices and increase the system reliability and autonomy. However, it is of utmost importance to circumvent the challenges related to WPT links in order to get all the benefits of wireless powering these sensors; from here emerges the main scope of the thesis. To enable WSNs, and hence the IoT, by means of WPT, the main challenges that need to be addressed can be shortly described as follows:

#### *1.5.1.1 Magnetic Coupling Variation*

The WPT concept is dependent on the fundamental principle of electromagnetic induction phenomena, where two coupled coils, mostly loosely coupled, exchange the energy through the flux linkage from the source/transmitter to the load/receiver coil. Consequently, the coupling coefficient between the two coils is a key factor that determines how much energy is transferred and how efficient the system is. From this perspective, if the WPT link is employed in a dynamic environment where there is a relative movement between the transmitter and the receiver, the coupling coefficient with evidently becomes variable [33]. Obviously, this would

lead to a change in the effective impedance at the transmitter side which leads to a change in the transferred power to the receiver.

#### *1.5.1.2 Components Tolerance*

The most common technique in inductive WPT is magnetic resonance, where the reactive impedance of the coils are compensated to form a resonance circuit at either the transmitter, or the receiver, or both of them. As we will explain in the next chapters, it is required to design the resonance circuits both at the transmitter and receiver sides such that they are fully-tuned at the same natural frequency [34]. The process of components selection assumes fixed components' values. However, components tolerance after manufacturing and temperature effect make the system prone for deviation from the optimal operating frequency. Moreover, the sensitivity of the system increases considerably following the increase of quality factor of the resonant circuit [35].

#### *1.5.1.3 Proximity Interfering Objects*

Conductive interfering objects in close proximity to the transmitter or the receiver have a great impact on the performance of the WPT system. An interfering objects having a complex impedance would cause a drift in the resonant frequency of the transmitter or the receiver or both of them depending on the relative distance of this object and its self-resonant frequency [36]. Moreover, the loading effect of the conductive object would cause a drop in the transferred power to the receiver. Whatsoever the effect of an interfering object, the resonant circuits at the interfered side (transmitter or receiver) has to be adaptively tuned to retain the proper system functionality.

#### *1.5.1.4 Load Variation*

The power transmitted to a receiver, as we will show, is a function of the equivalent load resistance at the receiver. Consequently, a device whose load varies depending on the operating condition, such as a system change from idle state to fully awake state, is going to affect the induced voltage, and the efficiency in essence, or current in the receiver side [37]. Consequently, an adaptive front-end is vital for maintaining a constant voltage/current operation.

### 1.5.2 Scope of the Thesis

As a consequence of the shortly aforementioned challenges of WPT systems, it becomes reasonable to address the challenges and push the boundaries of limiting factors towards an efficient and sufficient energy transmission for sensors in a dynamic environments. The efforts

of mitigating the bottleneck of WPT system performance is fundamentally achievable at the transmitter side or receiver side. However, it is more practical to focus on having a controllable receiver side because it is more adequate for single input-multiple output (SIMO) WPT links such as the case of powering multiple sensor nodes from a single transmitting power source.

Accordingly, the main scope of the thesis is to study and model the effects of mismatch in components and coupling variation on the performance of WPT systems including power transmission capabilities and efficiency. Subsequently, the efforts will be focus on developing an adaptive power management front-end that would enable the electronic self-tuning of WPT receivers against any mismatch in components values or system parameters variation. This would enable the WPT system to be designed at high quality factor without being significantly sensitive. Consequently, the maximum power delivery to the receiver would be retrieved automatically. As we will show in the subsequent chapters, the developed front-end should certainly be efficient in order to achieve the maximum power at the possible maximum efficiency since it is in the power path. The main scope of the thesis is depicted in Figure 1.10, where the main efforts will be directed to developing the adaptive front-end at the receiver side in a WPT system.

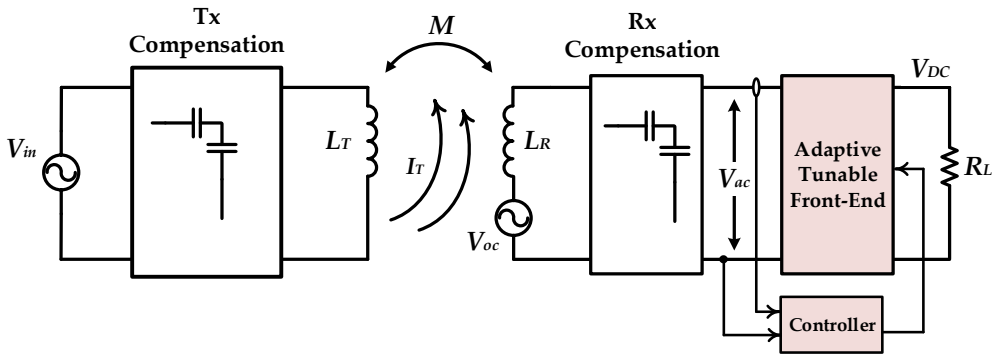


**Figure 1.10** Conceptual block diagram for the main goal of the thesis.

## 1.6 Thesis Outline

After introducing the main scope and objectives of this thesis, the general outline of the thesis starts by analyzing and modelling WPT systems and then investigates the limiting factors that affect power transmission in high quality factors resonant WPT. Thereafter, an adaptive power management front-end has to be proposed in order to ensure a fully-tuned WPT link. The proposed power management front-end should mainly ensure self-tunability in case of mismatch or interference in the WPT receiver. The subsequent chapters, then, will have the following outline:

Chapter 2 entitled “On the Theory and Modelling of Wireless Power Transfer” gives background about wireless power transfer kinds followed by a focus on resonant inductive coupling WPT. It presents, as well, a modelling and analysis of the main compensation topologies in WPT and the technical issues that limit their performance.

Chapter 3 revisit the gyrator circuit element and its application as a reactive element synthesizer. The switch-mode implementation of gyrator dedicated for power processing application is also discussed. The gyrator-based switch-mode reactive element synthesis is then evaluated in various design cases given as a proof of concept.

Chapter 4 presents a novel dual-loop control for switch-mode gyrator in WPT receivers. The design details and verification of the control operation is evaluated at design case of parallel-compensated WPT receiver. In order to mitigate the drawbacks of the dual-loop control, a further control approach entitled “quadrature phase-locked-loop” is presented and discussed. It has been shown that the quadrature PLL control is more reliable compared to the dual-loop control presented so far. Toward a fully integrated system, the chip pre-design of the switch-mode gyrator circuit and control blocks is also presented and the efficiency of the WPT receiver at different mismatch cases is also calculated with the help of the accurate models of XFAB 0.18μm HV process.

Chapter 5 discusses the adoption of phase-controlled switched converters for multifunctional operation by combining the self-tuning functionality with energy rectification functionality. It has been shown that the presented operation leads to a more compact circuit that tunes the WPT receiver while the energy is rectified and supplied to the load. The proposed operation has been verified and applied into two different switch-mode circuits, where the verification results have given.

Chapter 6 proposes a novel approach which presents a modified operation in the phase-controlled converter. The proposed novel operation enables active tuning, as a reactive power control, as well as output voltage regulation, as a real power control. Consequently, the proposed operation offers extended functionalities of active tuning, rectification and voltage regulation, altogether by means of a single stage switch-mode front-end.

Chapter 6 concludes the thesis. The main contribution of the thesis is summarized. As well, the list of publications as a result of the thesis is given. Finally, the suggested future work derived from the thesis work is given for further research lines that could improve the research findings in the future.

## 1.7 References

[1] C. Turcu, Ed., Deploying RFID - Challenges, Solutions, and Open Issues. InTech, 2011.

[2] EU FP7 Project CASAGRAS, "CASAGRAS final report: RFID and the inclusive model for the internet of things," 2009.

[3] J. Gubbi, R. Buyya, S. Marusic, and M. Palaniswami, "Internet of Things (IoT): A vision, architectural elements, and future directions," *Futur. Gener. Comput. Syst.*, vol. 29, no. 7, pp. 1645–1660, Sep. 2013.

[4] S. Haller, "Internet of Things: An Integral Part of the Future Internet," *SAP presentation*.

[5] Ian Chen, "Sensors Are a Primary Source for Big Data," EECatalog, 2014. [Online]. Available: *http://eecatalog.com/IoT/2014/05/16/sensors-are-a-primary-source-for-big-data/*. [Accessed: 26-Feb-2018].

[6] M. Botterman, "Internet of Things: an early reality of the Future Internet," Prague, 2009.

[7] H. Zhou, The Internet of Things in the Cloud: A Middleware Perspective. CRC Press, Taylor & Francis Group, 2012.

[8] V. Kumar, Fundamentals of pervasive information management systems. John Wiley & Sons Inc, 2013.

[9] J. Yick, B. Mukherjee, and D. Ghosal, "Wireless sensor network survey," *Comput. Networks*, vol. 52, no. 12, pp. 2292–2330, Aug. 2008.

[10] S. (Sergej) Fatikow and U. Rembold, Microsystem Technology and Microrobotics. Springer, Berlin, Heidelberg, 1997.

[11] P. Baronti, P. Pillai, V. W. C. Chook, S. Chessa, A. Gotta, and Y. F. Hu, "Wireless sensor networks: A survey on the state of the art and the 802.15.4 and ZigBee standards," *Computer Communications*, vol. 30, no. 7. Elsevier, pp. 1655–1695, 26-May-2007.

[12] J. L. Hill, "System Architecture for Wireless Sensor Networks," Ph.D Dissertation, Computer Engineering, University of California, Berkeley USA, 2003.

[13] Á. Asensio, R. Blasco, Á. Marco, and R. Casas, "Hardware architecture design for WSN runtime extension," *Int. J. Distrib. Sens. Networks*, vol. 2013, no. 4, p. 136745, Apr. 2013.

[14] R. G. Cid-Fuentes, A. Cabellos-Aparicio, and E. Alarcon, "Energy buffer dimensioning through energy-erlangs in spatio-temporal-correlated energy-harvesting-enabled wireless sensor networks," *IEEE J. Emerg. Sel. Top. Circuits Syst.*, vol. 4, no. 3, pp. 301–312, Sep. 2014.

[15] J. Carpenter and Y. Ramadass, "Fundamentals of ambient energy transducers in energy harvesting systems. (Smart Grid & Alternative Energy)," *ECN-Electronic Compon. News*, vol. 56, no. 6, p. 20(1), 2012.

[16] V. Raghunathan, A. Kansal, J. Hsu, J. Friedman, and M. Srivastava, "Design considerations for solar energy harvesting wireless embedded systems," in *2005 4th International Symposium on Information Processing in Sensor Networks, IPSN 2005*, 2005, vol. 2005, pp. 457–462.

[17] A. Montecucco, J. Siviter, and A. R. Knox, "The effect of temperature mismatch on thermoelectric generators electrically connected in series and parallel," *Appl. Energy*, vol. 123, pp. 47–54, Jun. 2014.

[18] W. Wang, V. Cionca, N. Wang, M. Hayes, B. O'Flynn, and C. O'Mathuna, "Thermoelectric energy harvesting for building energy management wireless sensor networks," *Int. J. Distrib. Sens. Networks*, vol. 2013, no. 6, p. 232438, Jun. 2013.

[19] P. Muralt, M. Marzencki, B. Belgacem, F. Calame, and S. Basrour, "Vibration Energy Harvesting with PZT Micro Device," in *Procedia Chemistry*, 2009, vol. 1, no. 1, pp. 1191–1194.

[20] A. Rahimi, Ö. Zorlu, A. Muhtaroğlu, and H. Külah, "Fully self-powered electromagnetic energy harvesting system with highly efficient dual rail output," *IEEE Sens. J.*, vol. 12, no. 6, pp. 2287–2298, Jun. 2012.

[21] H. Ulusan, K. Gharehbaghi, O. Zorlu, A. Muhtaroglu, and H. Kulah, "A fully integrated and battery-free interface for low-voltage electromagnetic energy harvesters," *IEEE Trans. Power Electron.*, vol. 30, no. 7, pp. 3712–3719, Jul. 2015.

[22] P. Glynne-Jones, M. J. Tudor, S. P. Beeby, and N. M. White, "An electromagnetic, vibration-powered generator for intelligent sensor systems," in *Sensors and Actuators, A: Physical*, 2004, vol. 110, no. 1–3, pp. 344–349.

[23] R. Vullers, R. Schaijk, H. Visser, J. Penders, and C. Hoof, "Energy harvesting for autonomous wireless sensor networks," *IEEE Solid-State Circuits Mag.*, vol. 2, no. 2, pp. 29–38, 2010.

[24] A. Sample and J. R. Smith, "Experimental results with two wireless power transfer systems," 2009 *IEEE Radio Wirel. Symp.*, pp. 16–18, Jan. 2009.

[25] A. S. Weddell, N. J. Grabham, N. R. Harris, and N. M. White, "Modular plug-and-play power resources for energy-aware wireless sensor nodes," in *2009 6th Annual IEEE Communications Society Conference on Sensor, Mesh and Ad Hoc Communications and Networks, SECON 2009*, 2009, pp. 1–9.

[26] C. Park and P. H. Chou, "AmbiMax: Autonomous energy harvesting platform for multi-supply wireless sensor nodes," in *2006 3rd Annual IEEE Communications Society on Sensor and Adhoc Communications and Networks, Secon 2006*, 2007, vol. 1, pp. 168–177.

[27] D. Porcarelli, D. Brunelli, M. Magno, and L. Benini, "A Multi-Harvester architecture with hybrid storage devices and smart capabilities for low power systems," in *SPEEDAM 2012 - 21st International Symposium on Power Electronics, Electrical Drives, Automation and Motion*, 2012, pp. 946–951.

[28] Y. Chen and Q. Zhao, "On the lifetime of wireless sensor networks," *IEEE Commun. Lett.*, vol. 9, no. 11, pp. 976–978, Nov. 2005.

[29] E. Bou-Balust, R. Sedwick, P. Hu, and E. Alarcon, "Advances in non-radiative resonant inductive coupling wireless Power Transfer: A comparison of alternative circuit and system models driven by emergent applications," in *Proceedings - IEEE International Symposium on Circuits and Systems*, 2014, pp. 2037–2040.

[30] V. V. Mai, W.-Y. Shin, and K. Ishibashi, “Wireless Power Transfer for Distributed Estimation in Sensor Networks,” *IEEE J. Sel. Top. Signal Process.*, vol. 11, no. 3, pp. 549–562, Apr. 2017.

[31] R. Zhang and C. K. Ho, “MIMO broadcasting for simultaneous wireless information and power transfer,” *IEEE Trans. Wirel. Commun.*, vol. 12, no. 5, pp. 1989–2001, May 2013.

[32] C. Shen, W. C. Li, and T. H. Chang, “Wireless information and energy transfer in multi-antenna interference channel,” *IEEE Trans. Signal Process.*, vol. 62, no. 23, pp. 6249–6264, Dec. 2014.

[33] C.-Y. Huang, J. E. James, and G. A. Covic, “Design Considerations for Variable Coupling Lumped Coil Systems,” *IEEE Trans. Power Electron.*, vol. 30, no. 2, pp. 680–689, Feb. 2015.

[34] J. T. Boys, G. A. Covic, and A. W. Green, “Stability and control of inductively coupled power transfer systems,” *IEE Proc. - Electr. Power Appl.*, vol. 147, no. 1, p. 37, 2000.

[35] A. Trivino, D. Fernandez, J. A. Aguado, and J. E. Ruiz, “Sensitivity analysis of component’s tolerance in Inductively Coupled Power Transfer system,” in *2013 International Conference on Renewable Energy Research and Applications (ICRERA)*, 2013, no. October, pp. 806–810.

[36] E. Bou, E. Alarcon, R. Sedwick, and P. Fisher, “Interference analysis on Resonant Inductive Coupled Wireless Power Transfer links,” in *Proceedings - IEEE International Symposium on Circuits and Systems*, 2013, pp. 2783–2786.

[37] M. Bojarski, E. Asa, and D. Czarkowski, “Effect of wireless power link load resistance on the efficiency of the energy transfer,” in *2014 IEEE International Electric Vehicle Conference (IEVC)*, 2014, pp. 1–7.

Chapter

# 2

# On the Theory and Modelling of Wireless Power Transfer

Wireless power transfer (WPT) is the process of transmitting electrical power from a source to a load without using conductors or wire. Other times, it is called "*contactless power transfer*". While WPT is a wide topic that covers many applications with different techniques and different ranges, our discussion would be limited to the overall scope that may coincide with IoT applications.

As it has been discussed in Chapter 1, WPT would be a promising technology for contactless powering of WSNs since it has more reliable characteristics compared to the random nature of energy harvesting. In this chapter, an overview of WPT systems and their categories will be discussed. Then, the resonant-inductive-coupling WPT will be discussed in detail because it enables energy transmission to wider distances compared to the non-resonant kind. The detailed analysis of the basic resonator compensation topologies will be also shown. Finally, the sensitivity and mistuning problem in parallel-compensated WPT receivers will be explained.

## 2.1 History of Wireless Power Transfer at a Glance

WPT is a field of study under development with many promising applications that could significantly change the whole society and leave its impact on every aspect of our life. It is important to go at first through the history of developing WPT before discussing the technical issues related to such impressive discipline. For the sake of highlighting the most important milestones in WPT development, the major events in WPT history should be revisited. It all started in 1891 at a lecture in Columbia College where Nicola Tesla was able to light a bulb from across a stage. Later in 1899, Tesla found that he could increase the distance by an LC resonator at the transmitter and receiver sides with both of them tuned to the same frequency [1]. This way, he was able to light three incandescent lamps by resonant inductive coupling at a

distance of about 30 m using high voltages in the order of 20 megavolts, where the findings of Tesla can be noted in [2], [3]. In the early 1960s, William C. Brown contributed to microwave power transmission when he invented what is called "rectenna" [4]. A combination of an antenna and a rectifier had been used to convert microwave power to DC electricity. Later on 1964, Brown was able to wirelessly power a model helicopter using microwaves. During the 1960s, inductive wireless power transmission has been revisited again by Schaldach where powering artificial hearts has been achieved [5]. Later in 1975, William Brown and Robert Dickinson were able to transmit high power through a distance of 1.54km using microwaves at a frequency of 2.388GHz [6].

During the 1990s, several work demonstrated successfully using microwave power transmission in aerospace applications [7], [8]. Alternatively, in 2007, a team in MIT transferred successfully a power of 60W over a distance of 2m with efficiency around 40% using coupled resonant coils of 25cm operating at 10 MHz [9]. The efforts of developing and promoting wireless power transmission gave rise to the establishment of the "Wireless Power Consortium" in 2008. The first inductive power transfer "Qi" resulted in 2009 to enable charging portable devices with a maximum of 5W.

In the last decade, rapid advances in WPT development have been proved by many commercial products supported by extensive research in most aspects of the technical issues involved in WPT design. Evidently, it is important here to distinguish between two different types of wireless power transmission, namely radiative microwave WPT and non-radiative magnetic coupling WPT. Accordingly, both kinds can be treated as different technologies with different characteristics and hence different potential applications.

## 2.2 Categories of Wireless power Transfer

As we have witnessed through the rich history of the development of wireless power transmission, it is evidently valid to categorize the wireless power transfer, in general, into two main categories, namely far-field radiative WPT and near-field non-radiative WPT. It consequently becomes obvious that in order to employ WPT in a specific application, one needs to understand which type of WPT is possibly more convenient for that application.

### 2.2.1 Far-Field Radiative WPT

Pioneered by William C. Brown, radiative WPT depends on transmitting energy through space using electromagnetic radio waves. In such a way, electrical power from a DC source is converted into radio-frequency (RF) power, then the RF power is transmitted to space toward a receiving point where the power is received and converted back into DC power [10].

Theoretically, electromagnetic waves WPT are best used for transmitting power at distant receiving ends in the range of multiple kilometers. The far-field radiative WPT, however, is realizable in other forms such as visible light laser, electromagnetic propagation and directive microwave [11]. Nonetheless, the fundamental difference between the far-field WPT and near-field WPT relies mainly on the characteristics of electromagnetic waves. The fundamental boundary between radiative and non-radiative fields has been postulated after the explanation derived by James Clerk Maxwell who established electromagnetism theory characterized by "*Maxwell's equations*". Then it becomes feasible to examine the field regions that surrounds, as shown in Figure 2.1, a transmitting RF power source as follows [12]:

- *Reactive near-field* region which is bounded by the distance $R_1$ from the power source. The distance $R_1$ is given by $0.62\sqrt{D^3/\lambda}$, where $D$ is diameter of the transmitting antenna and $\lambda$ is the wavelength of the electromagnetic wave.
- *Radiating near-field (Fresnel)* region is considered as a transition zone where this region is bound between distances of $R \geq 0.62\sqrt{D^3/\lambda}$ and $R < 2D^2/\lambda$. In this region, both the inductive and radiative fields exist, however the radiative field starts to dominate [12].
- *Far-field (Fraunhofer)* region exists at distances of $R \geq 2D^2/\lambda$ up to infinity. In this region, the radiative field is the dominant one.

The far-field WPT hence depends on transmitting the energy through the radiative field to a distant receiver. The receiving side then converts the energy, captured by the reception antenna, to DC using a rectenna configuration. The simplest structure of a rectenna is realized by an antenna combined with a rectifying RF diode connected across the antenna [11].

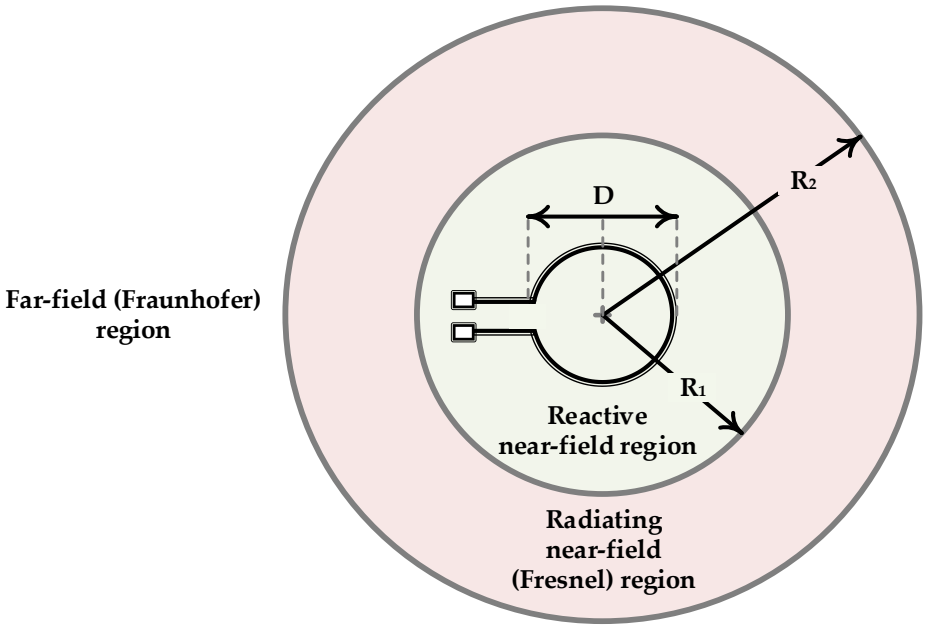


**Figure 2.1** Field regions of a transmitting antenna of dimension D [12].

The crucial performance metric for a WPT mechanism is power efficiency. The efficiency of the far-field radiative WPT system is a function of the transmitting and receiving aperture sizes, the wavelength of the electromagnetic waves, and the distance from the transmitting aperture to the receiving aperture [13]. By assuming a free space path loss, which can be considered as the dominant loss over long distances, it is possible to relate the received power to the transmitted power as follows [14]:

$$P_r = P_t G_t G_r (\frac{\lambda}{4\pi R})^2 \tag{2.1}$$

where $P_t$ is the transmitted power, $G_t$ is the transmitting antenna gain, $G_r$ is the receiving antenna gain and $\lambda$ is the wavelength. One can note that in order to receive the highest power, either the distance $R$ has to be small or the wavelength $\lambda$ has to be long enough. Unfortunately, the wavelength $\lambda$ constraints the size of antennas which would contradict with the space limitation in some applications [13]. Moreover, the far-filed radiative WPT requires uninterruptable line of sight between the transmitter and receiver, this, by the way, is more restricting for wide range of applications. It thus becomes evident that far-field radiative WPT is more feasible for limited applications such as to high-altitude Earth orbiting applications and solar-power satellites [10].

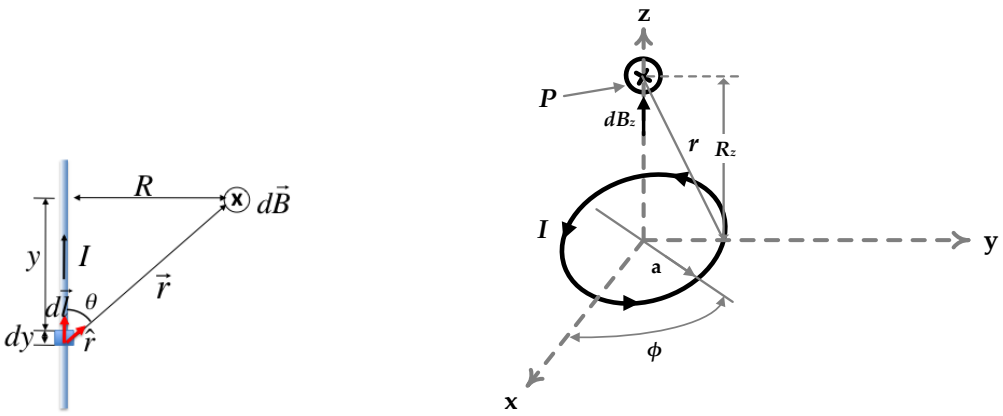


**Figure 2.2** Flux density B for **(a)** straight wire, **(b)** circular current loop [15].

## 2.2.2 Near-field non-Radiative WPT

Non-radiative WPT is characterized by the receiver being at a distance from the transmitter that lies in the near-field region. Fundamentally, the WPT mechanism takes advantage of electromagnetic induction theory rather than electromagnetic radiation. In such way, a current can be induced in a secondary conductor or coil by means of magnetic field generated by a

current passing through a primary conductor or coil. Normally, as the main feature of non-radiative WPT, the transmitter and the receiver are located in the near-field region where the distance between the transmitter and receiver is limited to small ranges, this is, several times the diameter of coils. As previously mentioned, the first demonstration for near-field electromagnetic induction-based WPT was achieved by Nikola Tesla in the early 1890s.

A representative inductive WPT system comprises a primary transmitting coil connected to an alternating current power source and a secondary receiver coil connected to the load. It is possible to approximate the fundamental theory by simultaneously using the basic electromagnetic laws and Faraday's induction law. Starting from the Biot-Savart law [16], assuming a straight wire made of infinitesimal segments with length *dl* as shown in Figure 2.2(a), the magnetic flux density at a point *P* generated by a current flow *I* in the wire can be given by:

$$B_P = \frac{\mu I}{4\pi} \int \frac{\sin\theta}{r^2} dl \tag{2.2}$$

where $\mu$ is permeability of medium, *r* is the distance from the element *dl*, and *I* is the current flowing in the wire [15]. The magnetic flux in Equation (2.2), however, turns into $\mu I/2\pi R$ for a conducting wire having infinite length at a distance *R* from the point of consideration *P*. On the other hand, as we expect in the case of having a circular shaped coil, Equation (2.2) can be modified for the circular coil in Figure 2.2(b) as follows:

$$B_P = \frac{\mu N I a^2}{2(a^2 + R_z^2)^{3/2}} \tag{2.3}$$

where *N* is the number of turns in the coil, *a* is the circular coil's radius, *I* is the current in the coil turns, and $R_z$ is the distance from the coil center to the point where the flux density is calculated. If the current *I* is alternating, this means that the magnetic flux density *B* will also be changing over time.

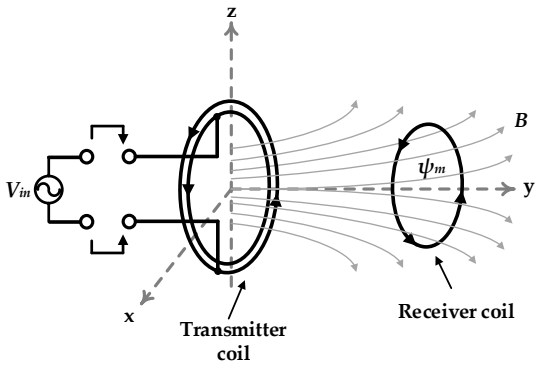


**Figure 2.3** Electromagnetic induction in circular coils.

Assuming that there is a coil connected to an alternating current source, the magnetic flux $\psi$ will have the direction shown in Figure 2.3. If another coil, let us call it the receiving coil, is placed close to the first coil such that it becomes linked by the time-varying flux, then the total magnetic flux $\psi_m$ that crosses the receiving coil can be expressed as:

$$\psi_m = \int_s B.ds \tag{2.4}$$

where $B$ is the generated magnetic flux by the transmitting coil and $s$ is the receiving coil's surface. This leads to Faraday's induction law which states that the induced voltage in the receiving coil can then be expressed by [15]:

$$V = -\frac{d\psi_m}{dt} \tag{2.5}$$

where $V$ is the open-circuit induced voltage in the receiving coil. If the receiving coil is closed by a circuitry, a current would pass due to the induced voltage, and hence the power can be successfully transferred from the transmitting coil to the receiving coil.

The amount of energy received by the receiving coil is dependent on the amount of magnetic flux that links its surface. This consequently is dependent on the surface of the coil itself, as one can note in Equation (2.4). On the other hand, as revealed by Equation (2.3), the magnetic flux density decays rapidly at the rate of $R^2$ from the transmitting coil. Obviously, and similar to Tesla's system, it is reasonably better to create resonant coils which would help in strengthening the magnetic field over a larger distance from the transmitting end so that the power could be received efficiently at higher distances. In that way, the name "*resonant inductive coupling*" WPT emerges to distinguish such system from the non-resonant inductive WPT. Consequently, resonant inductive coupling (RIC) WPT has attracted many applications due to its higher efficiency over a wider distance range. Early successful implementations for RIC-WPT can be noted in [17] where a maximum efficiency of 80% has been achieved at distance of 10mm. Similarly, an average efficiency of 60% has been achieved at long distances in the range of 2m [18].

Up to this point, it becomes apparent that RIC-WPT is one of the most convenient type for transmitting power to WSN in terms of power demand at higher distance with more flexibility that is not limited to direct line of sight between the power source and the receiving node. Thus, RIC-WPT is considered as a key enabling technology for a wide number of applications; however it is of utmost importance to study carefully the different parameters and system conditions that affect the design. Finding an accurate analysis and model would help in finding the optimal design parameters such as frequency of operation, transmitter and receiver coil

parameters and distance between the coils, which would open the way to develop new techniques that would increase the transmission efficiency and power range as well.

## 2.3 Resonant Inductive Coupling WPT

A generic system model for a RIC-WPT is shown in Figure 2.4. This system model comprises a power transmitter, and a power receiver. In addition, the model includes and optional wireless data connection between the transmitter and receiver. This model is still accepted for a wide range of applications that uses two-coil WPT, while in other improved systems, yet more complex, other relaying power coils may be embedded within the power link [11].

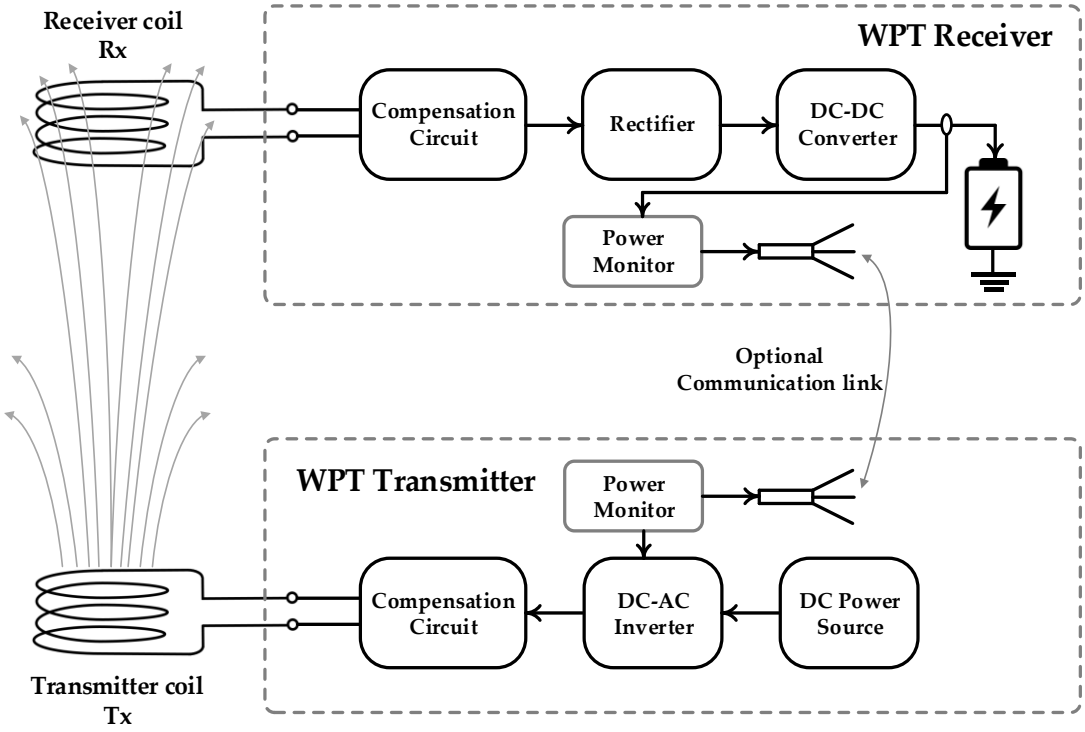


**Figure 2.4** A generic systematic model for RIC wireless power transfer system.

RIC-WPT is realized by two magnetically coupled coils with each coil being part of a resonance circuit both tuned at the same frequency. The resonance is created by means of a compensation circuit. The simplest compensation is realized by a capacitor connected either in series or parallel to each coil. In this case, an oscillating magnetic field is generated in the transmitter coil which helps sustaining the energy away from the coil and increase the distance where the energy still reachable before dying away slowly.

### 2.3.1 Analytical Model of RIC WPT

Analytical models are the keystone for estimating the performance of RIC-WPT towards system co-designing. Several analytical models have been followed extensively in research based on different theories [19]. Among them, coupled mode theory [18], [20], [21], reflected load theory [22]–[24], and lumped element circuit theory [25] are the most common theories adopted in literature. More recently, a gyrator-based model has been also developed for analyzing RIC WPT [26]. It is more adequate, however, to adopt the reflected load theory because it is simple and applicable for analyzing most of performance metrics such as efficiency, maximum power, voltage gain, current gain and output voltage characteristics. Figure 2.5 depicts a simplified block diagram for the RIC WPT system that will be studied in the next sections.

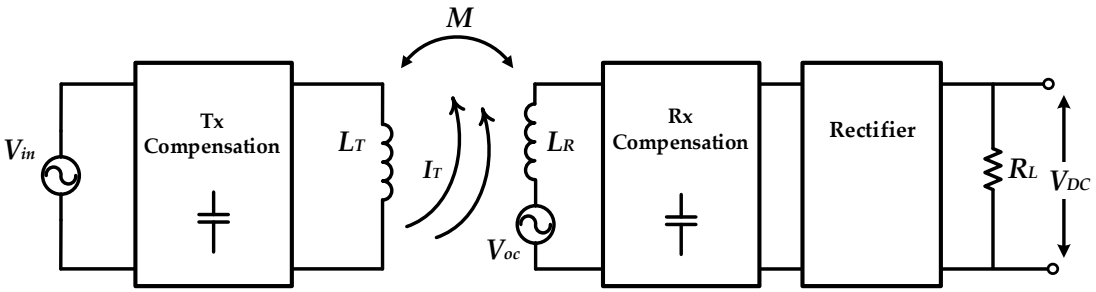


**Figure 2.5** General block diagram for RIC WPT system.

### 2.3.2 Compensation Topologies

The most frequently adopted way for creating the resonant circuit either at the transmitter or the receiver is to use a capacitance to compensate for the self (and the mutual) inductance of the transmitter and receiver coils. The capacitor would be connected either in series or parallel; hence the name "*series-compensated*" or "*parallel-compensated*" respectively. Consequently, four basic topologies, that represent all the possible combinations at the transmitter and receiver sides, emerge as shown in Figure 2.6 [27]. Depending on the connection of the capacitor at the transmitter and receiver, the topologies are called series-series, series-parallel, parallel-series and parallel-parallel. The power transfer capability and characteristics of each topology have been extensively discussed in the literature [27].

To understand the characteristics and performance metrics of every topology, it is important to analyze the major operation characteristics related to design parameters, which hence would help in selecting the optimum topology for WPT-enabled WSNs.

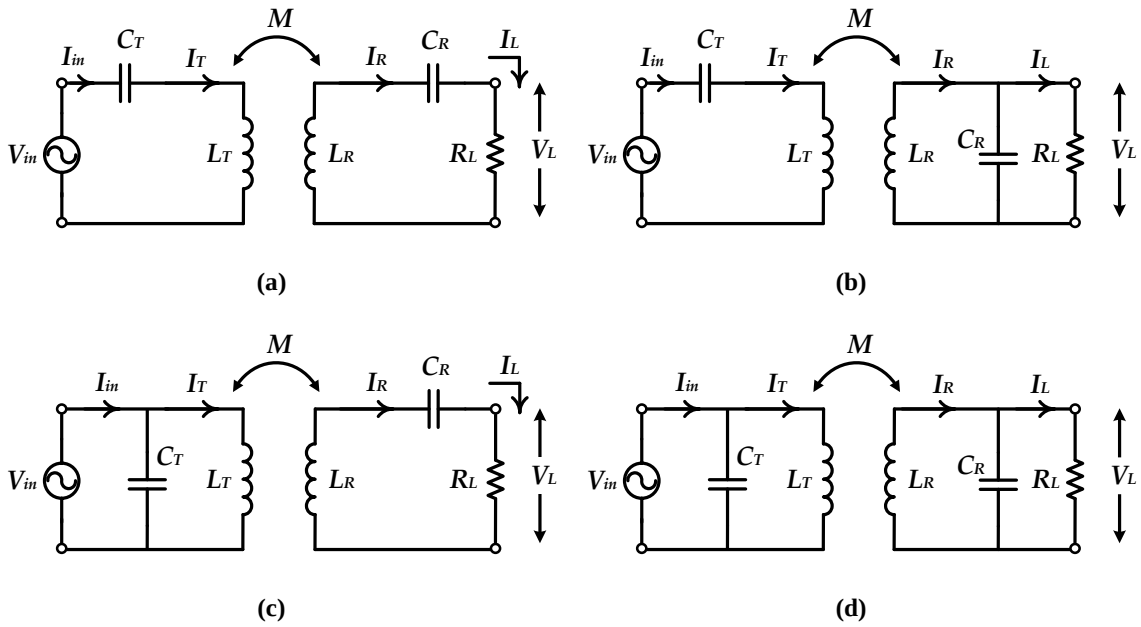


**Figure 2.6** Compensation topologies **(a)** series-series, **(b)** series-parallel, **(c)** parallel-series, **(d)** parallel-parallel.

## 2.4 Analysis of Basic RIC WPT Topologies

We have shown in the previous section the most common compensation topologies in RIC WPT systems. Every compensation topology offers some unique features which consequently matches the needs of a given range of applications. In this section, however, we focus on two basic topologies, namely the series-series and series-parallel topologies. The analysis of efficiency, power transfer capability, and voltage transfer ratio is to be reviewed as follows.

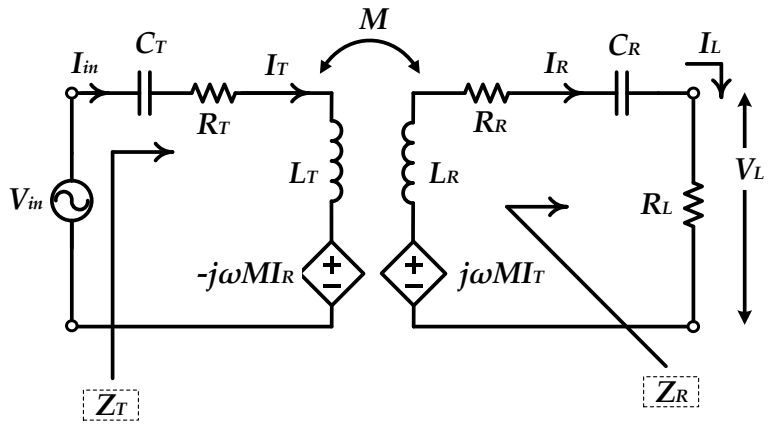


**Figure 2.7** Equivalent circuit of series-series compensated RIC WPT link.

## 2.4.1 Series-Series Compensation Scheme

The equivalent circuit of a series-series compensated RIC WPT link is shown in Figure 2.7. In this circuit, the induced voltage at the transmitter due to the receiver current $I_R$ is $-j\omega MI_R$, while the induced voltage at the receiver due to the transmitter current $I_T$ is $j\omega MI_T$. With the help of this equivalent circuit, the reflected load theory will be used to obtain the characteristic equations.

First, we start by deriving the total receiver impedance, which is given by:

$$Z_{Rs} = R_R + R_L + j\omega L_R + \frac{1}{j\omega C_R} \tag{2.6}$$

where $R_R$ is the copper-loss resistance of the receiver coil, $L_R$ is the self-inductance of the receiver coil, $C_R$ is the compensating capacitance, and $R_L$ is the equivalent load resistance. One can note that the equivalent circuit is assumed with no capacitors' ESR nor source resistance, just for the sake of simplicity. The series resonance circuit at the transmitter and the receiver results in angular resonance frequencies $\omega_T$ and $\omega_R$ respectively, which are given by:

$$\omega_T = \frac{1}{\sqrt{L_T C_T}} \qquad \omega_R = \frac{1}{\sqrt{L_R C_R}} \tag{2.7}$$

Moreover, for the series resonant circuit at the transmitter and receiver ends, the intrinsic quality factors $Q_T$ and $Q_R$ respectively, are given by:

$$Q_T = \frac{\omega L_T}{R_T} \qquad Q_R = \frac{\omega L_R}{R_R} \tag{2.8}$$

While otherwise load quality factor at the series-compensated receiver circuit is given by:

$$Q_{L-S} = \frac{\omega L_R}{R_L} \tag{2.9}$$

### *2.4.1.1 Maximum Power Transfer*

To calculate the power transfer capability of the series-series compensated WPT link, the reflected load theory will be used as has been discussed. Thus, the reflected impedance from the receiver to the transmitter is:

$$Z_{Rs-M} = \frac{\omega^2 M^2}{Z_{Rs}} = R_{Rs-M} + jX_{Rs-M} \tag{2.10}$$

where $Z_{Rs\text{-}M}$ is the reflected impedance from the receiver to the transmitter, $Z_{Rs}$ is the series-compensated receiver impedance as given in Equation (2.6), $R_{Rs\text{-}M}$ is the real part (resistive part) and $X_{Rs\text{-}M}$ is the imaginary part (reactive part). For a while, we assume that the transmitter coils is lossless, *i.e.* $R_T = 0$, so that the transmitter impedance $Z_T$ is calculated as:

$$Z_T = j\omega L_T + \frac{1}{j\omega C_T} + Z_{Rs-M} \tag{2.11}$$

which is elaborated to:

$$Z_T = \frac{\omega^4 M^2 C_R^2 (R_R + R_L) + j\omega^3 M^2 C_R (1 - \omega^2 L_R C_R)}{\omega^2 C_R^2 (R_R + R_L)^2 + (\omega^2 L_R C_R - 1)^2} + j(\omega L_T - {}^1\!/_{\omega C_T}) \tag{2.12}$$

The power delivered to the receiver $P_{Rs}$ is function of the real part $\Re(Z_T)$, written as:

$$P_{Rs} = |I_T|^2 \Re(Z_T) = |I_T|^2 \left\{ \frac{\omega^4 M^2 C_R^2 (R_R + R_L)}{\omega^2 C_R^2 (R_R + R_L)^2 + (\omega^2 L_R C_R - 1)^2} \right\} \tag{2.13}$$

With the help of Equations (2.7)-(2.9), and knowing that $M^2 = k^2 L_T L_R$, Equation (2.13) can be simplified as a function of $Q_R$, $Q_{L\text{-}S}$, $\omega_R$ as follows:

$$P_{Rs} = |I_T|^2 \frac{k^2 L_T \, \omega^3 / \omega_R^2 \; [{}^1\!/_{(Q_R \,//\, Q_{L-S})}]}{1/(Q_R \,//\, Q_{L-S})^2 + (\omega^2/\omega_R^2 - 1)^2} \tag{2.14}$$

The delivered power in Equation (2.14) is a function of the angular frequency; consequently, the frequency which corresponds to the maximum power can be estimated by taking the derivative of Equation (2.14) as $\partial P_{Rs}/\partial\omega = 0$, so that the angular frequency $\omega_{Pm}$ follows:

$$\omega_{Pm} = \frac{\omega_R}{\sqrt{1 - 1/2(Q_R \,//\, Q_{L-S})^2}} \tag{2.15}$$

The angular frequency at which the maximum power transfer is achieved is a function of $\omega_R$, $Q_R$ and $Q_{L\text{-}S}$. Typical values of $Q_R$ are around 100 while $Q_{L\text{-}S}$ is rarely exceeding 40 [28]. Accordingly, the term $(1/2(Q_R \,//\, Q_{L\text{-}S})^2)$ becomes approximately equal to zero and Equation (2.14) reduces to:

$$\omega_{Pm} \cong \omega_R \tag{2.16}$$

This means that the maximum power transfer to the load occurs when the operating frequency, or literally the transmitter frequency, is equal to the receiver resonance frequency $\omega_R$. At this frequency, from Equation (2.14), the maximum power transfer is approximated as follows:

$$P_{Rs-m} = |I_T|^2 k^2 L_T \omega_R (Q_R \,//\, Q_{L-S}) \tag{2.17}$$

The fact that the real part of $Z_T$, and consequently $P_{Rs}$, reaches a maximum at $\omega=\omega_R$ is shown in Figure 2.8 versus $\omega/\omega_R$ at different $Q_{L-S}$ (25 and 50) and different coupling coefficients (*k=0.1* and *k=0.2*). Note that the values in Figure 2.8 are normalized to ($\omega L_R$). The maximum power transfer in Equation (2.17) considers only the active power at the transmitter; however any reactive power at the transmitter circuit will degrade the WPT link efficiency. Moreover, we have already ignored the effect of $R_T$ on the delivered power because the power consumed by $R_T$ only counts for the WPT link efficiency as we will declare.

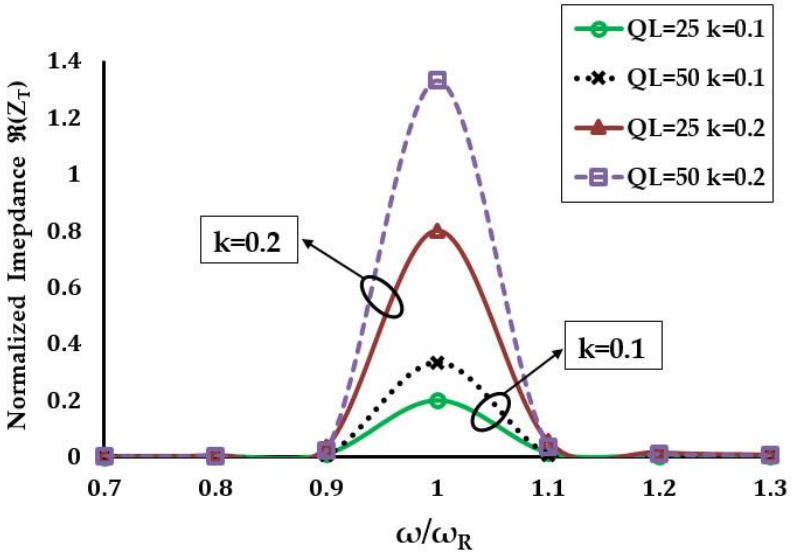


**Figure 2.8** Real part of $Z_T$ function of ($\omega/\omega_R$) at different load quality factors and coupling coefficients.

### *2.4.1.2 Transmission Efficiency*

The transmission efficiency is calculated as the ratio between the output power delivered to the load $R_L$ and the input power to the transmitter. It is more convenient to model the power flow from the input terminals of the transmitter to the load as shown in Figure 2.9. A more detailed model has been presented in [29] where the efficiency of power electronics circuits (such as the transmitter inverter, the receiver rectifier and regulator) are taken into account. In contrast, only the efficiency of the transmitter and receiver resonance circuit are included in Figure 2.9 for simplicity.

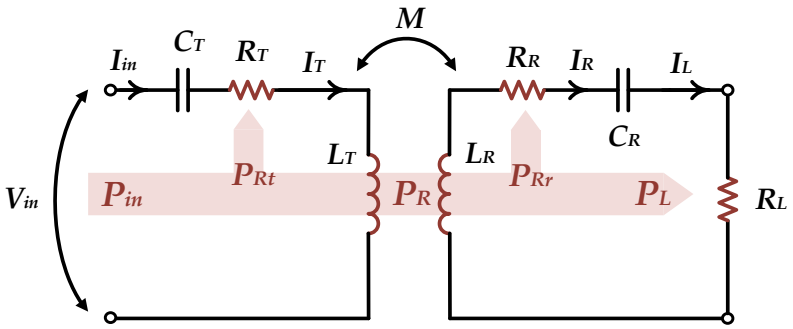


**Figure 2.9** Power distribution in series-series compensated WPT link.

The total transmission link efficiency can be obtained as:

$$\eta_{SS} = \eta_{T-S} \cdot \eta_{R-S} \tag{2.18}$$

where $\eta_{SS}$ is the total transmission efficiency of the series-series WPT scheme, $\eta_{T\text{-}S}$ is the efficiency of the series-compensated transmitter, and $\eta_{R\text{-}S}$ is the efficiency of the series-compensated receiver. As depicted in Figure 2.9, the receiver efficiency, which represents the amount of useful power consumed by the load, is obtained by:

$$\eta_{R-S} = \frac{P_L}{P_R} = \frac{R_L}{R_R + R_L} \tag{2.19}$$

On the other hand, the transmitter efficiency that indicates the amount of useful power transferred to the receiver is given by:

$$\eta_{T-S} = \frac{P_R}{P_{in}} = \frac{R_{Rs-M}}{R_T + R_{Rs-M}} \tag{2.20}$$

where $R_{Rs\text{-}M}$ is obtained by:

$$R_{Rs-M} = \Re\left(\frac{\omega^2 k^2 L_T L_R}{Z_{Rs}}\right) = \frac{\omega^2 k^2 L_T L_R (R_R + R_L)}{(R_R + R_L)^2 + (\omega L_R - 1/\omega C_R)^2} \tag{2.21}$$

Then, from Equations (2.19)-(2.21) into Equation (2.18), the total transmission efficiency is given by:

$$\eta_{SS} = \frac{\omega^2 k^2 Q_T (Q_R \,//\, Q_{L-S})/(\omega_R^2 (1 + Q_{L-S}/Q_R))}{[(Q_R \,//\, Q_{L-S})(\omega/\omega_R - \omega_R/\omega)]^2 + \omega^2 k^2 Q_T (Q_R \,//\, Q_{L-S})/\omega_R^2 + 1} \tag{2.22}$$

The total efficiency, as we see in Equation (2.22), is a function of the angular frequency $\omega$ and coupling coefficient $k$. Consequently, it is possible to solve for the maximum $\eta_{SS}$ at a specific $\omega$ by taking the derivative $\partial\eta_{SS}/\partial\omega=0$, so that the angular frequency of the maximum efficiency $\eta_{SS\text{-}m}$ is obtained by:

$$\omega_{\eta SS-m} = \frac{\omega_R}{\sqrt{1 - 1/2(Q_R \,//\, Q_{L-S})^2}} \tag{2.23}$$

One can note that the frequency $\omega_{\eta SS\text{-}m}$ that maximizes the series-series WPT link is interestingly equal to the frequency in Equation (2.15) at which the power transfer is at its maximum. Similarly, for high $Q_R$ and $Q_{L\text{-}S}$ values, the approximation $\omega_{\eta SS\text{-}m} = \omega_R$ holds. By substituting in Equation (2.22), the maximum transmission efficiency is given by:

$$\eta_{SS-m} = \frac{k^2 Q_T (Q_R \,//\, Q_{L-S})}{[1 + k^2 Q_T (Q_R \,//\, Q_{L-S})](1 + Q_{L-S}/Q_R)} \tag{2.24}$$

The maximum efficiency is shown in Figure 2.10(a) versus the normalized angular frequency $\omega/\omega_R$. At first, we note that the maximum efficiency occurs at an angular frequency approximately equal to $\omega_R$, however, the lower $Q_{L\text{-}S}$ the higher the efficiency. This fact is consistent with the nature of the series resonant tank at the receiver circuit because higher $Q_{L\text{-}S}$ means that the load resistance becomes very close and approaches the value of the parasitic resistance of the receiver coil $R_R$ [29]. Then, we also note that the increase in the coupling coefficient $k$ doesn't necessarily mean that the maximum efficiency will increase considerably. In other words, a change in the coupling coefficient $k$ means that the reflected impedance to the transmitter will change accordingly (as Equation (2.10) indicates) which results in a change in the impedance matching at the transmitter.

We recall that the coupling coefficient is representing the mutual coupling between the transmitter and receiver coils which in essence depends on the distance between the two resonating coils. A detailed analysis for the effect of $k$ variation on the power transmission efficiency has been presented in [30] assuming that the resonance frequency of the transmitter and receiver are matched. It has been shown that for a specific $k$ the load resistance, and thus the load quality factor $Q_{L\text{-}S}$, has to be optimized for maximum power in order to achieve the maximum possible efficiency. Finally, the approximation of Equation (2.23) (as $\omega_{\eta SS\text{-}m} = \omega_R$) depends on the fact that $Q_{L\text{-}S}$ is always higher than 10 in practice, and hence we show in Figure 2.10(b) the theoretical efficiency obtained from Equation (2.24) and the simulated efficiency of a WPT link obtained from PSpice. It shows that the maximum efficiency is roughly achieved at the vicinity of $\omega = \omega_R$.

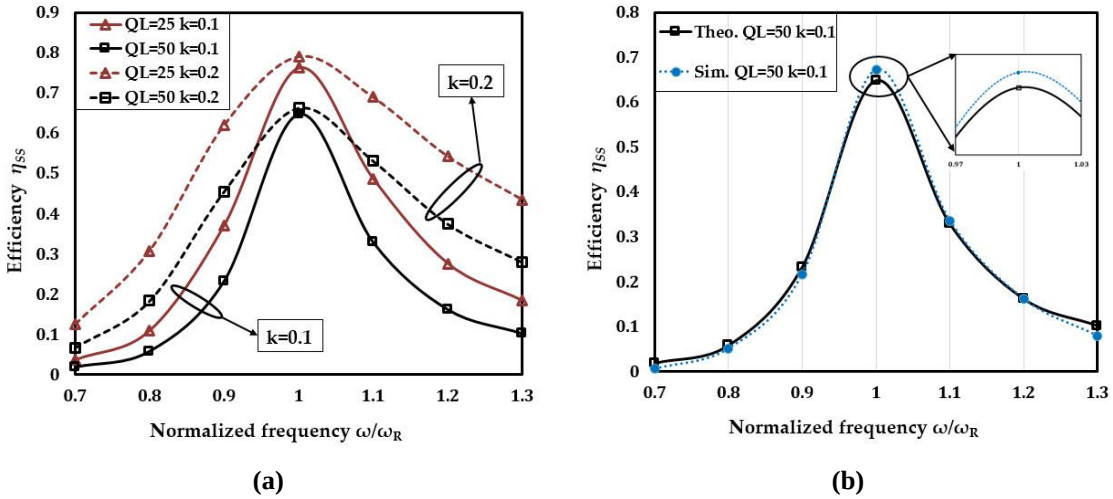


**Figure 2.10** Efficiency versus normalized frequency, **(a)** at different $k$ and $Q_{L\text{-}S}$; **(b)** theoretical versus PSpice simulated.

### *2.4.1.3 Link Gain and Transconductance*

In this section we will analyze the characteristics of voltage gain $A_{SS}$ and transconductance $G_{SS}$ of the series-series WPT link modeled by Figure 2.7. The output voltage that appears on the load can be written as:

$$V_{L-S} = j\omega M I_T \frac{R_L}{Z_{Rs}} \tag{2.25}$$

where $Z_{Rs}$ is already given in Equation (2.6) and the transmitter current is obtained in terms of $V_{in}$ by:

$$I_T = \frac{V_{in}}{Z_T} = \frac{V_{in}}{R_T + j(\omega L_T - 1/\omega C_T) + \omega^2 M^2 / Z_{Rs}} \tag{2.26}$$

The voltage gain from source-to-load is obtained by substituting Equation (2.26) into Equation (2.25):

$$A_{SS} = \frac{V_{L-S}}{V_{in}} = \frac{j\omega M R_L}{Z_{Rs}[R_T + j(\omega L_T - 1/\omega C_T)] + \omega^2 M^2} \tag{2.27}$$

As we note in Equation (2.27), the voltage gain $A_{SS}$ is a function of the angular frequency $\omega$, while it represents a complete transfer function that contains the amplitude and phase information. However, as we have previously shown, the series-compensated receiver circuit should be operated at resonance, *i.e.* ($\omega = \omega_R$). Consequently, we become more interested in the

amplitude of $A_{SS}$ at $\omega_R$. By knowing that ($Z_{Rs}$= $R_R$+$R_L$) at $\omega_R$, the amplitude of Equation (2.27) is obtained by:

$$|A_{SS}| = \left|\frac{V_{L-S}}{V_{in}}\right| = \frac{\sqrt{\omega_R M X_T R_L (R_R + R_L)^2 + \omega_R^2 M^2 R_L^2 [\omega_R^2 M^2 + R_T (R_R + R_L)]^2}}{[\omega_R^2 M^2 + R_T (R_R + R_L)]^2 + X_T^2 (R_R + R_L)^2} \quad (2.28)$$

where

$$X_T = \omega_R L_T - 1/\omega_R C_T \quad (2.29)$$

Despite the complexity of Equation (2.28), one can note that the source-to-load voltage gain is greatly dependent on the compensation at the transmitter side represented by the reactive part $X_T$. If the transmitter resonance circuit is designed to resonate at $\omega_R$, *i.e.* $\omega_T$ = $\omega_R$, then $X_T$ becomes zero and Equation (2.28) is simplified as follows:

$$|A_{SS}| = \frac{\omega_R M R_L}{\omega_R^2 M^2 + R_T (R_R + R_L)} \quad (2.30)$$

As we note, $A_{SS}$ is load-dependent which is certainly undesirable. Moreover, if the transmitter and receiver circuits are resonating at the same frequency, the losses of transmitter coil $R_T$ will have a considerable effect on the link gain. In contrast, the receiver coil loss $R_R$ has less effect on the link gain because $R_L \gg R_R$ in most practical situations.

The transconductance can be determined in a similar way as follows:

$$I_{L-S} = \frac{j\omega M I_T}{Z_{Rs}} = \frac{j\omega M V_{in}}{Z_{Rs}[R_T + j(\omega L_T - 1/\omega C_T)] + \omega^2 M^2} \quad (2.31)$$

$$|G_{SS}| = \left|\frac{I_{L-S}}{V_{in}}\right|_{\omega=\omega_R} = \frac{\sqrt{\omega_R M X_T (R_R + R_L)^2 + \omega_R^2 M^2 [\omega_R^2 M^2 + R_T (R_R + R_L)]^2}}{[\omega_R^2 M^2 + R_T (R_R + R_L)]^2 + X_T^2 (R_R + R_L)^2} \quad (2.32)$$

Applying the same assumptions of $\omega_T$ = $\omega_R$, $X_T$ becomes equal to zero and $G_{SS}$ is simplified to:

$$|G_{SS}| = \frac{\omega_R M}{\omega_R^2 M^2 + R_T (R_R + R_L)} \cong \frac{1}{\omega_R M} \quad (2.33)$$

The transconductance of a series-series WPT link is nearly $R_L$-independent as we notice in Equation (2.33). However, it is important to recall that the approximation of $G_{SS}$ =$1/M\omega_R$ assumes negligible transmitter coil losses which is the case in practical circuits having

$R_T \ll (R_R+R_L)$. The conclusion is that series-series WPT link has a load-dependent output voltage while it features a nearly load-independent output current.

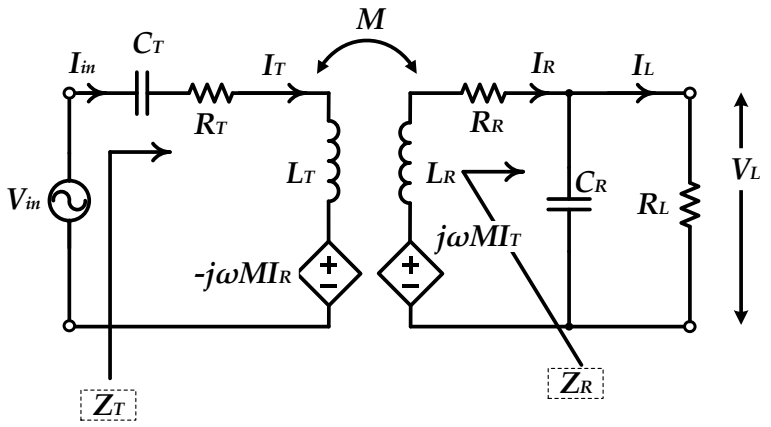


**Figure 2.11** Equivalent circuit of series-parallel compensated RIC WPT link.

## 2.4.2 Series-Parallel Compensation Scheme

Similarly, an equivalent circuit for series-parallel compensated RIC WPT link is shown in Figure 2.11. The induced voltages will be the same as it has been shown in Figure 2.7, however, the only difference will be in the receiver impedance $Z_R$. In the power transfer analysis we will assume that the coil losses are negligible (*i.e.* $R_T = R_R = 0$), otherwise the power transfer analysis would be too complex. Consequently, the total impedance parallel-compensated receiver is thus written as:

$$Z_{Rp} = j\omega L_R + \frac{1}{j\omega C_R + 1/R_L} \tag{2.34}$$

The resonance frequency of the transmitter and receiver circuit is still given by Equation (2.7). However, the load quality factor of the parallel-compensated receiver is now given by:

$$Q_{L-P} = \frac{R_L}{\omega L_R} \tag{2.35}$$

### *2.4.2.1 Maximum Power Transfer*

The power transfer capability of the series-parallel compensated WPT link is obtained by first evaluating the reflected impedance from the receiver to the transmitter, which is written as:

$$Z_{Rp-M} = \frac{\omega^2 M^2}{Z_{Rp}} = R_{Rp-M} + jX_{Rp-M} \tag{2.36}$$

where $R_{Rp\text{-}M}$ and $X_{Rp\text{-}M}$ are the real and imaginary parts of the reflected impedance respectively, which are given by:

$$R_{Rp-M} = \Re\left(\frac{\omega^2 k^2 L_T L_R}{Z_{Rp}}\right) = \frac{\omega^2 k^2 L_T L_R R_L}{\omega^2 L_R^2 + (\omega^2 L_R C_R R_L - R_L)^2} \tag{2.37}$$

$$X_{Rp-M} = \Im\left(\frac{\omega^2 k^2 L_T L_R}{Z_{Rp}}\right) = \frac{-\omega^3 k^2 L_T L_R [L_R + C_R R_L^2(\omega^2 C_R L_R - 1)]}{\omega^2 L_R^2 + (\omega^2 L_R C_R R_L - R_L)^2} \tag{2.38}$$

Using Equations (2.37) and (2.38), the input impedance $Z_T$ at the transmitter can be written as:

$$Z_T = R_{Rp-M} + j\left(\omega L_T - \frac{1}{\omega C_T} + X_{Rp-M}\right) = R_T + jX_T \tag{2.39}$$

where $R_T$ and $X_T$ are the real part and imaginary part of the transmitter impedance $Z_T$, respectively. The power delivered to the parallel-compensated receiver $P_{Rp}$ is obtained as a function of the input impedance $Z_T$, written as:

$$P_{Rp} = \frac{|V_{in}|^2}{\Re(Z_T)} = |V_{in}|^2 \cdot \frac{R_T}{R_T^2 + X_T^2} \tag{2.40}$$

The maximum power is obtained by taking the derivative of Equation (2.40) as $\partial P_{Rp}/\partial\omega = 0$, then we find the power transfer is maximized at angular frequency $\omega_{Pm}$, where at this frequency the real part $R_T$ is maximized, and given by:

$$\omega_{Pm} = \frac{\omega_R}{\sqrt{1 + 1/Q_{L-P}^2}} \cong \omega_R \tag{2.41}$$

where $Q_{L\text{-}P}$ is given in Equation (2.35). From Equation (2.41) into (2.40), the maximum power transfer is approximated as follows:

$$P_{Rp-m} = |V_{in}|^2 \cdot \frac{k^2 L_T R_L / L_R}{(k^2 L_T R_L / L_R)^2 + [\omega L_T (1 - k^2) - \frac{1}{\omega C_T}]^2} \tag{2.42}$$

In spite of the fact that the operating frequency of the series-parallel WPT link should be equal to the receiver resonant frequency $\omega_R$, it is important to note in Equation (2.42) that the transmitter resonance frequency has a different value, given by:

$$\omega_T = \frac{1}{\sqrt{L_T C_T (1 - k^2)}} \tag{2.43}$$

In other words, the resonance frequency of the transmitter circuit $\omega_T$ is dependent on the coupling factor. This fact has already been noted in [31], which can be explained by the help of Equation (2.38). A parallel-compensated receiver circuit with a WPT link operating at the receiver resonance frequency reflects a non-zero reactance. This means that the reflected reactance $X_{Rp\text{-}M}$ has to be compensated jointly with $L_T$ using the series capacitor $C_T$ [27]. Consequently, the power transfer of series-parallel WPT is dependent on the ability of compensating the total reactive power at the transmitter circuit.

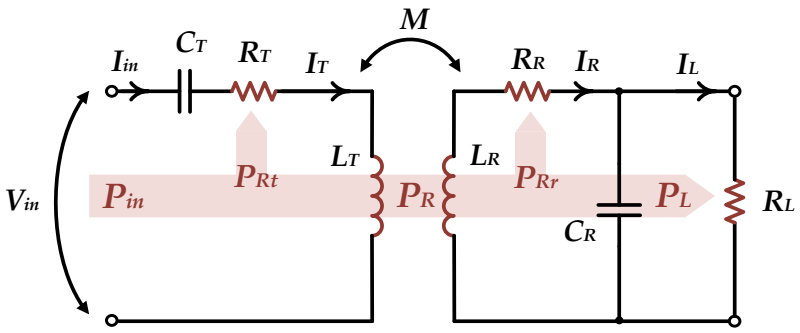


**Figure 2.12** Power distribution in series-parallel compensated WPT link.

### *2.4.2.2 Transmission Efficiency*

The analysis of transmission efficiency of series-parallel WPT link can be similarly derived by calculating the efficiency of the series-compensated transmitter $\eta_{T\text{-}S}$ and the efficiency of the parallel-compensated receiver $\eta_{R\text{-}P}$ and the WPT link efficiency is obtained by:

$$\eta_{SP} = \eta_{T-S} \cdot \eta_{R-P} \tag{2.44}$$

where $\eta_{T\text{-}S}$ and $\eta_{R\text{-}P}$ are given by:

$$\eta_{T-S} = \frac{P_R}{P_{in}} = \frac{R_{Rp-M}}{R_T + R_{Rp-M}} \tag{2.45}$$

$$\eta_{R-P} = \frac{P_L}{P_R} = \frac{\Re(Z_R)}{R_R + \Re(Z_R)} \tag{2.46}$$

where $Z_R$ in Equation (2.46) is given by Equation (2.34) after including the coil losses $R_R$ because the value of $R_R$ is affecting the total efficiency as depicted in Figure 2.12. Similarly,

$R_{Rp\text{-}M}$ in Equation (2.37) must be updated to include $R_R$. The new expression for $R_{Rp\text{-}M}$ is now obtained by:

$$R_{Rp-M} = \frac{\omega^2 k^2 L_T L_R (\omega^2 C_R^2 R_L^2 R_R + R_L + R_R)}{(\omega L_R + \omega C_R R_L R_R)^2 + (\omega^2 L_R C_R R_L - R_L - R_R)^2} \tag{2.47}$$

Due to the complexity of the derived expression, the total transmission efficiency can be simplified as [32]:

$$\eta_{SP} = \frac{1}{(1 + \Lambda_T)(1 + \Lambda_R)} \tag{2.48}$$

where $\Lambda_T$ and $\Lambda_R$ are respectively given by:

$$\Lambda_T = \frac{1/Q_T \left[\left(1/Q_R + Q_{L-P}(1 - \omega^2/\omega_R^2)\right)^2 + (1 + Q_{L-P}/Q_R)^2\right]}{\omega^2 k^2/\omega_R^2 \left[1/Q_R + Q_{L-P}(1 + \omega^2 Q_{L-P}^2/\omega_R^2 Q_R^2)\right]} \tag{2.49}$$

$$\Lambda_R = \frac{1}{Q_R Q_{L-P}} + \frac{\omega^2 Q_{L-P}}{\omega_R^2 Q_R} \tag{2.50}$$

The maximum efficiency $\eta_{SP\text{-}m}$ can be obtained by solving for $\partial\eta_{SP}/\partial\omega = 0$ to obtain the frequency $\omega_{\eta SP\text{-}m}$ that achieves $\eta_{SP\text{-}m}$ as follows:

$$\omega_{\eta SP-m} = \omega_R \frac{\sqrt{1 + 1/Q_R Q_{L-P}}}{(1 + k^2 Q_T / Q_R)^{1/4}} \tag{2.51}$$

By comparing the frequency $\omega_{\eta SP\text{-}m}$ with that in the series-series WPT topology $\omega_{\eta SS\text{-}m}$, we note that it is dependent on $Q_T$ in addition to the dependency on the coupling factor $k$. The dependency on $k$ is not a desirable property as one can argue. Fortunately, Equation (2.51) can be approximated once we know that in practice $Q_R Q_{L\text{-}P} \gg 1$ and $k \ll 1$, so that Equation (2.51) is approximated as follows:

$$\omega_{\eta SP-m} \cong \omega_R \tag{2.52}$$

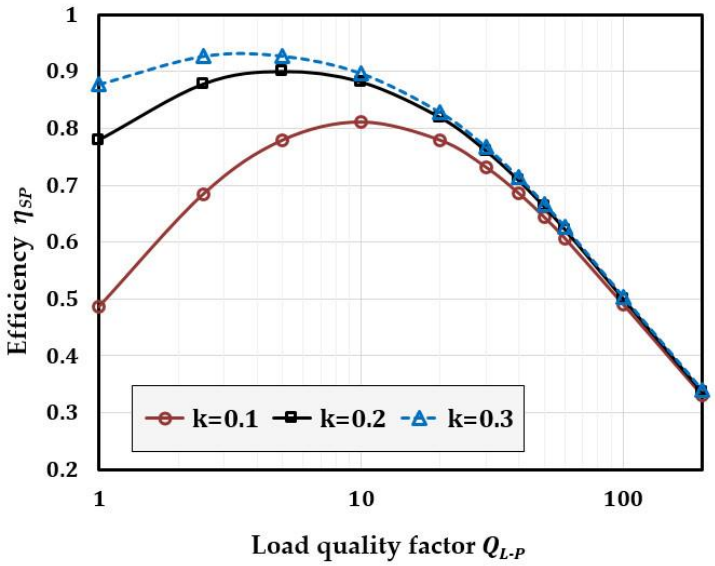


**Figure 2.13** Real part of $Z_T$ as a function of ($\omega/\omega_R$) at different load quality factors and coupling coefficients.

The maximum efficiency of the series-parallel WPT link can be obtained by substituting from Equation (2.52) into (2.48). Figure 2.13 shows the maximum efficiency as a function of the load quality factor $Q_{L\text{-}P}$ at different coupling factors $k$. We note that at low $Q_{L\text{-}P}$, the maximum efficiency drops considerably with the drop in $k$. On the other hand, for very high $Q_{L\text{-}P}$, the maximum efficiency becomes almost independent of $k$.

### *2.4.2.3 Link Gain and Transconductance*

The voltage gain of the series-parallel WPT link $A_{SP}$ is readily obtained by determining the load voltage from Figure 2.11 as follows:

$$V_{L-P} = j\omega M I_T \frac{R_L/(1 + j\omega C_R R_L)}{Z_{Rp}} \tag{2.53}$$

where $Z_{Rp}$ is given in Equation (2.34). The transmitter current $I_T$ in a series-parallel configuration is obtained by:

$$I_T = \frac{V_{in}}{R_T + j(\omega L_T - 1/\omega C_T) + \omega^2 M^2/Z_{Rp}} \tag{2.54}$$

The magnitude of the voltage gain is determined by substituting Equation (2.54) into Equation (2.53). The same assumption of the parallel-compensated receiver is operated at resonance, *i.e.* ($\omega = \omega_R$) would help in simplifying the voltage gain expression as follows:

$$A_{SP} = \frac{V_{L-P}}{V_{in}} = \frac{j\omega_R M R_L}{(1 + j\omega_R C_R R_L)(R_R + L_R/C_R R_L)[R_T + jX_T + M^2 R_L/L_R^2]} \quad (2.55)$$

where: $$X_T = \omega_T L_T - 1/\omega_T C_T - \omega_T M^2/L_R \quad (2.56)$$

The extended expression of $A_{SP}$ is however more manageable if the transmitter circuit is at resonant, *i.e.* $X_T = 0$, so that the magnitude of $A_{SP}$ is obtained by:

$$|A_{SP}| = \omega_R M R_L \frac{\sqrt{1 + \omega_R^2 C_R^2 R_L^2}}{(1 + \omega_R^2 C_R^2 R_L^2)(R_R + L_R/C_R R_L)[R_T + M^2 R_L/L_R^2]} \quad (2.57)$$

Furthermore, the output current characteristics of series-parallel topology is obtained likewise by determining the link transconductance $G_{SP}=I_{L\text{-}P}/V_{in}$ as follows:

$$I_{L-P} = \frac{V_{L-P}}{R_L} = \frac{j\omega M I_T}{Z_{Rp}(1 + j\omega C_R R_L)} \quad (2.58)$$

$$|G_{SP}| = \left|\frac{I_{L-P}}{V_{in}}\right|_{\omega=\omega_R} = \left|\frac{j\omega_R M}{(1 + j\omega_R C_R R_L)(R_R + L_R/C_R R_L)[R_T + jX_T + M^2 R_L/L_R^2]}\right| \quad (2.59)$$

where $X_T$ is given in Equation (2.56). Provided that the transmitter circuit is at resonance and $X_T = 0$, the series-parallel link transconductance is then simplified as:

$$|G_{SP}| = \omega_R M \frac{\sqrt{1 + \omega_R^2 C_R^2 R_L^2}}{(1 + \omega_R^2 C_R^2 R_L^2)(R_R + L_R/C_R R_L)[R_T + M^2 R_L/L_R^2]} \quad (2.60)$$

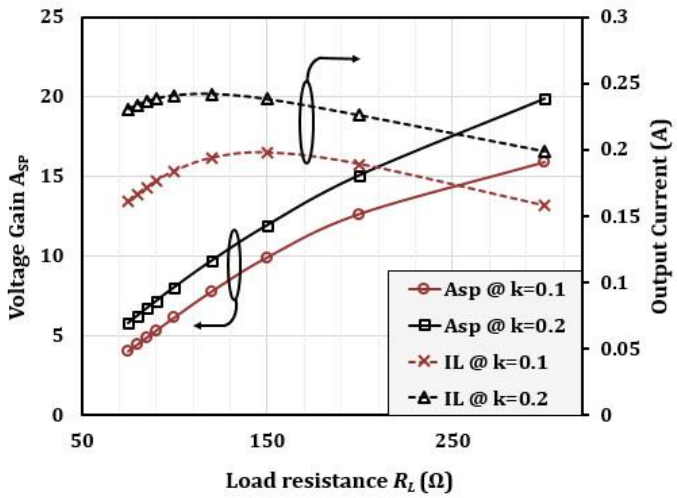


**Figure 2.14** Link gain and output current in series-parallel compensation topology.

The dependency of the voltage gain and the transconductance of series-parallel WPT link is depicted in Figure 2.14 as a function of $R_L$. The depicted results have been calculated using arbitrary values for transmitter and receiver circuits as: $L_R$=$L_T$=12μH, $\omega$ =200 kHz, $C_R$ =52.77 nF, $R_T$ =$R_R$ =150 mΩ. We note that while the voltage gain is dependent on $R_L$, the transconductance is however less dependent on $R_L$.

### 2.4.3 Compensation Topology Considerations

We have analyzed and discussed in detail the characteristics of series-series and series-parallel topologies amongst other. The same procedure could be followed for analyzing parallel-series and parallel-parallel compensation topologies. The literature is however very rich with more sophisticated compensation topologies such as LCL [33], LCC [34] or even LCCL [35]. Every developed topology offers more capabilities which couldn't be achieved by simple topologies compensated by a single capacitor. However, and despite the features that these developed topologies enjoy, it usually comes with other pitfalls such as the inherent complexity and increased size.

On the other hand, series-series and series-parallel compensation topologies are the most common topologies and have received wide interest and their detailed characteristics are well optimized [27], [32], [36]. As it has been stated, an adaptive control is preferably achieved at the receiver side to avoid malfunctions in other receivers in a multiple receiver WPT system driven by a single transmitter. Consequently, it is more convenient to consider the comparison between series-compensated and parallel-compensated receivers. From the load perspective, a series-compensated receiver coil is normally used for low-voltage applications in which the receiver has voltage source characteristics combined with a current boosting capability. On the other hand, a parallel-compensated receiver is suitable for most applications due to the inherent capability of voltage boosting which extends the system operation at very weak coupling conditions while still meeting the load voltage requirement [35]. Therefore, in the next section we focus on the discussion of mistuning issues in parallel-compensated WPT receivers.

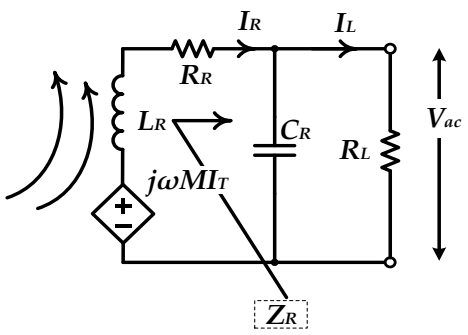


**Figure 2.15** A model of parallel-compensated WPT receiver.

# 2.5 Parallel-Compensated WPT Receivers

## 2.5.1 Performance

The inherent voltage boosting capability of parallel-compensated receivers can be examined apart from the transmitter circuit. Recalling Figure 2.15, the voltage induced in the receiver coil $L_R$ due to the flux linkage from the transmitter is represented as $j\omega MI_T$. Usually this voltage is called the open-circuit voltage $V_{oc}$ and is commonly modeled as a voltage source in series with $L_R$. It is evident that $V_{oc}$ is a function of the mutual coupling between the transmitter and receiver coils, which in turn is dependent upon the distance between them. Consequently, typical values of $V_{oc}$ are usually limited to few millivolts at very low coupling conditions. Fortunately, the load, or more precisely the rectifier circuit, receives the boosted voltage $V_{ac}$ rather than $V_{oc}$. The voltage ratio of the receiver parallel resonant tank ($V_{ac}/V_{oc}$) is given by:

$$\frac{V_{ac}}{V_{oc}} = \frac{1}{s^2 L_R C_R + sL_R/R_L + 1} \tag{2.61}$$

where $V_{ac}$ is the receiver resonant tank output voltage, and $s = j\omega$. Here we denote the resonance frequency of the parallel-compensated receiver as $\omega_{R0}$. For the fully-tuned case, (*i.e.* the resonance frequency of the receiver tank $\omega_{R0}$ is equal to the transmitter's frequency $\omega_T$), then Equation (2.61) can be reduced to:

$$V_{ac} = -j\frac{R_L}{\omega_{R0} L_R} V_{oc} = -jQ_{RL} V_{oc} \tag{2.62}$$

where $Q_{RL}$ is the receiver's load quality factor. Equation (2.62) shows that the resonant tank voltage $V_{ac}$ is boosted from the open-circuit induced voltage $V_{oc}$ by a factor that is equal to the load quality factor $Q_{RL}$. On the other hand, the power transmitted to the receiver is a function of the reflected impedance from the receiver to the transmitter circuit as it has been shown. The maximum power transfer to the parallel-compensated receiver is obtained function of $Q_{RL}$ as [37]:

$$P_{max} = \frac{\omega_{R0} Q_{RL} M^2 I_T^2}{L_R} = \frac{Q_{RL}^2}{R_L} V_{oc}^2 \tag{2.63}$$

## 2.5.2 Mistuning Effect on Power Delivery

The maximum power in Equation (2.63) refers to the load dependency; moreover, power transfer capability is greatly enhanced with higher quality factor $Q_{RL}$. However, the receiver circuit becomes more sensitive for any variations as $Q_{RL}$ increases. To illustrate the mistuning

effect on the receiver circuit, Figure 2.16 depicts possible variations in $L_R$ or $C_R$ modeled as $\Delta L_R$ and $\Delta C_R$ respectively.

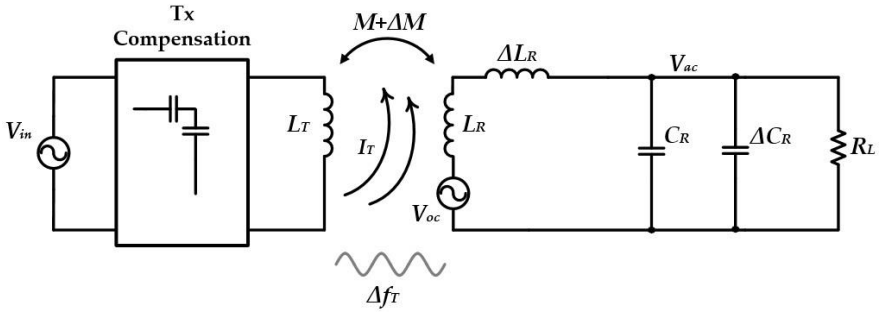


**Figure 2.16** A simplified model for WPT parallel-compensated receiver with possible components' variations modeled.

Note that $\Delta C_R$ (or $\Delta L_R$) comprises either positive or negative values (*i.e.* presuming over-tuned or under-tuned conditions). Including such variations implies that the resonance frequency of the receiver tank is either shifted to lower or higher values. Consequently, one can conclude that $V_{ac}$ and $P_{max}$ in Equations (2.62) and (2.63), respectively, are not relevant anymore. By including all the prospective mismatch sources altogether, it is possible to predict the accurate performance of the receiver tank. The obtained equations, however, would be cumbersome. Therefore, a simple case of variation $\Delta C_R$ in the compensation capacitor is assumed, as shown in Figure 2.16, in which $\Delta C_R$ presumes positive or negative values. Firstly, the capacitor variation $\Delta C_R$ is included in Equation (2.61) in which the voltage boosting ratio turns into:

$$\frac{V_{ac}}{V_{oc}} = \frac{1}{[(1-\omega^2 L_R(C_R+\Delta C_R)] + j\,\omega L_R/R_L} \tag{2.64}$$

Assuming that the transmitter frequency $\omega_T$ is constant, then the magnitude of Equation (2.64) is given by:

$$\left.\frac{V_{ac}}{V_{oc}}\right|_{\omega=\omega_{R0}} = \frac{Q_{RL}}{\sqrt{1+(Q_{RL}\gamma_C)^2}} \tag{2.65}$$

where ($\gamma_C = \Delta C_R/C_R$) is the capacitance mismatch ratio. By comparing Equation (2.65) with Equation (2.62), it is apparent that the voltage ratio of the receiver tank drops to a lower value due to the capacitance mismatch. It is even worse for ultra-high $Q_{RL}$ receiver circuits. Moreover,

the mistuning effect on the delivered power will also affect the reflected impedance expressions that become:

$$R_{Rp-M} = \frac{\omega_{R0} M^2 Q_{RL}}{L_R(1 + Q_{RL}^2 \gamma_C^2)} \tag{2.66}$$

$$X_{Rp-M} = \frac{\omega_{R0} M^2}{L_R} \times \frac{1 + L_R C_R Q_{RL}^2 \gamma_C (1 + \gamma_C)}{1 + Q_{RL}^2 \gamma_C^2} \tag{2.67}$$

Once more, while paying more attention to the real part in Equation (2.63), the mistuning factor $\gamma_C$ multiplied by a factor of $Q_{RL}^2$ results in a significant drop in the resistance reflected back to the transmitter. This necessarily appears as a serious drop in power delivery at the receiver circuit which is obvious by comparing Equation (2.63) with the new expression of delivered power:

$$P_{rms} = \frac{Q_{RL}^2}{R_L(1 + Q_{RL}^2 \gamma_C^2)} V_{oc}^2 \tag{2.68}$$

The given power delivery in Equation (2.68) is only applicable provided that the transmitter circuit is equipped by an adaptive tuning circuit to compensate for the modified reflected reactance in Equation (2.67). Otherwise, the transmitter circuit would be left with some amount of uncompensated *var* that would deteriorate the power transfer from another side. A clear consequence that arises from Equation (2.68) is that a significant drop in transferred power is inevitable as long as the receiver circuit is designed for high-Q operation.

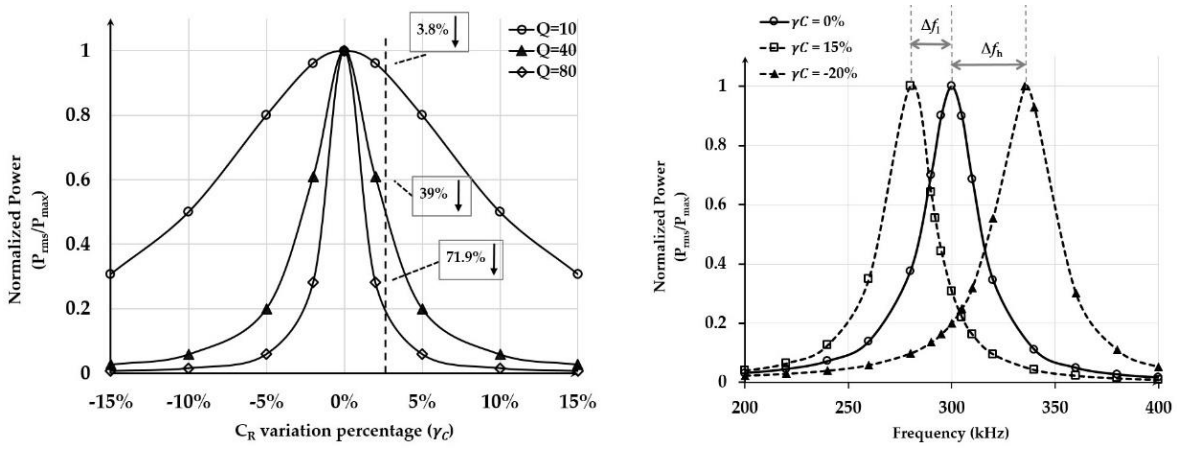


**(a)** **(b)**

**Figure 2.17** Mistuning effect on **(a)** normalized power; **(b)** receiver resonance frequency.

The effect of capacitance variation on the transferred power is shown in Figure 2.17(a), where the normalized power ($P_{rms}/P_{max}$) is plotted against $\gamma_C$ for three different values of $Q_{RL}$. It is obvious that the drop in power due to a small mismatch percentage of 2% is becoming noticeable for high-Q values.

As noted in Figure 2.17(a), the high-Q receiver circuit becomes extremely sensitive irrespective of the enhancement in power transfer capability at the tuned point. The case of $Q_{RL} = 80$ is an illustrative example in which a 71% drop in $P_{rms}$ is expected for a 2% mismatch in $C_R$. On the other hand, Figure 2.17(b) depicts the frequency drift by $\Delta f_l$ as a result of 15% mismatch while it drifts to a higher frequency by $\Delta f_h$ amount due to -20% mismatch. As a direct result, in order to overcome the pitfall of high-Q receivers, the $Q_{RL}$ is normally limited to less than 10 in most systems particularly for high power applications [38]. This, however, is not an adequate choice for low power applications that would demand energy from a distance that extends up to a few times the coil diameter. Consequently, to boost the power transfer capabilities by operating at high $Q_{RL}$, developing an adaptive power management front-end to deal with sensitivity and detuning issues is demanded.

## 2.6 Conclusions

In this Chapter we have revisited the history of wireless power transmission and the different evolving WPT technologies including near-field and far-field. It has been shown that near-field RIC WPT is the most promising candidate for powering WSNs. The different compensation topologies in transmitter and receiver have been investigated. Two basic topologies, namely series-series and series-parallel, are commonly adapted for a wide variety of applications due to their simplicity over other sophisticated topologies that add more capabilities but increase the size and complexity.

The detailed analysis of the series-series and series-parallel WPT links has been extended. From the load perspective, it has been shown that parallel compensation at the receiver side is more suitable for most applications due to its inherent voltage boosting capabilities which make it promising for systems that would work at very weak coupling conditions. Accordingly, the power capability and voltage boosting characteristics of high $Q_{RL}$ parallel-compensated WPT receivers have been investigated. The tradeoff between voltage and power boosting capability, from one side, and the increased sensitivity of the receiver tank, from the other side, add a fundamental bottleneck that has been simply alleviated in the literature by designing the system for low $Q_{RL}$. Designing an adaptive front-end would however help in gaining the advantages of high $Q_{RL}$ WPT receivers while the system is automatically tuned for optimal tuned point.

## 2.7 References

[1] M. A. K. Schwan and P. R. Troyk, “High efficiency driver for transcutaneously coupled coils,” in *Images of the Twenty-First Century. Proceedings of the Annual International Engineering in Medicine and Biology Society*, pp. 1403–1404.

[2] N. Tesla, “Experiments with alternate currents of very high frequency and their application to methods of artificial illumination,” *Trans. Am. Soc. Agric. Eng.*, vol. 8, no. 1, pp. 267–319, Jan. 1891.

[3] L.P. Wheeler, “Tesla’s contribution to high frequency,” *Electr. Eng.*, vol. 62, no. 8, pp. 355–357, Aug. 1943.

[4] C. Brown William, “Experimental airborne microwave supported platform,” *Rome Air Dev. Center*, NewYork, Tech. Report, RADC-TR-65-188, Contract AF30, vol. 3481, 1965.

[5] M. Schaldach, “Bioelectric energy sources for cardiac pacing.,” *Ann. N. Y. Acad. Sci.*, vol. 167, no. 2, pp. 1016–24, Oct. 1969.

[6] R. M. M. Dickinson, “Performance of a High-Power, 2.388-GHz Receiving Array in Wireless Power Transmission Over 1.54 km,” in *MTT-S International Microwave Symposium Digest*, 1976, vol. 76, pp. 139–141.

[7] V. S. Dokukin, A. K. Markeev, E. V. Mishin, J. J. Ruzhin, V. V. Fomichev, I. A. Zhulin, V. N. Ivchenko, G. P. Milinevsky, R. I. Moisya, and R. Z. Sagdeev, “Results of ZARNITZA-2, a rocket experiment on artificial electron beam injection in the ionosphere,” *Adv. Sp. Res.*, vol. 1, no. 2, pp. 5–15, Jan. 1981.

[8] H. Matsumoto and N. Kaya, “ISY-METS rocket experiment and its preparatory airplane experiment,” *IAF, Int. Astronaut. Congr. 43rd*, Washington, Aug. 28-Sept. 5, 1992. 5 p., 1992.

[9] A. Kurs, A. Karalis, R. Moffatt, J. D. Joannopoulos, P. Fisher, and M. Soljačić, “Wireless power transfer via strongly coupled magnetic resonances,” *Science* (80-. )., vol. 317, no. 5834, pp. 83–86, Jul. 2007.

[10] W. C. Brown, “The History of Power Transmission by Radio Waves,” *IEEE Trans. Microw. Theory Tech.*, vol. 32, no. 9, pp. 1230–1242, Sep. 1984.

[11] T. Sun, X. Xie, and Z. Wang, Wireless Power Transfer for Medical Microsystems. New York, NY: Springer New York, 2013.

[12] C. A. Balanis, Antenna theory : analysis and design. Wiley Interscience, 2005.

[13] W. C. Brown and E. E. Eves, “Beamed microwave power transmission and its application to space,” *IEEE Trans. Microw. Theory Tech.*, vol. 40, no. 6, pp. 1239–1250, Jun. 1992.

[14] M. Erol-Kantarci and H. T. Mouftah, “Challenges of wireless power transfer for prolonging User Equipment (UE) lifetime in wireless networks,” in *2014 IEEE 25th Annual International Symposium on Personal, Indoor, and Mobile Radio Communication (PIMRC)*, 2014, pp. 2140–2144.

[15] J. D. Kraus, Electromagnetics. McGraw-Hill, 1992.

[16] B. Thidé, Electromagnetic field theory. Upsilon Books Uppsala, 2004.

[17] P. Si, A. P. Hu, S. Malpas, and D. Budgett, "A frequency control method for regulating wireless power to implantable devices," *IEEE Trans. Biomed. Circuits Syst.*, vol. 2, no. 1, pp. 22–29, Mar. 2008.

[18] A. Kurs, A. Karalis, R. Moffatt, J. D. Joannopoulos, P. Fisher, and M. Soljačić, "Wireless power transfer via strongly coupled magnetic resonances," *Science* (80-. )., vol. 317, no. 5834, pp. 83–86, Jul. 2007.

[19] E. Bou, E. Alarcon, and J. Gutierrez, "A Comparison of Analytical Models for Resonant Inductive Coupling Wireless Power Transfer," *Prog. Electromagn. Res. Symp.*, no. 4, pp. 689–693, 2012.

[20] X. Shu and B. Zhang, "Single-Wire Electric-Field Coupling Power Transmission Using Nonlinear Parity-Time-Symmetric Model with Coupled-Mode Theory," *Energies*, vol. 11, no. 3, p. 532, Mar. 2018.

[21] H. Li, K. Wang, L. Huang, W. Chen, and X. Yang, "Dynamic Modeling Based on Coupled Modes for Wireless Power Transfer Systems," *IEEE Trans. Power Electron.*, vol. 30, no. 11, pp. 6245–6253, Nov. 2015.

[22] M. Kiani and M. Ghovanloo, "The circuit theory behind coupled-mode magnetic resonance-based wireless power transmission," *IEEE Trans. Circuits Syst. I Regul. Pap.*, vol. 59, no. 9, pp. 2065–2074, Sep. 2012.

[23] M. Kiani, U. M. Jow, and M. Ghovanloo, "Design and optimization of a 3-coil inductive link for efficient wireless power transmission," in *IEEE Transactions on Biomedical Circuits and Systems*, 2011, vol. 5, no. 6, pp. 579–591.

[24] G. A. Kendir, W. Liu, G. Wang, M. Sivaprakasam, R. Bashirullah, M. S. Humayun, and J. D. Weiland, "An optimal design methodology for inductive power link with Class-E amplifier," *IEEE Trans. Circuits Syst. I Regul. Pap.*, vol. 52, no. 5, pp. 857–866, May 2005.

[25] C. C. Kang and M. F. Bin Ain, "Lumped Element Equivalent Circuit for Wireless Power Transfer," in *2017 International Conference on Engineering Technology and Technopreneurship (ICE2T)*, 2017, pp. 1–4.

[26] Y. H. Sohn, B. H. Choi, G. H. Cho, and C. T. Rim, "Gyrator-Based Analysis of Resonant Circuits in Inductive Power Transfer Systems," *IEEE Trans. Power Electron.*, vol. 31, no. 10, pp. 6824–6843, 2016.

[27] C. Wang, G. a Covic, and O. H. Stielau, "Power Transfer Capability and Bifurcation Phenomena of Loosely Coupled Inductive Power Transfer Systems," *IEEE Trans. Ind. Electron.*, vol. 51, no. 1, pp. 148–157, 2004.

[28] K. van Schuylenbergh and R. Puers, "The concepts of inductive powering," in Inductive Powering - Basic Theory and Application to Biomedical Systems, Dordrecht: Springer Netherlands, 2009, pp. 41–76.

[29] K. van. Schuylenbergh and R. Puers, Inductive powering : basic theory and application to biomedical systems. Springer, 2009.

[30] E. Bou Balust, “Wireless power transfer : fueling the dots,” Universitat Politècnica de Catalunya, 2017.

[31] Y. H. Chao, J. J. Shieh, C. T. Pan, and W. C. Shen, “A closed-form oriented compensator analysis for series-parallel loosely coupled inductive power transfer systems,” in *PESC Record - IEEE Annual Power Electronics Specialists Conference*, 2007, pp. 1215–1220.

[32] W. Zhang, S.-C. Wong, C. K. Tse, and Q. Chen, “Analysis and Comparison of Secondary Series- and Parallel-Compensated Inductive Power Transfer Systems Operating for Optimal Efficiency and Load-Independent Voltage-Transfer Ratio,” *IEEE Trans. Power Electron.*, vol. 29, no. 6, pp. 2979–2990, Jun. 2014.

[33] J.-U. W. Hsu and A. P. Hu, “Determining the variable inductance range for an LCL wireless power pick-up,” in *2007 IEEE Conference on Electron Devices and Solid-State Circuits*, 2007, pp. 489–492.

[34] S. Li, W. Li, J. Deng, T. D. Nguyen, and C. C. Mi, “A Double-Sided LCC Compensation Network and Its Tuning Method for Wireless Power Transfer,” *IEEE Trans. Veh. Technol.*, vol. 64, no. 6, pp. 2261–2273, Jun. 2015.

[35] N. a. Keeling, G. a. Covic, and J. T. Boys, “A unity-power-factor IPT pickup for high-power applications,” *IEEE Trans. Ind. Electron.*, vol. 57, no. 2, pp. 744–751, 2010.

[36] X. Qu, H. Han, S.-C. Wong, C. K. Tse, and W. Chen, “Hybrid IPT Topologies With Constant Current or Constant Voltage Output for Battery Charging Applications,” *IEEE Trans. Power Electron.*, vol. 30, no. 11, pp. 6329–6337, Nov. 2015.

[37] M. Zaheer, N. Patel, and A. P. Hu, “Parallel tuned contactless power pickup using saturable core reactor,” in *2010 IEEE International Conference on Sustainable Energy Technologies (ICSET)*, 2010, pp. 1–6.

[38] J. T. Boys, G. A. Covic, and A. W. Green, “Stability and control of inductively coupled power transfer systems,” *IEE Proc. - Electr. Power Appl.*, vol. 147, no. 1, p. 37, 2000.

Chapter

# 3

# Switch-Mode Gyrators as a Potential Candidate for Self-Tuned WPT Receiver

In this chapter, the concept of gyrator as a variable reactive element synthesizer is revisited and explained. Driven by the goal of developing an adaptive front-end for WPT tuning, the different implementations of gyrator will be discussed based on their suitability for the WPT application. Among power processing gyrators, the topology of dual active bridge converter (DAB) will be selected as a good candidate for a switch-mode natural gyrator topology. Furthermore, the operation and design details of the candidate topology will be verified by means of state-space representation on MATLAB as well as on PSIM software. Moreover, the DAB-based reactive component synthesizer will be validated in different applications such as DAB-based miniaturized buck converter and DAB-based resonant ripple filter. However, these applications will be explored as design cases that provide more proof-of-concept for the proposed circuit operation.

## 3.1 Motivation

Reactive networks, composed of reactive elements such as inductors and capacitors, have always been a fundamental component for synthesis of many electrical and electronic systems. Such elements are key components that can be found in a wide range of applications such as signal processing and communication applications, as well as power electronics applications.

Despite the fact that reactive elements are used in almost every electrical and electronic system, they encounter limitations such as value degradation over time and temperature, lack of tunability and the large physical size of reactive elements with higher values. Furthermore, the cost increases considerably with the increase of values and electrical ratings [1]. While the aforementioned challenges are not significant for some applications, they are still critical for many other applications with stringent demands. To overcome these limitations, various

proposals have been introduced in the last decade. Several studies have been oriented toward increasing the value of the physical reactive element by using multipliers, such as capacitor multipliers and inductor multipliers [2], [3], [4]. Fundamentally, these techniques depend on using small-valued reactives to realize large-valued reactives by means of circuit techniques. Multiplication techniques offer an elegant opportunity for tuning the reactive element value by controlling the parameters of the multiplication circuit. Other efforts have considered the use of a variable reactive element array that is controlled by a switch array [5], [6]. In such approach, the reactive element value could be tuned according to the system requirement by switching different elements of the array either in series or parallel. Further researchers benefited from the gyrator element. Gyrator is a linear, lossless, passive, two-port network element that has been proposed as the fifth linear element by Bernard Tellegen in 1948 [7]. Due to its unique properties, the next sections will focus on the concept of gyrator element.

## 3.2 Revisiting Gyrator

### 3.2.1 Gyrator Theory

Gyrators are two-port, lossless, linear and power-conservative network elements that were introduced by Tellegen. Since then, the gyrator has been considered as an important two-port network element along with transformers. A symbolic representation is shown in Figure 3.1(a) [7], [8].

As reported by Tellegen, a gyrator has some general properties that match those of the transformer. Similar to a transformer, terminals voltages and currents in a gyrator are related by linear equations by means of constant coefficients and it neither generates nor stores energy. Unlike the transformer, a gyrator is a non-reciprocal element [7]. The input-output relations for a gyrator can be defined as (Figure 3.1(b)) [10]-[11]:

$$\begin{bmatrix} v_1 \\ i_1 \end{bmatrix} = \begin{bmatrix} 0 & \mathrm{g}^{-1} \\ \mathrm{g} & 0 \end{bmatrix} \begin{bmatrix} v_2 \\ -i_2 \end{bmatrix} \tag{3.1}$$

where $g$ is the gyrator conductance. Equation (3.1) gives the characteristics equation of a generic gyrator. As we see, the unique property of a gyrator is the trans-conductance relation between the input and output ports. This means that if, for instance, a voltage source $v_2$ is being connected to the output port, it would be seen as a current source $i_1 = g \cdot v_2$ at the input port. This property is very useful for some applications where a load having voltage-source characteristics, such as batteries, is to be supplied by a current from an input voltage source. Moreover, the gyrator effectively inverts any load, connected at the output port, to its duality as we will illustrate in the next section.

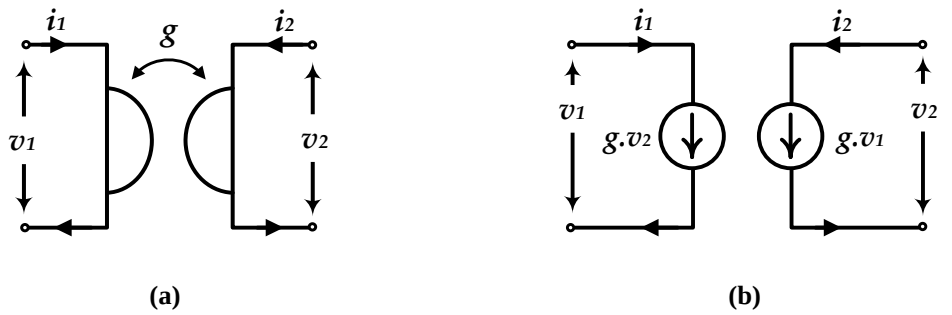


**Figure 3.1** A gyrator. **(a)** Symbolic representation. **(b)** Behavioral model.

### 3.2.2 The Gyrator as a Reactive Element Synthesizer

The importance of a gyrator in electric circuits lies in the main property of a gyrator, *i.e.*, turning one-port element into its dual as viewed from the other port. For instance, a gyrator could be used to transform any impedance, connected at the output port, to its dual as viewed at the input port such as capacitive to inductive reactance transformation, inductive to capacitive reactance transformation, and resistance to conductance transformation. All these cases are depicted in Figure 3.2. As a general rule, if an impedance $Z_o$ is connected to the output port of a gyrator, it will be viewed at the input port, with respect to gyration conductance, as:

$$Z_{in} = \frac{1}{g^2 Z_o} \tag{3.2}$$

Accordingly, a capacitance of value $C_o$ can be viewed at the input port as an inductance with an equivalent value of $C_o/g^2$. The equivalent impedance at the input terminals is shown in Figure 3.2 for different case of $Z_o$. If the gyration conductance could be designed for a condition of $g \ll 1$, a large inductive reactance could be obtained from a small capacitive reactance. In contrast, transformation from inductance to capacitance involve a multiplication process as $C = g^2 L$. Thus, the design of a gyrator with $g \gg 1$ would result in a large capacitive reactance out from a small inductive one. We note that the gyration conductance is a controllable design parameter in electronic gyrators which make it appropriate for synthesizing variable reactive elements with high values.

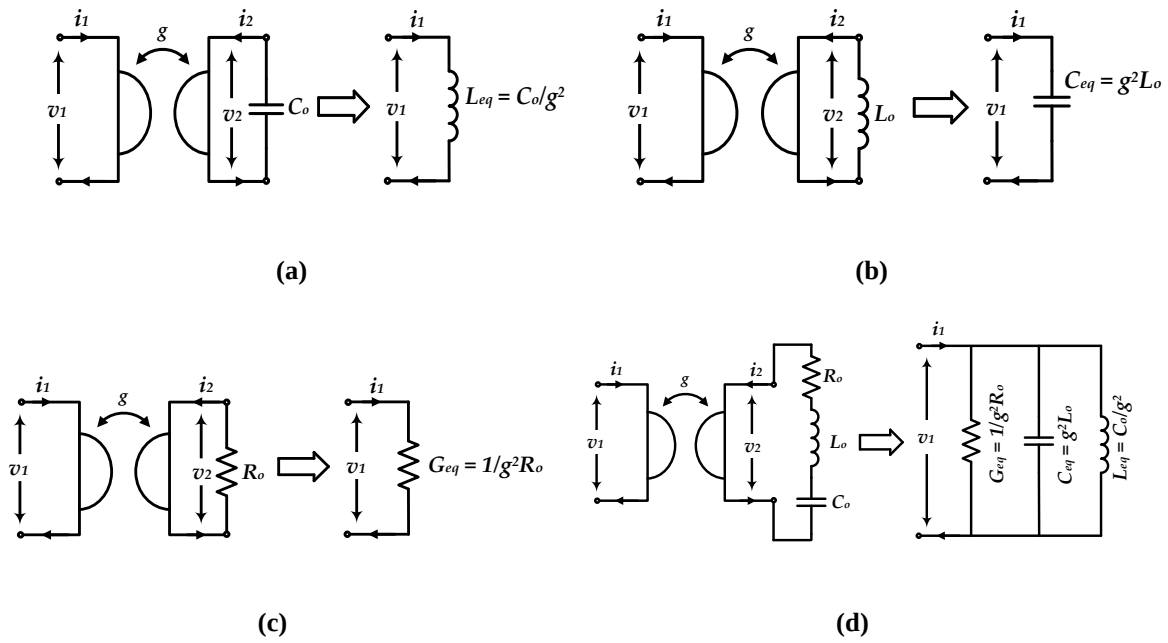


**Figure 3.2** Transformation property of a gyrator. **(a)** C transformation. **(b)** L transformation. **(c)** R transformation. **(d)** Series resonance transformation.

### 3.2.3 Gyrator Implementations

The gyrator realization is possible using different network elements provided that the characteristics Equation (3.1) is accomplished. Many successful realizations for gyrators have been suggested that range from simple transistor-based realizations up to advanced ones. The modest realizations are transistor based such as the one presented in [9], as shown in Figure 3.3(a). It is composed only of two MOS transistors $M_1$, $M_2$ and a biasing current $I_{bias}$. The circuit has been used as a gyrator-based active inductor where the load capacitance is the gate capacitance $C_{gs1}$. In this simple realization, the transconductance relation are carried out by the transconductance of $M_1$ and $M_2$ ($g_{m1}$ and $g_{m2}$ respectively). Another popular implementation is depicted in Figure 3.3(b), where two operational transconductance amplifiers (OTA) are cascaded and used as voltage controlled current sources to constitute the characteristics equation of a gyrator [10]. We note that, using well-known integrated circuit design techniques, a gyrator with variable trans-conductance is possible by controlling the biasing currents $I_{b1}$ and $I_{b2}$. More advanced circuit realizations have also been developed in the literature such as using two current conveyors (CC II) as indicated in Figure 3.3(c) [11]. This approach uses two second generation current conveyors with opposite polarities to implement the gyrator which offer a superior performance over the trans-conductance gyrator in terms of AC performance (frequency and quality factor) [12].

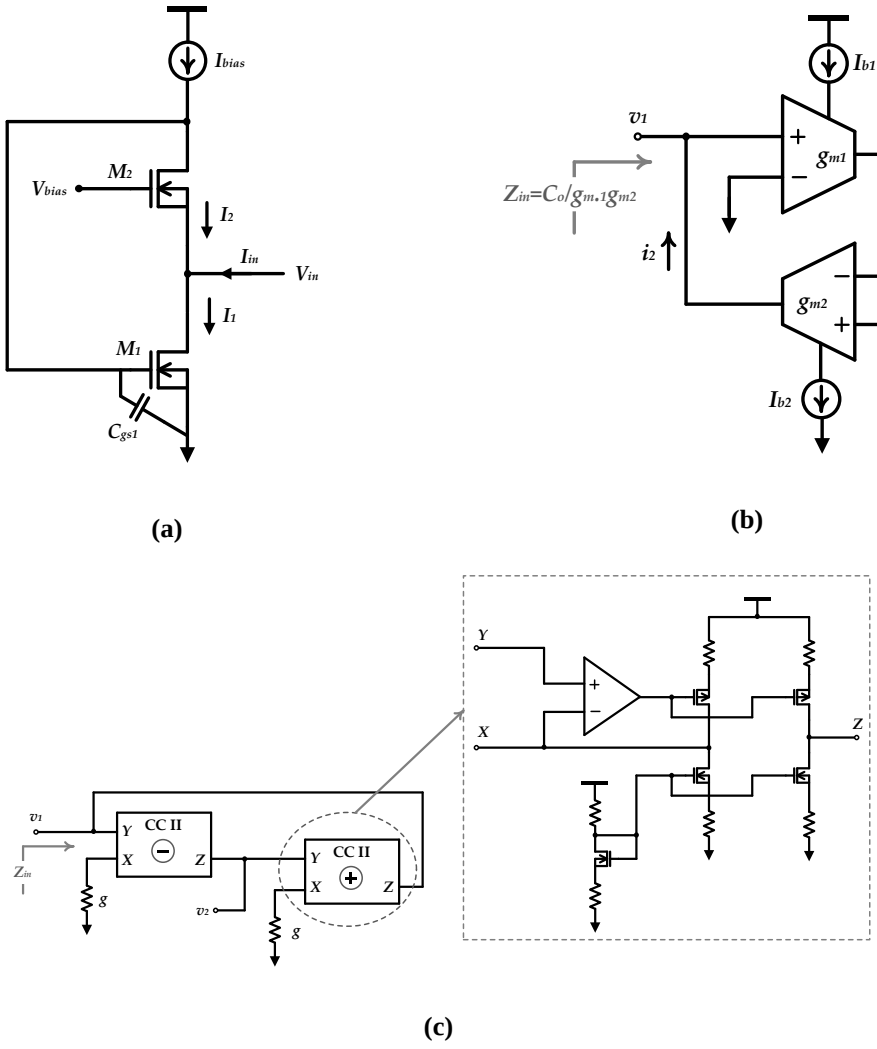


**Figure 3.3** Various gyrator realizations **(a)** Transistor based. **(b)** Transconductor based. **(c)** Current Conveyor II based.

As we have seen, most of the presented implementations for the gyrator are either based on small-signal transistors or based on linear amplifiers—current conveyors are even built using operational amplifiers— which make them inefficient at high power levels. The fact that all these implementations are always biased by current sources limit their applications to signal processing where high power delivery is not applicable [13]. For gyrators to be applicable to WPT application, power efficiency becomes a must.

A first demonstration for switch-mode gyrator realization has been introduced by S. Singer in [13], [14]. It has been shown that switch-mode power processing circuits enable loss-free gyrator synthesis. As a power-conservative element, the gyrator can be synthesized by means of any POPI circuit (output power equal input power) such as buck, buck-boost, cuk, and flyback converters, with appropriate control. As depicted in Figure 3.4, a closed loop control can be used to control the output current of a POPI switch-mode circuit such that it related to the input

voltage $V_{in}$ as satisfied by Equation (3.1) [14]. Then, the output current in Figure 3.4 is given by:

$$I_o = -\mathrm{g}V_{in} \tag{3.3}$$

Due to the power conservation property of the POPI circuit, the relation between the input current $I_{in}$ and output voltage $V_o$ is implicitly satisfied once Equation (3.3) is obeyed. The relation between $I_{in}$ and $V_o$ can be concluded as follows [14]:

$$\begin{cases} P_o = -I_o V_o = P_{in} = I_{in} V_{in} \\ I_{in} = -I_o V_o / V_{in} = -(-\mathrm{g}V_{in}) V_o / V_{in} = \mathrm{g}V_o \end{cases} \tag{3.4}$$

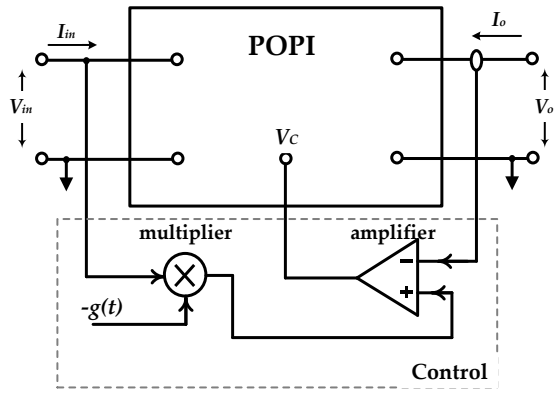


**Figure 3.4** Block diagram of gyrator realization by means of a POPI circuit.

Thus, it becomes clear from Equation (3.4) that a gyrator is fully realizable by means of an output current controlled POPI circuit. Similarly, a gyrator can be realized using an input current controlled POPI circuit. Consequently, a complete family of switch-mode gyrators can be derived depending on the intrinsic characteristics of the switch-mode converter topology. The realization of gyrators by means of buck converter, boost converter, and Čuk converter has been explored in [15]. A sliding-mode control has been used to force the gyration behavior of the converters shown in Figure 3.5(a). An important requirement imposed by the sliding-mode control in these topologies is to have a continuous non-pulsating current at the input and output of the converter. As depicted in Figure 3.5(a), this requirement has been met by adding an input filter and output filter to buck converter and boost converter, respectively [15]. This addition is of great importance due to complexity considerations.

On the other hand, a gyrator realization that uses controlled switched-capacitor cell has been presented in [16] as depicted in Figure 3.5(b). In addition to size reduction with no magnetics at all, this topology is more appropriate for current source input characteristics as well as

supplying high inductive loads. Still the main concept of having a gyrative characteristics is the same, the output current is controlled with respect to a reference current $I_{ref}$ that is generated as $I_{ref} = gv_{in}$. Most of the work presented in the literature for switch-mode gyrators is based on either sliding-mode control or hysteresis control [8], [13], [14], [16]─[19].

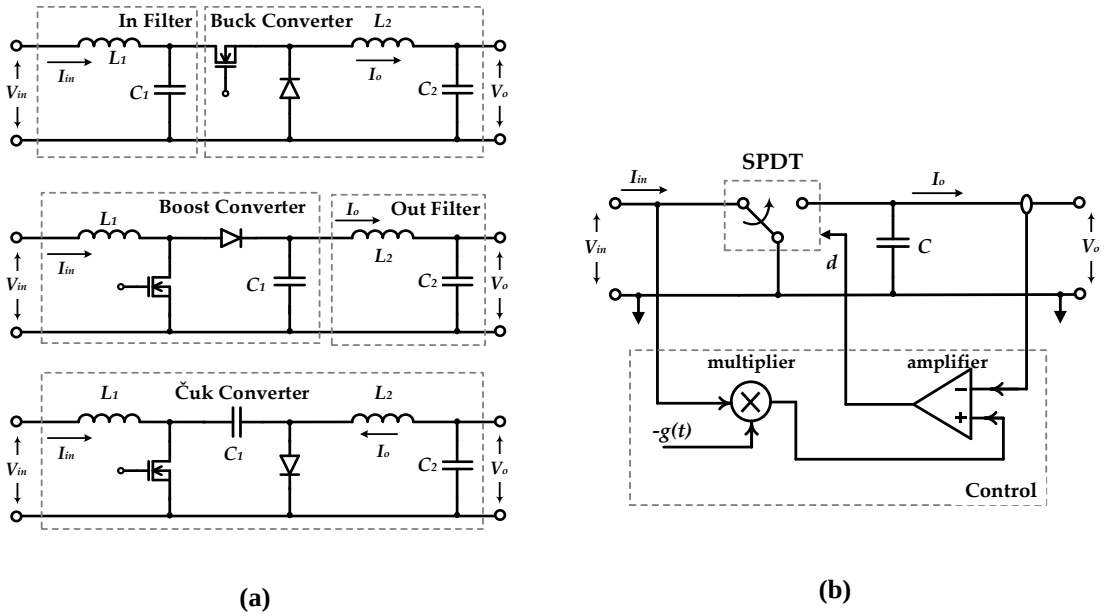


**Figure 3.5** Switch-mode gyrator realizations **(a)** Inductive-based. **(b)** Capacitive-based.

If these control techniques or any other technique is to be used for gyrator-based impedance emulation, two control loops will be required; one for forcing the gyrative characteristics and the other for achieving a variable gyration conductance $g$. Recall from Equation (3.2) that a variable $g$ is essential for synthesizing a variable impedance at the input port. An optimum topology for variable impedance synthesis based on switch-mode gyrator, for WPT receiver tuning, would have either a low complexity in the power stage or a low complexity in the control.

Clearly, for a circuit to behave as a gyrator, it is obtainable either through topology-based implementations like in the case of two back-to-back trans-conductors or through control-based realization. Interestingly, dual bridge converters (DBC) is a family of switch-mode converters that belongs to the first kind, *i.e.* topology-based gyrators. The dual active bridge converter (DAB) is a DBC switch-mode converter that is well-known as a control-free naturally gyrated converter [20], [21]. By using the DAB as control-free gyrator, the effort of forcing the gyrative behavior could be saved in favor of designing a simple control to tune the value of a DAB-based synthesized reactance. In the next subsection, the operation and adoption of DAB as a variable reactance synthesizer will be discussed.

# 3.3 Dual Active Bridge Converter as a Natural Gyrator

## 3.3.1 Circuit Description and Operation

The DAB converter, shown in Figure 3.6, is composed of two full bridges (input bridge $S_{11}$-$S_{12}$-$S_{13}$-$S_{14}$ and output bridge $S_{21}$-$S_{22}$-$S_{23}$-$S_{24}$) coupled by an inductor link. In the ideal case, the inductor link is following the "*AC inductor*" notion, where the average inductor current is zero [22].

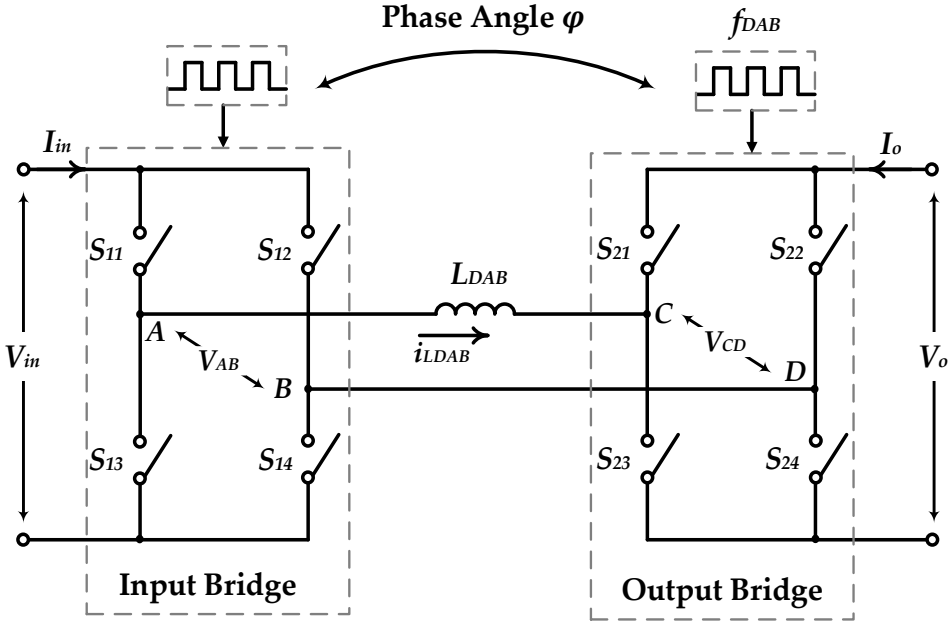


**Figure 3.6** The dual active bridge converter.

The operation of the DAB converter can be described as follows: The input bridge follows a switching sequence ($S_{11}S_{14}$, $S_{12}S_{13}$, $S_{11}S_{14}$ ...) and the same switching sequence is followed by the output bridge ($S_{21}S_{24}$, $S_{22}S_{23}$, $S_{21}S_{24}$ ...). The input and output bridges are switched at the same switching frequency $f_{DAB}$ with a duty-cycle of 50% and a phase-shift angle $\varphi$ between the two bridges. The DAB converter is a bidirectional topology where the power flow from input to output, or vice versa, is dependent upon the sign of the $\varphi$ angle. The converter operation could be demonstrated, more clearly, in the sense that every bridge converts the corresponding voltage source to a high-frequency AC signals where the two AC signals are phase shifted by $\varphi$. Then, the two AC signals are applied across the inductor which causes current to pass through it. Figure 3.7 shows the output voltage of the input bridge $V_{AB}$ when a sinusoidal input signal $V_{in}$ is applied.

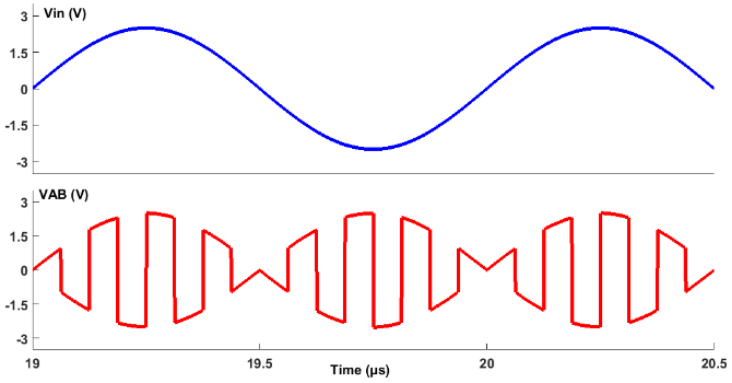


**Figure 3.7** Waveforms of the input bridge output $V_{AB}$.

The average power transfer can be given in terms of $f_{DAB}$, $L_{DAB}$, and $\varphi$ as [21]:

$$\langle P \rangle = \frac{V_{in} V_o}{\omega_{DAB} L_{DAB}} \left(\varphi - \frac{\varphi^2}{\pi}\right) \tag{3.5}$$

where the power in either directions is found to be controlled from zero to the peak value by controlling $\varphi$ from 0 to 90°. The average power in Equation (3.5) neglects the losses and the converter is considered ideal. According to the POPI concept, the system is conservative, hence the input current $I_{in}$ is found to be:

$$I_{in} = \frac{\langle P \rangle}{V_{in}} = \frac{V_o}{\omega_{DAB} L_{DAB}} \left(\varphi - \frac{\varphi^2}{\pi}\right) \tag{3.6}$$

The expression in Equation (3.6) can be rewritten as:

$$I_{in} = \mathrm{g} V_o \tag{3.7}$$

where

$$\mathrm{g} = \frac{1}{\omega_{DAB} L_{DAB}} \left(\varphi - \frac{\varphi^2}{\pi}\right) \tag{3.8}$$

It is clearly concluded from Equation (3.7) that the DAB converter exhibits a natural gyrative behavior where the gyration conductance in Equation (3.8) is entirely dependent on the circuit parameters, *i.e.* the angular frequency $\omega_{DAB}$, the inductance $L_{DAB}$, and the phase-shift $\varphi$. It is important to note that the DAB converter has been primarily introduced as a DC-DC converter for the purpose of power processing where all the converter switches shown in Figure 3.6 could be realized by a two-quadrant IGBT or MOSFET switch. However, the synthesis of

variable reactive components using the same converter imposes the capability of processing AC signals either at input or output sides. Thus, the DAB converter operation must allow bidirectional current flow and voltage polarity [23]. The capability of DAB converter for processing AC sinusoidal signals has been investigated in [24] where the conventional MOSFETs in DC-DC DAB converters are replaced by four-quadrant switches to enable a direct ac-ac power processing. A single-package four-quadrant switch is not yet commercially popular. Consequently, most of the applications that require four-quadrant switches are realized by combining two-quadrant MOSFET or IGBT with diodes in order to block current in both directions when the four-quadrant switch is OFF.

Figure 3.8 shows two preferred realizations that allow four-quadrant operation while are still more efficient among other realizations [24], [25]. The realization of Figure 3.8(b) uses two anti-series MOSFET-diode cells such that the current in either direction passes through one switch and one diode. In this case, switch $S_{1P}$ is switched ON only during a positive half cycle while $S_{1N}$ is switched ON during a negative half cycle. Due to the expected power loss in diodes, a better realization is shown in Figure 3.8(a), where two switches $S_{1a}$, $S_{1b}$ are switched ON or OFF simultaneously while reverse current is blocked by their anti-series connection of their body diodes. The latter four-quadrant switch ensures a faster switching speed while power loss is significantly decreased. Therefore, the four-quadrant switch in Figure 3.8(a) will be considered in our DAB-based gyrator.


**Figure 3.8** Four-quadrant switches **(a)** Two back-to-back MOSFETs. **(b)** Two anti-series MOSFET-diode.

### 3.3.2 State-Space Modelling and Simulation

The objective of this section is to develop a state-space representation of reactive element synthesis by means of the DAB gyrator. Figure 3.9(a) shows the DAB gyrator after replacing the ideal switches by four-quadrant switches. Moreover, the DAB gyrator is loaded by an output capacitor $C_{DAB}$ such that an equivalent inductive emulation is expected at the input terminals.

The different operation modes (*i.e.* Mode1, Mode 2, Mode 3, and Mode 4) of the DAB converter within one switching cycle is also illustrated in Figure 3.9(b). State-space representation for the system can be derived after defining the state variables such as the inductor current $i_{LDAB}(t)$ and the capacitor voltage $v_o(t)$. The state-space equations of each operation mode can be expressed by the full-order state matrices as:

*Mode 1*:
$$\frac{d}{dt}\begin{bmatrix} i_{LDAB}(t) \\ v_o(t) \end{bmatrix} = \begin{bmatrix} 0 & \frac{1}{L_{DAB}} \\ \frac{-1}{C_{DAB}} & 0 \end{bmatrix}\begin{bmatrix} i_{LDAB}(t) \\ v_o(t) \end{bmatrix} + \begin{bmatrix} \frac{1}{L_{DAB}} \\ 0 \end{bmatrix}[v_{in}(t)] \tag{3.9}$$

*Mode 2*:
$$\frac{d}{dt}\begin{bmatrix} i_{LDAB}(t) \\ v_o(t) \end{bmatrix} = \begin{bmatrix} 0 & \frac{-1}{L_{DAB}} \\ \frac{1}{C_{DAB}} & 0 \end{bmatrix}\begin{bmatrix} i_{LDAB}(t) \\ v_o(t) \end{bmatrix} + \begin{bmatrix} \frac{1}{L_{DAB}} \\ 0 \end{bmatrix}[v_{in}(t)] \tag{3.10}$$

*Mode 3*:
$$\frac{d}{dt}\begin{bmatrix} i_{LDAB}(t) \\ v_o(t) \end{bmatrix} = \begin{bmatrix} 0 & \frac{-1}{L_{DAB}} \\ \frac{1}{C_{DAB}} & 0 \end{bmatrix}\begin{bmatrix} i_{LDAB}(t) \\ v_o(t) \end{bmatrix} + \begin{bmatrix} \frac{-1}{L_{DAB}} \\ 0 \end{bmatrix}[v_{in}(t)] \tag{3.11}$$

*Mode 4*:
$$\frac{d}{dt}\begin{bmatrix} i_{LDAB}(t) \\ v_o(t) \end{bmatrix} = \begin{bmatrix} 0 & \frac{1}{L_{DAB}} \\ \frac{-1}{C_{DAB}} & 0 \end{bmatrix}\begin{bmatrix} i_{LDAB}(t) \\ v_o(t) \end{bmatrix} + \begin{bmatrix} \frac{-1}{L_{DAB}} \\ 0 \end{bmatrix}[v_{in}(t)] \tag{3.12}$$

The state-space model has been implemented using Simulink, as shown in Figure 3.10(a), where the input voltage and output voltage waveforms are shown in Figure 3.10(b) for the system conditions of ($V_{in}$=5 V, $f_{in}$= 500 kHz, $f_{DAB}$=8 MHz, $L_{DAB}$=25 nH, $C_{DAB}$=80 nH, $\varphi$=40°). We note that the synthesized inductance $L_{\varphi}$ is not purely lossless. This can be concluded from Figure 3.10(b) as the phase lag between input current and voltage is slightly less than 90° which denotes a series resistance. The calculated value of the synthesized inductance is 550 nH in series with $R_{\varphi}$ of 265 mΩ. The synthesized inductance is quite large compared to the reactive components (*i.e.* $L_{DAB}$ and $C_{DAB}$) used in the circuit. As the inductor size, and value, is the aspect of main concern, the synthesized inductance has to be compared to the inductor link of the DAB converter $L_{DAB}$. It is clear that $L_{\varphi}$ is around 22x of $L_{DAB}$, which proves the benefits of switch-mode gyrator circuits for synthesizing large reactive components.

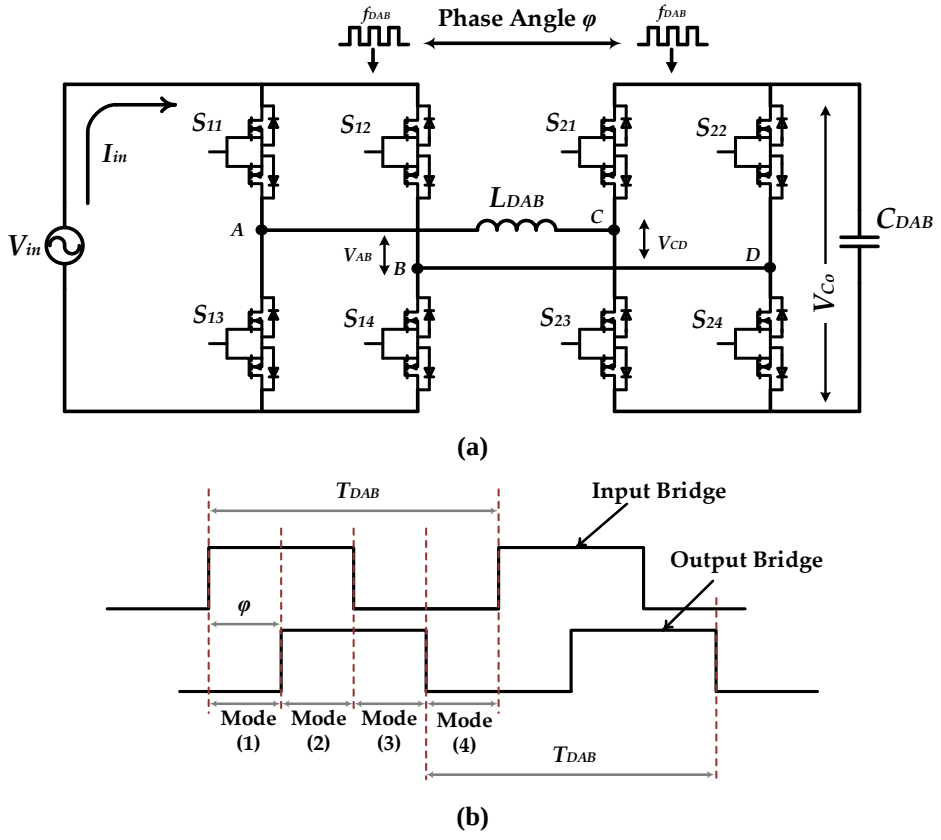


**Figure 3.9 (a)** DAB-based switch-mode inductance synthesis. **(b)** Operation modes.

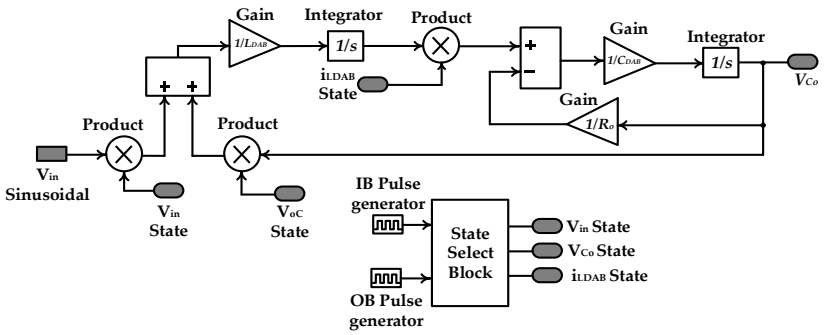


**(a)**

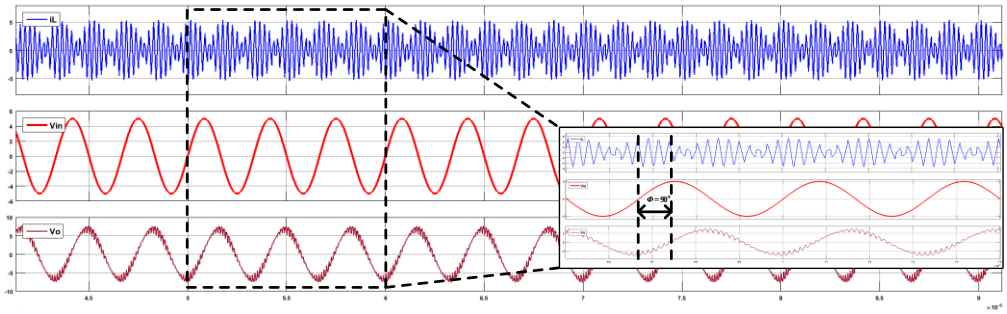

**(b)**

**Figure 3.10** State-space simulation using Simulink. **(a)** Block diagram. **(b)** Results.

### 3.3.3 Tunability Range of DAB-based Synthesized Inductance

Tuning the value of reactive components is of most importance for various applications. Using gyrator-based realization for reactive components, the gyration conductance could be freely tuned over an optimum range. As a natural gyrated topology, DAB converter has further increased degrees of freedom, as inferred by Equation (3.8). The tuning of the synthesized reactive component is possible by means of either switching-frequency $f_{DAB}$ tuning or phase-angle $\varphi$ tuning. Additionally, both of them could be concurrently tuned through a dual-loop tuning technique. Considering the capacitive load $C_{DAB}$ at the output, then the seen inductance at the input port can be derived from Equations (3.2) and (3.8) as:

$$L_{\varphi} = \frac{C_{DAB}}{\mathrm{g}^2} = \frac{\pi^2 \omega_{DAB}^2 L_{DAB}^2}{(\varphi\pi - \varphi^2)^2} \cdot C_{DAB} \tag{3.13}$$

The expression in Equation (3.13) gives the theoretical value of $L_{\varphi}$ assuming ideal circuit components. As previously stated, it has been noted that losses in a non-ideal DAB circuit cause a series resistance to arise. According to Figure 3.7, the input current $I_{in}$ is discontinues. In order to estimate the actual effective value of $L_{\varphi}$ and the series resistance $R_{\varphi}$, the fundamental input current can be estimated in simulation, and used to estimate the total impedance ($Z_{in}$= $R_{\varphi}$ + $j\omega_{in}L_{\varphi}$) for a specific AC input signal with frequency of $f_{in}$. The tuning of the DAB-based inductance is demonstrated by circuit-based simulation, where the phase-angle is varied over a range from 30° to 150°. The system parameters used are: ($V_{in}$=5 V, $f_{in}$= 500 kHz, $f_{DAB}$=8 MHz, $L_{DAB}$=25 nH, $C_{DAB}$=80 nH). The response of the synthesized inductance $L_{\varphi}$, series resistance $R_{\varphi}$, and gyration conductance is depicted in Figure 3.11. We note that the synthesized inductance could be tuned within the range from 237 nH to 922 nH by tuning the phase-shift $\varphi$ from 90° to 30° respectively. The behavior of $L_{\varphi}$ is inversely proportional to the gyration conductance $g$, as implied by Equation (3.13). On the other hand, the expected linear proportion between the synthesized inductance $L_{\varphi}$ and the switching-frequency $f_{DAB}$ is illustrated in Figure 3.12. The switching frequency is varied from 4 MHz to 16 MHz at a fixed phase-shift of 40°. In the same time, the phase-shift has been tuned at switching frequency of 8 MHz, 10 MHz, and 12 MHz as plotted in Figure 3.12. We note that the higher the switching frequency $f_{DAB}$, the higher the synthesized inductance $L_{\varphi}$. Consequently, the phase-shift and the switching frequency $f_{DAB}$ are actually two different parameters that could be controlled independently. Indeed, it is observed that the switching-frequency could be used to switch between different inductance ranges while the phase-shift could be used as a fine tuning parameter to reach the exact value.

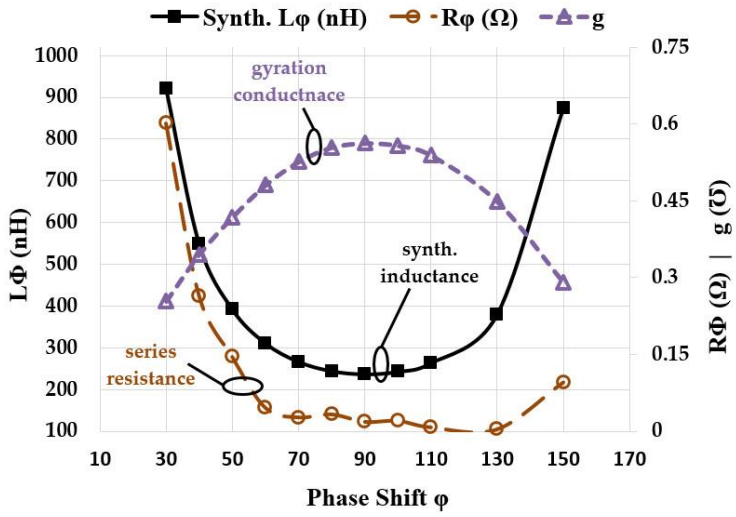


**Figure 3.11** DAB-based $L_{\varphi}$, g, and $R_{\varphi}$ versus phase-shift $\varphi$.

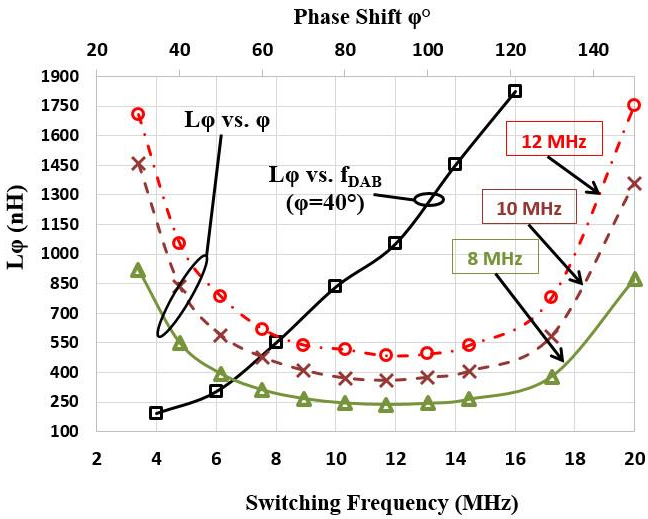


**Figure 3.12** Synthesized inductance $L_{\varphi}$ versus $\varphi$ at different switching frequency $f_{DAB}$.

## 3.4 Potential Applications for Switch-Mode DAB-Based Impedance Synthesis

Natural gyration of DAB converter is a remarkable feature that mitigate complexity of other candidates where two control loops are required, one to force the gyrative behavior whereas the other to drive the tunability feature. Hence, tunable DAB-L could be extended to a wide number of different power applications. The following cases are extended as a proof-of-concept in few potential applications.

### 3.4.1 Switch-Mode Resonators

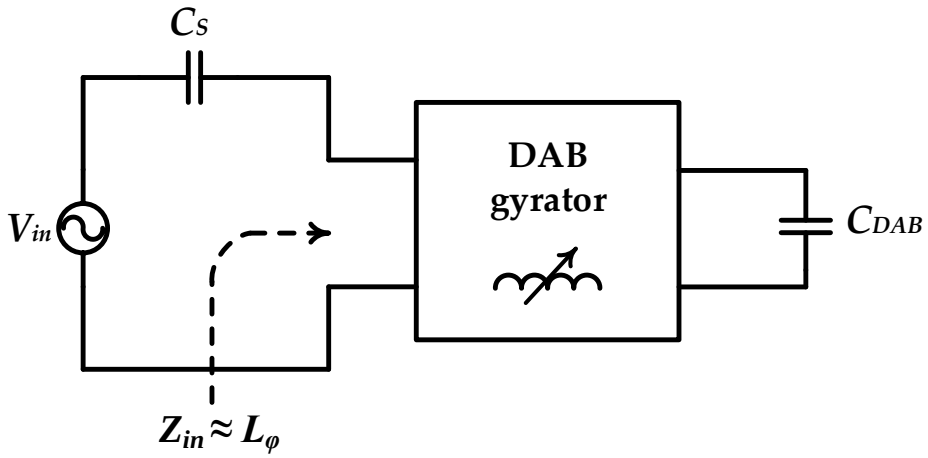


**Figure 3.13** Tunable switch-mode power resonator.

A common test bench for validating the performance of switch-mode synthesized impedance is to connect it in series or in shunt with a physical impedance in a sinusoidal circuit to form a resonance based test [26]─[28]. The proposed DAB-based synthesized inductance is investigated in a series resonance case along with DAB nominal parameters as follows: $f_{DAB}$ =8 MHz, $L_{DAB}$ =25 nH, $C_{DAB}$ = 80 nH, $\varphi$ = 45°. A fixed series capacitance $C_s$ = 246 nF, as shown in Figure 3.13, is used to form the series test bench, while the excitation source parameters are: $V_{in}$ =5 V, $f_{in}$ =500 kHz. The emulated inductance for the prescribed parameters has been calculated from simulation as 411.9 nH which resonates with a capacitance value of 246nF. The phase-shift has been swept over a range from 20° to 70° at different switching frequency $f_{DAB}$.

Figure 3.14 illustrates the resonant current magnitude and phase plot. We note that the tuned point that corresponds to a zero phase angle occur at the nominal value of $\varphi$ =45°. This tuned point corresponds to a synthesized inductance equal to 411.9 nH which resonate with $C_s$ at the given excitation frequency of 500 kHz. In general, the response of the tested circuit validate the wide tunability of the DAB-based inductance in which the tunablitiy is achieved either through phase-shift tuning or switching frequency tuning or both of them.

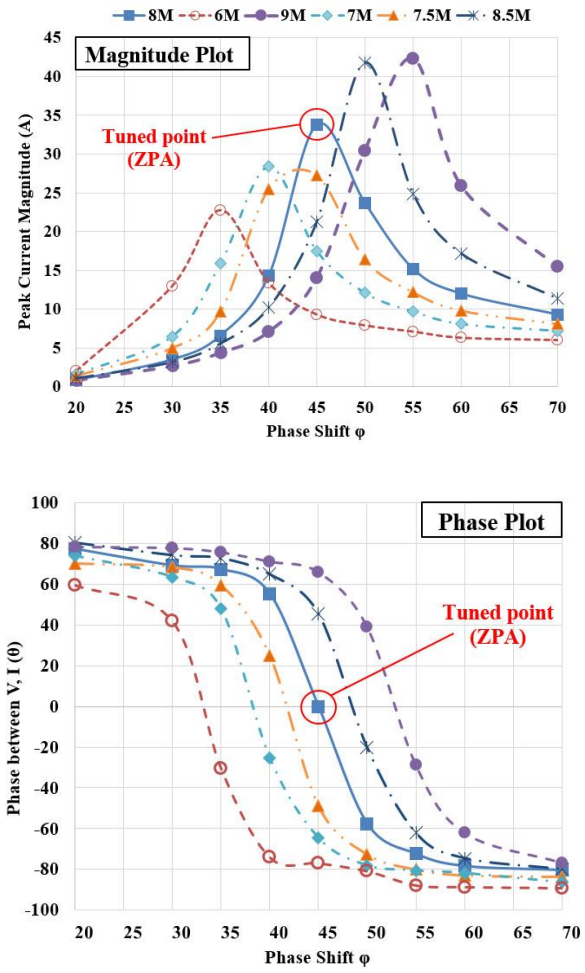


**Figure 3.14** Magnitude plot and phase plot of the resonant current in series resonant switch-mode testbench.

## 3.4.2 Switch-Mode Alternative to LDO

Low-dropout regulators (LDO) are preferred as a regulator for a wide range of applications that require small power levels, small size, and low noise. Nevertheless, LDOs are inefficient unless the output voltage ($V_{out}$) is close to input voltage ($V_{in}$). Switch-mode alternatives such as buck converter become more reasonable and reliable in terms of efficiency particularly in applications where the ratio $V_{out}/V_{in}$ is small. Nevertheless, bulky size of switch-mode buck converter is far beyond that of LDO for the same noise requirement. While switching noise of switch-mode converters is inevitable, output noise could be relaxed by means of high output filtering. DAB-based inductance would help in replacing the bulky physical inductor required for meeting a specific output noise margin without compromising the size.

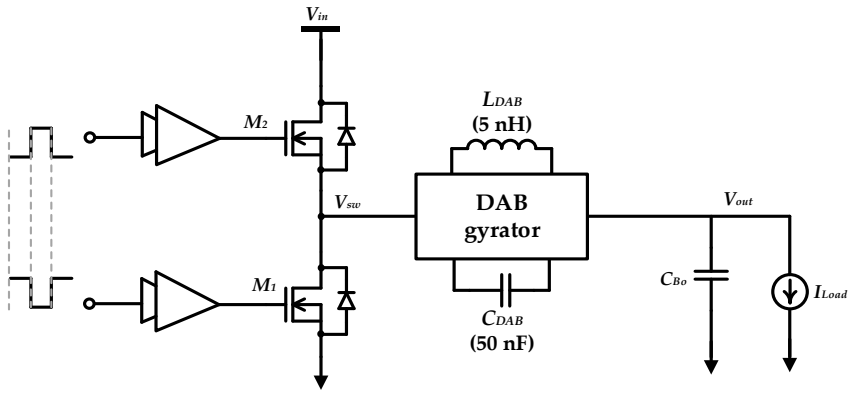


**Figure 3.15** Buck converter utilizing DAB-based synthesized inductance.

As a proof of concept, a buck converter switching at 5 MHz has been designed after replacing the physical inductor by a DAB-based synthesized inductance. The buck converter specifications are: $V_{in}$=3.3 V, $I_{Load}$=300 mA, $C_{Bo}$=1 μF, $D$= 0.6, and the DAB circuit is designed for: $L_{DAB}$=5 nH, $C_{DAB}$=50 nF, $\varphi$=90°, $f_{DAB}$=50 MHz. Figure 3.15 shows a schematic diagram for the system where the DAB physical reactive components are only shown while the DAB block is assumed to contain all the switches and the driving signals. Figure 3.16 shows the simulation results of the described system carried on Cadence-Virtuoso using XFAB 0.18μm CMOS process. The output ripple of the buck converter is 16 mV which is relatively small compared to ripple of 275mV that would result if a combination of ($L$=5 nH, $C_{Bo}$=1 μF) is used instead of $L_{\varphi}$. The figure as well shows the output voltage of DAB which, in principle, is $1/g$ of input current. The measured values of $L_{\varphi}$ and $g$ is equal to 151 nH and 0.502 S respectively. The peak-to-peak inductor ripple of 0.949 A is expected in this case, which also coincides with ($g * Vo_{DAB}$) that is given in simulation.

To clarify the effect of phase-shift $\varphi$ on inductance value, hence output ripple, Figure 3.17 shows the output ripple in response for phase-shift sweep. As we decrease the phase-shift, the synthesized inductance value increases, which gives rise to reduction in the buck output ripple. The low value of $L_{DAB}$ (5 nH), however, comes at the expense of the DAB switching frequency $f_{DAB}$ that has to be increased considerably. Recall that, from Equation (3.13), synthesizing a large inductance from using very small $L_{DAB}$, the switching frequency has to be increased. Indeed, this conclusion has also been illustrated in Figure 3.12. Unfortunately, the same trade-off of size versus efficiency applies as well for the DAB gyrator, *i.e.* using very small $L_{DAB}$ would be beneficial from size perspectives, however, the efficiency would be compromised.

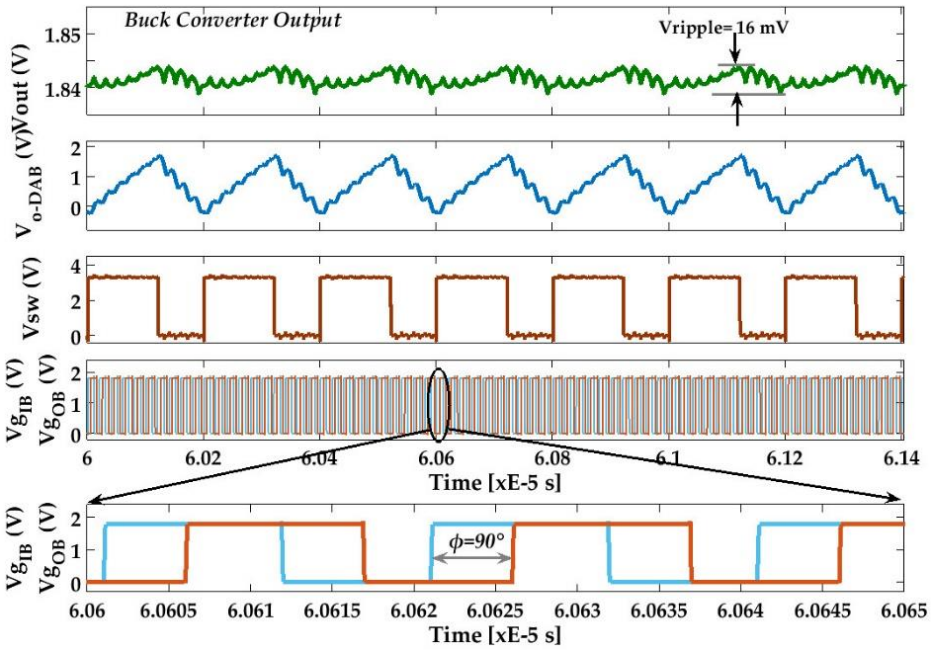


**Figure 3.16** Simulation results of buck converter utilizing DAB-based inductance.

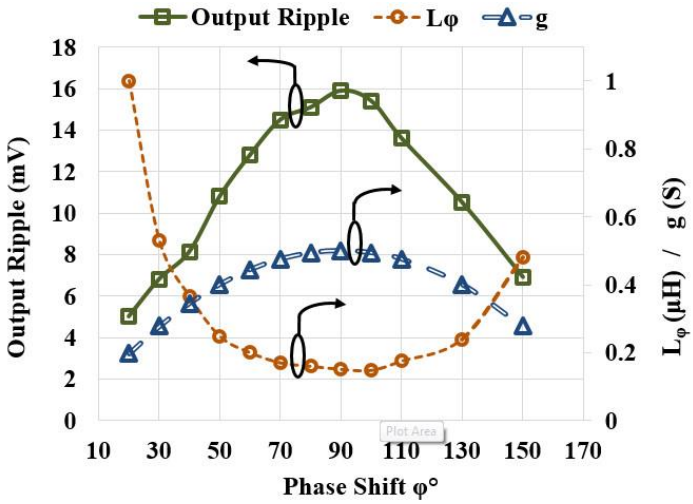


**Figure 3.17** Buck output ripple versus phase shift $\varphi$ in a DAB-based inductance.

## 3.4.3 DAB-Based Resonant Ripple Filter for Power Converters

To meet the critical noise constraints of some applications, resonant ripple filters offer the ability to attenuate the output ripples of power converters. A parallel/series-tuned resonant filter could be used in the power path to exhibit transmission null at a specified frequency such as switching frequency of the power converter [29], [30]. However, these resonant filters attenuate ripples at expense of occupied size. Moreover, resonant filters could fail to function properly at

the designed frequency due to expected manufacturing variations that cause filter detuning [30]. Consequently, an adaptive resonant filter would be an optimum solution to guarantee the optimal performance of this approach. The authors in [30] have proposed a solution by enabling a tunable switching frequency in buck converter, where the switching frequency would track the tuned point of the resonant output filter. Alternatively, as a design case, a DAB-based resonant ripple filter in a buck converter having a constant switching frequency is investigated in this section. Thus, it possible to the tune the synthesized inductance to match the output impedance characteristics of the buck converter by means of phase-shift tuning without the need to alter the switching frequency of the buck itself.

Figure 3.18 shows one possible topology, where the DAB-based inductance is employed in a parallel-tuned resonant filter in buck converter. The buck converter specifications are: $V_{in}$=3.3 V, $I_{Load}$=300 mA, $L_{Bo}$=90 nF, $C_{Bo}$=250 nF, $D$= 0.5, $f_{buck}$=5 MHz, $C_{notch}$= 6.15 nF, and the DAB circuit parameters are: $L_{DAB}$=5 nH, $C_{DAB}$=50 nF, $\varphi$=90°, $f_{DAB}$=50 MHz. The system in Figure 3.18 has been verified using Cadence-Virtuoso with XFAB 0.18µm CMOS process. As shown in Figure 3.19, the output ripple of buck converter with DAB-based resonant filter is equal to 62mV which shows more than 67% reduction in the output ripple of buck converter with the same specifications but without the resonant filter (*i.e.* single stage low-pass filter composed of $L_{BO}$ and $C_{BO}$ only). The waveforms shown in Figure 3.19 illustrates the system performance at fixed phase-shift in the DAB-based inductance ($\varphi$=90°). Then, it is possible to create a tracking loop by sensing the buck output current to control the DAB-based inductance such that the resonant filter becomes always tuned at the buck switching frequency. The PLL-based approach presented in [30] can be used to ensure a constant switching frequency operation while the resonant filter is always tuned.

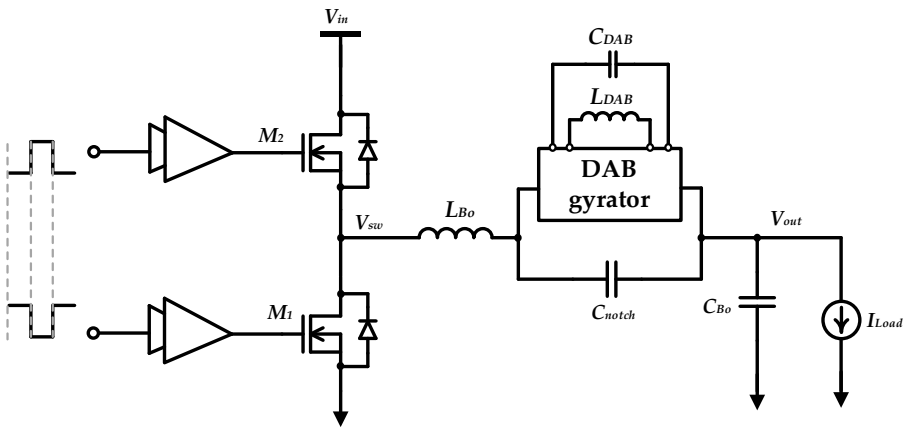


**Figure 3.18** Resonant ripple filter for buck converter based on DAB-based inductance.

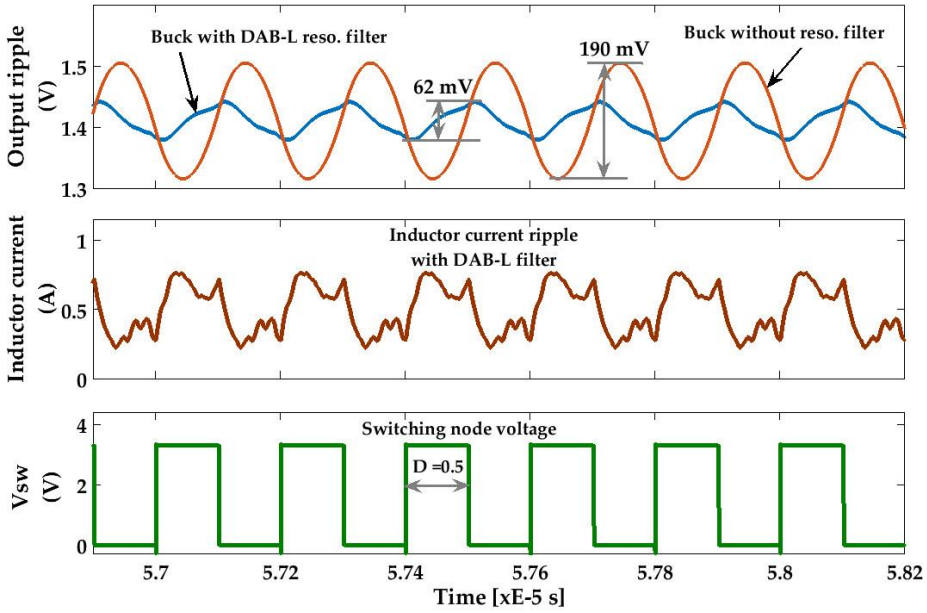


**Figure 3.19** Waveforms of buck converter utilizing DAB-based inductance.

### 3.4.4 Other Possible Applications

As previously mentioned, DAB-based synthesized inductance could be extended to a large variety of applications. It could be used, in conjunction with other circuits, as a matching front-end for energy harvesting applications such as RF energy harvesting [31], [32]. Tunability feature of DAB-based inductance could be employed as an alternative to replace bulky multi-permeability nonlinear inductor used to improve light load efficiency in buck converters [33]. Lastly, not least, DAB-based inductance could be employed in MPPT-controlled buck converter to extend continuous current operation from high to low solar insulation [34].

Similarly, which is also aligned with the thesis objectives, the DAB-based synthesized inductance is promising approach for a tunable WPT receiver circuit. In the next section, the application of DAB-based inductance in WPT receiver will be modeled toward a system co-design process.

## 3.5 Gyrator-Based Synthesized Inductance in WPT Receivers

Applying the DAB-based synthesized inductance in WPT receivers is not straightforward. It is important to co-design the value of the synthesizable inductance such that it tunes in parallel with the other physical reactive components; namely $L_R$ and $C_R$. Therefore, the DAB-based inductance can be utilized to retune the resonance frequency of the WPT receiver against any

mismatch. Obviously, the added DAB-based inductance should be tuned through the phase-shift which is more reasonable and reliable control parameter compared to the switching frequency $f_{DAB}$.

### 3.5.1 Generalized Model for the Proposed Dynamic Tuning Approach

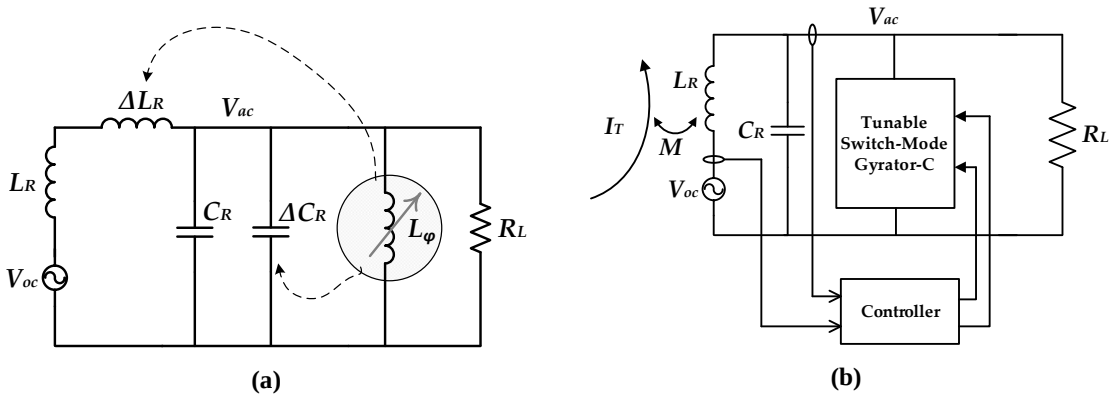


**Figure 3.20** A model for the proposed approach: **(a)** Basic concept; **(b)** DAB-based inductance dynamic tuning in WPT receiver.

Provided that we have no access to the physical values of the WPT receiver's coil $L_R$ and compensation capacitor $C_R$ once the system is already functioning in practice, one way to dynamically tune the resonance frequency $\omega_R$ of the receiver tank is to add a tunable active reactance to the circuit. A model for the WPT receiver with the connection of a generic variable inductance is illustrated in Figure 3.20(a). The variable inductance $L_\varphi$ is connected in parallel with the compensation capacitor $C_R$. Therefore, it can be deemed as an additional inductance connected in parallel with the receiver coil $L_R$ (and $\Delta L_R$) in essence. By referring to the Figure 3.20(a), then, a new parameter evolves as a combination between the added inductance $L_\varphi$ and $C_R$:

$$C_{\varphi R} = C_R - \frac{1}{\omega^2 L_\varphi} \tag{3.14}$$

where $C\varphi_R$ is the equivalent capacitance that includes the inductive behavior of $L_\varphi$. In accordance to Equation (3.14), the new expression for the resonance frequency of the receiver tank becomes:

$$\omega_R^2 = \frac{1}{L_R C_{\varphi R}} = \omega_{R0}^2 (1 + \frac{L_R}{L_\varphi}) \tag{3.15}$$

where $\omega_{R0}$ is the conventional resonance frequency of a parallel LC circuit, *i.e.* $\omega_{R0}^2 = 1/L_R C_R$. Since the new resonance frequency in Equation (3.19) is a function of $L_\varphi$, it

indicates that $\omega_R$ can be tuned over a wide range that is only limited by the tuning range of $L_\varphi$. With the help of Figure 3.20(a), including all the depicted mismatches ($\Delta L_R$, $\Delta C_R$), the power transferred to the receiver is calculated as:

$$P_{rms} = \frac{\omega^2 M^2 I_T^2 R_L}{(\omega^2 L_R C_{\varphi R}(1+\gamma_L)(1+\gamma_\varphi)R_L - R_L)^2 + \omega^2 L_R^2 (1+\gamma_L)^2} \tag{3.16}$$

where $\gamma_L = \Delta L_R / L_R$ and $\gamma_\varphi = \Delta C_R / C_\varphi$. Clearly, the transferred power in Equation (3.16) can be recovered to the maximum, nearly as given by Equation (2.63), by tuning $L_\varphi$ and thus $C_{\varphi R}$ subsequently. Thereby, the mistuning effect incurred by $\gamma_L$ and $\gamma_\varphi$ could be neutralized.

## 3.6 Conclusions

The gyrator as a linear power conservative network element has been utilized for synthesizing variable impedance in wide variety of applications. In this Chapter, we have reviewed the theoretical basis of the gyrator where the common circuit realizations for the gyrator have also been revisited. It has been shown that the transistor-based realizations are not adequate for power processing applications because they are not power-wise efficient. Consequently, the switch-mode implementations for the gyrator have been revised and discussed. Among these implementations, the DAB converter has been selected as an optimum candidate topology because it saves the efforts of forcing the gyration characteristics. The input/output voltage and currents characteristics of the DAB converter suggest that the converter works as a natural gyrator.

Accordingly, the DAB converter has been optimized for synthesizing variable inductive reactance. Different potential applications for DAB-based variable inductance synthesis have been proposed and tested as a proof-of-concept. The DAB converter switching at very high frequency, while utilizing small physical reactive components, can be used to synthesize large variable reactive components. Finally, a general model for DAB-based variable inductance in parallel-compensated WPT receivers has been discussed. It has been shown accordingly that the DAB-based inductance can be used as a variable reactive element in WPT receiver to retune the resonant tank at different mismatch cases.

## 3.7 References

[1] Q.-C. Zhong, "Active capacitors: Concept and implementation," in *2012 IEEE International Symposium on Industrial Electronics*, 2012, pp. 149–153.

[2] G. A. Rincon-Mora, "Active capacitor multiplier in Miller-compensated circuits," *IEEE J. Solid-State Circuits*, vol. 35, no. 1, pp. 26–32, 2000.

[3] I.-C. Hwang, "Area-efficient and self-biased capacitor multiplier for on-chip loop filter," *Electronics Letters*, vol. 42, no. 24. p. 1392, 2006.

[4] L. A. Milner and G. A. Rincon-Mora, "A novel predictive inductor multiplier for integrated circuit DC-DC converters in portable applications," in *ISLPED '05. Proceedings of the 2005 International Symposium on Low Power Electronics and Design*, 2005, pp. 84–89.

[5] Y. Lee and I. C. Park, "Capacitor array structure and switching control scheme to reduce capacitor mismatch effects for SAR analog-to-digital converters," in *ISCAS 2010 - 2010 IEEE International Symposium on Circuits and Systems: Nano-Bio Circuit Fabrics and Systems*, 2010, pp. 1464–1467.

[6] J. J. Kim, K.-H. Lee, J. Choi, Y. Park, K. Lim, and C.-H. Lee, "Ultra-wideband CMOS voltage-controlled oscillator with reconfigurable tunable inductors," *Electron. Lett.*, vol. 47, no. 4, p. 249, 2011.

[7] D. H. Tellegen, "The Gyrator, a New Electric Network Element," Philips Res. Reports, vol. 3, no. 2, pp. 81–101.

[8] S. Singer and R. W. Erickson, "Canonical modeling of power processing circuits based on the POPI concept," *IEEE Trans. Power Electron.*, vol. 7, no. 1, pp. 37–43, 1992.

[9] M. Ismail and H. Olsson, "A novel CMOS fully differential inductorless RF bandpass filter," *2000 IEEE Int. Symp. Circuits Syst. Emerg. Technol. 21st Century. Proc.*, vol. 4, pp. 149–152, 2000.

[10] T. Deliyannis, Y. Sun, and J. K. Fidler, Continuous-time active filter design. CRC Press, 1999.

[11] G. G. A. Black, R. T. Friedmann, and A. S. Sedra, "Gyrator implementation with integrable current conveyors," *IEEE J. Solid-State Circuits*, vol. 6, no. 6, 1971.

[12] G. G. A. Black, R. T. Friedmann, and A. S. Sedra, "Gyrator implementation with integrable current conveyors," *IEEE Journal of Solid-State Circuits*, vol. 6, no. 6. pp. 396–399, 1971.

[13] S. Singer, "Gyrators Application in Power Processing Circuits," *IEEE Trans. Ind. Electron.*, vol. IE-34, no. 3, pp. 313–318, Aug. 1987.

[14] S. Singer, "Loss-free gyrator realization," *IEEE Trans. Circuits Syst.*, vol. 35, no. 1, pp. 26–34, 1988.

[15] A. Cid-Pastor, L. Martinez-Salamero, C. Alonso, G. Schweitz, J. Calvente, and S. Singer, "Classification and synthesis of power gyrators," *IEE Proc. - Electr. Power Appl.*, vol. 153, no. 6, p. 802, Nov. 2006.

[16] D. Shmilovitz, "Gyrator Realization Based on a Capacitive Switched Cell," *IEEE Trans. Circuits Syst. II Express Briefs*, vol. 53, no. 12, pp. 1418–1422, Dec. 2006.

[17] A. Cid-Pastor, L. Martinez-Salamero, C. Alonso, R. Leyva, and S. Singer, "Paralleling DC–DC Switching Converters by Means of Power Gyrators," *IEEE Trans. Power Electron.*, vol. 22, no. 6, pp. 2444–2453, Nov. 2007.

[18] A. Cid-Pastor, L. Martinez-Salamero, C. Alonso, B. Estibals, J. Alzieu, G. Schweitz, and D. Shmilovitz, "Analysis and design of power gyrators in sliding-mode operation," *IEE Proc. - Electr. Power Appl.*, vol. 152, no. 4, p. 821, Jul. 2005.

[19] R. Haroun, A. Cid-Pastor, A. El Aroudi, and L. Martinez-Salamero, "Synthesis of Canonical Elements for Power Processing in DC Distribution Systems Using Cascaded Converters and Sliding-Mode Control," *IEEE Trans. Power Electron.*, vol. 29, no. 3, pp. 1366–1381, Mar. 2014.

[20] M. Ehsani, I. Husain, and M. O. BilgiC, "Inverse Dual Converter (IDC) for High-Power DC-DC Applications," *IEEE Trans. Power Electron.*, vol. 8, no. 2, pp. 216–223, 1993.

[21] M. Ehsani, I. Husain, and M. O. Bilgic, "Power converters as natural gyrators," *IEEE Trans. Circuits Syst. I Fundam. Theory Appl.*, vol. 40, no. 12, pp. 946–949, 1993.

[22] I. Zeltser and S. Ben-Yaakov, "Modeling, analysis and simulation of 'AC inductor' based converters," in *PESC Record - IEEE Annual Power Electronics Specialists Conference*, 2007, pp. 2128–2134.

[23] D. Shmilovitz, "Loss-free complex impedance network elements," *IEEE Trans. Circuits Syst. I Regul. Pap.*, vol. 53, no. 3, pp. 704–711, Mar. 2006.

[24] Hengsi Qin and J. W. Kimball, "Ac-ac dual active bridge converter for solid state transformer," in *2009 IEEE Energy Conversion Congress and Exposition*, 2009, pp. 3039–3044.

[25] R. W. (Robert W. Erickson and D. Maksimović, Fundamentals of power electronics. Kluwer Academic, 2001.

[26] H. Funato, A. Kawamura, and K. Kamiyama, "Realization of negative inductance using Variable Active-Passive Reactance (VAPAR)," *IEEE Trans. Power Electron.*, vol. 12, no. 4, pp. 589–596, 1997.

[27] M. T. Bina and D. C. Hamill, "Transient response and stability of the bootstrap variable inductance (BVI)," in *2001 IEEE 32nd Annual Power Electronics Specialists Conference*, vol. 2, pp. 510–515.

[28] N. T. Bina and D. C. Hamill, "Average model of the bootstrap variable inductance (BVI)," in *2000 IEEE 31st Annual Power Electronics Specialists Conference. Conference Proceedings*, 2000, vol. 2, no. c, pp. 967–972.

[29] E. Alarcon, G. Villar, S. Ferrandez, F. Guinjoan, and A. Poveda, "Ripple-reduction tuned filtering switching power converter topology," in *2004 IEEE 35th Annual Power Electronics Specialists Conference*, pp. 3739–3744.

[30] J. Phinney and D. J. Perreault, "Filters with active tuning for power applications," *IEEE Trans. Power Electron.*, vol. 18, no. 2, pp. 636–647, 2003.

[31] S. Agrawal, S. K. Pandey, J. Singh, and M. S. Parihar, "Realization of efficient RF energy harvesting circuits employing different matching technique," in *Proceedings - International Symposium on Quality Electronic Design*, ISQED, 2014, pp. 754–761.

[32] R. G. Cid-Fuentes, H. Martinez, A. Poveda, and E. Alarcon, "Electronically tunable switch-mode high-efficiency adaptive band-pass filters for energy harvesting applications," in *ISCAS 2012 - 2012 IEEE International Symposium on Circuits and Systems*, 2012, pp. 684–687.

[33] L. Wang, Y. Pei, X. Yang, Y. Qin, and Z. Wang, "Improving light and intermediate load efficiencies of buck converters with planar nonlinear inductors and variable on time control," *IEEE Trans. Power Electron.*, vol. 27, no. 1, pp. 342–353, 2012.

[34] L. Zhang, W. G. Hurley, and W. H. Wölfle, "A New Approach to Achieve Maximum Power Point Tracking for PV System With a Variable Inductor," *IEEE Trans. Power Electron.*, vol. 26, no. 4, pp. 1031–1037, Apr. 2011.

Chapter

# 4

# Self-Tuning Control for WPT Receivers based on Switch-Mode Gyrators

In the previous chapters, we have revisited the concept of reactive components emulation by means of gyrators. We have shown accordingly that the same concept could be applied in power processing applications where a switch-mode circuit is used for gyrator realization. The DAB converter has been shown as a good candidate for our application because it is naturally gyrated without the need for an external control that forces the gyration characteristics.

In order to utilize the DAB gyrator for realization of electronically tunable reactive element in the framework of self-tuning WPT receivers, a novel control approach is required. Consequently, the motivation of this chapter is to propose, discuss and evaluate novel control techniques for self-tuning in WPT receivers. Two different control techniques will be proposed and evaluated in this chapter, namely, dual-loop cascaded automatic tuning control and quadrature phase-locked-loop control.

## 4.1 DAB-Based Variable Inductance Design

Following the proposal of DAB converter as a natural gyrator, a system co-designing is required in order to apply the DAB converter as a variable inductance synthesizer in parallel-compensated WPT receivers. Figure 4.1 shows the complete power circuit of the WPT receiver as has been previously depicted in the block diagram of Chapter 3.

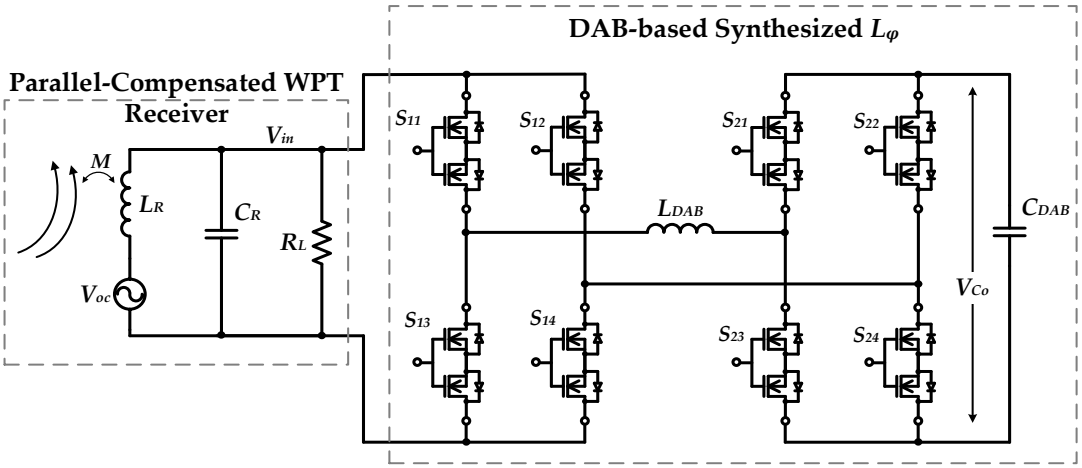


**Figure 4.1** A model of parallel-compensated WPT receiver.

The system frequency is chosen at 300 kHz. We recall that the switching frequency $f_{DAB}$ is affecting the design parameters while at the same time there is a perpetual trade-off between the circuit performance, efficiency and the switching frequency [1]. The higher the switching frequency is, the lower $L_{DAB}$ and $C_{DAB}$ for the same required $L_\varphi$ become. For the specified operating frequency, a switching frequency of 5 MHz is chosen in order to decrease the amount of ripple while maintaining lower $L_{DAB}$ and $C_{DAB}$.

The circuit parameters are given in Table 4.1, in which the circuit in Figure 4.1 has been characterized using the event-based PSIM simulation framework. Figure 4.2(a) indicates the gyration behavior of the four-quadrant DAB converter, in which the inductor current $IL_{DAB}$, the input bridge voltage $V_{AB}$, the output bridge voltage $V_{CD}$, and the DAB output voltage $V_{Co}$ are shown for the case of $\varphi = 50°$. The estimated value of synthesized inductance $L_\varphi$ at $\varphi = 50°$ is nearly 36 μH. It is observed in Figure 4.2(a) that the average current of $L_{DAB}$ is zero. Moreover, the input current of DAB is bipolar ($I_{in}$ is not shown in the figure) and discontinuous. However, it is still valid to infer the input current $I_{in}$ by referring to the DAB output $V_{Co}$ as an indication, a fact that is derived from the gyrator characteristic equation ($i_{in} = gv_o$). Therefore, the gyration behavior is denoted by the quadrature phase lag (in Figure 4.2(a)) between the DAB output voltage $V_{Co}$ and the input voltage $V_{in}$.

**Table 4.1** DAB circuit parameters.

| **Parameter** | $f_T$ | $f_{DAB}$ | $L_{DAB}$ | $C_{DAB}$ |
|---|---|---|---|---|
| **Value** | 300 kHz | 5 MHz | 367 nH | 100 nF |

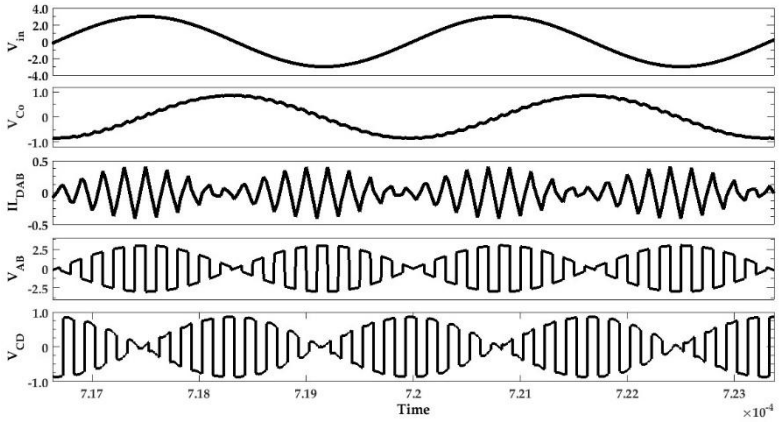


(**a**)

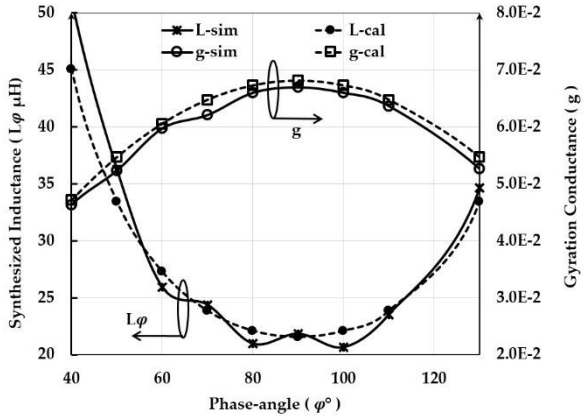


(**b**)

**Figure 4.2** Validation of DAB-based Inductance synthesis in WPT receiver **(a)** Waveforms at $\varphi$ = 50°; **(b)** synthesized inductance $L_\varphi$ and gyration conductance versus $\varphi$.

With regards to tuning capability, the phase-shift angle has been swept from 30°–150° and the synthesized inductance $L_\varphi$ as well as the gyration conductance $g$ versus $\varphi$ is shown in Figure 4.2(b). Although $L_\varphi$ is theoretically amenable to full–range tuning of 0°–180°, it has been noted that the synthesized inductance approaches very high values of $\varphi$ <20° or $\varphi$ >150°. Note that the shown data in Figure 4.2(b) is limited to the range of 40°–130° for the sake of clarity. Moreover, the given results shows a comparison between the values of $g$ and $L_\varphi$ obtained by circuit simulation with the calculated values that has been given mathematically in Chapter 3 as follows:

$$\mathrm{g} = \frac{1}{\omega_{DAB} L_{DAB}} \left(\varphi - \frac{\varphi^2}{\pi}\right) \tag{4.1}$$

$$L_\varphi = \frac{C_{DAB}}{\mathrm{g}^2} = \frac{\pi^2 \omega_{DAB}^2 L_{DAB}^2}{(\varphi\pi - \varphi^2)^2} \cdot C_{DAB} \tag{4.2}$$

The figure shows a good correlation between the calculated and simulated results. Indeed, the mismatch between the calculated and simulated values is due to the losses of the AC switches that are included in the simulation circuit while lossless circuit components have been considered in the theoretical expressions. Also, we recall that the gyration behavior in Figure 4.2(b) replicates symmetrically around $\varphi$ =90°, which closely correlates with Equation (3.13). This symmetry reveals that the synthesized inductance has only two valid tuning ranges either $\varphi$ =0°– $\varphi$ =90° or $\varphi$ =90°– $\varphi$ =180°. This fact should be taken into account in the process of designing a bidirectional tuning control for WPT receivers.

## 4.2 A Dual Loop Automatic Tuning Control for WPT Receiver

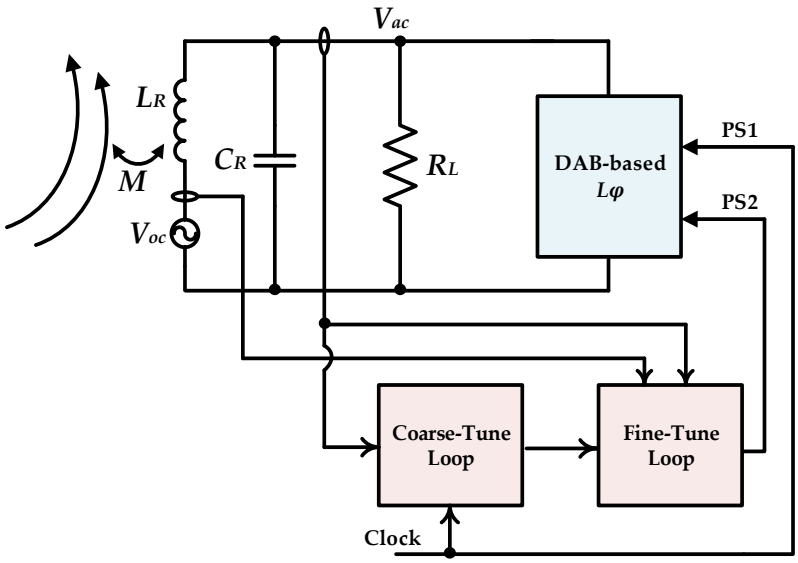


**Figure 4.3** Block diagram of dual-loop control for DAB-based adaptive tuning of WPT receiver.

When the parallel-compensated WPT receiver is fully-tuned at the operating frequency of the WPT link, it has been shown that the resonant tank voltage $V_{ac}$ is given by:

$$V_{ac} = -j\frac{R_L}{\omega_{R0} L_R} V_{oc} = -jQ_{RL} V_{oc} \tag{4.3}$$

Consequently, from Equation (4.3) we conclude that there are two facts that could be employed as a control method. When the receiver tank is fully-tuned: (a) the resonant tank voltage $V_{ac}$ is at

maximum value and equal $V_{ac} = Q_{RL} \cdot V_{oc}$, (b) the resonant tank voltage $V_{ac}$ lags the coil induced voltage $V_{oc}$. Since the first fact cannot be utilized autonomously for accurate tuning of high-Q receivers, a dual-loop control method is proposed in this section. The dual-loop control is composed of a coarse-tuning loop that exploits the first fact, while another fine-tuning loop exploits the second fact. Figure 4.3 shows a block diagram for the proposed control. The operation details of every loop is to be explained in the next subsections.

### 4.2.1 Coarse-Tuning Loop

Figure 4.4 shows the block diagram of the coarse-tuning (CT) loop, which is the first control loop that takes action for the tuning. The CT loop includes an envelope follower, a peak voltage detector, an up-down binary counter, and a phase-shift scan block. The role of CT loop is to coarsely lock for a phase-shift value $\varphi$ that corresponds to the peak of the envelope follower output $V_{env}$. The operation of the loop starts by enabling the counter that clocks the phase-shift scan circuit. The phase-shift scan circuit receives the driving signal of the input bridge $PS_1$ and outputs a driving signal for the output bridge $PS_{coarse}$ that is shifted from $PS_1$ by φ, where φ is moved up in a sequence according to the counter output, *e.g.* 10°, 20°, 30°, etcetera. During the phase-shift scan period, the envelope voltage of $V_{ac}$ is tracked by the envelope follower and sampled by the peak detector in every counter cycle. Once a voltage peak is detected, the peak detector output is used to disable the counter to freeze the phase-shift scan to the phase-shift value that corresponds to the highest peak.

The operation of the CT loop has been verified by simulation for a case study characterized by the system in Figure 4.3, where the DAB converter in Figure 4.1 is used as the tunable switch-mode inductance emulator. The parameter values of the verification system are given in Table 4.2, while the verification results are shown in Figure 4.5. The simulation results given in Figure 4.5 show how the CT loop sweeps over a multiple phase-shift values until a peak is detected indicating that the system is not yet fully-tuned, but is close to the exact tuning point. The peak detection signal, then, is used as a triggering signal for the FT loop toward a fully-tuning process.

**Table 4.2** Simulation Circuit Parameters

| **Parameter** | $f_T$ | $f_{DAB}$ | $C_{DAB}$ | $L_{DAB}$ | $C_R$ | $L_R$ | $Q_{RL}$ |
|---|---|---|---|---|---|---|---|
| **Value** | 300 kHz | 5 MHz | 100 nF | 66 nH | 260 nF | 5 μH | 30 |

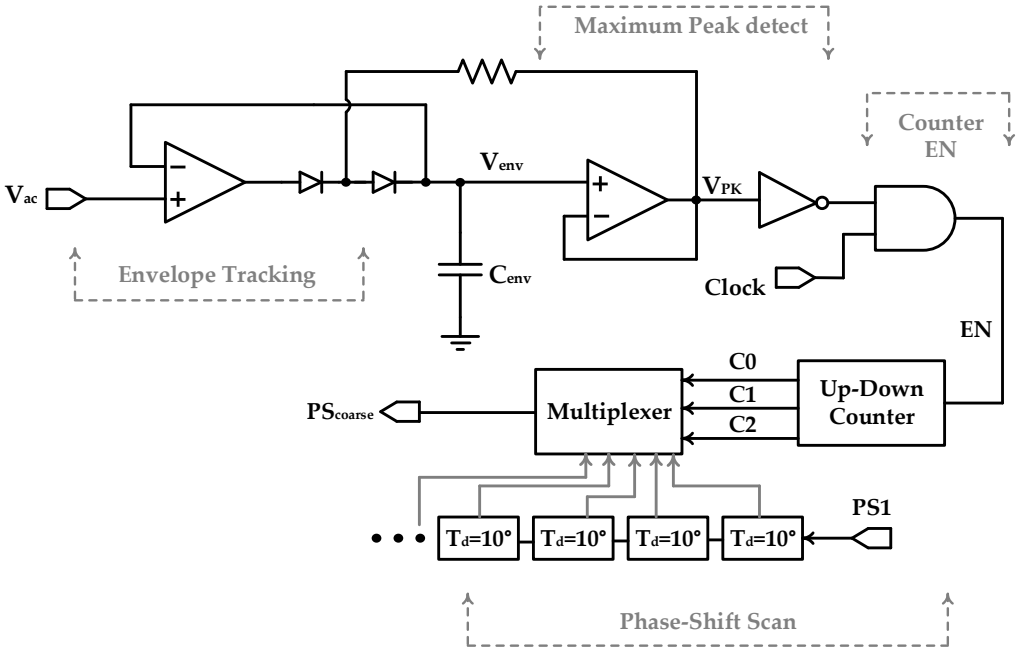


**Figure 4.4** Block diagram for coarse-tuning loop.

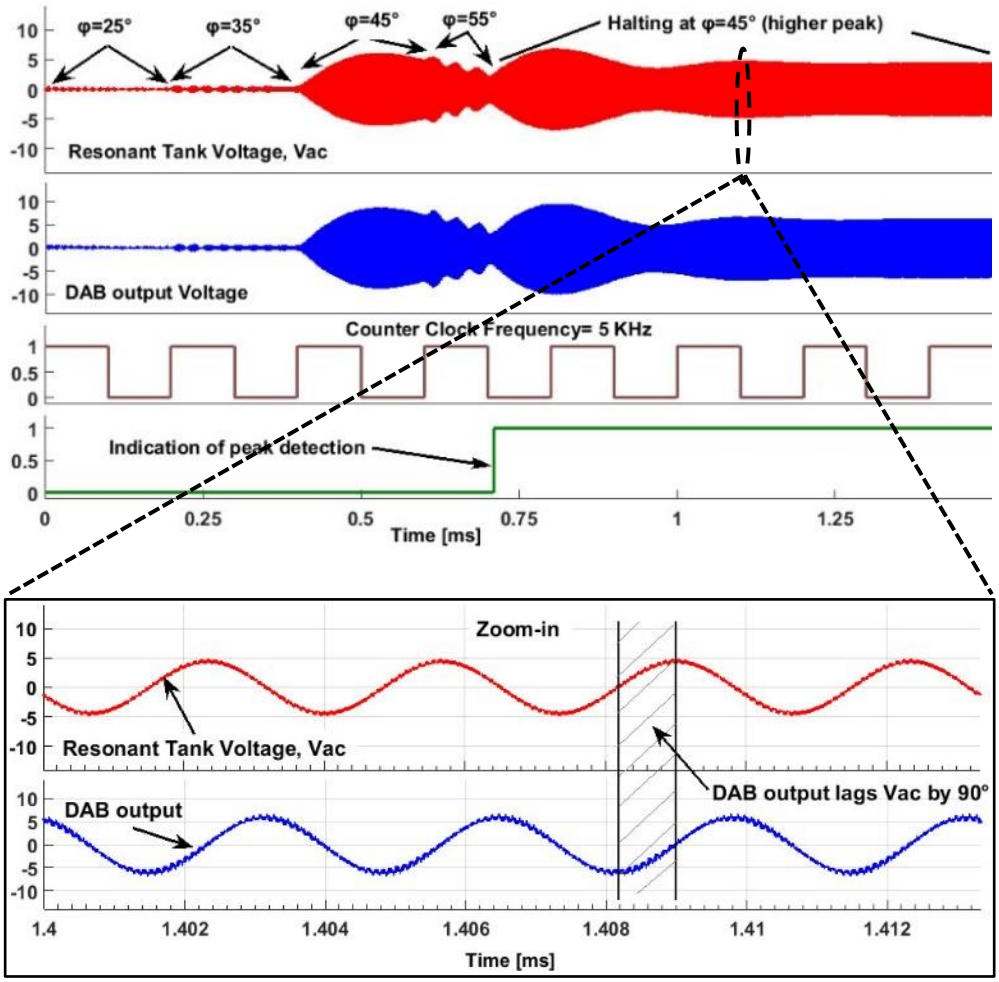


**Figure 4.5** Waveforms of the coarse-tune loop operation.

### 4.2.2 Fine-Tuning Loop

The fine-tuning (FT) loop is responsible for receiving the output signal $PS_{coarse}$ from the CT loop. As previously mentioned, since the CT loop cannot be merely used to fully tune the resonant tank, the FT loop receives the output of CT loop and starts a more accurate tuning process within a range of ($PS_{coarse}$+10°). The block diagram of the FT loop is depicted in Figure 4.6, comprising a phase detector, a low-pass filter (LPF), a hysteresis comparator, a counter and a fine-tuning scan block.

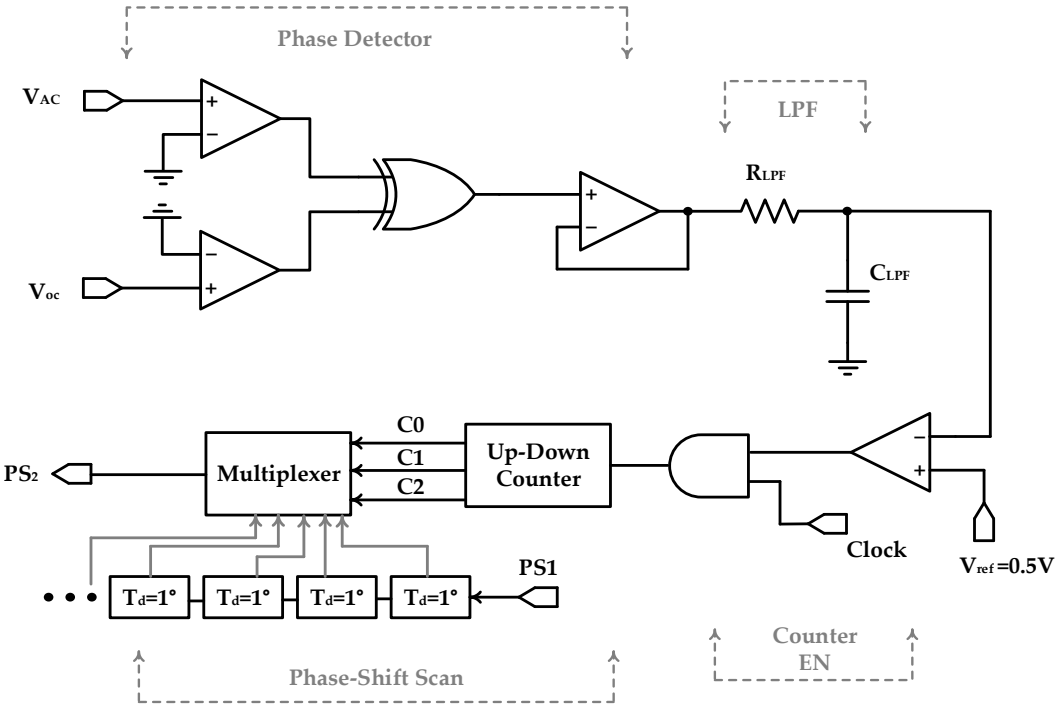


**Figure 4.6** Block diagram for fine-tuning loop.

The fine-tuning process utilize the fact that $V_{ac}$ lags $V_{oc}$ by 90° when the system is fully tuned. From that, a phase detector is used to detect the relative phase between $V_{ac}$ and $V_{oc}$ and feed a LPF that produces a DC voltage proportional to the phase difference. A phase-shift of 90° corresponds to a 0.5V output from LPF. Similarly, a phase-shift scan is enabled within a range ($PS_{coarse}$, $PS_{coarse}$+10°) by the counter, while the output of LPF is monitored by the hysteresis comparator. When the LPF output reaches 0.5V, a signal is applied to halt the FT process as an indication of a fully-tuned state. Figure 4.7 shows the verification waveforms for the dual-loop control including the CT and FT operation.

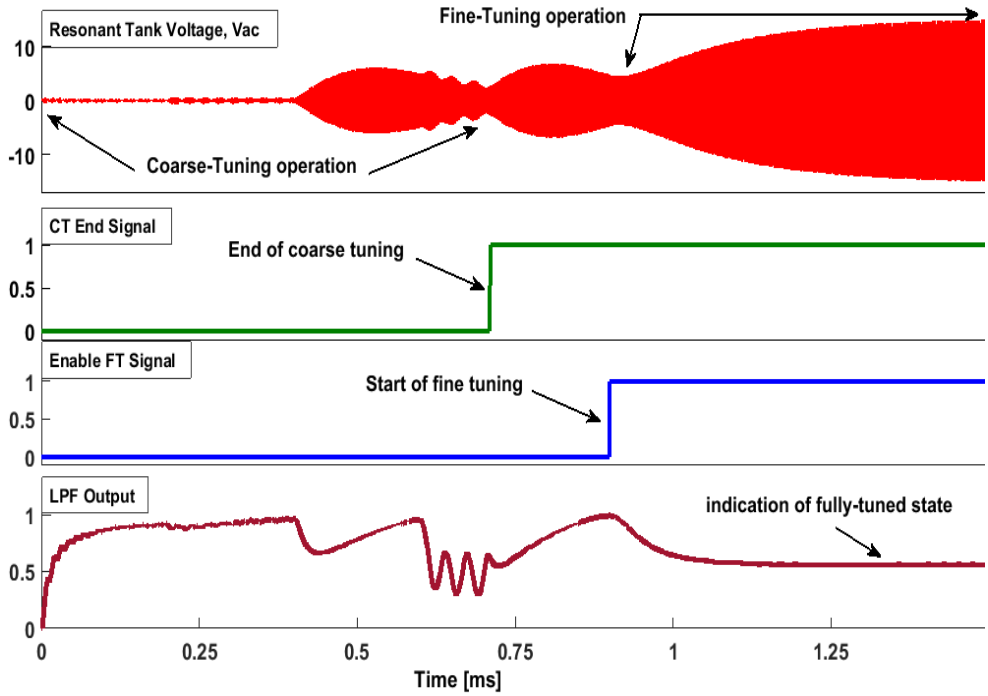


**Figure 4.7** Simulation waveforms of the system with FT operation indicated.

### 4.2.3 Performance discussion

The dual loop automatic tuning technique shows a preliminary good response, however the robustness and time response of the control is not so reliable. At first, the trade-off between accuracy and transient time applies, particularly for the coarse tuning loop. Based on the digital phase-shift scan mechanism, the transition from one phase-shift value to another, *e.g.* from $\varphi$ =10° to $\varphi$ = 20°, is around 200 μs which is determined by the clocking the counter at 5 kHz rate. This rate has been chosen to allow the resonant circuit voltage $V_{ac}$ to reach the steady state value every time a new phase-shift value is introduced, which in essence corresponds to a new value of $L_{\varphi}$. It is possible to decrease the total time of coarse tuning operation be increasing the clock frequency of the counter; however the accuracy will be affected considerably.

On other hand, if the system is already fully-tuned and a change in one of the WPT receiver's parameters occur, the control would need to restart the scanning process from the beginning, otherwise it would be impossible in this control mechanism to devise the correct tuning direction. Moreover, the reliability of the control is also unpredictable at some cases. Consider for example the case shown in Figure 4.8 where the control fails to tune correctly to the right value of $\varphi$, simply because the right value of lies between two phase-shift ranges and consequently has been skipped. In such cases, the control loop settles at a wrong value of $\varphi$.

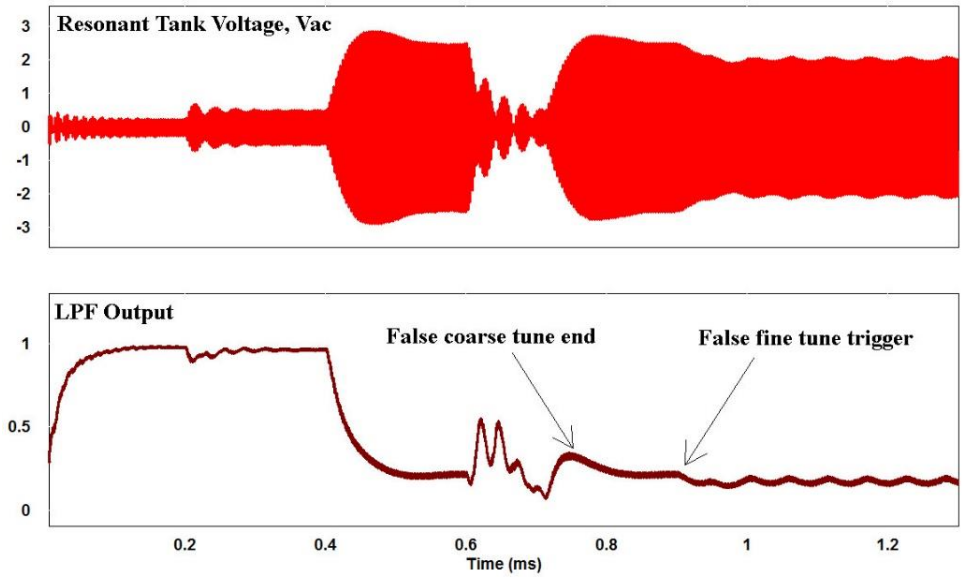


**Figure 4.8** False coarse tuning in the dual loop automatic control.

## 4.3 Quadrature Phase-Locked Loop Control

As we have discussed, the dual loop control approach is suffering from reliability issues due to the fixed phase-shift scanning mechanism. In this section, a better control approach is proposed that is based on PI compensated linear control. Figure 4.9 shows the block diagram of the parallel-compensated WPT receiver after adding the DAB gyrator as a tunable inductance synthesizer. We call the proposed control "*quadrature phase-locked loop*" (Q-PLL) control as it acts like a PLL in terms of phase difference tracking. The details and operation of the Q-PLL control is to be discussed in the next subsection.

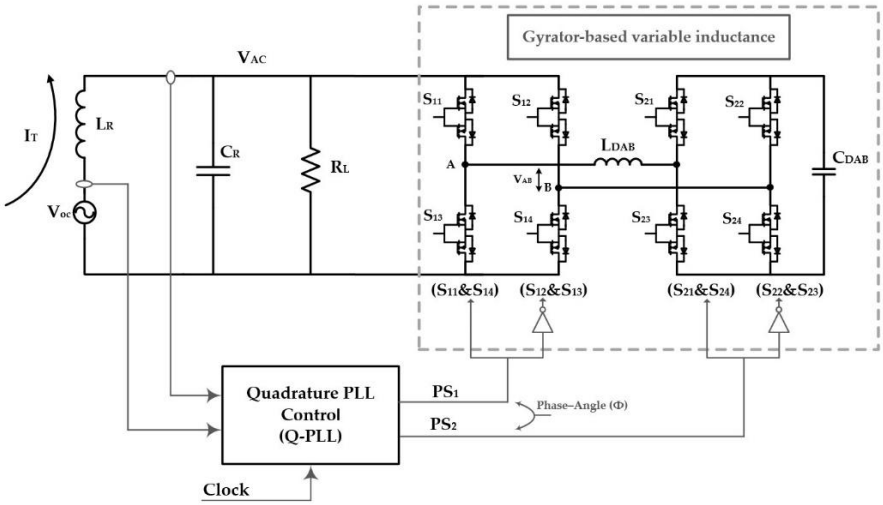


**Figure 4.9** Block diagram of the Q-PLL automatic tuning control for gyrator-based parallel WPT receiver.

### 4.3.1 PLL-Like Control—Theory and Operation

The ultimate goal of the controller is to guarantee autonomous dynamic tuning for the WPT receiver irrespective of any variations that would give rise to a mistuned tank. The controller finds out whether there is a mistuning in the WPT receiver, then responds accordingly by fine-tuning the phase-angle $\varphi$ of the DAB converter such that the corresponding $L_\varphi$ for retuning is dynamically achieved. We have already seen that tracking the maximum envelope voltage is not a reliable approach due to low accuracy issues [2]. On the other hand, taking advantage of the quadrature phase lag between $V_{ac}$ and $V_{oc}$ as illustrated in Equation (4.3) is a more accurate control parameter. Then, it would be possible to design a linear control that takes the phase difference between $V_{ac}$ and $V_{oc}$ in order to generate the optimum value of for a fully-tuned receiver tank. In a typical PLL circuit, the phase difference between two frequency signals is sensed and the negative feedback loop works toward decreasing the phase difference down to zero. In contrast, our objective is to sense the phase difference between $V_{ac}$ and $V_{oc}$ and apply a negative feedback loop that ensures a 90° phase shift; hence, the name quadrature PLL becomes more related. To analyze this concept, the transfer function of the parallel-compensated WPT receiver after adding the DAB variable inductance $L_\varphi$ is given as:

$$\frac{V_{ac}}{V_{oc}} = \frac{L_\varphi R_L}{-\omega^2 L_\varphi L_R C_R R_L + R_L\left(L_\varphi + L_R\right) + j\omega L_\varphi L_R} \tag{4.4}$$

As the control loop is supposed to sense the phase difference, it is of more importance to examine the phase angle between $V_{ac}$ and $V_{oc}$ by converting Equation (4.4) to the polar form. The phase angle can be expressed as:

$$\tan\theta = \frac{\omega L_\varphi L_R}{\omega^2 C_R L_\varphi L_R R_L - L_R\left(L_\varphi + R_L\right)} \tag{4.5}$$

where $\theta$ is the phase angle between $V_{ac}$ and $V_{oc}$. For $\theta$ to be equal to 90°, the right-hand term of Equation (4.5) has to approach infinity. In other words, the denominator of Equation (4.5) becomes:

$$\omega^2 C_R L_\varphi L_R R_L - \left(L_\varphi + L_R\right) = 0 \tag{4.6}$$

It is evident that for the angle in Equation (4.5) to be equal to 90°, the denominator in Equation (4.6) has to be equal to zero, which is only possible if $L_\varphi$ is adjusted such that the tank is fully-tuned $\{\omega_T=(L_\varphi+L_R)/L_\varphi L_R C_R\}$. Consequently, the control has to be designed as quadrature PLL-like. The control operates by sensing $V_{ac}$ and $V_{oc}$, then acts by tuning $\varphi$ toward

steady-state fully-tuned state that is fulfilled once $V_{ac}$ becomes lagging $V_{oc}$ by 90°. Figure 4.10 depicts the block diagram of the main control parts. It comprises an XOR phase-detector (PD), low-pass filter (LPF), an error amplifier compensated by a PI integrator, PWM block, and finally a phase-shift modulator (PSM).

In order for the control to work properly, the desired tuning range has to be designed according to the WPT receiver parameter, *e.g.* operating frequency $f_T$ and coil inductance $L_R$. Note that the tuning range of DAB-based synthesized inductance $L_\varphi$, as shown in Figure 4.2(b), is unidirectional either from 0°–90° or from 90°–180° as implied by the symmetrical gyration behavior around $\varphi$=90°. In order to allow a bidirectional tuning range, the synthesized inductance $L_\varphi$ has to be designed at the middle of the gyration curve, *e.g.* $\varphi$=90°, to resonate with $L_R$ and $C_R$ at the nominal operating frequency $f_T$. Therefore, tuning ranges of (0°-50°) and (50°-90°) are enabled depending on the sign of mismatch either in $\gamma_L$ or $\gamma_C$.

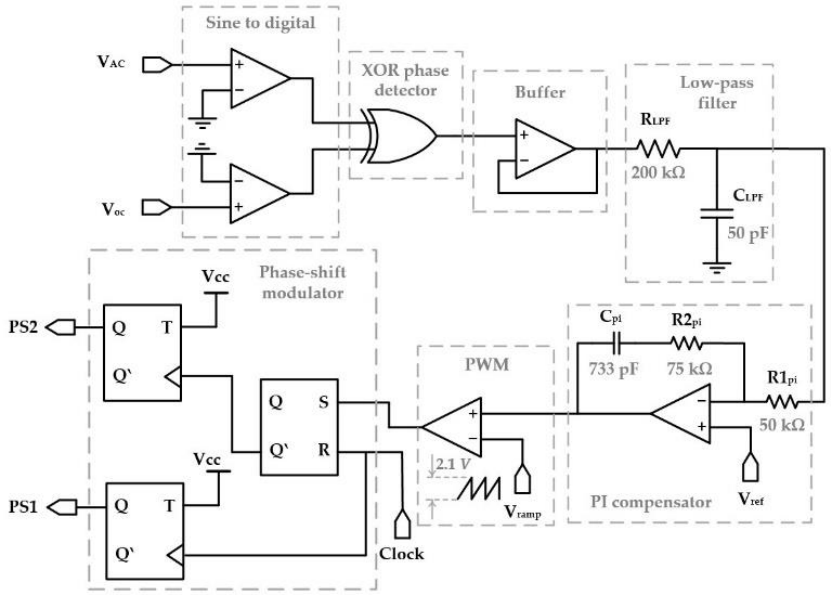


**Figure 4.10** Schematic Block diagram of the Q-PLL control for gyrator-based dynamic frequency tuning system in Figure 4.9.

## 4.3.2 System Integration and Validation Results

The Q-PLL dynamic tuning approach depicted in Figure 4.9 has been characterized and validated by simulation for the design specification parameters given in Table 4.2. The values of WPT transmitter coil $L_T$ and receiver coils $L_R$ have been designed to deliver about 500 mW to 200 Ω load at a coupling coefficient of $k$ =0.1 while operating at 200 kHz. The transmitter coil $L_T$ has been compensated by a series capacitor $C_T$ of 63.97 nF taking into account the reflected negative reactance (100 nF at coupling coefficient of $k$ =0.1) from a fully-tuned receiver as has

been previously shown in Chapter 2. Correspondingly, the DAB gyrator parameters have been designed and given in Table 4.2, where the PI control parameters have been designed at $k_p$=1.5 and $f_z$ = 66.7 kHz for stable operation.

As pointed out in the previous subsection, it turns out that for a wide bidirectional tuning range by means of the DAB gyrator inductance, the synthesized inductance $L_\varphi$ has to be designed in order to resonate in parallel with $L_R$ and $C_R$ while a sufficient $\varphi$ tuning margin is allowed. Therefore, the synthesized inductance $L_\varphi$ has been optimized at a value of 8.08 μH at $\varphi$=45°. The DAB circuit is switching at the rate of 1.5 MHz which is reasonably higher than the link signal frequency $f_T$. A higher switching frequency would be beneficial in terms of the required values for $L_{DAB}$ and $C_{DAB}$, as suggested by Equation (24). As a typical phenomenon in switch-mode circuits, the internal losses of the DAB circuit would increase proportionally with the switching frequency leading to the trade-off between components size and efficiency.

Following the system parameters design, the Q-PLL control for dynamic tuning has been implemented as shown in the block diagram in Figure 4.10, in which the components values are annexed to the same figure. Figure 4.11(a) shows the transient waveforms of the resonant tank voltage $V_{ac}$ where it shows that the tank voltage builds until it reaches the maximum at fully-tuned state. Also, the same figure shows the Q-PLL control signal $V_{Ctrl}$ and the corresponding control input variable $V_{LPF}$.

**Table 4.2** WPT link and DAB gyrator parameters.

| Parameter | Value |
|---|---|
| WPT link parameters | |
| $V_{in}$ | 2.12 $V_{rms}$ |
| $f_T$ | 200 kHz |
| $L_T$ | 10 μH |
| $C_T$ | 63.97 nF |
| $M$ | 447.2 nF (k≈ 0.1) |
| $L_R$ | 2.0 μH |
| $C_R$ | 395 nF |
| $R_L$ | 200 Ω (nominal) |
| DAB gyrator parameters | |
| $f_{DAB}$ | 1.5 MHz |
| $L_{DAB}$ | 480 nF |
| $C_{DAB}$ | 100 nF |
| B-switch $R_{ON}$ | 4 mΩ |
| $\varphi$ | 45° (nominal) |

It is evident that $V_{LPF}$, which represents the phase difference between $V_{ac}$ and $V_{oc}$, reaches $V_{ref}$=0.5 V indicating that $V_{ac}$ lags $V_{oc}$ by 90° as the typical state of a fully-tuned parallel resonant tank. Moreover, Figure 4.11(b) shows a close-in view for the steady-state waveforms for which the phase difference between $V_{ac}$ and $V_{oc}$ (scaled by $Q_{RL}$) is highlighted. Figure 4.11(b) shows, as well, how the duty-cycle generated by the control is translated to the corresponding phase-angle $\varphi$ (almost 45° at the specified system parameters in Table 4.2) between the gating signals *PS1* and *PS2*.

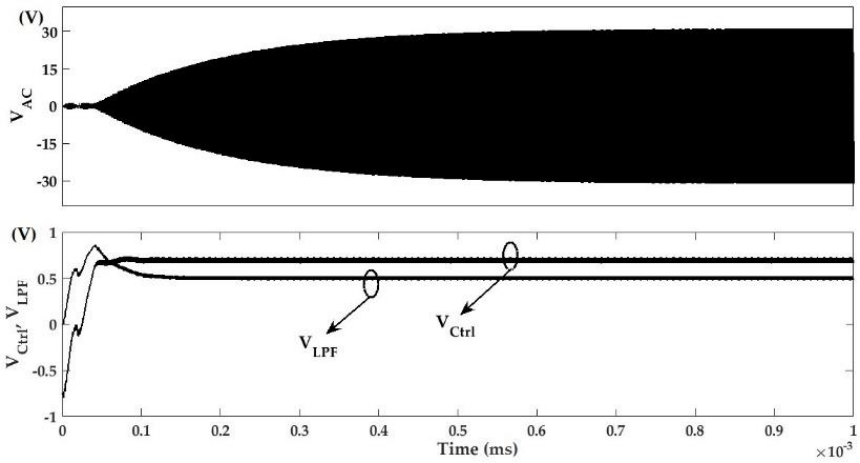


**(a)**

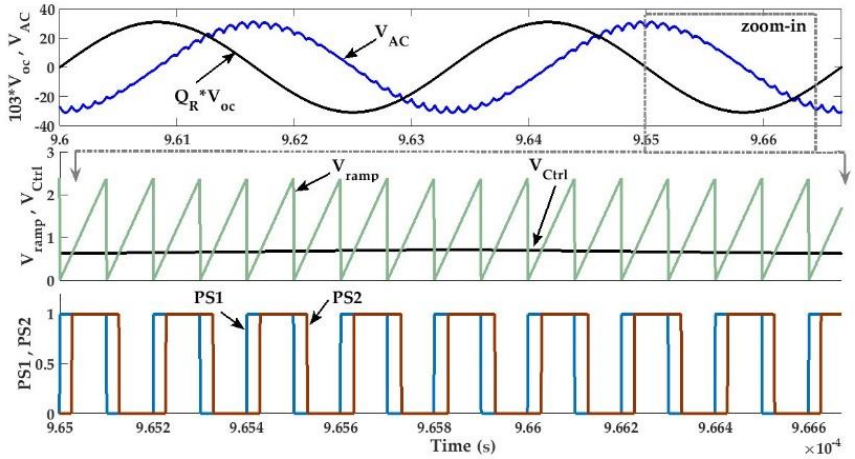


**(b)**

**Figure 4.11** System operation waveforms: **(a)** steady-state waveforms of $V_{Ctrl}$, $V_{LPF}$ and $V_{ac}$; **(b)** a zoom-in showing the waveforms of [$Q_{RL}\cdot V_{oc}$], $V_{ac}$, $V_{ramp}$, $V_{Ctrl}$, and DAB gating signals PS1 and PS2.

Further, Figure 4.12 shows the performance of the gyrator-based dynamic tuning approach in response to mismatch in $C_R$ and $L_R$. The system operation for -11% mismatch in $C_R$ followed by -11% mismatch in $L_R$ is illustrated in Figure 4.12(a), in which the figure shows how $\varphi$ is dynamically controlled to retune the resonant tank. To neutralize the under-compensation effect

of decreased $C_R$ and $L_R$, the effective synthesized $L_\varphi$ has to be increased which is apparent in the phase-angle stepping down from the nominal value of $L_\varphi$=45° (refer to Figure 4.2(b). Moreover, Figure 4.12(b) indicates the system performance for an increase in $C_R$ and $L_R$ for the same amount of +11%. Once more, the controller acts by decreasing increasing $\varphi$ to counteract the over-compensated tank by lowering the effective value of $L_\varphi$. In order to be able to track the variation imposed by the controller in $\varphi$, the phase difference between *PS1* and *PS2* is sensed and filtered, and subsequently it is post-processed to show the phase-angle in degrees. Figure 4.13 is aiming to show the wide tunability and robustness of the suggested approach in response to irregular successive changes in $C_R$ and $L_R$. As pointed out earlier, the allowable tuning range is limited either by the phase-angle $\varphi$ of DAB-based inductance or by a saturated control output. This effect is to be discussed in the next section.

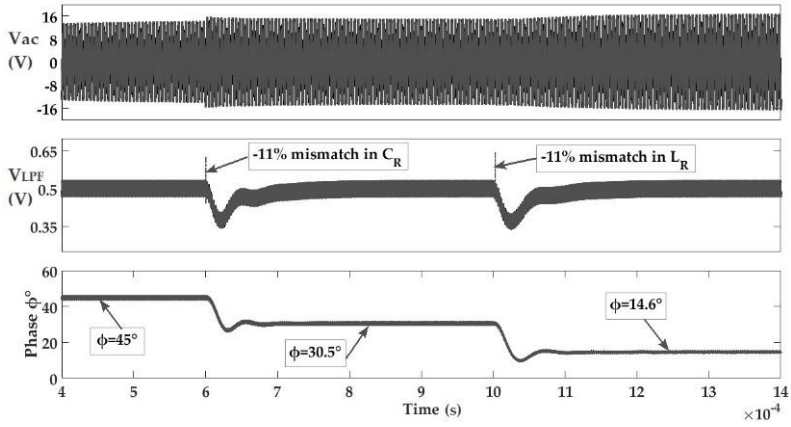


**(a)**

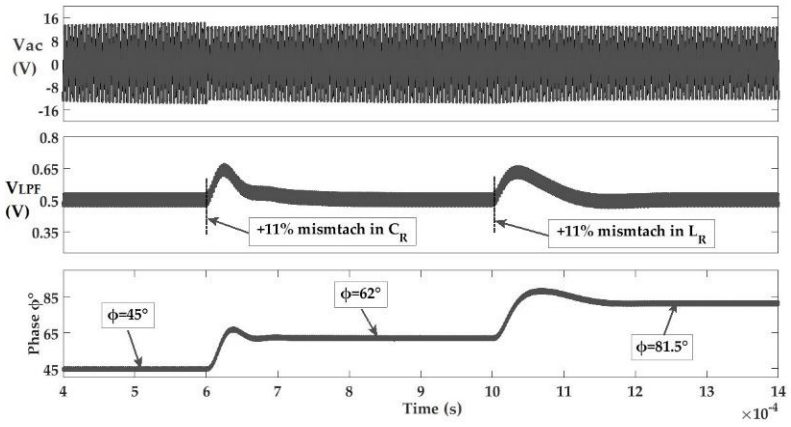


**(b)**

**Figure 4.12** System response to component variations showing $V_{ac}$, $V_{LPF}$ and the phase-angle $\varphi$: **(a)** Case of -11% variation in $C_R$ followed by -11% variation in $L_R$; **(b)** Case of +11% variation in $C_R$ followed by +11% variation in $L_R$.

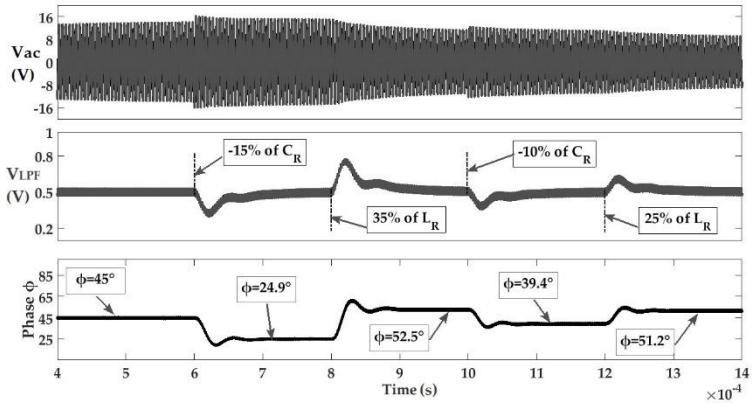


**Figure 4.13** Waveforms of system response to irregular change in $C_R$ and $L_R$.

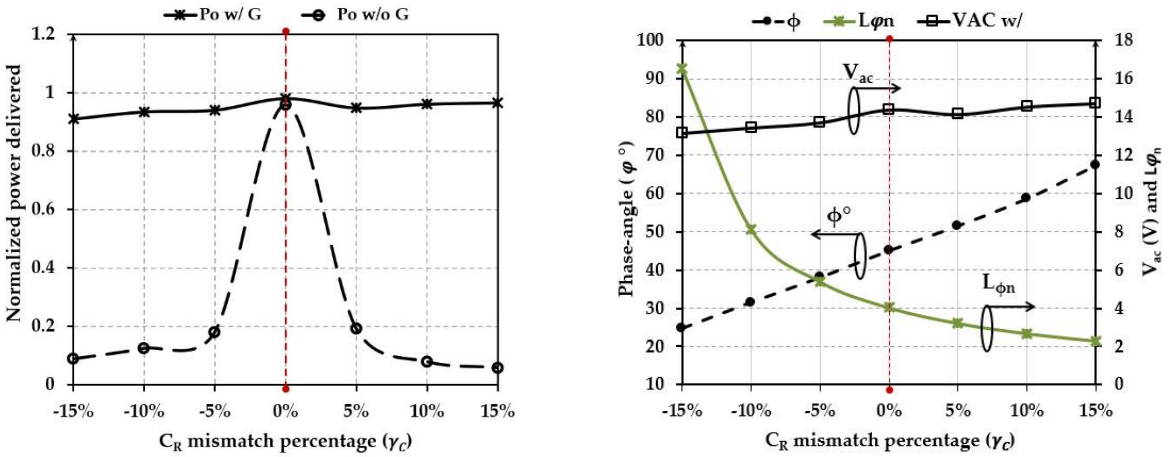


**(a)** **(b)**

**Figure 4.14** Demonstration of system performance versus $C_R$ mismatch of ±15%: **(a)** Normalized delivered power with dynamic tuning ($P_o\ w/\ G$) and without ($P_o\ w/o\ G$); **(b)** The synthesized inductance $L_\varphi$, the corresponding $\varphi$ and $V_{ac}$ versus $C_R$ mismatch.

Figure 4.14(a) shows the normalized power delivered versus different $C_R$ mismatch percentages with and without the gyrator-based synthesized inductance at $R_L$ =200 Ω (system specifications defined in Table 4.2). By comparing the normalized received power with using the gyrator-based dynamic tuning, it is evident that the system is successfully capable of compensating the mismatch effect by tuning the synthesized inductance. It is noted that the delivered power at 0% is almost the same either with or without the dynamic tuning approach, which is because the receiver parameters have been optimized at fully-tuned condition in the nominal case of no mismatch. Nonetheless, we note that the delivered power drops slightly with using the gyrator-based dynamic tuning due to the losses of the DAB converter that affect the tank analogously as being the series resistance of $L_\varphi$.

Further, Figure 4.14(b) shows the optimal phase-shift $\varphi$ and the corresponding synthesized inductance $L_{\varphi n}$ (normalized to the $L_R$). We note that at no mismatch, *i.e.* 0% on the plot, the

corresponding $L_\varphi$ is approximately four times the coil inductance $L_R$ which is nominal value at $\varphi$ = 45° for the optimized parameters in Table 4.2. Moreover, it is interesting to notice that $\varphi$ extends from 24.7°–67.3° approximately for a mismatch range ±15% of $C_R$, which is far enough from the theoretical limit of $\varphi$ from 0°–90°. This implies that the dynamic tuning range extends arbitrarily beyond the verified range of ±15%. The resonant tank RMS voltage $V_{ac}$ is plotted versus $\gamma_C$ to show that the tank is fully-tuned in response of the mismatch in $C_R$. Again, we note that there is a slight change in $V_{ac}$ due to a slight drop in $Q_{RL}$ due to losses in DAB.

### 4.3.3 Chip Implementation for the Proposed DAB-based Inductance Synthesizer

In order to reduce the size of the proposed DAB-based dynamic frequency tuning, the target of fully integrating the DAB cell and the Q-PLL control on a single silicon die is of crucial interest. Given the system parameters in Table 4.2, a full chip implementation is becomes more reasonable feasible in terms of size and performance. Figure 4.15 shows a schematic diagram for the main parts to be integrated into the chip. The receiver coil $L_R$, the compensation capacitor $C_R$, the output load $R_L$, the DAB inductance $L_{DAB}$, and the DAB output capacitor $C_{DAB}$ are planned as off chip components. All the other components including the DAB power switches and the Q-PLL controller could be integrated into a single chip.

The chip implementation is realized by a 0.18µm XFAB HV process. High-voltage triple-well isolated MOSFETs are used for realizing the power switches. As shown in Figure 4.15, a two back-to-back switches sized at (60000µm/0.35µm) are used to implement every AC switch. It has been verified through the accurate models of the process that the nominal channel resistance of every AC switch is around 22 mΩ. Consequently, with four AC switches closed simultaneously (two switches at every bridge), a total conduction resistance of 88 mΩ is included in the loop. The higher the channel resistance of a power MOSFET, the more power it consumes. The channel resistance of every switch could be decreased by sizing the power MOSFETs at higher width. However, this will be at the expense of the total chip area and switching losses. Note that, the details of transistor-level design of control blocks are not shown in Figure 4.15. However, the power consumption of control circuits are verified on Cadence Virtuoso using the accurate models offered by the foundry. The total power consumption of the control is 74.8 mW.

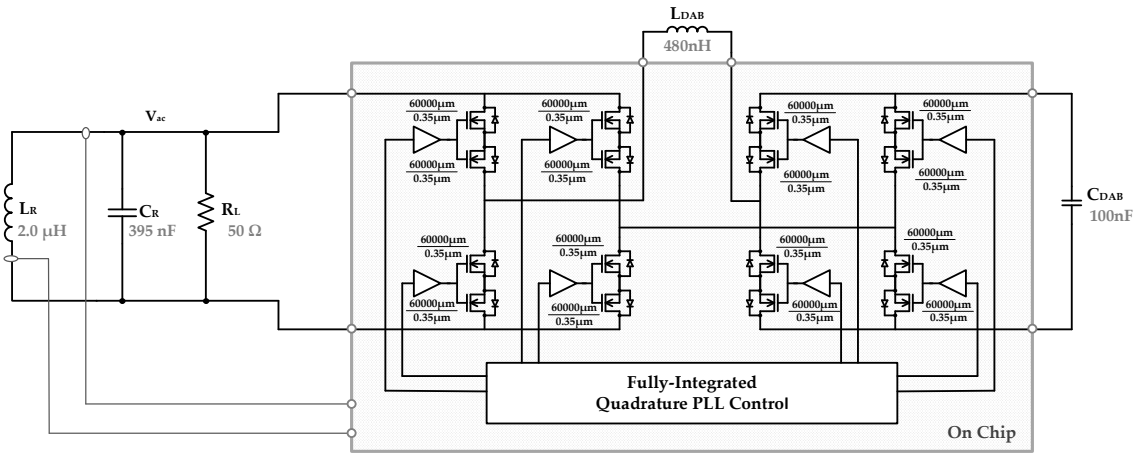


**Figure 4.15** Schematic diagram for on chip implementation for gyrator-based dynamic tuning.

The non-ideal yet functional waveforms of the designed chip are shown in Figure 4.16. A phase-lag of 90° between $V_{ac}$ and $V_{oc}$ is clear in Figure 4.16(a), where the phase-difference output (VPD) demonstrates this fact. Moreover, the averaging circuit output ($V_{LPF}$) reaches a steady-state value of 900 mV represent the average of $V_{PD}$. Note that, when the receiver tank is tuned, $V_{PD}$ has 50% duty-cycle while its high-level is at 1.8V due to the implementation of the phase-difference circuit using 1.8V low-voltage devices. Furthermore, Figure 4.16(b) shows the real-time results of the controller signals including error amplifier output $V_{Ctrl}$ compared to a ramp signal $V_{ST}$. A comparator realized by a fast folded-cascode wide-swing stage is used to compare $V_{Ctrl}$ with $V_{ST}$ and the $V_{duty}$ output is then translated to the phase-shift $\varphi$ between the driving signals of the DAB circuit.

With using coupled-coils model in Cadence for the coupling between the transmitter and receiver, the total power delivered to the receiver is 5 W. The real power that is consumed by the load ($R_L$= 50 Ω in Figure 4.15) was 3.74 W, this leads to an estimated efficiency of 74.8%. The total power loss of the chip counts up to 1.26 W which is divided into 74.8 mW (1.5% of total power) in the controller and 1.185 W (23.7% of total power) consumed by the DAB power switches. It is noted that the higher power consumption is due to the losses of power switches. However, the DAB losses can be decreased by up-sizing the width of the DAB power MOSFETs at the expense of more silicon area. The designed chip has been tested over a wide range of variation in $L_R$ and $C_R$ (-10% to +10% in $\Delta L_R$ and $\Delta C_R$) and the rms power delivered to the load is shown in Figure 4.16(c). It is noted that load rms power is slightly affected by the variations due to the effect on the total quality factor of the receiver tank. The efficiency given in Figure 4.16(c) has been calculated as ($P_L/P_R$) where $P_L$ is the power consumed by the resistive load $R_L$ and $P_R$ is the actual power received by the WPT coil $L_R$. While the quiescent power consumption by the control circuits stay almost constant at 75 mW, we found that the

power consumption of the DAB power switches is main contribution to the losses. A minimum efficiency of 73.4% has been found at $\Delta C_R$ of +10%. Though, still the total power recovered by the DAB-based dynamic tuning approach is promising compared to a mistuned WPT receiver tank.

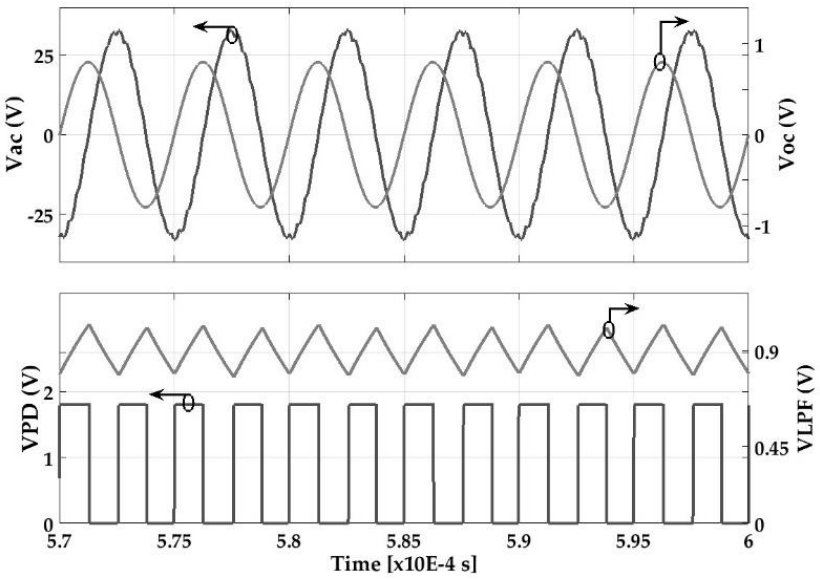


**(a)**

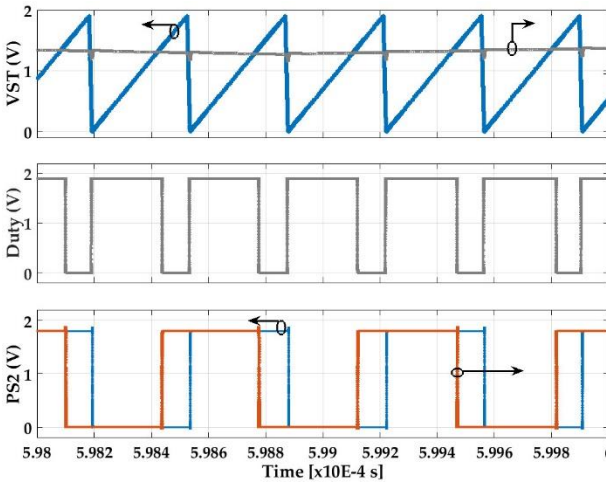


**(b)**

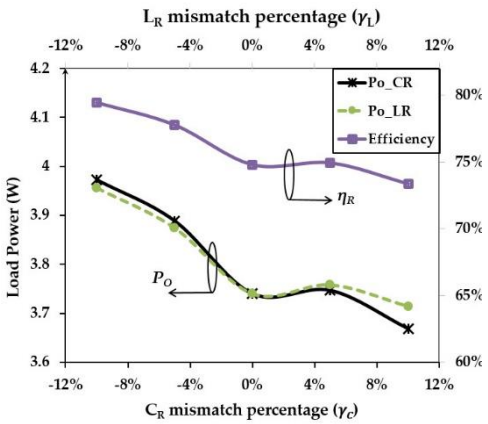


**(c)**

**Figure 4.16** Real-time chip design results: **(a)** tuned point steady-state waveforms of $V_{ac}$, $V_{oc}$ and $V_{PD}$; **(b)** the corresponding duty-cycle generated and driving signals for DAB circuit; **(c)** output power versus variations in $C_R$ and $L_R$ as well as the WPT receiver efficiency $\eta_R$ based on real-time simulated chip implementation.

## 4.3.4 System Design Consideration—Performance Discussion

The design details and system validation of Q-PLL control for DAB-based automatic tuning in WPT receivers shows a superior performance in terms of wide tunability and flexibility. However, the different performance metrics need to be discussed in this section.

### *4.3.4.1 Efficiency and Quality Factor*

The analytical expression for the mistuning effect on the RMS delivered power in Equation (3.16), assumed an ideal circuit with loss-free components including the gyrator-based synthesized inductance. In practice, the losses related to circuit components – such as coils, capacitors, switch-mode DAB, rectifier and any other circuit in the power path– have a significant effect on the quality factor of the resonant tank and, in turn, upon the WPT link efficiency. The loss analysis and efficiency evaluation including most of non-idealities in the receiver circuit has been previously discussed in [3]. The quality factor as a definition– the ratio of stored energy to the lost energy – is a valid implicit indication for the efficiency of a circuit. Referred to our parallel-compensated WPT receiver, we recall the power transfer link efficiency for a fully-tuned receiver circuit can be given in terms of the quality factor as [4]:

$$\eta_{SP} = \frac{k^2 Q_T Q_{RL-P}}{1 + k^2 Q_T Q_{RL-P}} \left(1 - \frac{Q_{RL-P}}{Q_R}\right) \tag{4.7}$$

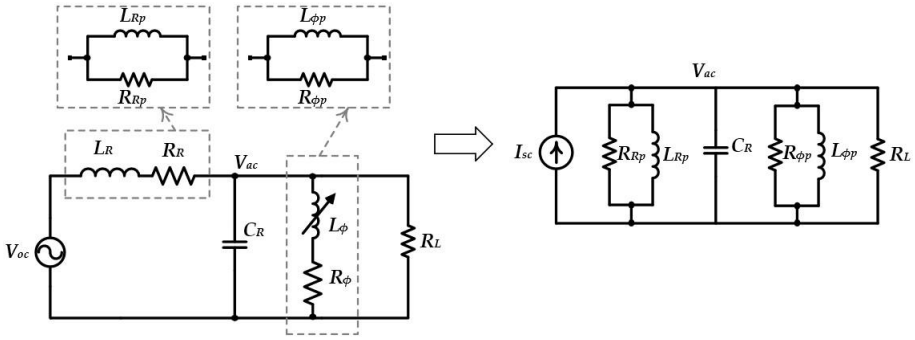


**Figure 4.17** Receiver circuit with parasitic resistances included and the Norton equivalent of circuit.

where $Q_T$ is the transmitter coil's quality factor, $Q_{RL\text{-}P}$ is the quality factor of the receiver circuit as given in (3), $Q_R$ is the quality factor of the receiver coil and $k$ is the coupling factor between transmitter and receiver coils. The total efficiency given in Equation (4.7) is only given to highlight how other components losses would affect the power transfer efficiency. In order to investigate the effect of the gyrator losses, the receiver circuit is analyzed from the perspective of quality factor using the model shown in Figure 4.17. In this model, we include the receiver

coil series resistance $R_R$, the load resistance $R_L$, and the gyrator losses modeled as a resistance $R_\varphi$ in series with the synthesized inductance $L_\varphi$. To facilitate the analysis, the circuit can be converted to the Norton equivalent as shown in Figure 4.17, where $L_{\varphi p}$, $L_{Rp}$, $R_{Rp}$ and $R_{\varphi p}$ are given by:

$$R_{\varphi p} = (1 + Q_\varphi^2)R_\varphi \cong Q_\varphi^2 R_\varphi \tag{4.8}$$

$$L_{\varphi p} \cong L_\varphi \tag{4.9}$$

$$R_{Rp} = (1 + Q_R^2)R_R \cong Q_R^2 R_R \tag{4.10}$$

$$L_{Rp} \cong L_R \tag{4.11}$$

where ($L_{Rp}$, $R_{Rp}$) and ($L_{\varphi p}$, $R_{\varphi p}$) are the equivalent values of ($L_R$, $R_R$) and ($L_\varphi$, $R_\varphi$) $R_R$ and $R_\varphi$ after converting the series networks ($L_R$, $R_R$) and ($L_\varphi$, $R_\varphi$) to parallel networks, while $Q_R$ and $Q_\varphi$ are the quality factors of $L_R$ and $L_\varphi$ respectively. At fully-tuned state, the resonant voltage of the circuit in Figure 4.17 can be given as:

$$V_{ac} = -jQ_{RL-P}\frac{1}{\left(1 + {R_L}/{R_{Rp}} + {R_L}/{R_{\varphi p}}\right)}V_{oc} = -jQ_{Rx}V_{oc} \tag{4.12}$$

Equation (4.12) develops a new term $Q_{Rx}$ as the total quality factor of the receiver tank, which contains the losses of $L_R$ and $L_\varphi$. A similar term could be developed to study the effect of $C_R$ series resistance. It is worth to mention that the losses of the DAB gyrator have been represented as a series resistance $R_\varphi$ while indeed it represents the total energy loss due to switching and conduction loss simultaneously.

In order to maintain a very high $Q_{Rx}$, the DAB gyrator circuit has to be optimized for high efficiency operation. Loss evaluation for AC-AC DAB topology has been already given in [5], which could be used to accurately optimize the DAB gyrator efficiency. However, deriving equations for power loss in the DAB circuit is not straightforward as the system is complex in nature. The power consumed by the DAB gyrator is a function of switching frequency $f_{DAB}$, which, in turn, has to be much higher than the operating frequency $f_T$. At the same time, the losses are closely dependent on the resonant tank output voltage $V_{ac}$ that in turn is a linear function of $Q_{Rx}$. Consequently, a mathematical modelling for the total efficiency has to be extended while considering the interaction between the DAB parameters and those of the receiver resonant circuit.

#### *4.3.4.2 Comparison with Other Solutions in the Literature*

In comparison with other proposed ideas in the literature for retuning and impedance matching, the aim is to discuss how the proposed gyrator-based adaptive tuning is performing. The main comparison metrics are number of components, tuning mechanism and reliability. A common solution for tuning is to add a switched matrix of reactive components such as capacitors. In [6]─[8], a switch-capacitor matrix is proposed for impedance matching either at the transmitter or receiver side. The proposed work in [6] uses seven capacitors and AC switches. While the total number of seven capacitors and AC switches has been testeds as one example, the solution would be extended to $M$ by $N$ capacitor matrix. This technique is reconfigurable to connect the capacitors in series or parallel with the WPT coil. A digital algorithm has been suggested to search for the matched point. In comparison, our proposed gyrator-based uses a fixed number of components, total of eight AC switches, one inductor and one capacitor. On the other hand, it is not affected by the searching steps for the tuned point. It is already concluded from [7], [8], that for a higher resolution in the searching algorithm, either the number of switch-capacitors has to be increased or the searching steps would increase. In that point, the gyrator-based is more appealing as monotonic wide-range tuner with lower complexity.

On the other hand, an inductance-capacitance-inductance (LCL) network has been proposed as a compensation network at the transmitter side [9]. The LCL compensation offers many advantages such as load independent voltage characteristics and zero-phase-angle which improves the efficiency and reliability of the transmitter inverter. However, a self-tuning at the receiver is still inevitable to avoid the incurred reactive power increase at the transmitter side [6]. Another work in [10] assumes that all the receivers coupled to the transmitter are perfectly tuned and studies the effect of tuning at the transmitter. On the other hand, employing LCL compensation at the receiver side as proposed in [11] and [12] has already reported the sensitivity of the output voltage to variations in the compensation components.

It has been shown that the sensitivity is a function of the quality factor Q, which clearly needs to be designed at low value in order to avoid the losses in the system due to high-Q mistuned receiver. Therefore, a saturable-core magnetic amplifier has been proposed for tuning LCL-compensated receivers which is considered as a bulky solution suitable for high power applications [13]. Similarly, a double-sided inductance-capacitance-capacitance (LCC) compensation has been proposed in [14] to achieve a unity power factor at the transmitter and the receiver. The presented compensation technique has been proposed to offer k-independent and load-independent constant resonance frequency while achieving a zero-voltage-switching at the transmitter driver. Still, the proposed technique has not been introduced in the context of

tuning the mismatch due to component variation or interference that would occur from external conducting devices. Therefore, the proposal of a gyrator-based adaptive tuning shows its validity toward an autonomous tuning in multiple receivers WPT system.

### *4.3.4.3 Design Oriented Characterization*

PI controllers are widely used for controlling power converter targeting zero steady-state error unless advanced dynamic performance is required. The proposed closed-loop Q-PLL control has been stabilized using a PI controller by ensuring a zero steady-state error in the quadrature phase difference between $V_{ac}$ and $V_{oc}$. To ensure a stable dynamic tuning control action, a simplified system dynamics are assumed in which the simplified block diagram of the system is shown in Figure 4.18. Such simplification tends to limit the analyzed system variables by interpreting the gyrator as a linear inductance synthesizer $L_{\varphi}$ that is function of the control output $\varphi$. However, the system involves multiple correlated parameters, namely, PI zero frequency $f_z$, receiver operating frequency $f_T$, and PWM switching frequency $f_{DAB}$, LPF crossover frequency $f_{LPF}$, $V_{ref}$, resonant tank parameters ($L_R$, $C_R$, $R_L$), DAB parameters ($L_{DAB}$, $C_{DAB}$), PWM ramp amplitude $V_m$, all which affect the quantitative interplay between the different dynamics of the system. Consequently, the system can exhibit different kinds of instabilities in complex dynamic cases such as slow-scale instabilities (SSI), fast-scale instabilities (FSI) – associated to period-doubling, bifurcation and chaotic regimes [15]. Such behavior has been already investigated in [16].

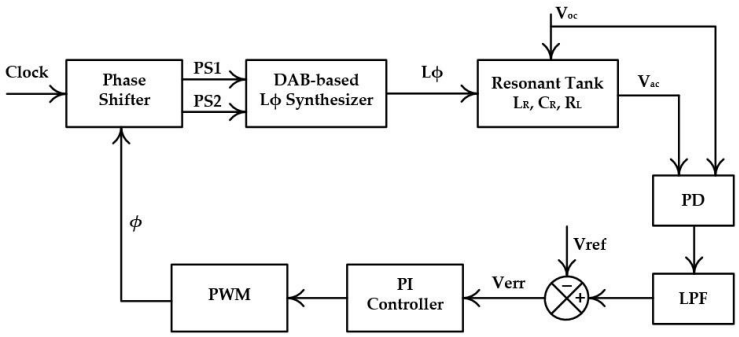


**Figure 4.18** Simplified block diagram for the closed-loop control.

Such kinds of instabilities have been found and characterized for our proposed control. A design-oriented characterization of the system dynamics requires obtaining transient performance under different small- or large-signal excitation for representative cases of the parameter space. Figure 4.19 shows the system response where $K_p$=1.5 and $f_z$ has been shifted from deliberately from 66.7 kHz to 142.8 kHz. It is clear that once $f_z$ has been pushed toward the tank operation frequency $f_T$, the system has moved from period-1 stability region toward SSI

region. Moreover, the system tends to show a FSI instabilities for high $K_p$ values such as that shown in Figure 4.20 at $K_p$=5.5 and $f_z$=66.7 kHz.

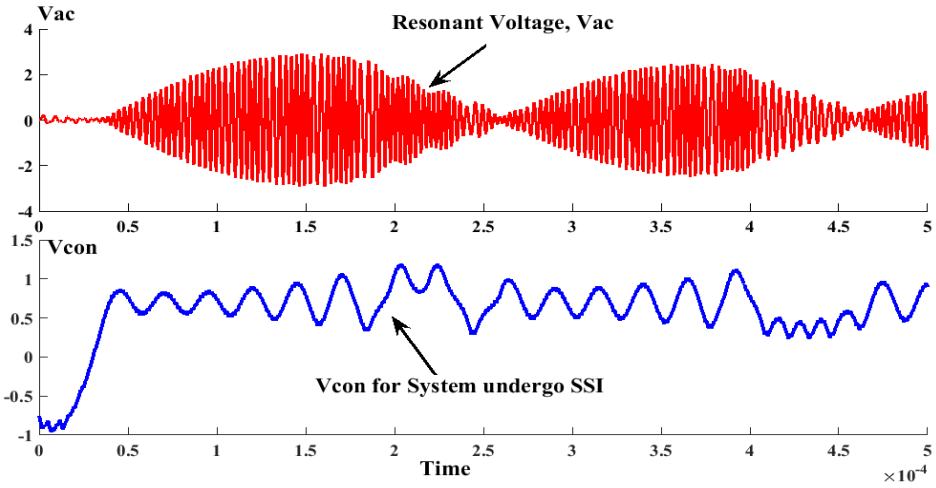


**Figure 4.19** System SSI at $K_p$=1.5 and $f_z$=142.8 kHz.

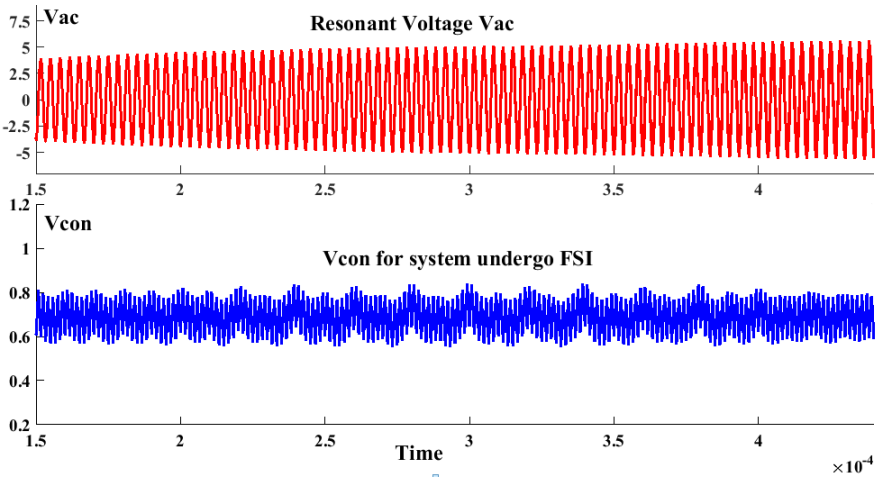


**Figure 4.20** System FSI at $K_p$=5.5 and $f_z$=66.7 kHz.

It is thus possible to design the system at a stable point; however, such design may shift due to plant and controller parameter deviations and take different dynamic routes to other instability regions. The possible routes from a stable starting point can be defined provided that the initial and final states of the system are well defined [15]. Therefore, small-signal average model for the DAB as a reactive element synthesizer is required to facilitate the task of designing a robust controller. Nonetheless, characterizing the full dynamic behavior of the system yet requires an accurate exploration for all the system parameters. This would lead to a more complex but comprehensive bifurcation maps. To limit the scope of this study, a one-dimensional design space for our system has been characterized by performing a parametric

sweep over a space of ($K_p$, $f_z$) as shown in Figure 4.21. As depicted, starting from our target design period-1 point of (1.6, 66.7 kHz), the system my take different dynamic behaviors that end up in either SSI or FSI regions.

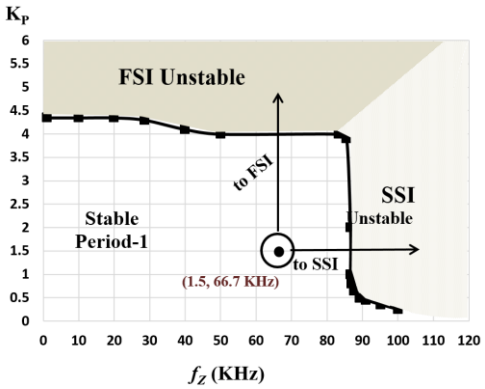


**Figure 4.21** Characterization of stability boundaries over the space ($K_p$, $f_z$).

### *4.3.4.4 Complexity and Cost*

To this point, the proposal of switch-mode gyrator-based variable reactive element synthesizer is potentially promising for WPT. As revealed in the literature, the WPT has extra cost compared to conventional wired systems in terms of magnetically coupled coils and the power electronics circuitry for power management [17], [18]. In this regard, the added complexity of the dynamic tuning or even adaptive impedance matching techniques need to be evaluated in terms of how much power is retrieved compared to how many components would be added to the system.

Clearly the DAB switch-mode gyrator has a unique advantage as a natural gyrator which saves the effort paid for designing a sophisticated closed-loop control to force the gyration behavior. However, it comes with larger number of components, which adds to the cost, and size of the system. Yet, a combined bidirectional switch module is not available commercially. This means that for implementation of the DAB converter using two-quadrant switches, a total number of sixteen MOSFETs is required. Nevertheless, the DAB gyrator-based approach is still comparable to other solutions in [6], [8] and [19] where capacitor bank is switched on or off by means of switch network for adaptive tuning.

## 4.4 Conclusions

The DAB converter utilized as switch-mode gyrator has been used for variable inductance synthesis in WPT receiver. In this chapter we have proposed two control approaches in order to achieve self-tuning operation in parallel-compensated receivers. The first control technique uses dual-loop approach where the first coarse-tuning loop tracks the maximum peak voltage of the resonant tank voltage. On the other hand, the fine-tuning loop tracks the phase difference relations between the induced voltage in the receiver coil and the resonant tank voltage. The verification results have shown that there is a trade-off between the accuracy and transient time of the control. Consequently, an alternative linear control has been proposed, this time it is based on the quadrature phase difference between the receiver coil's induced voltage $V_{oc}$ and the resonant tank voltage $V_{ac}$. The wide tuning range of the DAB-based self-tuned WPT receiver has been verified at different mismatch percentages in the coil inductance $L_R$ or the compensation capacitor $C_R$. Moreover, the chip implementation for the DAB converter and the quadrature PLL control has been discussed carried out by the XFAB 0.18µm technology.

The system performance and design consideration has been discussed as compared to other solutions in the literature. It has shown that despite the complexity and number of switches used in the DAB converter, it is still considered as a reasonable solution if we consider the reliability and wide tuning range of the solution.

## 4.5 References

[1] Hengsi Qin and J. W. Kimball, “Ac-ac dual active bridge converter for solid state transformer,” in *2009 IEEE Energy Conversion Congress and Exposition*, 2009, pp. 3039–3044.

[2] M. Saad, E. Bou-Balust, and E. Alarcon, “Switch-mode gyrator-based emulated inductor enabling self-tunability in WPT receivers,” in *2017 IEEE International Symposium on Circuits and Systems (ISCAS)*, 2017, pp. 1–4.

[3] G. Di Capua, N. Femia, and G. Lisi, “Impact of losses and mismatches on power and efficiency of Wireless Power Transfer Systems with controlled secondary-side rectifier,” *Integr. VLSI J.*, vol. 55, pp. 384–392, Sep. 2016.

[4] R. F. Xue, K. W. Cheng, and M. Je, “High-efficiency wireless power transfer for biomedical implants by optimal resonant load transformation,” *IEEE Trans. Circuits Syst. I Regul. Pap.*, vol. 60, no. 4, pp. 867–874, Apr. 2013.

[5] H. Qin and J. W. Kimball, “A comparative efficiency study of silicon-based solid state transformers,” in *2010 IEEE Energy Conversion Congress and Exposition*, 2010, pp. 1458–1463.

[6] Y. Lim, H. Tang, S. Lim, and J. Park, “An adaptive impedance-matching network based on a novel capacitor matrix for wireless power transfer,” *IEEE Trans. Power Electron.*, vol. 29, no. 8, pp. 4403–4413, Aug. 2014.

[7] W.-S. Lee, H.-L. Lee, K.-S. Oh, and J.-W. Yu, “Switchable Distance-Based Impedance Matching Networks For a Tunable HF System,” *Prog. Electromagn. Res.*, vol. 128, no. May, pp. 19–34, 2012.

[8] T. Duong and J.-W. Lee, “A Dynamically Adaptable Impedance-Matching System for Midrange Wireless Power Transfer with Misalignment,” *Energies*, vol. 8, no. 8, pp. 7593–7617, Jul. 2015.

[9] C. Y. Huang, J. E. James, and G. A. Covic, “Design considerations for variable coupling lumped coil systems,” *IEEE Trans. Power Electron.*, vol. 30, no. 2, pp. 680–689, Feb. 2015.

[10] M. Kissin, Chang-Yu Huang, G. A. Covic, and J. T. Boys, “Detection of the tuned point of a fixed-frequency LCL resonant power supply,” *IEEE Trans. Power Electron.*, vol. 24, no. 4, pp. 1140–1143, Apr. 2009.

[11] N. a. Keeling, G. a. Covic, and J. T. Boys, “A unity-power-factor IPT pickup for high-power applications,” *IEEE Trans. Ind. Electron.*, vol. 57, no. 2, pp. 744–751, 2010.

[12] J.-U. W. Hsu and A. P. Hu, “Determining the variable inductance range for an LCL wireless power pick-up,” in *2007 IEEE Conference on Electron Devices and Solid-State Circuits*, 2007, pp. 489–492.

[13] J.-U. W. Hsu, A. P. Hu, and A. Swain, “A Wireless Power Pickup Based on Directional Tuning Control of Magnetic Amplifier,” *IEEE Trans. Ind. Electron.*, vol. 56, no. 7, pp. 2771–2781, Jul. 2009.

[14] S. Li, W. Li, J. Deng, T. D. Nguyen, and C. C. Mi, “A Double-Sided LCC Compensation Network and Its Tuning Method for Wireless Power Transfer,” *IEEE Trans. Veh. Technol.*, vol. 64, no. 6, pp. 2261–2273, Jun. 2015.

[15] E. Rodriguez Vilamitjana, Chaos in switching converters for power management. Springer, 2014.

[16] M. Saad, H. Martinéz-García, P. Alou, and E. Alarcón, "A PLL Control for Self-Tuning of Parallel Wireless Power Transfer Receivers Utilizing Switch-Mode Gyrator Emulated Inductors," in *2017 19th European Conference on Power Electronics and Applications*, EPE 2017 ECCE Europe, p. 1-10.

[17] A. Abdolkhani, "Fundamentals of Inductively Coupled Wireless Power Transfer Systems," in Wireless Power Transfer - Fundamentals and Technologies, InTech, 2016, pp. 3–26.

[18] S. Li and C. C. Mi, "Wireless power transfer for electric vehicle applications," *IEEE J. Emerg. Sel. Top. Power Electron.*, vol. 3, no. 1, pp. 4–17, Mar. 2015.

[19] G. A. Covic, J. T. Boys, A. M. W. Tam, and J. C. H. Peng, "Self tuning pick-ups for inductive power transfer," in *Power Electronics Specialists Conference*, PESC 2008. IEEE, 2008, pp. 3489–3494.

Chapter

# 5

# Phase-Controlled Converters for Active Tuning in WPT Receivers

In the previous chapters, we have explored and discussed, in detail, the feasibility of gyrator-based approach for emulating variable reactive elements for the sake of automatic tuning in WPT receivers. Gyrators have shown a superior performance in which the synthesis of variable reactive elements is a straightforward transformation between duality of components, *i.e.* inductive reactance from capacitive reactance and vice versa. This approach of variable reactive elements synthesis is based on average behavior where the relation between average voltage and current constitutes the same for either an inductance or capacitance. In fact, as we shown previously, the gyrator approach implies a complexity either in the topology structure or control circuitry.

The motivation of this chapter is to develop novel techniques for active tuning of WPT receivers by more compact circuit topologies where the same design goals are met while maintaining simplicity of the topology. In this chapter, a compact adaptive front-end for WPT receiver that combines dual functionality by reflecting a controlled reactance for tuning purpose as well as transferring the energy to the output. In other words, the proposed circuit offers an adaptive tuning while regulates the AC voltage to charge an output energy reservoir.

## 5.1 State of the art of WPT Receivers for Battery Charging

Developing an automatic frequency tuning for WPT receivers has always been a challenge due to the trade-off between the size and efficiency of every solution. While the size, and accordingly the cost, is dependent on circuit and control complexity, the efficiency of the automatic tuning approach becomes crucial as one of the most important metrics of a WPT system. The more complexity of the automatic tuning approach, the more size it consumes. On

the other hand, adding more components will lead to more losses in the circuit and a considerable reduction in the total efficiency of the WPT link.

Following the same objective of automatic tuning of WPT receiver, diverse solutions in the literature have been introduced. Among the wide variety of presented solutions, we limit our exploration to the most significant proposals in terms of size and efficiency. In one idea, the authors in [1] proposed a frequency control method to regulate the output power of a WPT link against variations in load, coupling and circuit parameters. Their approach depends on adding a soft-switched variable capacitor at the transmitter side to control the frequency of operation by tracking the output power of the system. Despite the fact that this approach requires only two capacitors and two switches to achieve a variable controlled capacitance, the method depends mainly on controlling one parameter at the transmitter side (which is the operating frequency) based on information sensed at the receiver side. Most of the time, in order to send information about the loading condition at the receiver side, a communication link is required. On the other hand, this solution is still limited to single receiver applications because frequency control is not practical for multiple receiver applications. The same method of controlling the operating frequency at the transmitter side has been proposed in [2], however, the authors haven't shown whether the receiver is resonant or non-resonant and how to adaptively tune the receiver resonant tank in accordance to the variation in the WPT link frequency.

Other research ideas take advantage of advanced magnetics structures such as the work proposed in [3] where a saturable reactor is used as a variable dc-feed inductance in class E inverter used for driving the transmitter coil. In such approach, the inductance of the saturable reactor is controlled via a DC current, hence a tuning at the transmitter side is achieved by means of closed-loop control. In the proposed work, no feedback control has been suggested, however the basic idea of a variable inductance saturable reactor based tunable class E inverter is properly verified. Similar to this approach, the authors in [4] presented a directional power flow control method where a magnetic amplifier is used as a variable inductance in LCL compensation technique. This time, the tuning has been achieved at the receiver side to retune against the possible variations of load and coupling conditions between the transmitter and the receiver coils. According to the fact that the tuning process is achieved at the receiver side which helps in leveraging the approach for multiple receiver WPT systems, however, the size of the magnetic amplifier is a big concern specifically for consumer electronics applications.

Alternatively, a power flow control method for moving sensors has been presented in [5] to adaptively match a wide range of load variation. The presented work, shown in Figure 5.1(a), uses a soft-switched variable inductance to detune the receiver resonant tank according to the loading condition. Similar to the principles of phase-controlled reactors that are used for reactive power compensation in flexible AC transmission systems (FACTS) [6], the phase delay

in which an inductor is being engaged to the AC source could be used as a control parameter for achieving a variable inductive reactance. In [5], the variable inductance has been used as a detuning element to match the power needs of a variable load. Consequently, the presented idea assumes a fully-tuned receiver tank designed at the maximum power, then the receiver tank is detuned at lower loading conditions. The same idea has been employed with a different implementation in [7], however, this time the proposed approach has been presented for self-tuning WPT receivers. As shown in Figure 5.1(b), by applying the phase-controlled self-tuning approach, a high-Q WPT receiver tank becomes applicable without limitations of system sensitivity to the variations at the load, the WPT link frequency, or the circuit components values. Unfortunately, an additional rectifier and power converters are inevitably required for regulating the receiver tank energy such that the output load requirements are met.

The fact of using a single inductor to synthesize a variable inductive reactance controlled by a phase-delay is significant in terms of size and low complexity, which in essence means better efficiency. It is important to revisit the fundamentals of phase-controlled reactors used in FACTS in order to employ it in a more compact multifunctional solution for WPT receivers toward an ultimate goal of an adaptive miniaturized front-end.

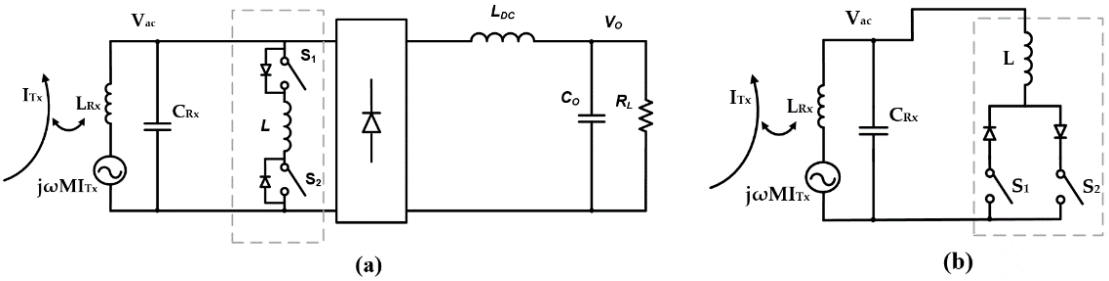


**Figure 5.1** Two phase-controlled inductor WPT receivers in [5] and [7] respectively.

## 5.2 Fundamentals of Variable Phase-controlled Reactance

A topic of wide interest in FACTS system is how to compensate for reactive power in high-voltage AC power systems due to the loading effect of a load with complex impedance. The static reactive power compensators, also known as "static *var* compensators", have been evolved as a significant solution. It mainly depends on connecting, in either shunt or series, a variable reactor to consume the reactive power generated by a capacitive load. On the other hand, a capacitor bank could be used for generating the reactive power to balance the effect of an inductive load added to the power system. In both cases, the goal is to bring the system near a unity power factor condition, which improves the system efficiency and reliability.

The static *var* compensators uses modern semiconductor switches to switch either in or out a reactor (or a capacitor) to the system. Consequently, two different types of static *var* compensators have emerged, namely, "thyristor-switched reactors/inductors" and "thyristor-switched capacitors". It is important, then, to refer that the term "thyristor" has been conceptually used because the early presentation of these techniques has been realized by means of high power thyristors and later have been replaced by other semiconductor devices with superior switching characteristics such as power MOSFETs and IGBTs. Therefore, throughout this section the thyristors will be depicted as a generic switch that is supposed to be realized with modern semiconductor devices such as MOSFETs.

### 5.2.1 Phase-Controlled Inductive Reactance

The fundamental circuit of a phase-controlled inductor is shown in Figure 5.2. This circuit is one of the elementary power electronics circuits used where it has been used for static *var* compensation in power systems. It comprises a constant physical inductor $L$ and bidirectional switch. The implementation of the bidirectional switch, however, has been principally introduced based on thyristor valves few decades ago, that's why it is well known in flexible AC transmission systems as "thyristor controlled reactors". However, the bidirectional switch shown in Figure 5.2 is realized by the configuration of two antiparallel diode-switch ($S_1$, $S_2$) structure.

The operation, as depicted by the waveforms in Figure 5.2, is based on controlling the current through the inductor $i_L(\alpha)$ from zero to the maximum by controlling the delay-angle ($\alpha$). Consequently the maximum allowable current through the inductor is achieved while the bidirectional switch is always ON, *i.e.* $\alpha = \pi/2$, while the current starts to decrease the more we increase the value of $\alpha$ from $\pi/2$ up to $\pi$ [6]. Consequently, it becomes evident that varying the delay-angle results in a variable current magnitude through the inductor, which is effectively would be seen by the circuit as a variation in the effective reactance of $L$. This relation can be explained by considering the voltage and current waveforms in Figure 5.2, if the applied voltage $v_{ac}$ is equal to $V_P \sin \omega t$, then the current through the inductor is obtained as:

$$i_L(t) = \frac{1}{L}\int_{\alpha}^{\omega t} V_P sin(\omega t)dt = \frac{V_P}{X_L}(\cos\alpha - \cos\omega t) \qquad (5.1)$$

where $X_L$ is the reactance of $L$ and $\alpha$ is the delay-angle where $\pi/2 \leq \alpha \leq \pi$. The expression of Equation (5.1) is however valid only for the range $\alpha \leq \omega t \leq \pi - \alpha$. The expression in Equation (5.1) is valid for positive half cycles while it will be of reversed polarity in negative half cycles and the sign of Equation (5.1) will be reversed accordingly. The effect of the delay-angle on the

effective impedance is obtained by first noting that the current is discontinuous for $\alpha \geq \pi/2$, consequently the fundamental inductor current can be given by Fourier analysis, and then the magnitude of the fundamental current becomes:

$$I_{LF}(\alpha) = \frac{V_P}{X_L}(2 - \frac{2}{\pi}\alpha - \frac{1}{\pi}\sin 2\alpha) \tag{5.2}$$

The effective fundamental inductance in the case of Equation (5.2) is readily obtained function of the delay-angle as:

$$L_\alpha = L \cdot \frac{\pi}{(2\pi - 2\alpha - \sin 2\alpha)} \tag{5.3}$$

As we note, a new fundamental variable inductance is obtained as function of α as concluded from Equation (5.3), however, it is important to note that the behavior phase-controlled inductance has been analyzed assuming that the effects of current harmonics is negligible.

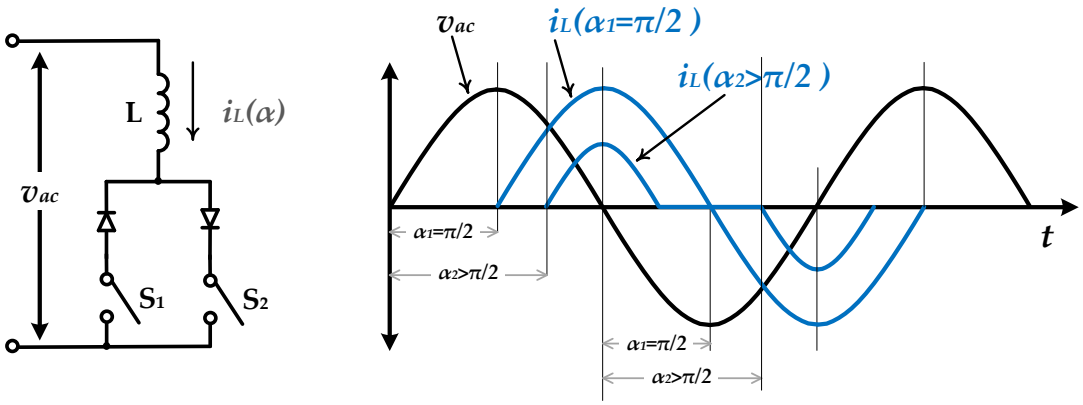


**Figure 5.2** Elementary phase-controlled inductor and its voltage and current waveforms.

## 5.2.2 Phase-Controlled Series Capacitive Reactance

Similar to the shunt type of phase-controlled inductors, a series variable reactive element is realized using a capacitor. As shown in Figure 5.3, the phase-controlled series capacitor is composed of a fixed capacitor accompanied with a bidirectional switch connected in parallel. At a given current, the capacitor voltage $v_c$ is controlled by adjusting the phase-angle of switching the AC switch relative to the current $i_c$ in each half cycle. In contrast to the phase-controlled inductor, the turn-off delay of the switch is controlled in this case. When the turn-off phase delay of the parallel switch is $\gamma=\pi/2$, the voltage across the capacitor $v_c(\gamma)$ is the same as a

conventional capacitor. If the turn-off delay of the switch is increased above $\pi/2$, the voltage across the capacitor becomes variable and can be given function of the delay angle as [6]:

$$v_C(t) = \frac{1}{C}\int_{\gamma}^{\omega t} I_P sin(\omega t)dt = I_P X_C(\cos\gamma - \cos\omega t) \tag{5.4}$$

where the series current is assumed equal to $I_P\, sin(\omega t)$, $X_C$ is the capacitor reactance, and $\gamma$ is the phase-angle delay ($\pi/2 \leq \gamma \leq \pi$). It is evident from Equation (5.4) that the capacitor's voltage magnitude can be controlled by varying the turn-off delay angle $\gamma$. In a similar way to the variable equivalent inductance in Equation (5.3), the equivalent reactance of the phase-controlled series capacitor is obtained by deriving the fundamental capacitor voltage $V_{CF}(\gamma)$. Consequently, the equivalent variable capacitance is obtained by [6]:

$$C_\gamma = C \cdot \frac{\pi}{(2\pi - 2\gamma - \sin 2\gamma)} \tag{5.5}$$

The phase-controlled series capacitor can be used as a variable reactive component or it can be used alternatively in combination with the phase-controlled inductor to realize a variable impedance. While different combinations already exist with different characteristics and features, the main concept of phase-controlled *var* generation is similarly applied.

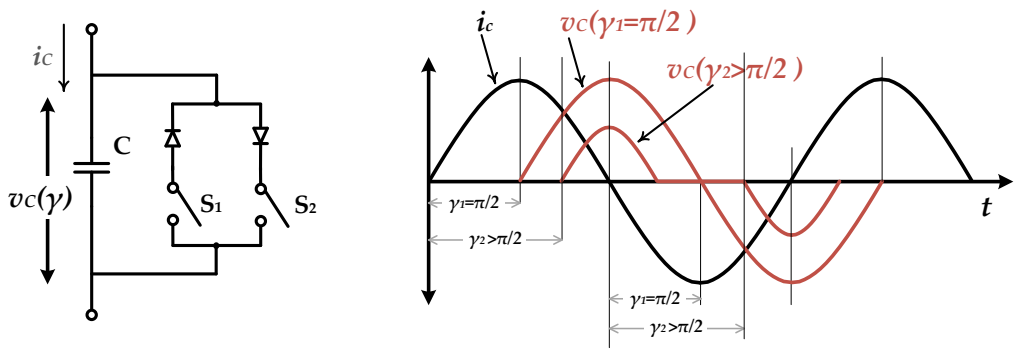


**Figure 5.3** Elementary phase-controlled series capacitors and its voltage and current waveforms.

## 5.3 Phase-Controlled Switched Inductor Converter

It is possible to incorporate the concept of variable inductive reactance, based on the concept of phase-switching explained in the previous section, not only for synthesizing a variable reactance but also for rectification or even more advanced functionality of rectification and regulation. The basic idea is to avoid using separate circuits for achieving the multiple functionalities, by using a single inductor that is switched with a phase-delay with respect to the ac input. The proposed scheme applies a phase-delay with respect to the AC input during a first

time interval in which the inductor is energized from the input AC source. Then, the energy is rectified to the output during a second time interval, following the first time interval, by connecting the inductor to the output energy buffer. This sequence of operation repeats at every half cycle, either positive or negative half cycles. This means that the proposed converter has a switching rate that is double that of the input AC source.

Figure 5.4 shows the schematic diagram of the phase-controlled switched-inductor converter. It comprises a single inductor $L_{DC}$ that is switched via four switches ($S_{C1}$, $S_{C2}$, $S_{D1}$, and $S_{D2}$) and an output capacitor $C_{out}$ that represents a battery or energy reservoir. Nearly the same circuit structure has been presented in [8] where the converter has given the name "switched-inductor" as an efficient rectifier for low-power energy harvesting applications. Alternatively, the proposed converter here adapts the same circuit topology to incorporate a complex impedance synthesis by relatively switching the inductor $L_{DC}$ in accordance to an adaptive phase-delay.

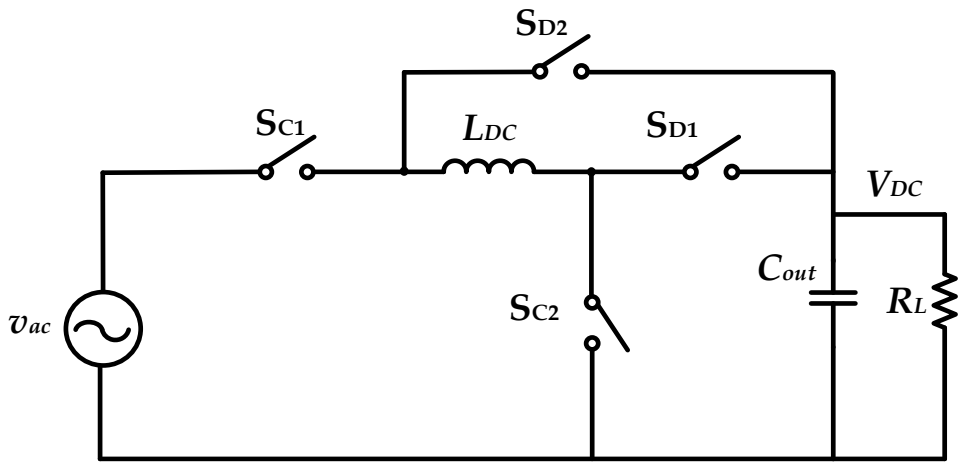


**Figure 5.4** Schematic diagram of phase-controlled switched-inductor converter.

## 5.3.1 Circuit Operation

The detailed operation modes can be described with the help of the depiction in Figure 5.5, where the converter cell is excited by a sinusoidal input source having an amplitude $V_P$ and frequency $f_{in}$. During the positive half cycle, all the switches are opened during a time interval $t_\alpha$ that is synchronized with zero crossing of the positive cycle. At the end of $t_\alpha$, switches $S_{C1}$ and $S_{C2}$ are closed to charge the inductor from the AC source with a current in the direction illustrated in Figure 5.5(a). This interval is called the positive charging interval $t_{cp}$. The inductor current $i_L(t_{cp})$ is a function of the AC input voltage $V_P \sin(2\pi f_{in} t)$, given as:

$$i_L(t_{cp}) = \frac{1}{L_{DC}} \int_{t_\alpha}^{t} V_P sin(2\pi f_{in} t) dt \tag{5.6}$$

The positive charging interval $t_{cp}$ finishes once the AC input voltage reach zero, *i.e.* at the end of the positive half cycle, then the positive discharging interval $t_{dp}$. As shown in Figure 5.5(b), the positive discharging interval starts by opening switch $S_{C2}$ and closing switch $S_{D1}$. The inductor $L_{DC}$ is now connected between the ac input source and the output buffer $C_{out}$, thus, the energy stored in $L_{DC}$ is released to the output and $i_L$ is drained to zero. During this interval $t_{dp}$, the inductor current $i_L(t_{dp})$ is a function of the input ac voltage $V_P\ sin(2\pi f_{in} t)$ and the output dc voltage $V_{DC}$ as follows:

$$i_L(t_{dp}) = \frac{1}{L_{DC}} \int_{\pi}^{t} [V_P sin(2\pi f_{in} t) - V_{DC}] dt \tag{5.7}$$

In the negative half cycle, the inductor is not allowed to charge unless the same delay interval $t_\alpha$ is already elapsed. Then, the negative charging cycle $t_{cn}$ starts by closing switches $S_{C1}$ and $S_{C2}$ to allow a charging current to pass through the inductor $L_{DC}$ in the opposite direction. This interval is illustrated in Figure 5.5(c), in which the current $i_L(t_{cn})$ is given by:

$$i_L(t_{cn}) = \frac{1}{L_{DC}} \int_{\pi+t_\alpha}^{t} V_P sin(2\pi f_{in} t) dt \tag{5.8}$$

Similarly, the negative charging interval $t_{cn}$ reaches the end once the negative ac voltage reaches zero, which also corresponds to a negative $i_L(t_{cn})$ peak. Then, the discharging interval $t_{dn}$ starts by opening switch $S_{C1}$ and closing switch $S_{D2}$ as indicated in Figure 5.5(d). This energy stored in $L_{DC}$ is again released to the output buffer $C_{out}$ and $L_{DC}$ becomes fully depleted by the end of this interval. The inductor current $i_L(t_{dn})$ is given by:

$$i_L(t_{dn}) = \frac{1}{L_{DC}} \int_{2\pi+t_\alpha}^{t} -V_{DC}\ dt \tag{5.9}$$

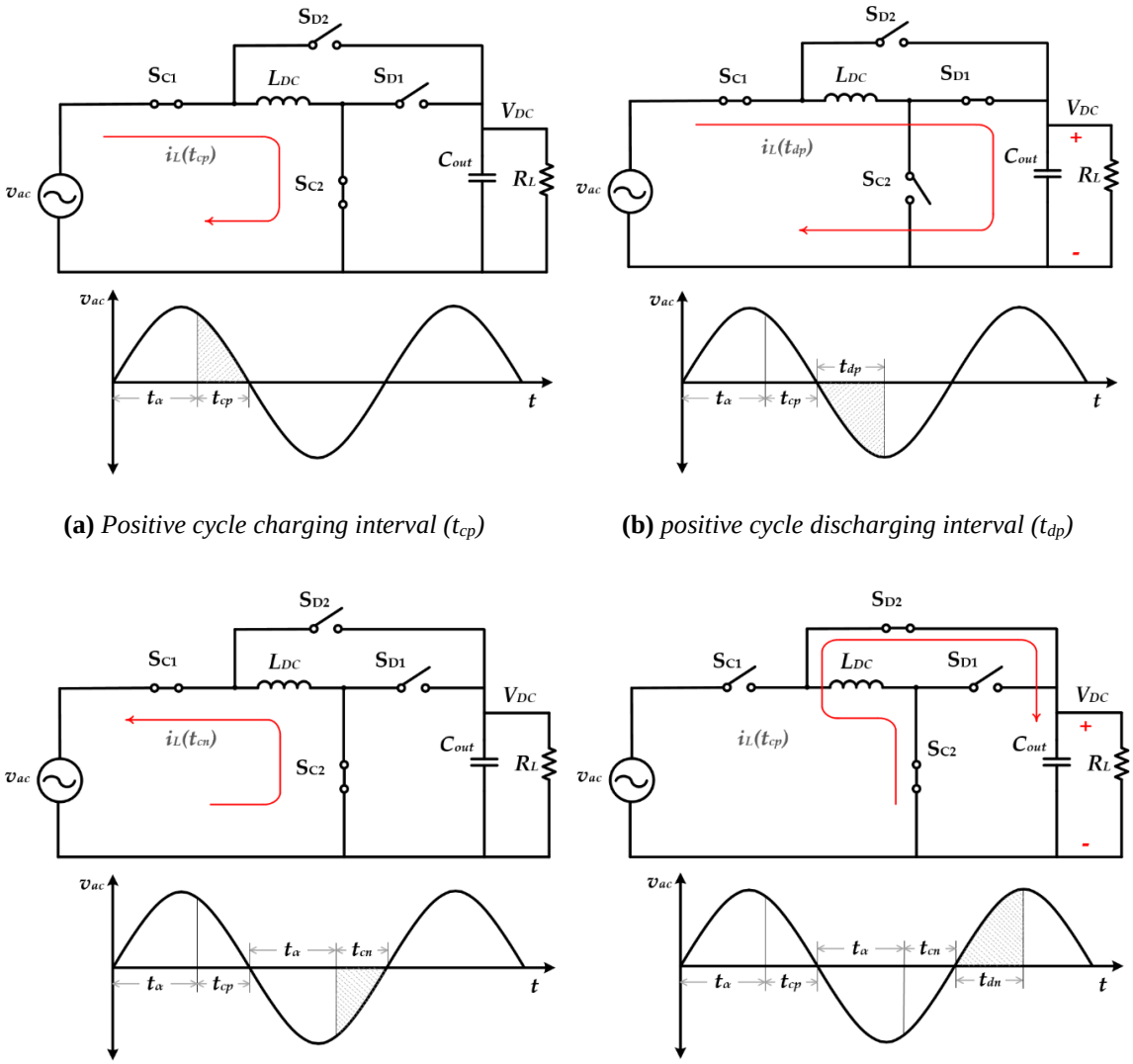


**(a)** *Positive cycle charging interval ($t_{cp}$)*

**(b)** *positive cycle discharging interval ($t_{dp}$)*

**(c)** *Negative cycle charging interval ($t_{cn}$)*

**(d)** *Negative cycle discharging interval ($t_{dn}$)*

**Figure 5.5** Operation modes of phase-controlled switched-inductor converter.

The aforementioned operation modes are repeated every full cycle of the AC input voltage. Figure 5.6 shows the time-domain waveforms of the converter verified by simulation. The parameters used for simulating the converter are: $v_{ac}$ = $10V_{p\text{-}p}$, $f_{in}$ = 200 $kHz$, $L_{DC}$ = 9 $\mu H$, $C_{out}$ = 100 $\mu F$, and $R_L$ = 20 $\Omega$. In Figure 5.6(a), the waveforms are shown at $t_\alpha$ = 1.46 $\mu s$ or 1.83 rad, while Figure 5.6(b) shows the waveforms at $t_\alpha$ = 1.67 $\mu s$ or 2.09 rad.

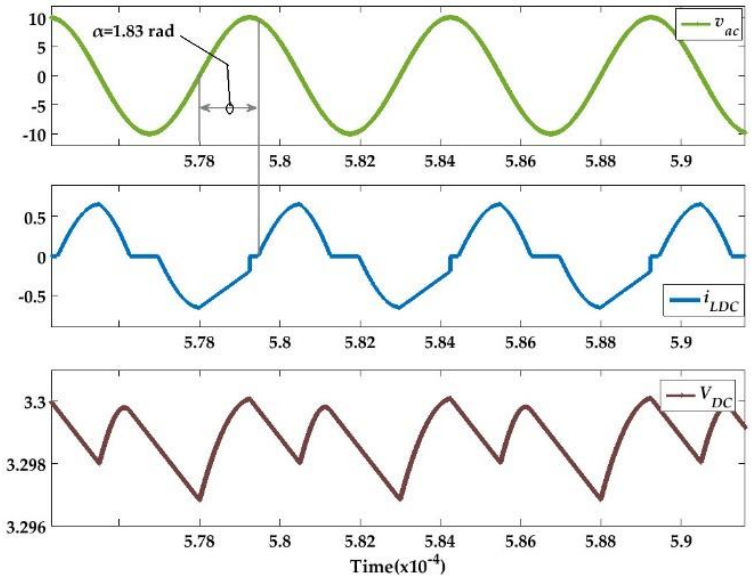


**(a)**

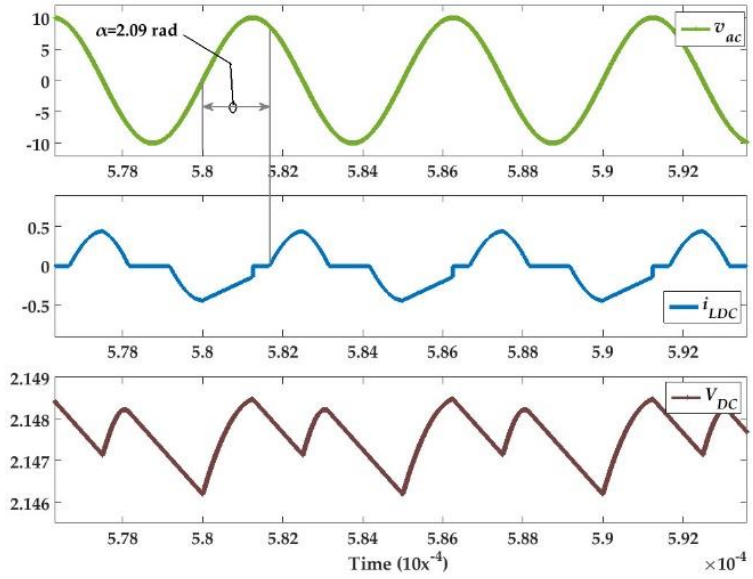


**(b)**

**Figure 5.6** Time-domain waveforms at: **(a)** α=1.83 rad, and **(b)** α=2.09 rad.

## 5.3.2 Circuit Characterization

The operation described in the previous section combines dual functions. First, the applied delay interval implies that the input current always lags the input voltage $v_{ac}$, which creates an equivalent inductance $L_{\alpha}$. This equivalent inductance appears as a reactive load connected between the terminals of the input source $v_{ac}$. Furthermore, the energy delivery to the output during intervals $t_{dp}$ and $t_{dn}$ implies that an equivalent resistance $R_{\alpha}$ is also loading the input source. Consequently, a simplified average model for the converter can be developed as shown

in Figure 5.7. It has been noted that the inductor current $i_{LDC}$ is discontinuous, which means that it constitutes a fundamental component at the fundamental frequency of $v_{ac}$ in addition to harmonics at higher frequencies. Thus, the current $I_{ac}$ shown in Figure 5.7 represents the fundamental component of $i_{LDC}$.

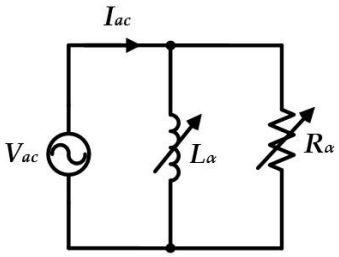


**Figure 5.7** Simplified model for the phase-controlled switched-inductor converter in Figure 5.4.

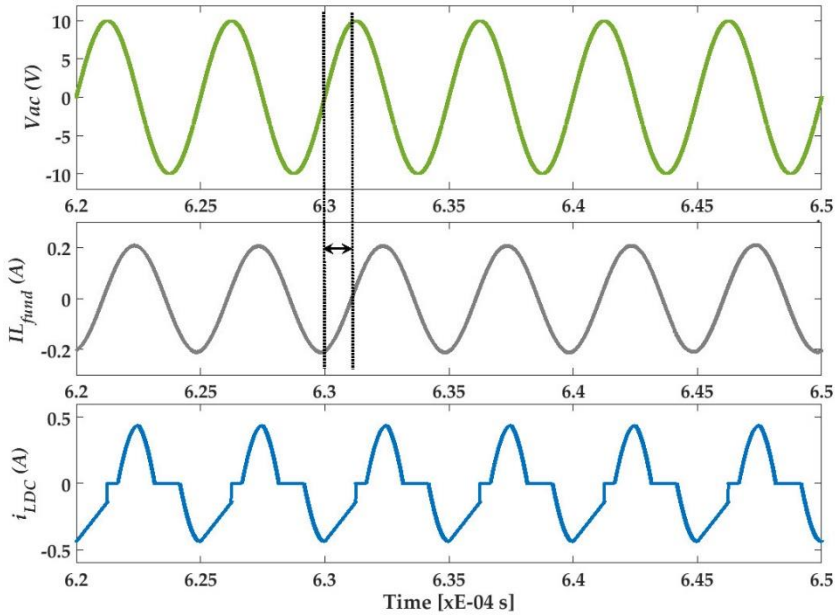


**Figure 5.8** Input current's fundamental component lagging input voltage $v_{ac}$.

The simulation waveforms of the fundamental component of $i_{LDC}$ is shown in Figure 5.8. This current is obtained in simulation by sensing the inductor current and applying the sensed current to a bandpass filter centered at the fundamental frequency of the sinusoidal input $v_{ac}$. It is clear in from Figure 5.8 that the current's fundamental component lags the input voltage by a phase less than 90°. This implies that an equivalent network of inductive-resistive elements is seen by the input source, which is still consistent with the simplified circuit model depicted in Figure 5.7.

Following the model in Figure 5.7, the equivalent inductance $L_\alpha$ and the equivalent resistance $R_\alpha$ are both variable. Clearly, both of them, *i.e.* $L_\alpha$ and $R_\alpha$, are function of the delay interval $\alpha$. Moreover, Equations (5.6) and (5.8) suggest that $L_\alpha$ is also function of $L_{DC}$. Similarly, Equations (5.7) and (5.9) imply that is a function of $R_L$, which is closely affecting $V_{DC}$. In order to obtain an expression for $L_\alpha$ and $R_\alpha$, we have to derive the amplitude of the fundamental component of $L_\alpha$ and $i_{LDC}$. As we have shown for the case of conventional phase-controlled inductors (section 5.2), the step of deriving the fundamental component of the time-domain inductor current $i_{LDC}$ is possible using simple Fourier series calculations. However, developing an expression for the equivalent inductance $L_\alpha$ by deriving the fundamental current of $i_{LDC}$ is no longer straightforward as a result of $V_{DC}$ dependency during the energy rectification interval, as indicated by Equations (5.7) and (5.9). Moreover, with the novel functionality of output energy delivery, an additional $R_\alpha$ is emulated at the input source terminals which is a function of $\alpha$ as well. Otherwise, circuit simulation could be used as means for characterizing the circuit performance in terms of the control parameter $\alpha$. Figure 5.9 shows the inductance ratio ($L_\alpha/L_{DC}$) and resistance ratio ($R_\alpha/R_L$) versus the time-delay $\alpha$ at different $L_{DC}$ values.

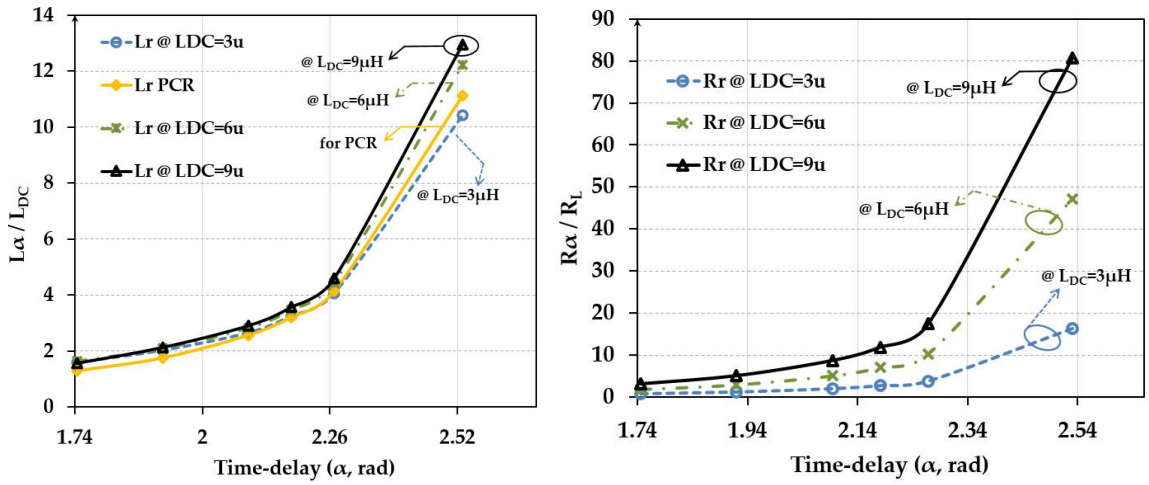


**(a)** **(b)**

**Figure 5.9** Effect of time-delay on inductance ratio and resistance ratio: **(a)** Inductance ratio $L_r$ at $L_{DC}$=3µH, 6µH, 9µH and $L_r$ of conventional PCI, and **(b)** Resistance ratio $R_r$ at $L_{DC}$= 3µH, 6µH and 9µH.

In Figure 5.9, $L_r$ is the ratio between the equivalent emulated inductance $L_\alpha$ and the actual inductance $L_{DC}$, while $R_r$ is the ration between the equivalent resistance $R_\alpha$ and the actual load resistance $R_L$. The curves shown in Figure 5.9(a) is extended for three different values of $L_{DC}$ which would give good insights into how $L_\alpha$ changes as a function of $\alpha$. Compared to the inductance ratio of classical PCI (solid yellow in Figure 5.9(a)), it is evident that the proposed phase-controlled switched-inductor circuit follows the same trend of $L_\alpha$ variation with respect to

$\alpha$. As the time-delay is varied from $0.5\pi$ toward $\pi$, $L_\alpha$ increases monotonically. Consequently, $L_\alpha$ could be varied over a range that starts from $L_{DC}$ up to $10xL_{DC}$ by varying the delay-time from $\alpha = 0.5\pi$ to $\alpha = 0.8\pi$, respectively. Similarly, Figure 5.9(b) illustrates the variation of the AC resistance seen at the input of phase-controlled switched-inductor converter $R_\alpha$ with respect to $\alpha$. We note that, while $R_\alpha$ tends to increase as $\alpha$ increases, it also increases at higher $L_{DC}$ values. This response keep tracks of $i_{LDC}$ which is, undoubtedly, inversely proportional to $L_{DC}$.

## 5.3.3 Active Tuning in WPT Receivers using Switched-Inductor Topology

### *5.3.3.1 Implementation and integration in WPT receivers*

The double functionality of phase-controlled switched-inductor could be employed in WPT receivers in order to achieve active tuning for the receiver resonant tank in addition to voltage rectification. Therefore, the phase-controlled switched-inductor model given in Figure 5.7 can be modified to incorporate the simple model of a parallel-compensated WPT receiver. This would help in co-designing the switched-inductor converter toward an active tuner and rectifier for the WPT receiver. The model is shown in Figure 5.10.

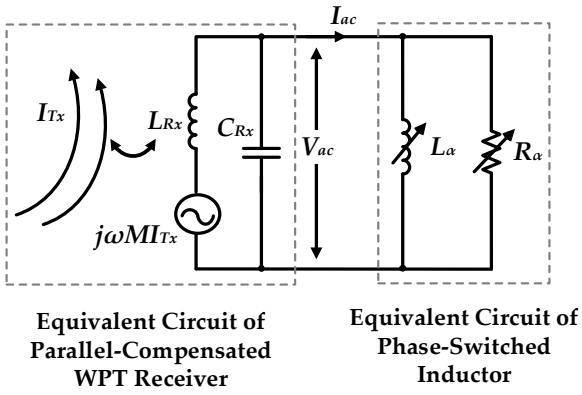


**Figure 5.10** Simple model of a WPT receiver enable by phase-controlled switched-inductor.

As shown in Figure 5.10, the converter is replaced by the variable inductance $L_\alpha$ representing the emulated variable inductance for active tuning and the equivalent ac resistance $R_\alpha$ representing the real power delivery to the output. The resonance frequency of the receiver tank, according to the model in Figure 5.10, is given by:

$$\omega_{Rx}^2 = \frac{L_{Rx} + L_\alpha}{C_{Rx} L_{Rx} L_\alpha} = \frac{1}{C_{Rx} L_{eq}} \tag{5.10}$$

where $\omega_{Rx}$ is the angular resonance frequency of the WPT receiver tank after adding the equivalent impedance of the phase-controlled switched-inductor. It can be seen in Equation (5.10) that a new equivalent inductance $L_{eq}$ appears as a parallel combination of $L_{Rx}$ and $L_{\alpha}$, which implicitly is a function of $\alpha$. It is important to note, however, that Figure 5.9(a) illustrates that the variation of $L_{\alpha}$ is possible in one direction as $\alpha$ increases from 90° and upwards. In order to allow a bidirectional tuning capability, the value of $L_{\alpha}$ for nominal tuned tank has to be designed in the middle of the characteristics curve, *e.g.* at $\alpha = 0.7\pi$.

Figure 5.11 shows a complete WPT parallel-compensated receiver enabled by a phase-controlled switched-inductor. A possible realization for the converter's switches is shown in the figure as well. It has been already noted that switches $S_{C1}$ and $S_{C2}$ must allow current flow in both directions while they are closed, whereas they must be able to block current in both directions while they are open. Thus, switches $S_{C1}$ and $S_{C2}$ have been realized by two series connected back-to-back NMOS transistors to realize a bidirectional four-quadrant switch. With respect to $S_{D1}$ and $S_{D2}$, they have been also realized by a four-quadrant bidirectional switch as shown in Figure 5.11, so they block any conduction path between the input and output while they are opened and the charging intervals are carried on.

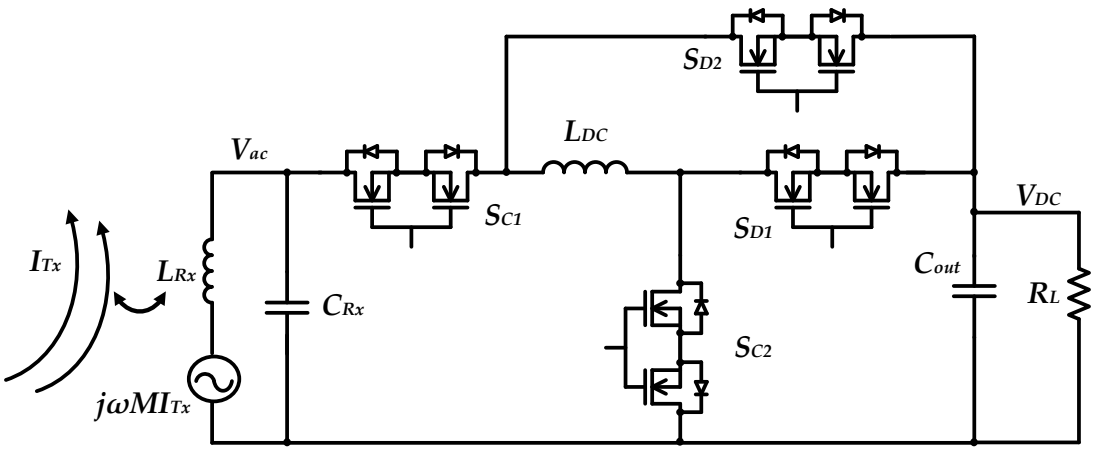


**Figure 5.11** Implementation of the proposed phase-controlled switched-inductor tuner and rectifier in WPT receiver.

### *5.3.3.2 Verification (Design Case)*

The proposed phase-controlled switched-inductor converter employed as an impedance tuner and rectifier as shown in Figure 5.11. It has been simulated using PSIM tools. A 12μH WPT receiver coil $L_{Rx}$ was chosen for verifying the operation of the converter. The received energy at the receiver coils has been modeled by a voltage source ($V_{oc} = \omega MI_{Rx}$) in series with $L_{Rx}$ to emulate the induced voltage in the receiver coil. A capacitor $C_{Rx}$ has been designed to resonate

with the parallel combination between $L_{Rx}$ and $L_{\alpha}$ at operating frequency of 200 kHz. Table 5.1 shows all the parameters used for the design case.

Figure 5.12 displays the system functionality at the specified parameters in Table 5.1. It is noted that there is a 90° phase shift between the coil's induced voltage $V_{oc}$ and the receiver resonant tank voltage $V_{ac}$. This phase shift is considered as an indication for a fully-tuned parallel resonant tank, a fact that could be used for control design. Moreover, the gating signals for switches $S_{C1}$ and $S_{C2}$ are also shown. It is obvious that the switching sequence of charging and discharging the inductor $L_{DC}$ is repeated twice within one full cycle of $V_{ac}$. As well, the charging intervals $t_{cp}$ and $t_{cn}$ are both engaged after a time delay $\alpha = 0.68\pi$ with respect to the starting of a positive cycle and negative cycle respectively.

**Table 5.1** WPT receiver and phase-controlled converter.

| Parameter | Value |
|---|---|
| WPT receiver | |
| $V_{oc}$ | 0.707 $V_{rms}$ |
| $I_{Tx}$ | 1.414 $I_{rms}$ |
| $M$ | 398 nF |
| $f_T$ | 200 kHz |
| $L_{Rx}$ | 12.0 µH |
| $C_{Rx}$ | 77 nF |
| $R_L$ | 20 Ω (nominal) |
| Phase-controlled converter parameters | |
| $L_{DC}$ | 9.0 µF |
| $C_{out}$ | 100 µF |
| B-switch $R_{ON}$ | 4 mΩ |
| $\alpha$ | 0.68π (nominal) |

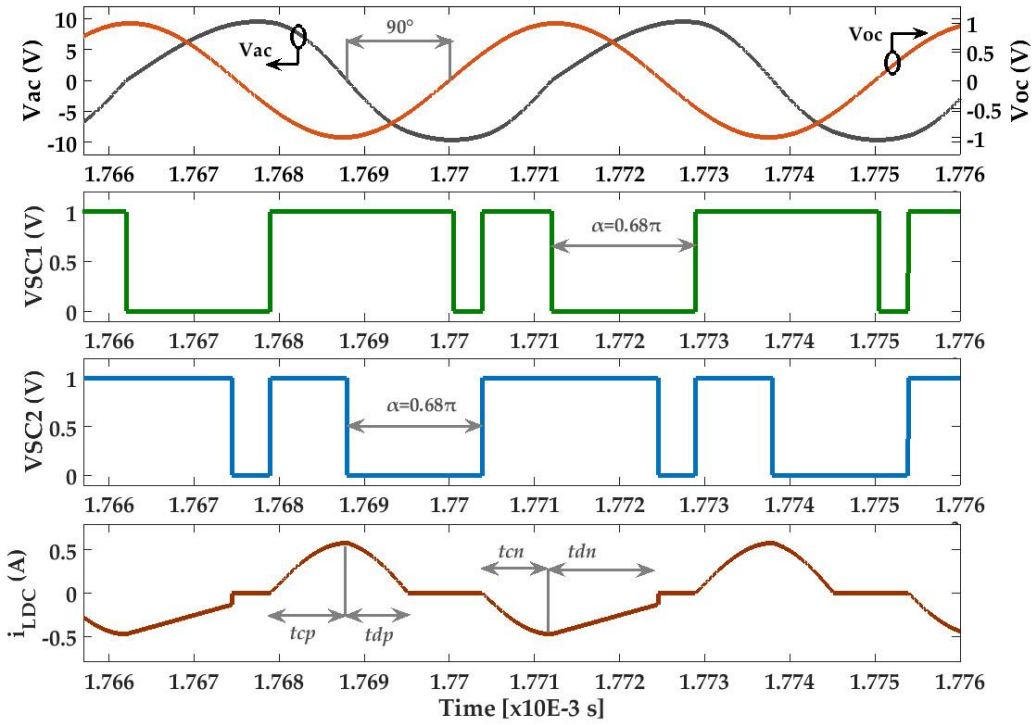


**Figure 5.12** Time-domain simulation for receiver with phase-controlled switched-converter optimized for tuning and rectification.

In Figure 5.13 time-domain commutation events between different switches at positive and negative half cycles of the resonant tank voltage $V_{ac}$ are shown. First, inductor current $i_{LDC}$ during a positive cycle comprises the charging interval $t_{cp}$ where the charging current flows through $S_{C1}$ and $S_{C2}$ while both $S_{D1}$ and $S_{D2}$ are opened with zero current, as shown in Figure 5.13(a). Then, the interval $t_{dp}$ starts by discharging the inductor through $S_{C1}$ and $S_{D1}$ while the current through $S_{C1}$ and $S_{C2}$ drops to zero during this interval. The energy is delivered to the output, *i.e.* rectified, during the interval $t_{dp}$, as indicated in Figure 5.13(a) by the ramping of $V_{DC}$ voltage. It is important to note in Figure 5.13(a) that the inductor current is fully discharged to zero before the compulsory end of $t_{dp}$.

Further, during negative cycle displayed in Figure 5.13(b), inductor current $i_{LDC}$ flows through $S_{C1}$ and $S_{C2}$ while both of them are closed during interval $t_{cn}$. Then, switch $S_{C1}$ is opened to discharge the inductor current through $S_{C2}$ and $S_{D2}$. Again, it is noted that the inductor is not fully depleted into $C_{Cout}$ during $t_{dn}$ mainly because the negative half cycle the circuit works as a buck-boost configuration as declared in Figure 5.5(d).

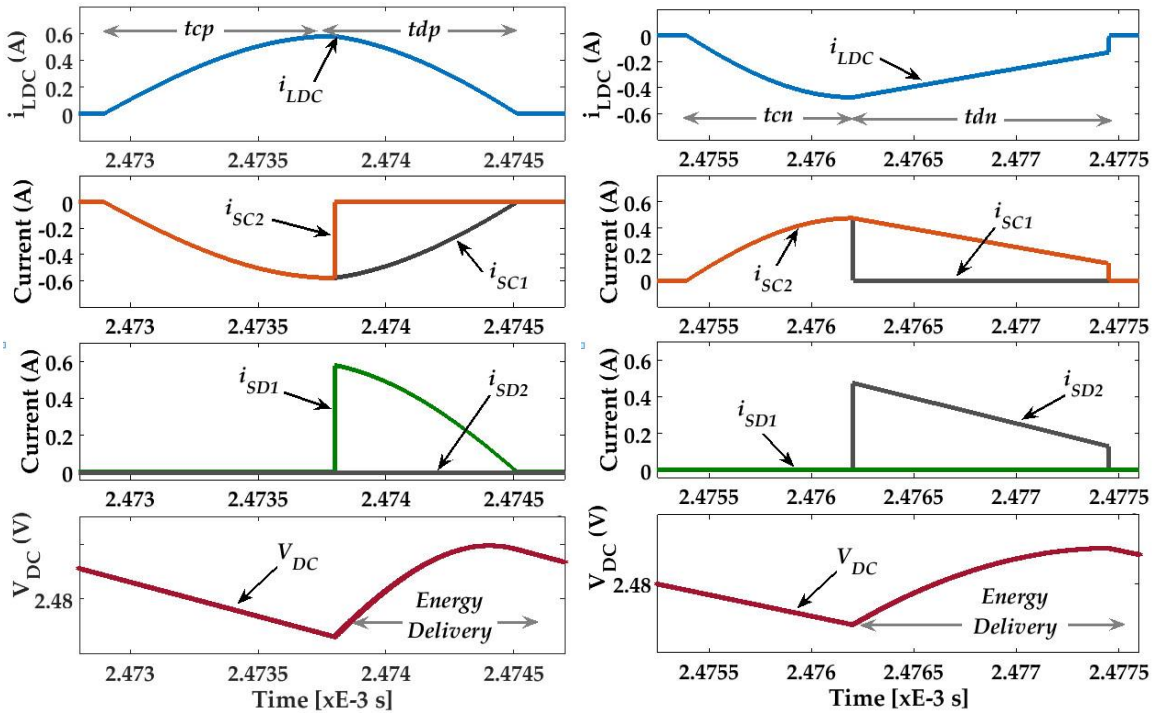


**(a)** **(b)**

**Figure 5.13** Time-domain waveforms of switches current and commutation events at: **(a)** positive current cycle, and **(b)** negative current cycle.

In order to verify the active tuning functionality, different variation percentages in $C_{Rx}$ have been applied and the corresponding $\alpha$ required for retuning is obtained at every variation case. As the variation in capacitor $C_{Rx}$ ranges from -10% to +10%, the corresponding time delay $\alpha$ moves from $0.72\pi$ down to $0.63\pi$, as shown in Figure 5.14(a). The variation in the equivalent inductance $L_\alpha$ is also shown ranging from 4.26x$L_{DC}$ to 2.2x$L_{DC}$. Every value of the time delay $\alpha$ corresponds to a specific value of the equivalent inductance $L_\alpha$ that yields a fully-tuned receiver tank irrespective of the variation percentages. A similar response curve could be generated for other kinds of variations in the circuit. Furthermore, the effect of the equivalent resistance $R_\alpha$ has been investigated on the total power of the WPT receiver. Figure 5.14(b) illustrates that the total power received is variable as a function of $R_\alpha$, which in essence is a function of $\alpha$. In order to describe this effect, we recall the maximum power of a parallel-compensated receiver as:

$$P_{max} = \frac{Q_{RL}^2}{R_\alpha} V_{oc}^2 = \frac{R_\alpha}{\omega_T^2 L_{Rx}^2} V_{oc}^2 \tag{5.11}$$

where $\omega_T$ is the induced voltage angular frequency which is also equal to the angular frequency of the transmitter circuit. As the maximum power received in Equation (5.11) is a function of $R_\alpha$, which in turn is a function of $\alpha$ as seen in Figure 5.7b, we see that the maximum output

power is not constant. This fact is aligned with the simulated result in Figure 5.14(b), where the maximum power is moving according to $\alpha$ following a variation in circuit components. However, still the power delivered to the WPT receiver (denoted as "Po_PSI" in Figure 5.14(b)) is the maximum one at the fully-tuned state. The fact that $R_\alpha$ is variable, *i.e.* is modulated, is mainly because the time intervals of energy rectification $t_{dp}$ and $t_{dn}$ are not regulated to maintain the output power constant. Instead, these intervals are dependent on the amount of time delay required for realizing a specific equivalent inductance $L_\alpha$. Therefrom, the following relations are more expressive:

$$t_{cp} = \pi - \alpha$$
$$t_{cn} = \pi - \alpha \tag{5.12}$$

As given in Equation (5.12), the amount of $\alpha$ is interrelated with the amount of time available for charging $L_{DC}$, which in turn affects how much energy is rectified and transferred to the load. The described operation for the proposed phase-controlled converter presumes a single control parameter, *i.e.* the time delay $\alpha$. However, still the power received at the WPT receiver using phase-controlled converter is higher the power received at a conventional mistuned WPT receiver (denoted as "$P_o$_w/o"), as shown in Figure 5.14(b).

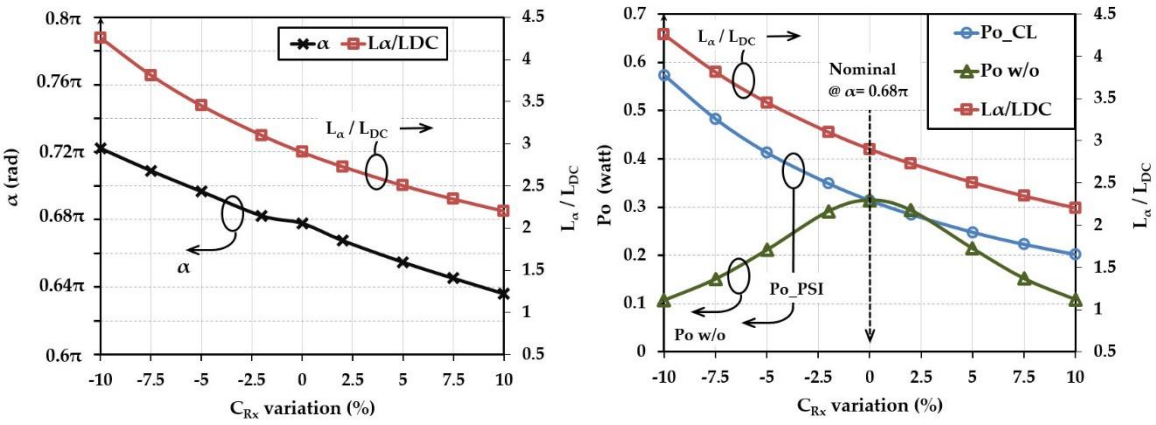


**(a)** **(b)**

**Figure 5.14** Simulated WPT receiver performance at different $C_{Rx}$ variation percentage **(a)** corresponding α and $L_\alpha/L_{DC}$; and **(b)** corresponding output power.

## 5.4 Phase-Controlled Split-Capacitor Converter

Another candidate topology for phase-controlled converters is to be discussed and evaluated in this section. The topology has been originally derived from the dual-polarity boost converter presented in [10]. The topology, as shown in Figure 15.15(a), has been presented within the context of an AC-DC power processing circuit for low-power low-voltage energy harvesting

applications. It consists of two inductors and two series-connected split capacitors. In general, it works as a direct AC-DC converter with one boost converter ($L_1 - M_N - D_1 - C_1$) working during the positive half cycle while the other boost converter ($L_2 - M_P - D_2 - C_2$) works during the negative half cycle. With the cost of an extra inductor and extra capacitor, the topology supposes an efficient solution by eliminating the input bridge rectifier. Later in [10], another topology has been proposed that operates on the same principles while still uses one inductor as shown in Figure 5.13b.

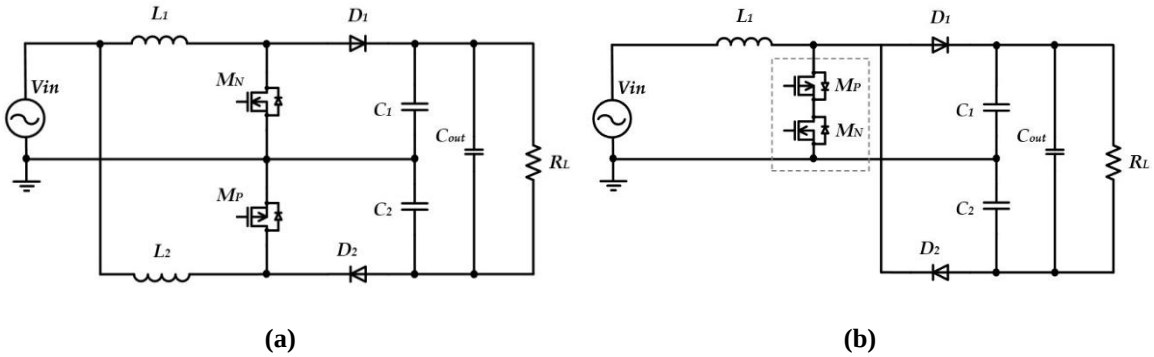


**Figure 5.15** Rectifier-free AC-DC topologies: **(a)** dual-polarity boost converter [9]; and **(b)** direct AC-DC split capacitor [10].

Both of the topologies in Figure 5.15 are good candidates for a phase-controlled converter. However, we will focus on the single inductor topology shown in Figure 5.15(b) which undoubtedly has a higher power density.

## 5.4.1 Circuit Operation

The split-capacitor topology, as a rectifier-free AC-DC boost converter, has been proposed to work in discontinuous conduction mode (DCM) with a switching frequency much higher than the input AC source. However, in order to incorporate the phase-controlled operation, it only has to be switched at twice the frequency of the input AC source. Figure 5.16 shows the operation states of this topology.

During the positive half cycle, all the switches are opened until a time interval $t_\alpha$ is elapsed. Then, switch $S_C$ becomes ON and the inductor $L_1$ charges from the input source during a positive charging interval $t_{cp}$, as shown in Figure 5.16(a). The interval $t_{cp}$ starts from $t_\alpha$ and finishes by the end of the positive half cycle, consequently it is also given by Equation (5.6). The inductor current $i_L(t_{cp})$ is a function of the input voltage $V_{in}$, where $V_{in} = V_P sin(2\pi f_{in} t)$. Then, the positive discharging interval $t_{dp}$ starts by turning OFF switch $S_C$ and turning ON switch $S_{D1}$ as depicted in Figure 5.16(b). The inductor $L_1$ is now connected between the input source and the first output capacitor $C_1$, thus, the energy stored in $L_1$ is fully depleted into $C_1$. During this

interval $t_{dp}$, the inductor current $i_L(t_{dp})$ is similar to Equation (5.7) except that the voltage over $C_1$ is now half of the dc output voltage $V_{DC}$ as follows:

$$i_L(t_{dp}) = \frac{1}{L_1}\int_{\pi}^{t}[V_P sin(2\pi f_{in}t) - \frac{1}{2}V_{DC}]dt \tag{5.13}$$

The same switching mechanism is followed during the negative half cycle. The circuit waits for the elapsing of the same delay interval $t_\alpha$, then the negative charging cycle $t_{cn}$ starts by turning ON switches $S_C$ to charge $L_1$ in the opposite direction. This interval is shown in Figure 5.16(c), in which the current $i_L(t_{cn})$ becomes the same expression given in Equation (5.8). Once the input voltage reaches zero, the negative charging interval $t_{cn}$ reaches the end. Note that the inductor current $i_L(t_{cn})$ reaches a negative peak at the end of this interval. Thereafter, the discharging interval $t_{dn}$ starts by turning OFF $S_C$ and turning ON switch $S_{D2}$ as indicated in Figure 5.16(d). The energy stored in $L_1$ is again depleted into the second output capacitor $C_2$. The inductor current $i_L(t_{dn})$ during this interval is different from the one in Equation (5.9) as follows:

$$i_L(t_{dn}) = \frac{1}{L_1}\int_{2\pi+t_\alpha}^{t}[V_P sin(2\pi f_{in}t) - \frac{1}{2}V_{DC}]\,dt \tag{5.14}$$

As we see in Equations (5.13) and (5.14), the energy in every half cycle is accumulated in different output capacitors, where the energy of the positive half cycles is accumulated in $C_1$ and the energy of the negative half cycles is accumulated in $C_2$. Finally, the total output voltage across $C_{out}$ is:

$$V_{DC} = V_{C1} + V_{C2} \tag{5.15}$$

where $V_{C1} = V_{C2}$ provided that $C_1 = C_2$. Figure 5.17 shows the time-domain waveforms of the converter verified by simulation for $L_{DC} = 5\ \mu H$, $C_1 = 10\ \mu F$, $C_2 = 10\ \mu F$, $C_{out} = 47\ \mu F$, and $R_L = 20\ \Omega$ at $t_\alpha = 1.67\mu s$ or $\alpha = 2.1$ rad. It is clear from Figure 5.17 that capacitor $C_1$ charges during positive half cycles while $C_2$ charges during the negative half cycles. As $C_1 = C_2$, the voltage $V_{C1}$ is a mirrored replica of $V_{C2}$ and vice versa. Consequently, during one half cycle, a single capacitor is charging while the other one is discharged to $C_{out}$, such that the voltage ripple at the total output $V_{DC}$ is much lower than the ripple on $V_{C1}$ or $V_{C2}$ [10].

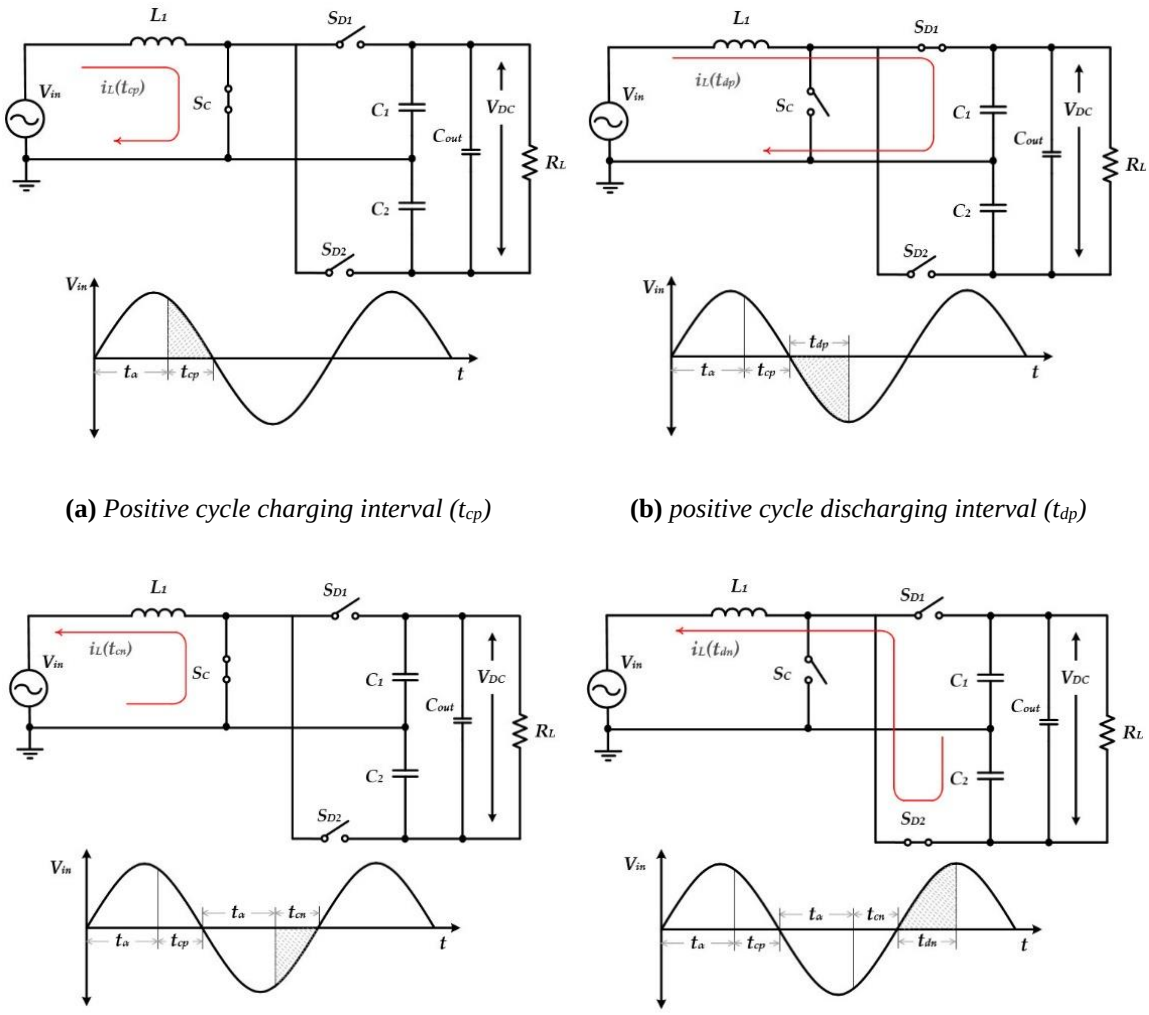


**(a)** *Positive cycle charging interval ($t_{cp}$)*

**(b)** *positive cycle discharging interval ($t_{dp}$)*

**(c)** *Negative cycle charging interval ($t_{cn}$)*

**(d)** *Negative cycle discharging interval ($t_{dn}$)*

**Figure 5.16** Operation modes of phase-controlled split-capacitor converter.

## 5.4.2 Circuit Characterization

Given the operation of the phase-controlled split-capacitor converter, it is still valid to follow the same model in Figure 5.7. Similarly, $L_\alpha$ will represent the function of variable equivalent inductance synthesis, while $R_\alpha$ represents the energy rectification function declared by having a DC output voltage. In addition, as the inductor current $i_{L1}$ is discontinuous, the fundamental current component is supposed to lag the input voltage $V_{in}$ by a phase slightly less than 90°. It is also important to recall that both the equivalent inductance $L_\alpha$ and the equivalent resistance $R_\alpha$ are function of $\alpha$, and thus both of them are variable. For characterization purpose, Figure 5.18 shows the inductance ratio ($L_\alpha$ / $L_1$) and resistance ratio ($R_\alpha$ / $R_L$) versus the time-delay $\alpha$ at different $L_1$ values. In Figure 5.18, the ratio between the equivalent emulated inductance $L_\alpha$ and

the actual inductance $L_1$ is represented by $L_r$, while $R_r$ is the ration between the equivalent resistance $R_\alpha$ and the actual load resistance $R_L$.

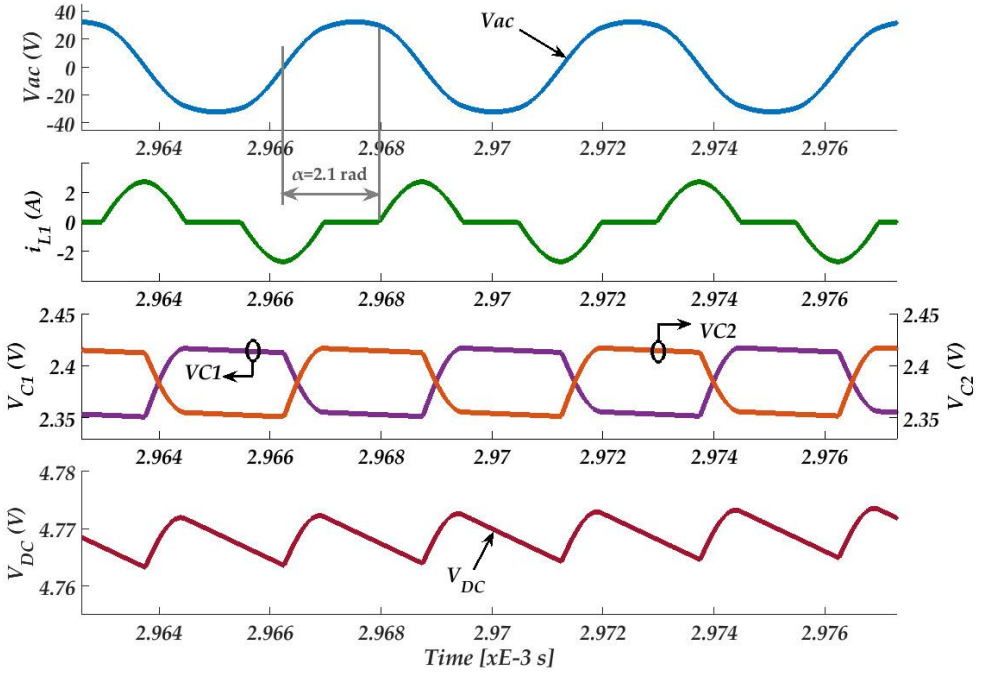


**Figure 5.17** Time-domain simulation of phase-controlled split-capacitor showing $i_{L1}$, $V_{C1}$, $V_{C2}$, and $V_{DC}$.

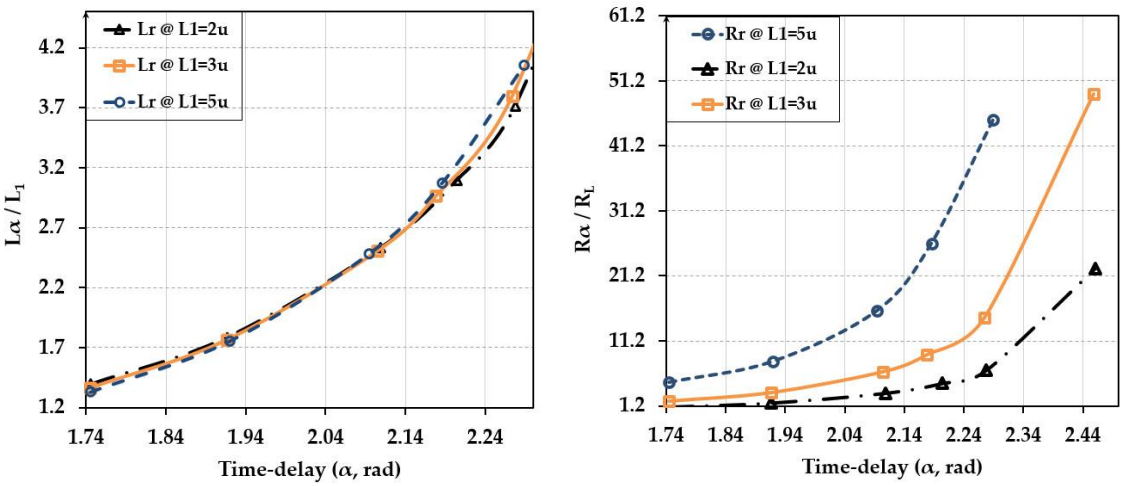


**(a)** **(b)**

**Figure 5.18** Split-capacitor converter characteristics versus $\alpha$: **(a)** Inductance ratio $L_r$ at $L_1$=2µH, 3µH, 5µH; and **(b)** Resistance ratio $R_r$ at $L_1$= 2µH, 3µH and 5µH.

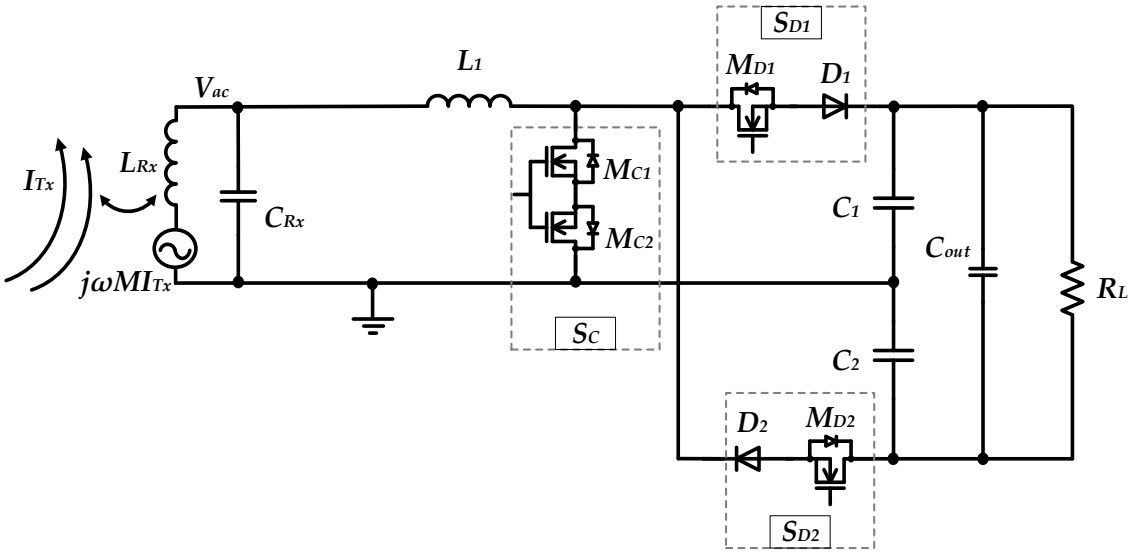


**Figure 5.19** Implementation of the phase-controlled split-capacitor converter in WPT receiver.

It is obvious that the actual inductance $L_1$ that is used in the split-capacitor converter has no significant effect on the equivalent inductance $L_\alpha$, as we notice in Figure 5.18(a). Moreover, $L_\alpha$ roughly extends over a range from 1.33x$L_1$ up to 4x$L_1$. On the other hand, we note that $R_\alpha$ has a strong dependency on the value of $L_1$. It tends to increase exponentially with respect to $\alpha$, however, the slope of the function tends also to increase with respect to $L_1$. We recall that $R_\alpha$ represents the effective load being seen by the input source. Consequently, at higher $L_1$ the effect resistance $R_\alpha$ increases rapidly which would be considered as the input source being lightly loaded. This fact can be noted in Figure 5.18(b) where $R_\alpha$ reaches a value of $45xR_L$ at $\alpha = 0.73\pi$ only.

## 5.4.3 Active Tuning in WPT Receivers

### *5.4.3.1 Transistor Implementation and integration in WPT receivers*

Figure 5.19 shows the transistor implementation of the phase-controlled split-capacitor converter. Compared to the conventional split-capacitor converter in Figure 5.15(b), two MOSFET switches $M_{D1}$ and $M_{D2}$ in series with $D_1$ and $D_2$ respectively. The reason for adding these two switches is to control the false forward bias of one of the diodes due to the addition of the delay interval $\alpha$. Still the diodes could be replaced by a self-synchronized MOS switch such as the one presented in [8]. Moreover, a bidirectional switch realized by $M_{C1}$ and $M_{C2}$ connected back-to-back such that their body diodes are used to block current when the both of the switches are OFF.

The detailed time-domain commutation events of the phase-controlled split-capacitor converter is illustrated in Figure 5.20. At positive half cycle shown in Figure 5.20(a), inductor $L_1$ is charged via switch $S_C$ which is ON, while the current through $S_{D1}$ and $S_{D2}$ is zero. This constitutes the charging interval $t_{cp}$ that ends once the input voltage $V_{ac}$ reaches zero. Following, switch $S_C$ is turned OFF switch $S_{D1}$ is turned ON to discharge the inductor into $C_1$ as indicated by $V_{C1}$ which is pumped during interval $t_{dp}$. At the end of $t_{dp}$, inductor $L_1$ becomes fully depleted and $i_{L1}$ is zero. The same operation is carried on during the negative half cycle, where $S_C$ is turned ON to charge in the opposite direction from the negative input voltage during interval $t_{cn}$. Further, the second discharge phase $t_{dn}$ starts by turning OFF $S_C$ and turning ON $S_{D2}$. This time, the inductor $L_1$ discharges the energy into $C_2$ as indicated by the voltage $V_{C2}$ in Figure 5.20(b). We note here, specifically during $t_{dn}$, that the inductor current $i_{L1}$ is fully depleted into $C_2$ compared to the residual energy in $L_1$ in Figure 5.13(b). In other words, as the circuit configuration during positive half cycle and negative half cycle are both symmetrical, this means that the same net energy is equally rectified and delivered to the output capacitors during every half cycle, no matter it is pumped into $C_1$ or $C_2$.

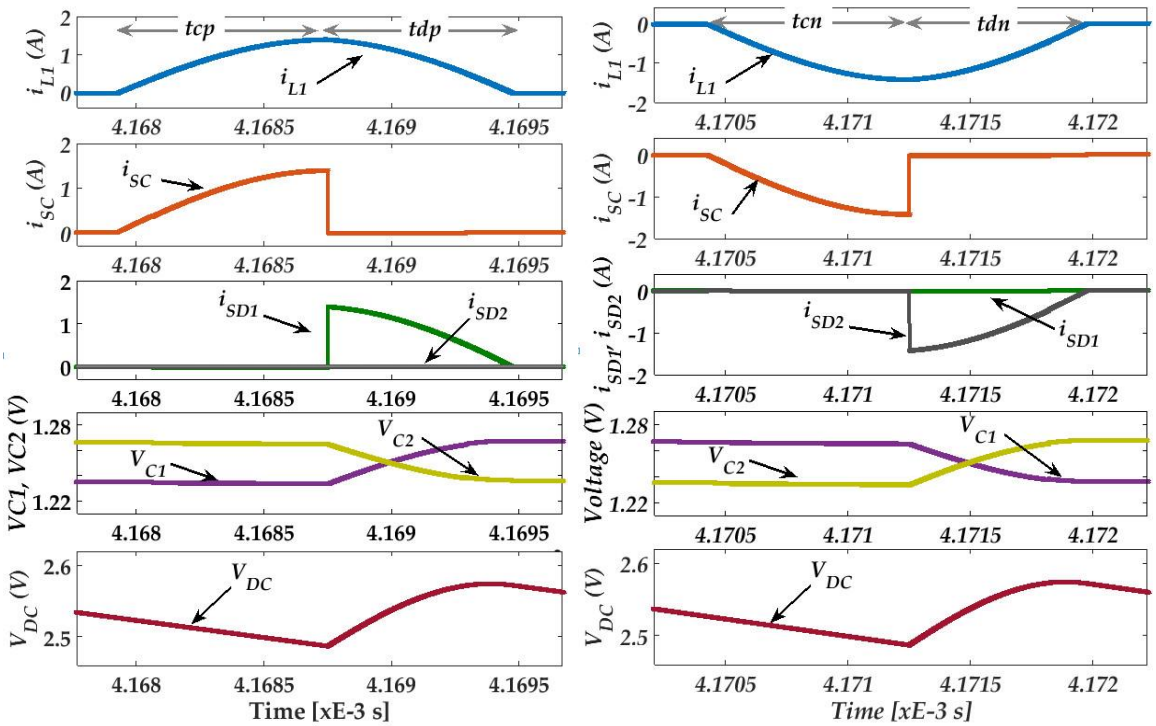


**Figure 5.20** Time-domain waveforms of switches current and commutation of split-capacitor converter: **(a)** positive current cycle, and **(b)** negative current cycle.

### *5.4.3.2 Verification of System Operation*

The fundamental operation of the phase-controlled split-capacitor converter, as indicated previously in the characterization section, suggests that it could be employed for active tuning plus rectification as a double functionality subsystem in WPT receivers. Consequently, the same model that has been presented in Figure 5.10 holds here. The verification of the operation of the split-capacitor converter has been carried by circuit simulation, where the converter has been employed as a tuner and rectifier for a WPT receiver. The simulated system parameters are given in Table 5.2. The converter has been optimized to synthesize an equivalent inductance of $L_\alpha = 7.52\ \mu H$ at a delay angle of $\alpha = 0.67\pi$ such that a compensation capacitor $C_{Rx} = 137\ nF$ is required to compensate the WPT receiver at this nominal operating point. Later, the converter delay angle $\alpha$ has to be tuned accordingly to address for any mismatch in the WPT receiver. Figure 5.21 illustrates the time-domain waveforms of the parallel-compensated WPT receiver utilizing phase-controlled split-capacitor converter for active tuning. Once more, the resonant tank voltage $V_{ac}$ and the coil open-circuit induced voltage $V_{oc}$ are shown as an indication for the tuning condition of the parallel-compensated receiver.

**Table 5.2** Parameters of WPT receiver and split-capacitor converter.

| Parameter | Value |
|---|---|
| WPT receiver | |
| $V_{oc}$ | 0.707 $V_{rms}$ |
| $I_{Tx}$ | 1.414 $I_{rms}$ |
| $M$ | 398 nF |
| $f_T$ | 200 kHz |
| $L_{Rx}$ | 12.0 µH |
| $C_{Rx}$ | 137 nF |
| $R_L$ | 20 Ω (nominal) |
| Split-Capacitor converter parameters | |
| $L_1$ | 3.0 µH |
| $C_{out}$ | 47 µF |
| $C_1$ | 10 µF |
| $C_2$ | 10 µF |
| *B-switch* $R_{ON}$ | 4 mΩ |
| $\alpha$ | 0.67π (nominal) |

The waveforms of the system operation as shown in Figure 5.21 are obtained in the open-loop configuration, *i.e.* the delay angle is decided based on the required $L_\alpha$ for a fully-tuned receiver tank, and consequently the corresponding delay angle $\alpha$ is obtained accordingly from the characterization curves given in Figure 5.18. However, for an autonomous self-tuned WPT receiver to operate, a closed-loop control is required for tracking the tuning condition and automatically adjusting the delay angle $\alpha$.

The tunability of the proposed operation has been verified by applying variations in the parallel compensation capacitor $C_R$. Figure 5.22 illustrates the tuning range of $L_\alpha$ in response to the variations in $C_R$. At every variation percentage in $C_R$, the corresponding $L_\alpha$ in the curve is the value that guarantees a fully-tuned receiver tank. Note that the corresponding delay angles are not shown in the curve as we already have shown the relation between $L_\alpha$ and $\alpha$ in Figure 5.18. It is also important to notice that the receiver output power is not constant despite the fact that the receiver tank is fully-tuned. A similar result has been obtained in the case of the phase-controlled switched-inductor converter. However, such variation in the received power is inherent in the proposed operation due to the fact that $R_\alpha$, which in fact represents the energy delivered to the load, is also dependent on the delay angle $\alpha$.

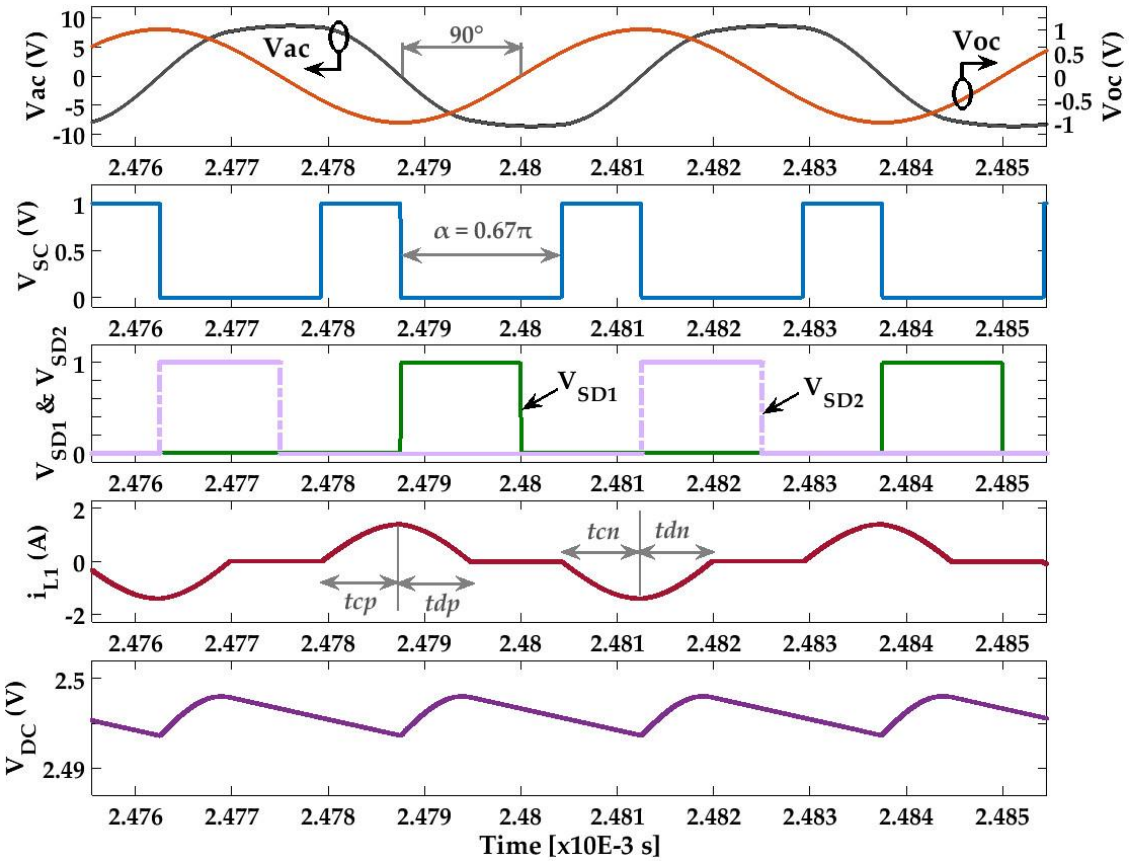


**Figure 5.21** Time-domain waveforms of the phase-controlled split-capacitor converter in a WPT receiver at $\alpha = 0.67\pi$.

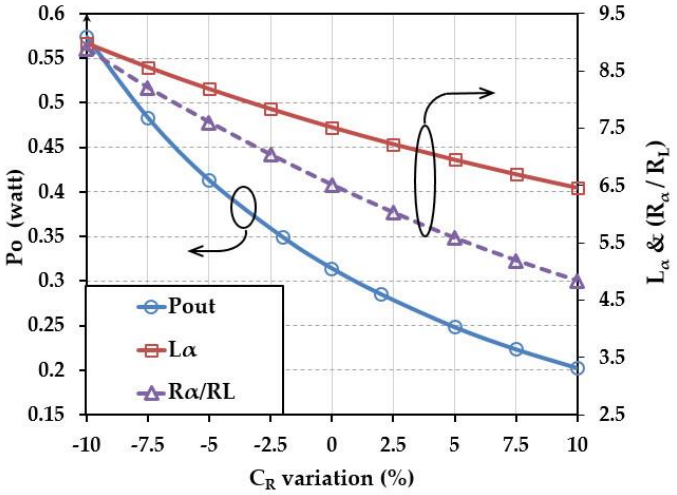


**Figure 5.22** Performance of the phase-controlled split-capacitor converter in response to variation in $C_R$.

## 5.5 Self-Tuning Control Design

After verifying the operation principle of the phase-controlled converters as a candidate for automatic tuning and rectification in WPT receivers, the control design has to be designed to enable self-tuning whenever a mismatch or interference happens to occur in the WPT receiver circuit. Figure 5.23 illustrates the block diagram of the proposed self-tuning control for a parallel-compensated WPT receiver. The objective of the control is to ensure that the receiver resonant frequency is matched with the frequency of the magnetic flux linked to the receiver coil $L_{Rx}$. The fact that the receiver resonant output voltage $V_{ac}$, for a fully-tuned parallel-compensated tank, lags the induced voltage $V_{oc}$ by 90° is once again used in the control design. The phase detector, shown in the control block diagram, is used to sense and track the phase difference between $V_{ac}$ and $V_{oc}$ which is then translated to a quasi-DC voltage $V_{PD}$ using a simple RC low-pass filter. The error amplifier (EA) ensures that $V_{ac}$ lags $V_{oc}$ by 90° indirectly by comparing $V_{PD}$ with a fixed reference $V_{ref}$ of 0.5V.

On the other hand, in order to synchronize the switching gates of the split-capacitor power stage with the zero crossing of $V_{ac}$, a PLL produces a clock reference and sawtooth signal at twice the rate of $V_{ac}$. This way, the switching sequence is repeated at the positive and negative half cycles of $V_{ac}$. A PI compensator is used for compensating the closed loop which is sufficient for the slow dynamics of mistuning in the WPT receiver.

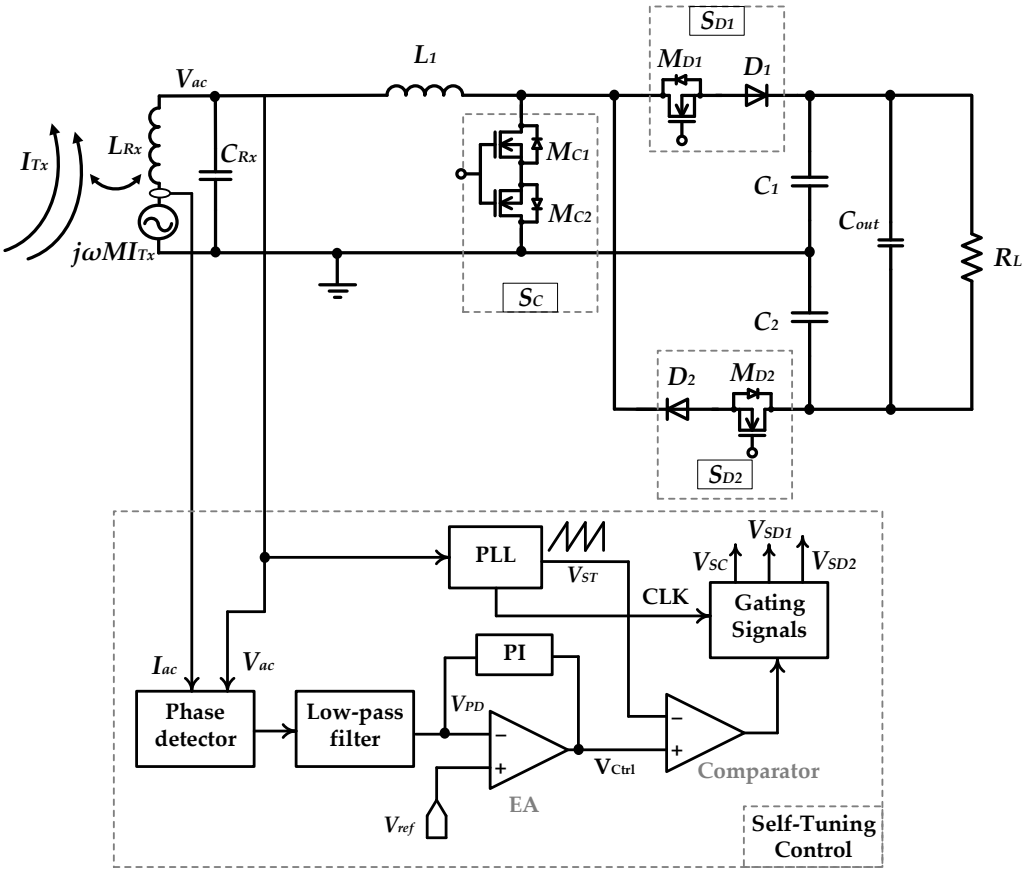


**Figure 5.23** Block diagram of the self-tuning control for the phase-controlled split capacitor converter.

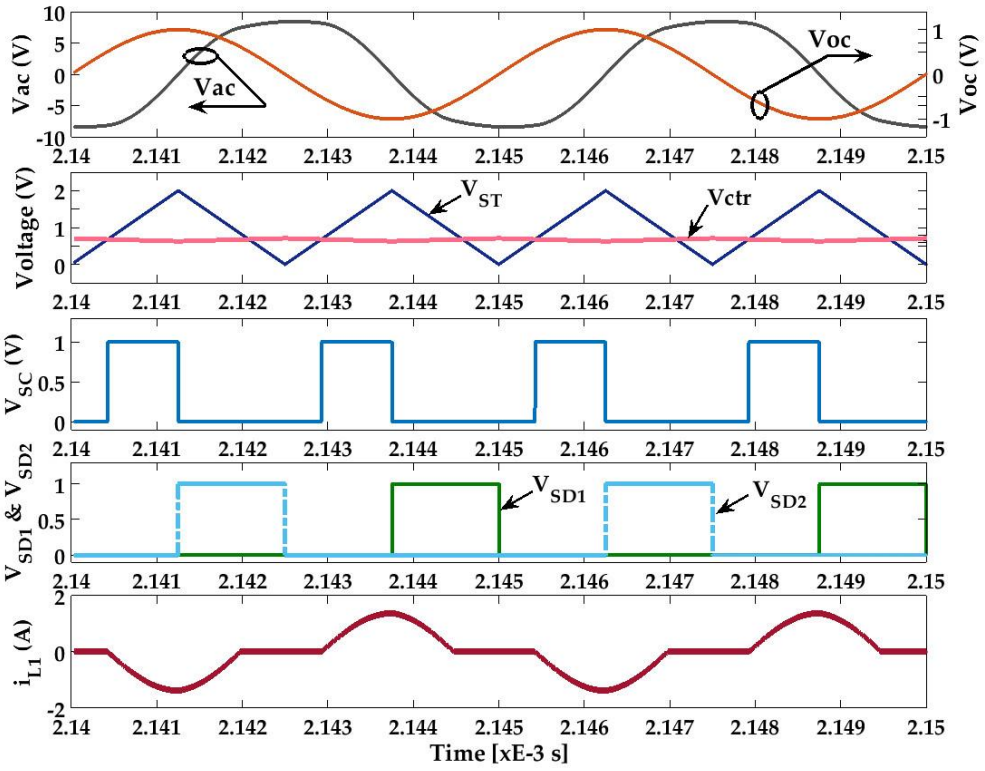


**Figure 5.24** Time-domain waveforms of the self-tuning control of Figure 5.23.

The same system parameters in table 5.2 had been leveraged to verify the control operation. Figure 5.24 shows the time-domain waveforms of the basic control signals. As it can be observed, the sawtooth signal $V_{ST}$ is compared with the control output to generate the delay-angle $\alpha$ required for a fully-tuned receiver tank. The delay angle is then translated by a gating block to produce the gating signals for the power MOSFETs $V_{SC}$, $V_{SD1}$ and $V_{SD2}$. Further verification for the control has been carried out through applying a step change in the receiver resonant circuit.

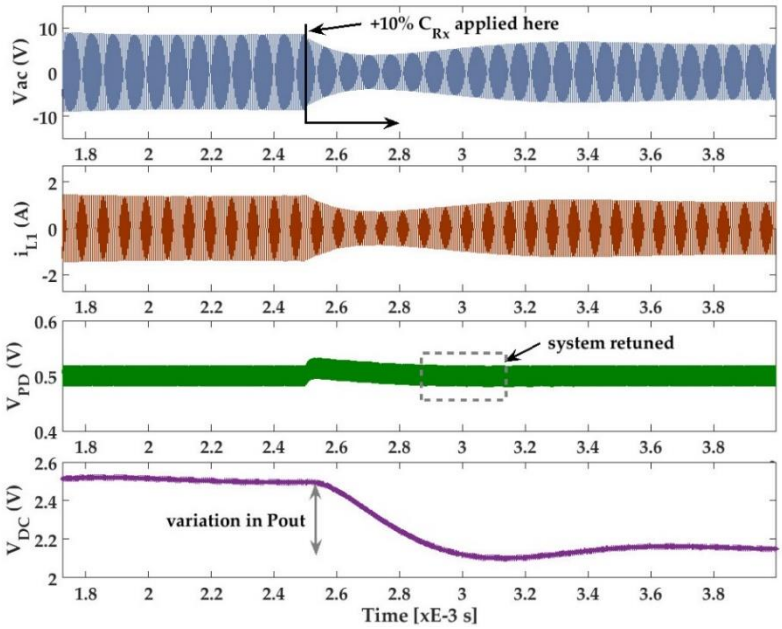


**(a)**

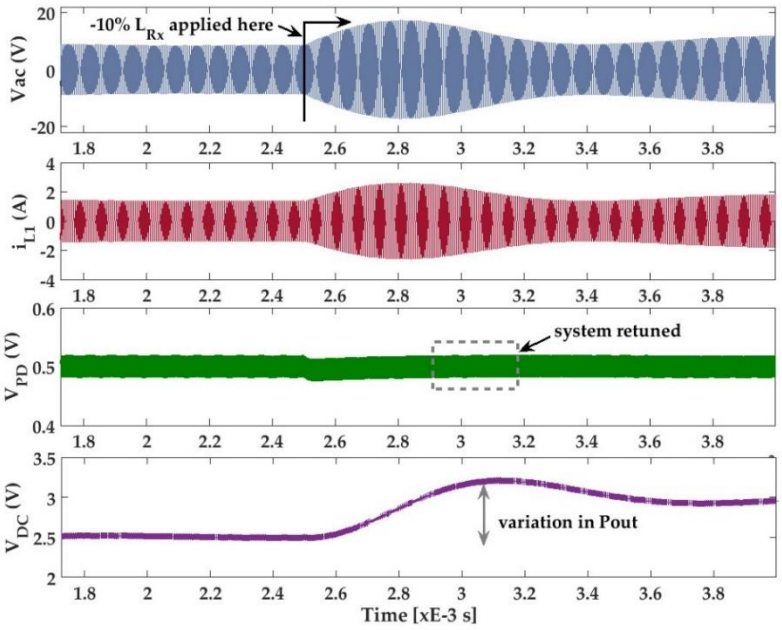


**(b)**

**Figure 5.25** Control response to change in system parameters; **(a)** +10% change in $C_{Rx}$, **(b)** -10% change in $L_{Rx}$.

In Figure 5.25(a), a change of +10% in the compensation capacitor $C_{Rx}$ is applied. One note to observe is that the system takes approximately 500μs to settle back to the fully-tuned state; however, this time represents the dynamics of the parallel resonant circuit while the control dynamics itself are much faster. On the other hand, we also note the effect of retuning the delay-angle $\alpha$ on the output power change which is clearly evident by the drop in the output voltage $V_{DC}$.

Moreover, Figure 5.25(b) shows the response of the control in the case of -10% change in the receiver coil's self-inductance $L_{Rx}$. Once again, the control dynamics takes few microseconds to settle down to the steady-state value as indicated by the phase-difference voltage $V_{PD}$. Furthermore, we notice that the output power increases due to the increase in the receiver tank voltage $V_{ac}$.

## 5.6 Conclusions

In this chapter we have introduced the concept of phase-controlled converter utilized as variable reactive element synthesis. Phase-controlled reactors have been primarily used in FACT systems for static *var* compensation. Consequently, it has been shown that the same concept could be applied in order to synthesize variable reactive elements for active tuning in WPT receivers. At first, a phase-controlled switched-inductor converter has been proposed to actively tune the WPT receiver tank while the same converter circuit is developed to rectify the energy from the WPT receiver tank to the output load. Secondly, the same operation has been proposed with a different topology, namely, phase-controlled split-capacitor converter. Similarly, the split-capacitor converter is developed to actively tune the WPT receiver by means of phase delay control, while the energy is rectified and delivered to the load.

The dual functionality, *i.e.* active tuning plus rectification, results in a compact topology with a higher power density. It has been also shown that the intended operation of the proposed converters leads to different output powers every time a mismatch occurs and the WPT receiver is automatically retuned. A possible solution for this problem could be achieved by adding another control parameter that adjusts the amount of energy delivered to the output. Consequently, a constant output power can be supplied to the load irrespective of the automatic tuning process.

## 5.7 References

[1] P. Si, A. P. Hu, S. Malpas, and D. Budgett, "A Frequency Control Method for Regulating Wireless Power to Implantable Devices," *IEEE Trans. Biomed. Circuits Syst.*, vol. 2, no. 1, pp. 22–29, Mar. 2008.

[2] P. P. Nayak, D. P. Kar, S. K. Panda, and S. Bhuyan, "Automatic frequency tuning wireless charging system for enhancement of efficiency," *Electron. Lett.*, vol. 50, no. 24, pp. 1868–1870, Nov. 2014.

[3] S. Aldhaher, P. C.-K. Luk, A. Bati, and J. F. Whidborne, "Wireless Power Transfer Using Class E Inverter With Saturable DC-Feed Inductor," *IEEE Trans. Ind. Appl.*, vol. 50, no. 4, pp. 2710–2718, Jul. 2014.

[4] J.-U. W. Hsu, A. P. Hu, and A. Swain, "A Wireless Power Pickup Based on Directional Tuning Control of Magnetic Amplifier," *IEEE Trans. Ind. Electron.*, vol. 56, no. 7, pp. 2771–2781, Jul. 2009.

[5] A. P. Hu and S. Hussmann, "Improved power flow control for contactless moving sensor applications," *IEEE Power Electron. Lett.*, vol. 2, no. 4, pp. 135–138, 2004.

[6] N. G. Hingorani and L. Gyugyi, Understanding FACTS : concepts and technology of flexible AC transmission systems. Wiley-IEEE Press, 2000.

[7] J. James, J. Boys, and G. Covic, "A variable inductor based tuning method for ICPT pickups," in *7th International Power Engineering Conference*, IPEC2005, 2005, vol. 2005.

[8] D. Kwon, G. A. Rincon-Mora, and E. O. Torres, "Harvesting Ambient Kinetic Energy With Switched-Inductor Converters," *IEEE Trans. Circuits Syst. I Regul. Pap.*, vol. 58, no. 7, pp. 1551–1560, Jul. 2011.

[9] P. D. Mitcheson, T. C. Green, and E. M. Yeatman, "Power processing circuits for electromagnetic, electrostatic and piezoelectric inertial energy scavengers," in *Microsystem Technologies*, 2007, vol. 13, no. 11–12, pp. 1629–1635.

[10] R. Dayal, S. Dwari, and L. Parsa, "Design and Implementation of a Direct AC-DC Boost Converter for Low-Voltage Energy Harvesting," *IEEE Trans. Ind. Electron.*, vol. 58, no. 6, pp. 2387–2396, June.

Chapter

# 6

# Real and Reactive Power Control in WPT Receivers

In this chapter, we propose a modified operation in phase-controlled converters in order to enable real power flow control in addition to the self-tuning of WPT receivers. We have shown in Chapter 5 that phase-controlled converters are good candidates for variable reactive element synthesis in the applications of active tuning in WPT receivers. This way, it is possible to control the reactive power generated in the receiver resonant tank due to mistuning, which leaves some amount of uncompensated *var*. We have verified the concept of variable delay-angle implementation in order to synthesize an average reactive element which is utilized for compensating the WPT receiver tank automatically towards the fully-tuned condition. However, it has been shown that, during the energy rectification intervals, the amount of energy delivered to the load depends upon the amount of delay-angle applied for active tuning.

Accordingly, we explore and propose in this chapter a modified operation that adds an additional control parameter in order to control the real power flow and supply the load with a regulated output voltage.

## 6.1 Power Management Topologies in WPT Receivers — an Overview

As pointed out before, in a representative RIC-WPT link, a transmitter coil $L_{Tx}$ is driven by a current to produce a magnetic field. At the receiver side, the receiver coil $L_{Rx}$ is linked by the magnetic flux lines which cause an open-circuit voltage $V_{oc}$ to be induced in the coil. Due to the weak coupling between the transmitter and receiver coil, the induced voltage $V_{oc}$ is usually very low. Consequently, a compensation circuit is used to form a resonance circuit in order to boost either the voltage or the current. Compensation topologies have been discussed earlier in Chapter 2, where we have pointed out that parallel-compensated WPT receiver tank is more

controllable and suitable for many applications. In a parallel-compensated WPT receiver, the induced voltage $V_{oc}$ is boosted to the resonant tank output voltage $V_{ac}$, as follows:

$$V_{ac} = Q_{R-L} V_{oc} \tag{6.1}$$

where $Q_{R\text{-}L}$ is the load quality factor of the parallel-compensated receiver tank. In a WSN node or any other application, the voltage at the terminals of the receiver resonant circuit $V_{ac}$ has to be conditioned in order to charge a small battery or supercapacitor or supply the sub-circuits of the WSN node directly. In both cases, a power management system is required which comprises a voltage rectification stage, followed by a voltage regulation stage. Furthermore, a separate active tuning stage is added in order to retune the receiver tank to ensure maximum power delivery to the node. Figure 6.1 shows a representative block diagram for power management in a parallel-compensated WPT receiver.

As we note in Figure 6.1, the complete power management system can be conceptualized in two parts, the first part deals with reactive power control, while the latter is related to active power control. Reactive power control is mainly related to the active tuning in the receiver resonant tank such that it compensates for any amount of uncompensated *var* that may appear due to mistuning. On the other hand, a rectifier followed by a voltage regulator is usually used for active power control where a regulated output voltage $V_{DC}$ is maintained across the load. The rectifier block is thus responsible for converting the receiver tank voltage $V_{ac}$ to a rectified voltage $V_{Rec}$. Various schemes are commonly available for voltage rectification such as half-wave rectification, full-wave rectification, and class-E rectifiers [1]. Different considerations are taken into account when it comes to the selection among the different rectifier schemes such as the required DC level and efficiency. After the rectification stage, a voltage regulator is used to supply the load by a constant dc voltage $V_{DC}$. As depicted in Figure 6.1, a boost converter is typically used for active power flow control in parallel-compensated WPT receivers.

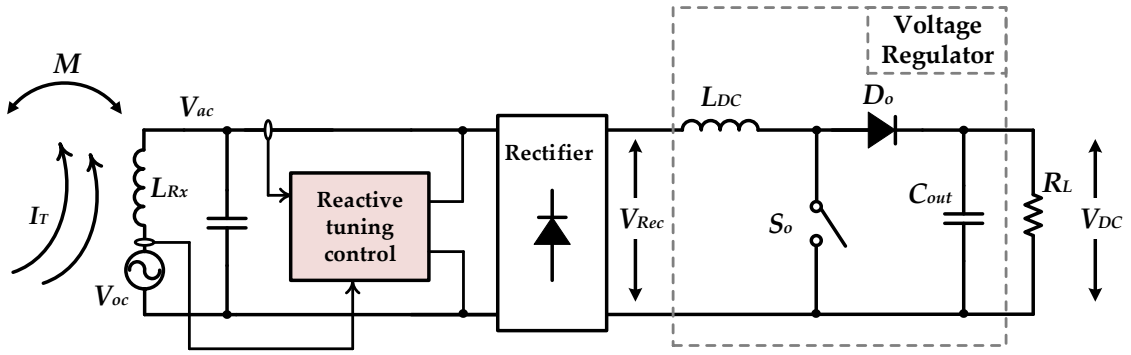


**Figure 6.1** Block diagram of power conditioning system for parallel WPT receiver.

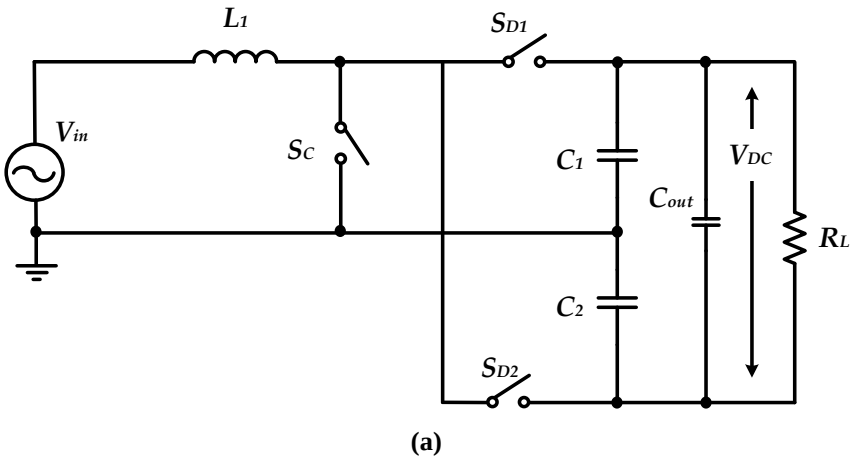


**(a)**

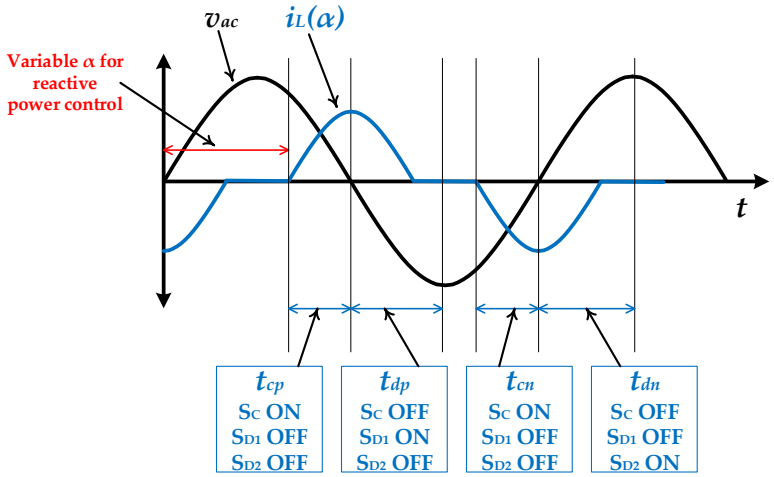


**(b)**

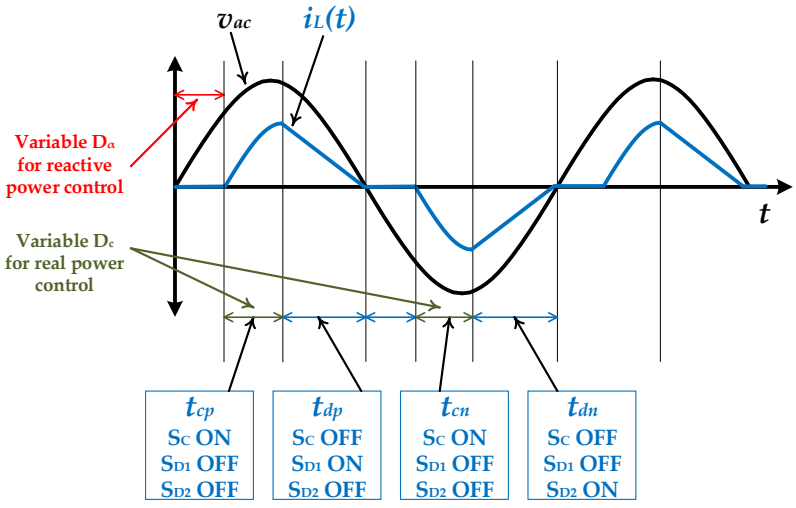


**(c)**

**Figure 6.2** Phase-controlled split-capacitor converter, **(a)** the topology, **(b)** reactive power control operation, **(c)** real and reactive power control operation.

## 6.2 Real Power Control in Phase-Controlled Converters

The operation details of phase-controlled converters have been discussed in Chapter 5 where it has been shown that by controlling one parameter, the delay-angle $\alpha$, the reactive power control is realized and active tuning of the WPT receiver is possible. We recall this concept from Figure 6.2, where the split-capacitor converter is shown in this case. The reactive power control operation is shown in Figure 6.2(b) where the delay-angle $\alpha$ is controlled to vary the amount of generated reactive power by the converter. The voltage rectification is then realized during intervals $t_{dp}$ and $t_{dn}$ in positive and negative half cycles respectively. Clearly, the intervals in which the inductor $L_1$ is energized, *i.e.* intervals $t_{cp}$ and $t_{cn}$, are out of control and they are is varied upon the variation of $\alpha$. That was a clear reason for the variation of the real power that is delivered to the load whenever a mistuning occurs in the WPT receiver tank.

In order to enable real power control as well as reactive power compensation in the parallel-compensated WPT receiver, another control parameter is necessary. Figure 6.2(c) illustrated a diagram for a modified operation in the split-capacitor converter. As shown, a variable $D_c$ is considered in order to control the intervals during which the inductor $L_1$ is energized. This means that the time intervals $t_{cp}$ and $t_{cn}$ are no longer constant nor they are varied upon $\alpha$.

Lastly, the modified operation is explained as follows. The interval $t_\alpha$ is synchronized with the zero-crossing of $V_{ac}$ to allow symmetrical operation during positive and negative half cycles accordingly. Also, all the converter switches, *i.e.* $S_C$, $S_{D1}$ and $S_{D2}$, are open during the interval $t_\alpha$. Then the positive inductor energizing interval $t_{cp}$ starts by closing switch $S_C$. At the end of interval $t_{cp}$, switch $S_C$ is opened and switch $S_{D1}$ is closed to release the inductor $L_1$'s stored energy into the capacitor $C_1$. The same switching sequence is repeated during the negative half cycle, the inductor is energized in the reverse direction during interval $t_{cn}$, and then the energy is released into the capacitor $C_2$.

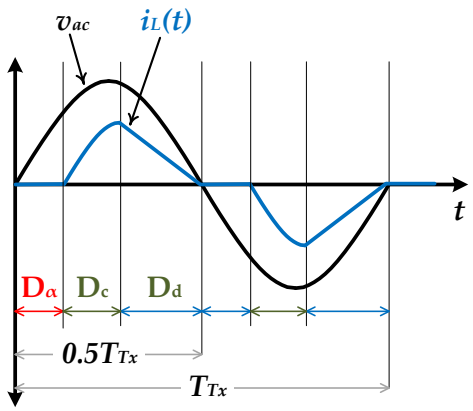


**Figure 6.3** Operation modes for reactive and real power control phase-controlled split-capacitor converter.

The novelty of the modified operation of the split-capacitor converter is the incorporation of an additional control parameter to control the energizing interval of the inductor which enables a controlled real power delivery to the load. The inherent modified operation is thus retaining the same principles of delay-angle control for reactive power injection into the tank while the interval $t_{cp}$ (and $t_{cn}$) is controlled towards a fixed real power delivery. The proposed operation is thus valid for combining several functionalities including active tuning, rectification and regulation within the same compact circuit structure. However, the modified operation imposes some limitations on the operating ranges which need to be characterized. In order to explain these limitations, Figure 6.3 illustrates the proposed operation modes of the split-capacitor converter. The operation intervals are now written as duty ratios function of the transmitter magnetic field's frequency $f_{Tx}$. Then, it is valid to express the duty ratios as follows:

$$T_{Tx} = 2D_\alpha + 2D_c + 2D_d \tag{6.2}$$

or, in other form, as:

$$D_\alpha + D_c + D_d = \frac{1}{2}T_{Tx} \tag{6.3}$$

where $D_\alpha$ is the duty ratio of the phase delay interval, $D_c$ is the duty ratio of the inductor energizing interval, and $D_d$ is the duty ratio of the load energy delivery interval, all within a half period of the transmitter ac current $T_{Tx}$. The allowable margin for reactive power control is clearly limited by the range of $D_\alpha$. On the other hand, the range of real power control is limited by the available operation range $D_c$. At the end, Equation (6.3) controls the total range for both duty cycles. It becomes evident that the allowable range for either real power or reactive power control is a trade-off design aspect that needs to be determined and dimensioned upfront depending upon the application.

## 6.3 Characterization and Simulation Results

In order to characterize the converter operation in terms of real and reactive power control, the circuit in Figure 6.2(a) has been tested in a parallel-compensated WPT receiver for the given parameters in Table 6.1. Figure 6.4 illustrates the time-domain waveforms of simulation results at two cases of $D_c$ = 0.1 and $D_c$ = 0.3 both at $D_\alpha$ = 0.36. As noticed, the WPT receiver tank is fully-tuned at both cases, as indicated by the 90° phase lag between $V_{ac}$ and $V_{oc}$. However, the value of the compensation capacitor $C_{Rx}$ that perfectly tunes the receiver tank has been achieved manually. In practice, the compensation capacitor value will be designed and then the controller has to adjust the phase-delay duty ratio $D_\alpha$ accordingly to achieve the fully-tuned case. Furthermore, the inductor current $i_{L1}$ is shown to emphasize the aforementioned operation.

**Table 6.1** Parameters of WPT receiver and split-capacitor converter.

| Parameter | Value |
|---|---|
| WPT receiver | |
| $V_{oc}$ | 1.414 $V_{rms}$ |
| $f_T$ | 100 kHz |
| $L_{Rx}$ | 1.0 μH |
| $C_{Rx}$ | 2.86 μF |
| $R_L$ | 50 Ω (nominal) |
| Split-Capacitor converter parameters | |
| $L_1$ | 3.0 μH |
| $C_{out}$ | 47 μF |
| $C_1$ | 10 μF |
| $C_2$ | 10 μF |

At the first case of $D_c$ = 0.1 and $D_\alpha$ = 0.36, the WPT receiver tank is fully-tuned as shown in Figure 6.4(a), in which the synthesized inductance at the aforementioned duty cycles has been evaluated from the simulation as 23.7 μH which is approximately 7.9 times the actual $L_1$ used in the split-capacitor converter. Moreover, at $D_c$ = 0.1 and $D_\alpha$ = 0.36 as well, an output voltage $V_{DC}$ = 44.2 V has been obtained with a total output power of 39 W which corresponds to an equivalent AC resistance of $R_\alpha$ = 8.1 Ω. On the other hand, the synthesized inductance, at the case of $D_c$ = 0.3 and $D_\alpha$ = 0.36, is evaluated as 8.53 μH which is approximately 2.84 times $L_1$. Furthermore, a total output power of 19 W is obtained with the DC output voltage at 30.4 V. In other words, an equivalent AC resistance of $R_\alpha$ = 3.8 Ω is being effectively *seen* by the receiver tank at $D_c$ = 0.3 and $D_\alpha$ = 0.36. One may note that both $L_\alpha$ and $R_\alpha$ are dependent not only on $D_\alpha$ but also on $D_c$ as well.

Figure 6.5 shows the characterization curves for the converter as a function of $D_\alpha$ at different $D_c$ values. These curves has been obtained as follows: At first, the inductor charging interval Dc has been kept constant while the phase-delay duty ratio is swept from 0.3 to 0.6. At every point, the equivalent reactance is calculated from simulation and the DC output voltage is also obtained. In Figure 6.5(a), the ratio between the equivalent synthesized inductance $L_\alpha$ and the converter DC inductance $L_1$ is shown versus $D_\alpha$, while the output voltage of the converter versus $D_\alpha$ is indicated in Figure 6.5(b).

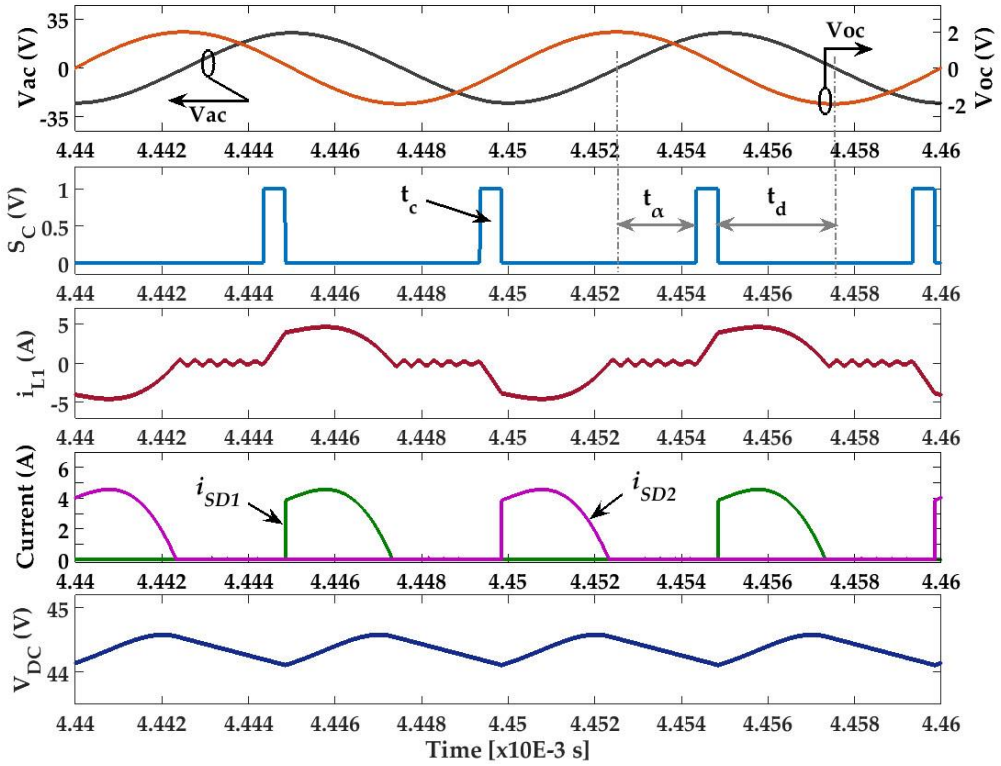


**(a)**

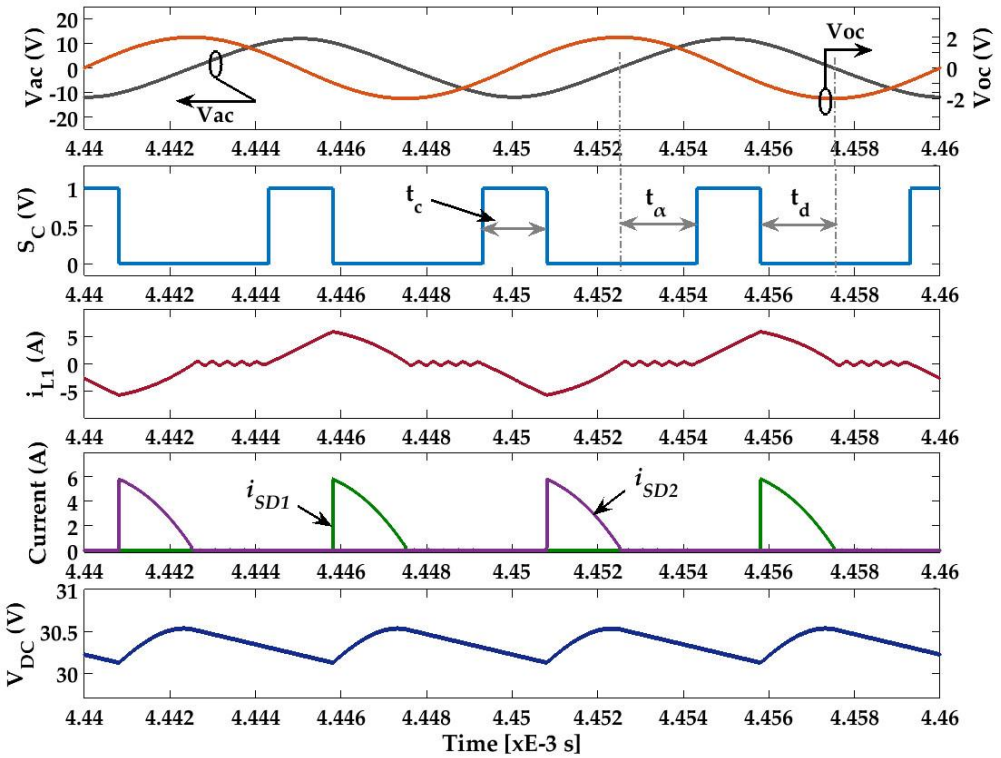


**(b)**

**Figure 6.4** Time-domain waveforms of real power and reactive power control in split-capacitor, **(a)** at $D_\alpha$=0.36 and $D_c$=0.1, **(b)** at $D_\alpha$=0.36 and $D_c$=0.3.

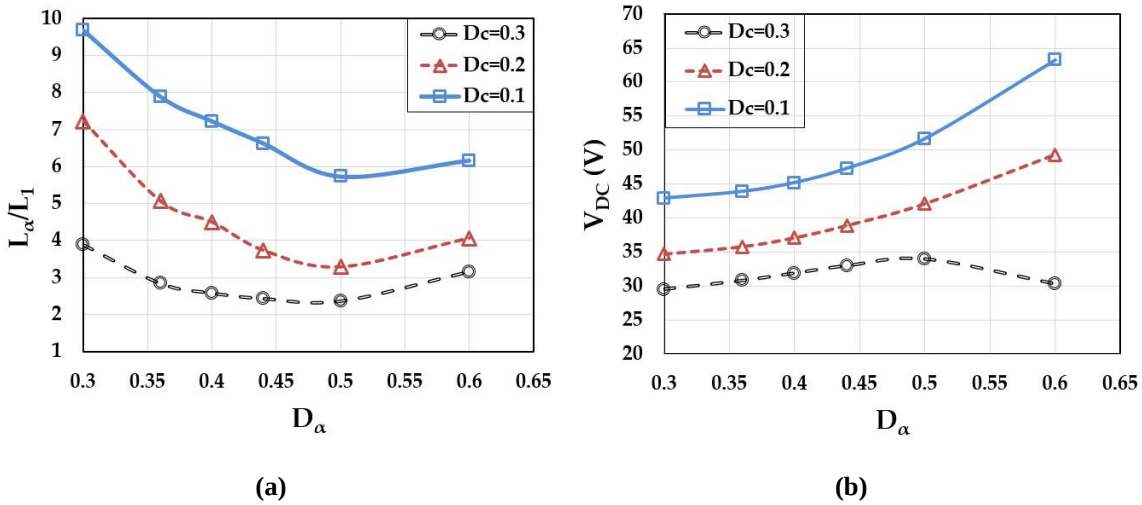


**Figure 6.5** Characteristic curves versus phase-delay duty cycle $D_\alpha$ at $D_c$=0.1, 0.2, and 0.3, **(a)** synthesized inductance ratio $L_\alpha/L_1$, **(b)** DC output voltage $V_{DC}$.

The parameters dependency of the synthesized values of $L_\alpha$ and $R_\alpha$, as illustrated in Figure 6.5, indicate clearly that no matter the real power or reactive power is being controlled, both $D_\alpha$ and $D_c$ have to be adjusted consistently. For instance, the correlative dependency of the real power, represented by means of $R_\alpha$, is shown in Figure 6.6 which indicates that while $R_\alpha$ is mainly function of $D_c$, it also has a minor dependency on the $D_\alpha$ which is a fact that has to be considered while the control loops are designed.

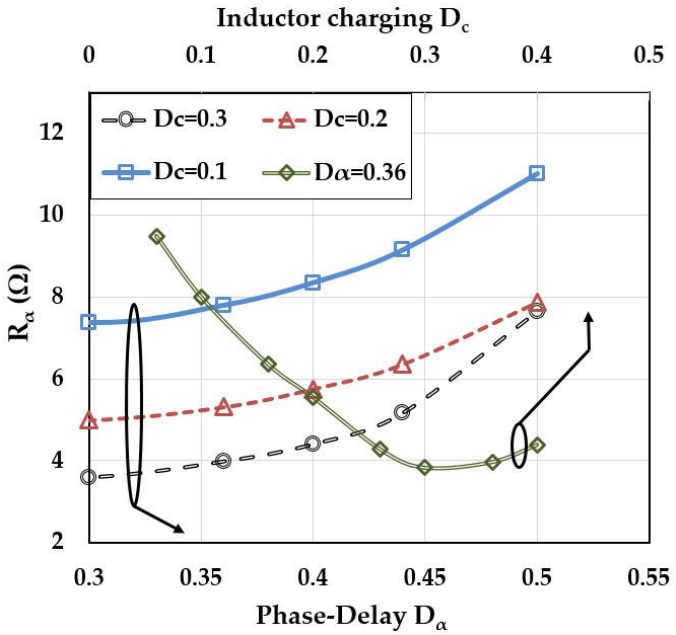


**Figure 6.6** Effective AC resistance of the split-capacitor converter versus $D_\alpha$ and $D_c$.

## 6.4 Insights into Control Design for Simultaneous Real and Reactive Power Control

In Chapter 5, we have proposed and discussed the control design for the split-capacitor converter as a self-tuner and rectifier. In a parallel-compensated WPT receiver, the fact that tracking the phase detection between $V_{ac}$ and $V_{oc}$ has been used for self-tuning control design. The same fact and almost the same control sub-blocks can be employed in this case for reactive power control to ensure maximum power delivery in a fully-tuned receiver tank. Evidently, the controller will be responsible for adjusting the duty-cycle $D_{\alpha}$. In contrast, it has been characterized that the duty-cycle $D_c$ is best used for real power control to supply a regulated voltage to the output load. Consequently, another feedback loop is needed to sense and track the output voltage $V_{DC}$ and adjust $D_c$ accordingly.

Figure 6.7 depicts a conceptual block diagram for real power and reactive power control in WPT receiver. The shown approach utilizes two separate loops, one for tracking the tuning condition of the receiver tank and another one for regulating the output voltage. A similar approach has been used in [2] and [3] for designing control loops for active tuning and output voltage regulation.

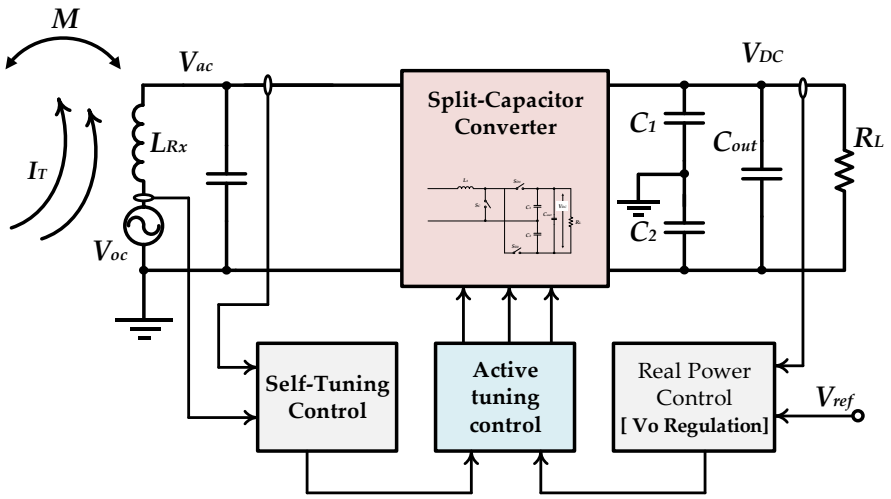


**Figure 6.7** Conceptual block diagram for real power and reactive power control in WPT receivers.

## 6.5 Conclusions

In this chapter, a novel technique has been proposed to enable real power control in the proposed split-capacitor converter that has been discussed in Chapter 5. The same topology and the same technique for active tuning, or reactive power control, has been followed while a major modification in the operation has been proposed and designed. The modified operation adds another control parameter that enables the control of power flow to the output. Consequently, the novel operation has the following benefits:

- It allows reactive power control by adjusting the control parameter $D_\alpha$, thus the WPT receiver tank is self-tuned which maximizes the power received.
- It allows real power control by adjusting the control parameter $D_c$, which indeed makes it possible to obtain a regulated output voltage.
- It maintains the same principles of bridgeless operation, as a main feature of the split-capacitor converter. Thus the AC voltage at the WPT resonant tank is topologically rectified.

The characterization of the proposed approach has shown that the real power and reactive power control cannot be achieved separately as they are both dependent on $D_\alpha$ and $D_c$. Finally, the control design has been discussed conceptually by showing a block diagram for a potential two separate control loops WPT self-tuned system.

## 6.6 References

[1] K. van. Schuylenbergh and R. Puers, *Inductive powering : basic theory and application to biomedical systems*. Springer, 2009.

[2] Z. Pantic and S. M. Lukic, "Framework and Topology for Active Tuning of Parallel Compensated Receivers in Power Transfer Systems," *IEEE Trans. Power Electron.*, vol. 27, no. 11, pp. 4503–4513, 2012.

[3] E. Ozalevli, S. Member, N. Femia, S. Member, G. Di Capua, R. Subramonian, D. Du, J. Sankman, S. Member, and M. El Markhi, "A Cost-Effective Adaptive Rectifier for Low Power Loosely Coupled Wireless Power Transfer Systems," *IEEE Trans. Circuits Syst. I Regul. Pap.*, pp. 1–12, 2017.

Chapter

# 7

# Conclusions, Contributions and Suggested Future Work

## 7.1 Conclusions

The technology advancement and the promising future of a global ubiquitous network, a network that would connect every object, has opened the door for various research lines to enable seamless operation of such network. Among the main research lines is the enabling of autonomous wireless sensor network, which is one of the main pillars of internet of things. The advanced sensing and communication tasks of wireless sensor nodes increase their power requirement, which in turn brings a technology bottleneck that conflicts the high performance with the autonomy of wireless sensor networks. Usually, the main energy source for a sensor node is a small coin battery which makes the power budget very limited and the lifetime of such sensing nodes is shortened accordingly.

Therefore, the main objective of the thesis was to propose the enabling of wireless sensor nodes, as a part of the Internet of Things, by means of wireless power transmission. In contrast to the common techniques of harvesting RF electromagnetic energy, or any other energy harvesting resource, we have shown that near-field resonant-inductive-coupling WPT is a more appealing option for a wide range of applications, more specifically for indoor and industrial applications. However, resonant-inductive-coupling WPT shows a strong dependency on quality factors of the resonating transmitter and receiver circuits. On the other hand, pushing the quality factor while aiming to increase the power transmission range and efficiency is very challenging due to the increased sensitivity of the WPT system. Consequently, the WPT system becomes more vulnerable for detuning problems that would degrade the system performance or even results in a nonfunctional system.

A wide overview and general background about the internet of the things and its main system building blocks and challenges has been presented in Chapter 1. It has been shown that the energy source in a sensor node is one of the most key limiting blocks as it puts more constraints on the performance of the communications and sensing functions according to the limited power budget. Due to the random nature of energy harvesting, a multi-source energy harvesting is probably a reasonable solution. Also the limited power budget from energy harvesting technologies for indoor and industrial applications has been discussed, where WPT is proposed as key enabling technology for power sensor nodes. Accordingly, the problem statement has been given where the current challenges in deploying WPT in dynamic environments has been discussed. It has been shown that a fundamental tradeoff between power transmission range and system reliability exists which is widely mitigated in the literature by employing low quality factor resonant WPT systems.

In Chapter 2, the theory and modelling of WPT technologies has been discussed, including the fundamental and theoretical differences between near-field non-radiative WPT and far-field electromagnetic WPT. Due to the non-radiative confined field nature of near-field WPT, it is well known to have higher efficiency, becoming the most adequate power transmission type for WSNs. On the other hand, resonant-inductive-coupling near-field WPT is a more reliable and efficient technology for power transmission over a distance that extends across several times coil diameters, as compared to the non-resonating alternative. The basic simple compensation topologies for resonant-inductive-coupling WPT have been accordingly discussed. However, the detailed mathematical and system analysis has been only conducted for series-series and series-parallel topologies, because these topologies are the most simple, widely adopted ones. The series-parallel compensation topology has been chosen as the main option for powering WSNs over large distances due to their voltage-boosting characteristics which would help in boosting the very low EMF induced voltage up to several volts. Following the topology selection consideration, the challenges of high-Q sensitivity in parallel-compensated WPT receivers have been studied.

Following the system-aware discussion and analysis carried out in Chapter 2, the motivation of developing an adaptive switch-mode power technique for self-tuning in WPT receivers has been discussed in Chapter 3. The gyrator concept as a variable impedance synthesizer has been revisited. Different gyrator realization topologies have been explored, so that the DAB converter has been chosen among others. The DAB converter is generally well-known for its inherent gyration characteristics, consequently it can be adopted as a natural-gyrator in switch-mode impedance synthesizers. The characterization of the DAB gyrator shows that the gyration ratio is a function of two circuit parameters, namely, the switching frequency and the phase-angle. Consequently, the phase-angle has been considered as a more adequate control

parameter. The characterization results, verified mathematically and by simulation, have shown that the gyration ratio is variable over two valid tuning ranges from 0°– 90° and 90°–180°. Accordingly, a synthesized inductance has been realized by means of DAB converter loaded by a capacitor. Following the characterization of the DAB as a gyrator-based inductance synthesizer, the circuit has been tested in several cases as a proof-of-concept as follows:

- A switch-mode resonator has been formed by using the DAB as a variable inductance synthesizer in a series resonance circuit. The tunability of the synthesized inductance is characterized by varying the phase-angle at different switching frequencies, where the series current magnitude and phase is obtained at every point. As we one can expect, the circuit works at resonance at a single phase-angle/switching frequency combination where the equivalent inductive reactance from the DAB-based synthesizer cancels the capacitive reactance of the series capacitor.
- The potential miniaturization feature of the DAB-based inductance has been integrated in a buck DC-DC converter, which replaces the physical inductance that is usually used in buck converters. By switching the DAB circuit at very high switching frequency (of 50 MHz), it is possible to utilize a very small inductance (only 5 nH) to achieve a synthesized inductance with relatively higher value (150 nH) while a significant reduction in size is guaranteed. By doing so, it has been shown that a similar approach is potentially applicable for miniaturization of magnetic components in buck converters.
- The DAB converter has been also tested in a resonant ripple filter for buck converter, where the synthesized inductance is used in a shunt resonant filter while the tuned point of the filter can be electronically tuned using the DAB's phase-angle. This would help in designing a fixed switching frequency buck converters that mitigate the mistuning problem in resonant ripple filters.

In parallel-compensated WPT receivers, the DAB-based synthesized inductance has been presented as a variable inductance in parallel with the compensation capacitor. Thus, the synthesized inductance can be used to automatically tune the receiver resonance frequency against any mismatch that would cause a resonance frequency drift. To enable self-tuning operation, a control circuit is required to monitor the tuning state of the WPT receiver and react by tuning the DAB converter control parameter, *i.e.* the phase-angle.

In Chapter 4, two control techniques have been presented and evaluated. The first control approach utilizes a dual-loop approach for maintaining the fully-tuned state; the coarse tuning loop first scans the full range of phase-angle tuning from 0° to 90°, where the loops determines how close the tuned point is by tracking the maximum peak voltage of the receiver tank voltage. Complementarily, the fine tuning loop monitors the phase difference between the open-loop induced voltage and the receiver tank output voltage and reacts by fine tuning the phase-angle

of the DAB converter. The fully-tuned state is then determined by the receiver phase angle reaching the steady state value (receiver tank output voltage lagging the induced voltage by 90°). The detailed block description of the proposed dual-loop control has been supported with simulation results that proves the prescribed operation. The performance limitations of this proposal, included transient time and accuracy issues, have been discussed showing that there is a trade-off between the control transient time and accuracy of the tuning process.

In order to improve the accuracy and achieve a faster response, a PLL-like control has been also proposed. The control is fundamentally based on sensing the phase difference between the receiver output voltage and the receiver induced voltage (or receiver coil's current) and subsequently the phase-difference information is compared with a fixed reference to generate the correct duty cycle for a phase-shift modulation block. The validation results of the proposed control shows high accuracy while the control transient time is only limited by the response of the PI compensator. The proposed control, named as Quadrature-PLL based, has been tested at different mismatch percentages in the receiver circuit, for which the overall goal of a self-tuned WPT receiver was promisingly achieved. Furthermore, the transistor-level implementation of the DAB converter and the proposed control has been designed and validated using XFAB 0.18µm process on Cadence virtuoso. The power stage design and power MOSFETs sizing has been optimized for high efficiency operation without compromising the total size of the chip. The tested results based on foundry's accurate models have shown that an average efficiency of 75% is obtained over a wide range of mistuning cases in circuit components. Higher efficiency is also achievable by up-sizing the power MOSFETs, however the total size of the chip would increase considerably. For a general evaluation for the DAB-based self-tuning approach, the different performance aspects has been discussed, where the main drawback of high number of components is highlighted and compared with other solutions in the literature.

In the last part of Chapter 4, the discussion of performance aspects of gyrator-based DAB synthesized inductance approach has illustrated that despite the effectiveness of the control technique in achieving a self-tuned WPT receiver, the whole DAB circuit and the control circuits are used as an auxiliary automatic tuning block. This means that, in a complete WPT receiver circuit, the receiver resonant tank should have a rectifier circuit followed by a voltage regulator in order to supply the load or the battery by the required voltage. In this case, the DAB-based self-tuning approach is only used for automatic tuning with no power exchange.

Consequently, in Chapter 5, we have proposed a novel technique that utilizes switch-inductor converters in order to provide built-in dual functionality: 1) automatic tuning by means of variable reactive component synthesis; 2) AC/DC voltage regulation. Accordingly, the power density would be increased by combining dual functions using the same converter circuit. The fundamental concept depends on switching an inductor between the receiver resonant tank and

the load according to a variable phase-delay. Thus, the fundamental inductor current constitutes a variable inductive reactance that is a function of the phase-delay.

The characterization results of the phase-controlled switched-inductor converter indicated that the proposed converter operation can be modeled by a variable inductance in parallel with a variable resistance, where the variable inductance represents the tuning effect and the variable resistance represents the voltage rectification and energy delivery to the load. Integrating the proposed phase-controlled switched-inductor in a parallel-compensated WPT receiver has been validated. The results have shown that the phase-delay can be used effectively to tune the WPT receiver circuit by synthesizing a variable reactance. However, it has been also shown that the output power delivered to the load is not constant due to the variation that occurs in the equivalent resistance, which is similarly a function of the phase-delay.

Finally, in Chapter 6 we have proposed a modification to the split-capacitor converter topology to allow real power control as well as self-tuning reactive power control by means of the same topology. Typically, two different stages for active tuning and voltage rectification/regulation are used in power conditioning systems of WPT receivers. The proposed operation assists in decreasing the size and cost of the power conditioning front-end by enabling multiple functionalities into the same compact circuit structure. The time-domain results have shown that the proposed operation offers a reasonable range for self-tuning in the WPT receiver tank while the output voltage is regulated simultaneously. However, the proposed modification imposes some limitations over the self-tuning range if a specific output voltage is required while the limit for output voltage control is reached.

## 7.2 Contributions of This Thesis

The main contribution of the thesis work can be summarized as follows:

- Analyzing the effect of resonant tank high quality factors upon the sensitivity of parallel-compensated WPT receivers, showing the effect on maximum power transmission due to mismatch in components.
- Proposing and developing the switch-mode gyrator-based variable reactive impedance synthesis, where the DAB converter has been chosen as switch-mode natural gyrator topology. The developed circuit has been validated in several switch-mode power conversion applications. Despite the complexity, the wide tunability and simplicity of the control are very promising features for other applications.
- Proposing a dual-loop control scheme for self-tuning in WPT receivers. The coarse tuning loop tunes the variable synthesized inductance by coarsely searching for the phase-angle that corresponds to the maximum envelop peak voltage. The fine tuning

loop then proceeds by tuning for the accurate phase-angle for a fully-tuned WPT receiver tank.

- Developing a quadrature-PLL (Q-PLL) control for the gyrator-based synthesized inductance that outperforms the dual-loop control. The Q-PLL control dynamically tunes the phase-angle of the DAB converter in accordance to the phase-difference information sensed at the WPT receiver tank.
- Proposing a phase-controlled switched-inductor converter for dual functional approach that combines active tuning and voltage rectification within the same converter cell. The developed control dynamically tunes the WPT receiver circuit by switching an inductor with a relative phase in accordance to the resonant tank voltage. The same inductor is used to rectify the energy from the WPT receiver tank to the load.

The above contributions have been published in several articles and conference papers as a result of this thesis. In addition, one patent has been filed based on the gyrator-based self-tuning approach. The list of already published journals and conference papers are as follows:

**Journals and Conferences**:

[1] M. Saad and E. Alarcón, "Insights into Dynamic Tuning of Magnetic-Resonant Wireless Power Transfer Receivers Based on Switch-Mode Gyrators," *Energies 2018*, Vol. 11, Page 453, vol. 11, no. 2, p. 453, Feb. 2018.

[2] M. Saad, H. Martinez-Garcia, P. Alou, and E. Alarcon, "A PLL control for self-tuning of parallel wireless power transfer receivers utilizing switch-mode gyrator emulated inductors," in *2017 19th European Conference on Power Electronics and Applications (EPE'17 ECCE Europe)*, 2017, p. P.1-P.10.

[3] M. Saad, E. Bou-Balust, and E. Alarcon, "Switch-mode gyrator-based emulated inductor enabling self-tunability in WPT receivers," in *2017 IEEE International Symposium on Circuits and Systems (ISCAS)*, 2017, pp. 1–4.

[4] M. Saad and E. Alarcon, "Tunable switch-mode emulated inductive elements for enhanced power converter miniaturization," in *IECON 2016 - 42nd Annual Conference of the IEEE Industrial Electronics Society*, 2016, pp. 1184–1189.

[5] M. Saad, N. Egidos, E. Bou-Balust, and E. Alarcon, "On tunable switch-mode reactive networks: A gyrator-based resonator emulation," in *2016 IEEE International Symposium on Circuits and Systems (ISCAS)*, 2016, vol. 2016–July, pp. 642–645.

**Patents**:

[6] M. Saad, E. Bou-Balust, and E. Alarcon, "System and method for tuning wireless power transfer receivers," 2017/2 ES. App. Number: P201730148

## 7.3 Suggested Future Work

The work carried out in this thesis has focused in investigating the sensitivity and reliability issues in high quality factor WPT receivers due to mistuning in the resonant compensation tanks. Consequently, two different techniques have been proposed and verified for self-tuning of WPT receivers. The suggested future work driven from the two techniques can be listed as follows:

**Switch-mode gyrator-based self-tuning:**

- In the presented dual loop control of gyrator-based reactive element synthesis, the problem of reliability due to fixed phase-shift-based scanning could be mitigated by designing an improved version. In the modified version, it is possible to add a variable phase-shift step that is adapted as the system gets closer to the correct fully-tuned point.
- It is also possible to combine the dual loop into one loop by simply applying the variable phase-shift scanning while the orientation and step size is decreased by monitoring the phase lagging relation between $V_{oc}$ and $V_{ac}$.
- The DAB topology has been selected based on the unique feature of natural gyration without an external control. However, the complexity of the topology in the proposed function of complex impedance synthesis imposes some limitation on the total efficiency of the WPT link. The total size also remains debatable unless a chip design integrating the whole solution is realized. Other topologies with less component count and gyrators has to be investigated, such that the high efficiency and reduced size features are combined with unique features of switch-mode gyrators.
- A simple PI controller has been designed for stabilizing the self-tuning control which has been found sufficient if we consider the slow dynamics nature of mistuning that would occur in the WPT receiver tank. However, in a very fast dynamic environment, the controller would fail to retune the receiver tank. Consequently, it is more reasonable to derive a small-signal model for the DAB-based converter in order to ensure robust control design that performs fast enough.

**Phase-controlled converters for self-tuning:**

- As we noted in the phase-controlled converters operation, the output power delivered to the load, represented by an AC resistance synthesized by the converter $R_{\alpha}$, is an uncontrolled variable every time a mistuning occurs and the control retunes the system back to fully-tuned condition. However, it is crucial to derive mathematically the exact formulas of $L_{\alpha}$ and $R_{\alpha}$ in terms of the phase-delay angle, such that a quantitative analysis for the expected output power over the entire tuning range is possible during the design task.

- The selection of the switch-inductor converter or split-capacitor converter for the proposed phase-controlled variable reactive element synthesis has been considered due to their capability of processing AC signals directly without the need of a bridge for AC-DC rectification. However, the use of bidirectional switches, which are capable of handling current in both directions, becomes inevitable. It would be more advantageous to employ simple topologies such as boost converters or buck-boost converters to achieve the same operation while being preceded by a separate rectifier circuit. Thereby, the advanced gate drive circuits for bidirectional switches would be avoided at the expense of lower efficiency and reduced power density.

**Real power and reactive power control in phase-controlled converters:**

- The proposed real power control and reactive power control operation needs to be mathematically analyzed in order to obtain accurate expressions for $L_\alpha$ and $R_\alpha$ specially after adding another control parameter $D_c$. A robust and reliable control design would not be feasible unless the interrelated dependency of $D_c$ and $D_\alpha$ is clearly established.
- The novel operation of utilizing a single-stage for rectification, tuning, and voltage regulation has been already discussed in Chapter 6. However, the control design for self-tuning and automatic load power control is required.

# On-Chip Adaptive Power Management for WPT-Enabled IoT

**Abstract:** Among other IoT's pillars, wireless sensor network (WSN) is one of the main parts comprising massive clusters of spatially distributed sensor nodes dedicated for sensing and monitoring environmental conditions. The lifetime of a WSN is greatly dependent on the lifetime of the small sensor nodes, which, in turn, is primarily dependent on energy availability within every sensor node. Predominantly, the main energy source for a sensor node is supplied by a small coin battery which has a limited capacity in essence. Consequently, powering the sensor nodes becomes a key limiting issue, which poses important challenges for their practicality and cost. Therefore, in this thesis we propose enabling WSN, as the main pillar of IoT, by means of resonant inductive coupling (RIC) wireless power transfer (WPT). Mainly, the thesis deals with technical challenges of enabling efficient contactless energy delivery at distant range by means of high quality factor RIC-WPT system. Therefore, the main thesis objective is to develop and design an adaptive efficient switch-mode front-end for self-tuning in WPT receivers in multiple receiver system.

**Keywords:** Internet of Things; Wireless Sensor Networks; Wireless Power Transfer; Resonant Inductive Coupling; Active Tuning; Efficient; Switch-Mode